Neutron Stars and the Determination of the Dense Matter Equation of State

Sebastien Guillot

Department of Physics
McGill University
Montréal, Québec
Canada

July 2, 2014

A Thesis submitted to McGill University
in partial fulfillment of the requirements of the degree of
Doctor of Philosophy

À mon père et à ma mère.

Contents

List of Figures

List of Tables

Abstract

A physical understanding of the behaviour of cold ultra-dense matter – at and above nuclear density – can only be achieved by the study of neutron stars. The surface thermal emission from neutron stars in quiescent low-mass X-ray binaries (qLMXBs) inside globular clusters has proven useful for that purpose. These systems rely on the relatively precisely measured distances to globular clusters to produce measurements of the radiation radius of neutron stars R_∞, the radius as seen from infinite distance. Such measurements can be compared to the Mass-Radius relation resulting from proposed dense matter equations of state. Individually, the R_∞ measurements from qLMXBs do not produce stringent constraints on the dense matter equation of state. However, when several of these qLMXBs spectra are combined in a coherent manner, they can lead to useful constraints on the dense matter equation of state.

This work first presents the discovery of a new spectrally identified qLMXB inside a globular cluster, and the spectral analysis of high signal-to-noise ratio data from another qLMXB, leading to a precise R_∞ measurement. Then, spectra from multiple qLMXBs hosted in globular clusters are combined in a simultaneous analysis using a Markov-Chain Monte-Carlo approach, placing new constraints on the dense matter equation of state. This method and the Bayesian approach developed in this analysis permits including all quantifiable sources of uncertainty (e.g., in the distance, the hydrogen column density) to produce the most conservative constraints on the dense matter equation of state. Finally, this Bayesian approach is modified and adapted to quantitatively reject or confirm a selection of proposed equations of state.

Résumé

Une compréhension physique du comportement de la matière froide ultra-dense – à des densités supérieures à celle du noyau atomique – peut uniquement être obtenue par l'étude des étoiles à neutrons. L'émission thermique de surface des étoiles à neutrons des binaires X de faible masse en quiescence (qLMXB, pour *quiescent low-mass X-ray binaries* en anglais) localisées dans les amas globulaires sont très utiles à cette fin. Grâce aux distances relativement bien connues des amas globulaires hébergeant ces systèmes binaires, ces dernières peuvent engendrer des mesures du rayon projeté des étoiles à neutrons, R_∞, le rayon tel que vu par un observateur à l'infini. Ces mesures peuvent ensuite être comparées aux relations Masse-Rayon qui résultent des équations d'état proposées. Cependant, individuellement, les mesures de R_∞ des qLMXBs fournissent difficilement des limites observationnelles sur les différentes théories de la matière dense. Par contre, en combinant d'une manière cohérente les spectres X de plusieurs de ces qLMXBs, des limites utiles peuvent être obtenus pour les équations d'état de la matière dense.

Cette thèse présente, en premier lieu, la découvert d'une nouvelle qLMXB dans un amas globulaire, identifiée grâce à son spectre X. Est également rapportée, l'analyse spectrale d'une autre qLMXB ayant des spectres X à grand rapport signal sur bruit. Cette analyse débouche sur une mesure précise du rayon R_∞ de l'étoile à neutrons dans ce système qLMXB. Ensuite, les spectres de plusieurs qLMXBs localisées dans des amas globulaires sont combinés dans une analyse simultanée, en utilisant une approche de Monte-Carlo par chaînes de Markov. Avec cette méthode, de nouvelles limites sur l'équation d'état de la matière dense sont obtenues. De plus, cette méthode et l'approche Bayésienne développées dans cette thèse permettent d'inclure toutes les sources quantifiables d'incertitude (par exemple, pour la distance, ou pour la densité de colonne d'hydrogène) afin de produire les limites les plus fiables sur l'équation d'état de la matière dense. Enfin, cette méthode est modifiée pour être adaptée afin de rejeter ou de confirmer de manière quantitative une sélection d'équations d'état proposées.

Un résumé détaillé pour les non-spécialistes est proposé en appendice de cette thèse (Appendix A).

Acknowledgments

First, I would like to thank my supervisor, Bob Rutledge. I am truly grateful for his availability, his patience, and his many pieces of advice about research, career choices, or other aspects. His resolute and rigorous approach toward research surely guided me on the way to become a better scientist over the past seven years.

During these years at McGill, I have had the chance to interact on countless occasions with faculty members of the physics department. I am thinking in particular about Ken Ragan, with whom I shared many discussions. I would also thank Vicky Kaspi for her support of the astronomy outreach activities at the Physics department.

I have a particular thought for friends and colleagues of AstroMcGill. For more than two years now, we have shared our passion of astronomy with kids of all ages and adults alike. It was not always easy, but it was surely rewarding.

Friends and colleagues, at McGill or those I met during conferences, also ought to be acknowledged, for the many useful and less useful discussions about neutron stars, research, science in general, and many other topics. This statement is general enough that I am not forgetting anyone.

Last, but definitely not the least, I would like to acknowledge the Gouvernment of Canada / Gouvernement du Canada, which provided support during my PhD via the Vanier Canada Graduate Scholarship program.

Contributions of Authors

Chapters 4–6 of this thesis correspond to three articles published in the Astrophysical Journal (ApJ), and Chapter 7 is an article to be submitted:

- **Chapter 4** was published as: S. Guillot, R. E. Rutledge, E. F. Brown, G. G. Pavlov, and V. E. Zavlin. *Discovery of a Candidate Quiescent Low-mass X-Ray Binary in the Globular Cluster NGC 6553.* ApJ, 738:129, Sept.2011.

- **Chapter 5** was published as: S. Guillot, R. E. Rutledge, and E. F. Brown. *Neutron Star Radius Measurement with the Quiescent Low-mass X-ray Binary U24 in NGC 6397.* ApJ, 732:88, May 2011.

- **Chapter 6** was published as: S. Guillot, M. Servillat, N. A. Webb, and R. E. Rutledge. *Measurement of the Radius of Neutron Stars with High Signal-to-noise Quiescent Low-mass X-Ray Binaries in Globular Clusters.* ApJ, 772:7, July 2013.

- **Chapter 7** will be submitted as a short letter in Nature, entitled: *Excluding proposed dense-matter equations of state with quiescent low-mass X-ray binaries.*

While I am the primary author of these articles, I would like to acknowledge the contributions of the co-authors for the preparation of these manuscripts:

- George G. Pavlov, Mathieu Servillat, Natalie A. Webb and Vyacheslav E. Zavlin for their very useful comments and suggestions that improved the original manuscripts.

- Edward F. Brown for his very useful comments and suggestions and for the calculation of the core temperature of the neutron star in the quiescent low-mass X-ray binary in NGC 6397 (Section 5.4).

- And finally Robert E. Rutledge for his patience reading the manuscripts and providing many improvements to the original text. I would also like to acknowledge him for the original idea that led to the novel analysis presented in Chapters 6 and 7. He also performed the variability analysis in Chapter 5.

In this thesis, the two introductory chapters (Chapters 1 and 2) are original work providing a literature review serving as a comprehensive introduction to the Chapters 4–7. Nonetheless, for this thesis to be a cohesive document, and to avoid redundancy between the introductions of the published articles, I have used part of the original text in these introductions to write Chapter 2. Finally, small parts of Sections 2.4.3, 3.4.1 and 3.4.2 have been published in my M.Sc. thesis.

List of Abbreviations

2MASS	–	Two-Microns All Sky Survey
BI	–	Back-Illuminated
CCD	–	Charge-Coupled Device
CDF	–	Cumulative Distribution Function
CMD	–	Colour Magnitude Diagram
CV	–	Cataclysmic Variable
DCH	–	Deep Crustal Heating
DOF	–	Degrees of Freedom
EEF	–	Enclosed Energy Fraction
EPIC	–	European Photon Imaging Camera
EoS	–	Equation of State
FI	–	Front-Illuminated
FWHM	–	Full Width at Half Maximum
GC	–	Globular Cluster
HB	–	Horizontal Branch
HST	–	*Hubble Space Telescope*
INS	–	Isolated Neutron Star
LMXB	–	Low-Mass X-ray Binary
MS	–	Main Sequence
MC	–	Monte Carlo
MCMC	–	Markov-Chain Monte Carlo
NASA	–	National Aeronautics and Space Administration
NS	–	Neutron Star
NHP	–	Null Hypothesis Probability $p_{\rm null}$
PL	–	Power Law
PRE	–	Photospheric Radius Expansion
PSF	–	Point Spread Function
qLMXB	–	Quiescent Low-Mass X-ray Binary
RGB	–	Red Giant Branch
S/N	–	Signal-to-Noise Ratio
TT	–	Terrestrial Time
WD	–	White Dwarf

Neutron Stars and the Determination of the Dense Matter Equation of State

1

Introduction

This chapter begins with an detailed summary of the work, written without technical terminology. Section 1.1 is intended for non-specialists, introducing the necessary background and presenting the main results of this thesis work. Scientific research should be shared and made accessible to the general public. Astronomy and astrophysics have the chance to naturally attract people of all ages, mostly with stunning images and mind-blowing facts. Section 1.1 does not attempt to convince the reader of the usefulness of this research, but rather attemps to explain this work in a comprehensible way, to be able to reach as many as possible. The summary does not contain any reference to previous publications, nor any acronyms that would hinder the reading. It is also provided in French for francophone readers (Appendix A).

After the non-technical summary, a section presents a short historical overview of dense matter and neutron stars over the last 100 years, since the theoretical prediction of the neutron. This historical review serves as an introduction to the section that follows it, where this thesis work is motivated in a more general context. Finally, a short section presents each of the chapters.

1.1 A Summary for Non-Specialists

This research consists, in a certain way, in performing autopsies of dead stars. What is inside? What type of matter composes their core? These are two questions to which astrophysics and nuclear physicists do not have a clear answer. Unlike a medical investigator who can look directly inside a corpse, it is impossible to directly look

inside stars, dead or not. There are however indirect observational methods that are briefly described. But before that, it is important to explain what is called a dead star, and to motivate the reason behind these autopsies.

A star is "dying" when it runs out of the material fueling the nuclear reactions happening in its core during its lifetime. When this happens, the delicate balance between the inward force of gravity and the outward pressure of nuclear burning is broken. The fate of a dying star then depends on its initial mass:

- A low-mass star, like our Sun, will eject most of its outer layers in a colourful nebula and leave behind an object called white dwarf, a dead star without nuclear reactions. These are dense slowly cooling objects with about half the mass of the Sun compressed in a sphere about the size of the Earth. That corresponds to densities about 1 million times that of water[1].

- A star with a higher mass (more than eight times the mass of our Sun) dies in a radically different, more dramatic manner by exploding into a supernova. During the supernova explosion, the core of the progenitor star gets compressed to incredible densities, due to gravity. What is left after the supernova depends again on the initial mass of the progenitor star. The supernova explosions of the most massive stars lead to the formations of black holes; these mysterious compact objects that attract everything, even light, around them without any chance to ever escape. But if the dying star is not massive enough to form a black hole (but still above eight times the mass of our Sun), the remnant of a supernova explosion is a neutron star, the objects of interest in this thesis.

These objects are composed of the densest form of matter than we know. Anything denser, i.e., more compact, than a neutron star would collapse to a black hole, from which it is impossible to obtain any direct observational information.

[1] A teaspoon of white dwarf would have a mass of 5000 kg.

Figure 1.1 – This illustration compares the size of a neutron star with the size of a city, such as Montréal. Source: *NASA*'s Goddard Space Flight Center.

In that sense, neutron stars are more interesting than black holes, since they actually have an observable surface allowing astrophysicists to investigate many of their properties. Nonetheless, they are mysterious objects. Extreme densities have been mentioned above: try to imagine – if it is even possible – the mass of the Sun[2] compacted into a sphere roughly the size of Montréal (Figure 1.1). A teaspoon of neutron star matter would have a mass of about three billions metric tons. This is because the atoms have been compressed so much that all the empty space inside atoms (and there is a lot of it at normal densities) has been replaced by the nuclei of other atoms. A simple analogy would be to completely fill up the interplanetary space in our Solar System with many planets. No laboratory on the Earth is anywhere close to reproducing matter with such densities. In fact, neutron stars are the only place in the Universe where this type of matter exists. Therefore, observing neutron stars is the only way to understand how such dense matter can exist. This quest aims at finding one of the missing pieces in the grand scheme of matter.

[2]Our Sun has a mass of 2×10^{30} kg, that is 2,000,000,000,000,000,000,000,000,000,000 kg, or 2 billions of billions of billions of metric tons!

In the absence of experimental data from laboratories, nuclear physicist are proposing a plethora of theoretical models to describe the behaviour of ultra-dense matter, i.e., how the pressure of matter changes when the density increases. Without means to test those experimentally, neutron stars provides the laboratories needed. There are several ways to probe the interior of neutron stars and discriminate between the multiple nuclear physics theories. The most common method is to measure the radii and/or the masses of neutron stars. Indeed, each of the proposed theories corresponds to very specific mass-radius relations for neutron stars. Therefore, measuring the masses and radii of neutron stars allows us to tell whether a theory appropriately describes ultra-dense matter or not.

The method used in this thesis consists in measuring the radius of neutron stars. This is basically done by measuring how hot and bright the surfaces of neutron stars are. A model of a neutron star surface can then help us convert the brightness into the actual radius of the neutron star. However, this method requires knowing the distance to the object observed. This is a frequent issue in astronomy. Without knowing the distances to astronomical objects, it is difficult to measure most of their properties. It is like looking at a light source (without any other point of reference) and trying to estimate how bright it is. Is it a dim and nearby light, or is it a bright and distant light? To answer this question, our brain interprets the surroundings to deduce the distance or the brightness. This is the same in astronomy where researchers need independent distance measurements in order to determine the brightness of objects.

Back to neutron star radius measurements: in this thesis, neutron stars inside clusters of stars are considered. Astronomers have developed independent techniques to measure the distances to star clusters. Therefore, neutron stars inside clusters have well measured distances, and therefore intrinsic brightnesses, compared to the other neutron stars for which we do not know the distance, for example, those wandering in our Galaxy. With those well known brightnesses, we deduce the radii of the neutron stars we observe.

However, there is another complication. For this radius-measurement method to work properly, we need to observe neutron stars with a quiet behaviour. Most neutron stars that could be use for radius measurements are in very active binary systems, with dramatic explosions on their surface, making the measurement of the radius difficult. Neutron stars often have a bright disk of matter revolving around them which dominates the brightness and therefore complicates the observation and the radius measurement. To avoid this problem, we can only use inactive, or *quiescent* neutron stars for which the emission we see is well understood and comes exclusively from the surface. There are only a few of these systems with known distances, i.e., inside the star clusters of our Galaxy.

From these few sources, we measured the radius of neutron stars to be between 7 km and 11 km (the size of a large city). This turns out to be smaller than expected from most of the theoretical models proposed by nuclear physics. The range of uncertainties of our result is still large and therefore there is still a lot of work to be done to obtain better measurements. But if such small values of the radius were to be confirmed, it might require revisiting the theory of ultra-dense matter. There are several ways to reduce the uncertainties in our radius measurement. For example, the distances to the clusters hosting the neutron stars we use are not perfectly known, and this lack of certainty of the distance measurements reflects on the radius measurement.

Overall, a lot more work remains to be done in the quest to understand ultra-dense matter, but this thesis work has made an important step toward it.

1.2 Historical Background

The historical background provided here first presents the physical and astrophysical knowledge related to neutron stars before their discovery. It is then followed by a section describing the first observations of neutron stars.

1.2.1 Before the First Observations of Neutron Stars

A short history of nuclear matter (a collection of neutrons and protons held together) is presented here. While it is not meant to be an exhaustive review of nuclear physics, it is an overview of the state of knowledge of nuclear physics before the first observational discovery neutron stars. The theoretical prediction of these objects preceded their actual discovery by more than 35 years. This section also serves as a precursor to Section 1.3 which motivates the work performed during this PhD thesis. This historical overview arbitrarily begins with the discovery of the proton and the neutron by Lord Ernest Rutherford.

In his formulation of the atomic structure, Rutherford described the atom as a *"central positive charge $N \times e$ surrounded by a compensating charge of N electrons"* (Rutherford, 1911). This deduction from the "gold foil experiment" was then followed in 1917 by experiments showing that the hydrogen nucleus was a building block of all heavier nuclei (Rutherford, 1919, 1921). It was realized afterwards that the hydrogen nuclei extracted from heavier atoms during the experiment were in fact protons. In 1920, Rutherford proposed the existence of neutrons as a way to reconcile the measured atomic masses with the number of positive charges (protons) observed in nuclei (Rutherford, 1920). Before the experimental confirmation of this prediction, Landau speculated about stars denser than white dwarfs in which atomic nuclei are compacted to form *"one gigantic nucleus"* (Laudau 1932, cf. Haensel et al. 2007). In the absence of proof regarding the existence of neutrons, Landau also recognized that such a star would violate quantum mechanics by allowing electrons inside nuclei (cf. Haensel et al., 2007).

Twelve years after Rutherford's prediction of neutrons, their existence was demonstrated by J. Chadwick (Chadwick 1932, Physics Nobel Prize in 1935, c.f. Haensel et al. 2007). Shortly after, the first attempt at describing dense nuclear matter showed that the compression of matter implied a neutronization of the nuclei (Sterne, 1933). The existence of compact objects, almost exclusively composed of neutrons was pre-

dicted only a few years after the experimental discovery of neutrons. These compact objects, named neutron stars, were postulated to result from the supernova explosions of massive stars (Baade and Zwicky, 1934). A first estimate of the density inside neutron stars was then proposed to be $\rho \sim 10^{12} - 10^{15}\,\mathrm{g\,cm^{-3}}$ (Hund, 1936). The first theoretical model of neutron stars quickly followed. By solving the equations of stellar stucture for an ideal gas of free neutrons in the relativistic regime (a somewhat crude approximation), neutron stars were predicted to have a maximum mass of $M_{\mathrm{NS,max}} = 0.71\,M_\odot$ for $R \sim 10\,\mathrm{km}$ (Oppenheimer and Volkoff, 1939). Because such a mass was less than the $1.4\,M_\odot$ predicted maximum mass for white dwarfs supported by electron degeneracy pressure (Chandrasekhar, 1931), it was remarked that neutron stars would not form from the collapse of ordinary stars. Nonetheless, it was also realized that higher maximum neutron star masses could be attained should some repulsive neutron-neutron interaction exists. At the time, without more knowledge of nuclear forces, more realistic models for dense matter could not be proposed.

While neutron stars were a purely theoretical prediction, describing the interactions between protons and neutrons (nucleon-nucleon interactions) to understand the structure of atomic nuclei had been at the heart of nuclear physics. What held the nucleons of atoms together remained a mystery to physicists. In other words, why were the protons of a nucleus, positively charged, not repelling each other? Another force, stronger than the electromagnetic repulsion was necessary to explain the observed stability of nuclei. The first efforts to explain nucleon-nucleon interactions were made by Yukawa, in which the mediating particle between two nucleons was a meson (Yukawa, 1935). He received the Nobel Prize for his theoretical work twelve years after, in 1949, when the confirmation of the meson exchange was demonstrated by the experiments of Powell, who also received the Nobel Prize the following year. With this newly discovered attractive force, the stability of atoms – not disintegrating under the electromagnetic repulsion – was explained. However, the mediator particle of this new interaction was not a fundamental particle as predicted by Yukawa.

By demonstrating the importance of the nuclear force and introducing effective nucleon-nucleon interactions (developed by Skyrme 1959) in the equation of the neutron star structure, it was shown that the maximum neutron star mass could be as high as $2\,M_{\odot}$(Cameron, 1959). This reconciled neutron stars with the standard stellar evolution framework in which they form after the collapse of massive stars (see Section 2.1.1). At around the same time, the first propositions were made that neutron stars actually contained more exotic forms of matter, such as hyperons (Salpeter, 1960; Ambartsumyan and Saakyan, 1960). In addition, the superfluid state of the neutron star interior was suggested (Migdal, 1959), before it was realized that only the outer parts of neutron stars could experience superfluidity, because the core was too dense to support superfluidity (Wolf, 1966).

As the number of known particles grew in the 1940s and 1950s, it became clear that the proton, neutron, and other known particles, were not the most basic particles, in other words, they were composed of smaller, more fundamental, particles. The existence of quarks was theorized in 1964 (Gellmann, 1964; Zweig, 1964), and the first observations of quarks as the building blocks of particles were made a few years later (e.g., Bloom et al., 1969). The discovery of quarks, amongst other discoveries, led to the development of the standard model of particle physics and quantum chromodynamics in which quarks have an additional property called "colour" that other particles do not have (Peskin and Schroeder, 1995), and hadrons (protons, neutrons, mesons, etc...) are composed of quarks held together by gluons, the mediating particle of the "strong force" or quantum chromodynamics. In addition, the force responsible for keeping nucleons together was renamed the "residual strong force" (or nuclear force), which is mediated by pions (or pi mesons), as theorized by Yukawa. The nuclear potential of the residual strong force is attractive at distances of $\sim 1 - 2\,\mathrm{fm}$, holding hadrons together, but highly repulsive at smaller distances $< 0.7\,\mathrm{fm}$. Shortly after the discovery of quarks, the idea of a compact star composed of quarks instead of neutrons was also put forth (Ivanenko and Kurdgelaidze, 1965, 1969; Pacini, 1966).

Many unsolved problems of nuclear physics remain to be explained. For example, quarks only exist in hadrons and cannot be observed individually. The reasons for this "confinement" of quarks are still unknown. In addition, the nature of the nuclear force is still not well understood, and while the two-nucleons interaction can now be calculated, the stability of more complex nuclei remains unexplained. Section 1.3 places the study of neutron stars in the context of the quest to understand quantum chromodynamics and nuclear forces. But before, the following section discusses the first observations of neutron stars.

1.2.2 Since the First Neutron Stars Discovered

Almost forty years passed between the theoretical hypothesis of the existence of neutron stars (Baade and Zwicky, 1934) and the observational discovery of these objects. In 1962, one of the first X-ray satellites observed the first X-ray source outside of the Solar System, Scorpius X-1 (Giacconi et al., 1962). However, the neutron star nature of this source was not immediately recognized. A few years later, additional X-ray and optical observations led to the suggestion that Scorpius X-1 is an accreting neutron star, based on observations suggesting a hot plasma ($T \sim 5{\times}10^8\,\mathrm{K}$) confined to an emission area having a radius of $\sim 10\,\mathrm{km}$ (Shklovsky, 1967).

During the same year, on August 6th, 1967, Jocelyn Bell recorded on paper, at the Mullard Radio Astronomy Observatory in the United Kingdom, the signal from a source of astronomical origin. Later that year, the improved time resolution of the radio telescope allowed for the discovery of regular radio pulses from this source, recurring every 1.33 seconds. After the discovery of a few similar pulsating sources in the sky, it became clear that these were of cosmic origin and not caused by radio-interference. In 1968, a publication reported the discovery and suggested that these radio pulses originated from compact objects (Hewish et al., 1968). It was also immediately recognized that these objects would be valuable targets to study the behaviour of dense nuclear matter. Since then, radio observatories dramatically improved in sen-

sitivity and time resolution. They have led to the detection of over 2000 radio pulsars (Manchester et al., 2005) with a wide range of periods (Section 2.1.3).

Not only did the discovery of neutron stars confirm a 40-year-old theoretical prediction, but it also provided physicists with unique laboratories to test proposed nuclear physics theories which sometimes contradict each other. In the second half of the 20^{th} century, nuclear physics developed the tools to calculate the interactions of matter (nucleons or exotic particles) at increasingly larger density. However, the density expected in the core of neutron stars was and still remains out of reach of calculations and accurate predictions.

1.3 The Big Picture, or Why Study Neutron Stars?

The understanding of the behaviour of cold dense matter, such as that found in the core of neutron stars, still eludes nuclear physicists and astrophysicists alike. The behaviour of bulk nuclear matter is generally described by an *equation of state*, i.e., the relation between pressure and density of matter. Here, the term "cold dense matter" is meant to describe degenerate matter[3] under the most extreme conditions, at densities close to and above normal nuclear density $\rho_0 = 2.8{\times}10^{14}\,\mathrm{g\,cm^{-3}}$ (also called saturation density), as expected in the cores of neutron stars. Because the temperature inside neutron stars is of the order of $10^7\,\mathrm{K}$, the adjective "cold" is a relative term. Here, it mostly means that the temperature is sufficiently low that the degeneracy pressure is mostly temperature independent. Inside neutron stars, the mixture of neutrons, protons and electrons is in beta equilibrium, i.e., the *beta*-decay of neutrons is balanced by the electron-capture reactions (inverse *beta*-decay).

At the densities (and temperatures) encountered inside neutron stars, matter has a stable configuration, but nuclear physics still cannot explain how it remains so. Improving its understanding has attracted the attention of physicists and astrophysi-

[3]Degenerate matter refers to matter in which the resistive pressure is not caused by thermal energy, but by the fact that all lowest energy levels are filled, forcing fermions to higher levers, and therefore creating repulsive pressure.

cists for several decades. Unfortunately, the behaviour of degenerate dense matter cannot be tested in Terrestrial laboratories because such matter would disintegrate within $\sim 10^{-20}$ sec (Haensel et al., 2007). By colliding heavy nuclei together, particle accelerators can obtain information about energetic "hot" matter at high densities, but not "cold" degenerate matter. In more technical terminology, neutron stars lie in a portion of the quantum chromodynamics phase diagram (temperature as a function of density) that particles accelerators cannot currently probe (see Figure 1.2). In addition, no simulations of quantum chromodynamics (called lattice quantum chromodynamics) can at the moment simulate the neutron star matter phase. Therefore, only neutron stars can currently place constraints on the behaviour of cold dense matter.

The importance of understanding such matter is two-fold. From a nuclear physics point of view, it is necessary to know the equation of state of cold dense matter since it is the type of matter that composes large nuclei. Nucleons are composed of three quarks held together by the strong force, while the residual strong force (or nuclear force) is responsible for holding nucleons together and forming nuclei (Fritzsch, 1983). These two components of the strong force are not well understood for nuclei with more than three nucleons, i.e., anything heavier than lithium. In other words, nuclei heavier than lithium are known and observed in nature, but quantum chromodynamics cannot currently explain how they remain stable. Because the interior of a neutron star is thought to be a large collection of nucleons (i.e., analogous to a single 10-km wide atomic nuclei) or of more exotic particles, their study will provide information to shed light on the theory of quantum chromodynamics. Studying the behaviour of matter inside neutron stars will also ultimately help determine whether the ground state of matter at high densities is composed of hadrons, or if it is composed of deconfined quarks (i.e., not held together by gluons, see Figure 1.2).

Another important unknown element of nuclear physics is the symmetry energy, the difference in energy per baryon between pure neutron matter and symmetric

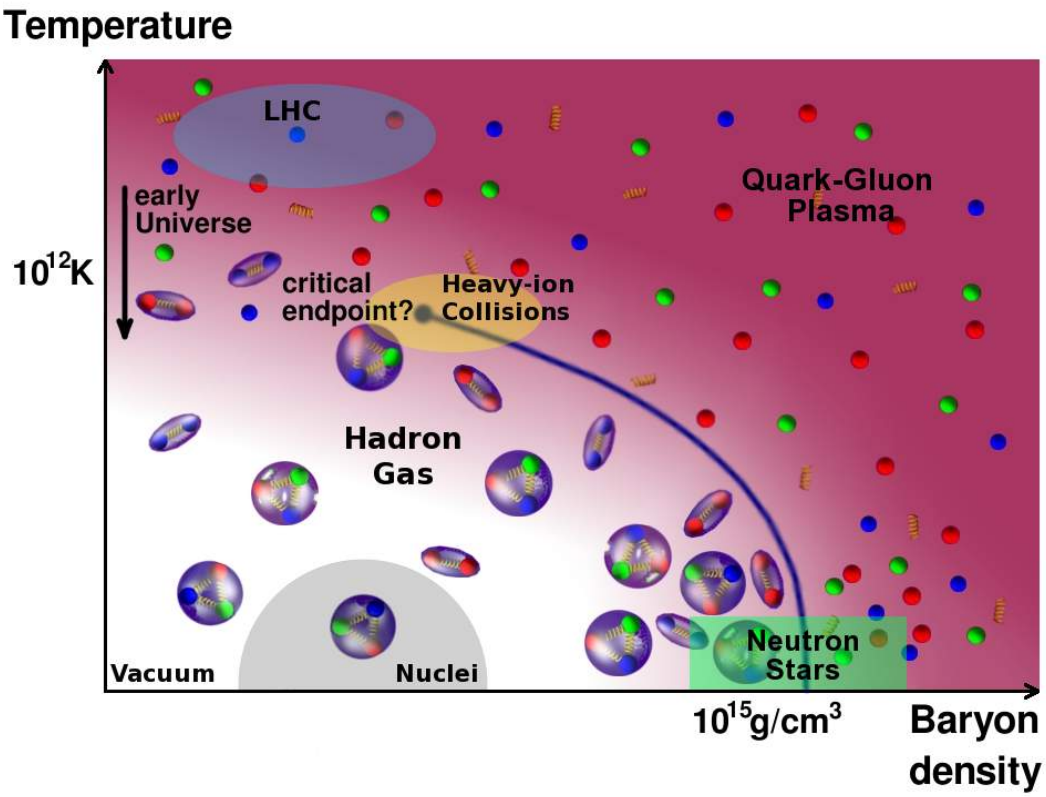

Figure 1.2 – This schematic diagram shows the phases of matter, as a function of temperature and density. Red, green and blue spheres represent quarks of different flavours. The spring-like shapes are the gluons, the mediating particle of the strong force necessary for the hadrons (2 or 3 quarks) to exist. In the bottom-left part of the phase diagram, matter is in the form of a hadron gas, while the top-right half of the diagram corresponds to the hypothesized quark-gluon plasma phase, where the blue line separates hadrons from deconfined quarks. Neutron stars lie in the low-temperature/high-density portion of the quantum chromodynamics phase diagram, shown here to extend over hadronic matter and deconfined quark matter, because of the current state of knowledge. This region is not attainable by current experiments such as the Large Hadron Collider (LHC) and heavy-ion collider experiments. Figure adapted from Endrodi (2013). Some labels were added for the purpose of this section.

matter (equal number of protons and neutrons). The density dependence of the symmetry energy is poorly known, and its predicted or measured value at saturation density ρ_0 is still uncertain: in the 25–40 MeV range (Hebeler et al., 2013). Studying neutron stars by probing their internal structure informs about the symmetry energy since the equation of state of dense matter is highly dependent on it.

The study of the neutron star interior matter, and by extention, the understanding of the cold dense matter equation of state, is also crucial from an astrophysical point of view. For example, the flux of neutrinos emitted during supernova explosions depends on the stability of neutrons againt decay (emitting an anti-neutrino), as well as the rate of conversion of protons into neutrons via electron capture (emitting a neutrino). The rates of these reactions, as well as the neutrino opacities in dense matter, are governed by the symmetry energy (Swesty et al., 1994; Roberts et al., 2012). As another example, in neutron stars, the thickness and thermal properties of the crust are dependent on the symmetry energy (Page and Reddy, 2012). Finally, the neutron star radius, tightly linked to the symmetry energy (Horowitz and Piekarewicz, 2001a,b), plays a role in the gravitational wave signals from the merger of a neutron star with a black hole, or with another neutron star (Lackey et al., 2012; Foucart et al., 2013).

Ultimately, neutron star astrophysics and nuclear physics are tighly related. In other words, the physical properties and emission mechanisms of neutron stars in a variety of scenarios (supernova, cooling neutron stars, mergers, ...) are strongly connected to the physics at nuclear scales. Combining the astrophysical observations to the theoretical advances of nuclear physics, as well as the results from nuclear physics experimental data, is necessary to make progress toward a full understanding of the dense matter equation of state and the strong force. The work presented in this thesis addresses the constraints from astrophysical observations of neutron stars, using one of the several available methods.

1.4 Short Description of the Chapters

After the non-technical summary, the historical reviews and the "big picture" presented above, Chapter 2 will provide a description of neutron stars, how they are formed, and of what they are made. The sub-class of neutron stars studied for the work of this thesis is described extensively, including the interpretation and modeling of their surface emission, as well as the globular clusters in which they are observed. Finally, Chapter 2 also contains a section regarding the equation of state of dense nuclear matter. Since the goal of this thesis work is to place constraints on the dense matter equation of state, a discussion of the various proposed theories describing matter in the core of neutron stars is proposed. In short, Chapter 2 stands as a comprehensive introduction to the other chapters of this thesis, ensuring that all points addressed in other chapters (corresponding to published articles) are properly introduced. Chapter 3 serves as a short review of X-ray astronomy, describing the observational aspect of this work, as well as the details necessary to understand the X-ray observations used in this thesis. It first includes a historical review, followed by a technical description of how X-ray photons are collected and detected during observations of X-ray sources. Chapter 3 also describes in details the two X-ray observatories that were used for the work of this thesis.

Chapters 4, 5, 6 and 7 are ordered in the logical progression of the work. They cover, respectively, the search for neutron stars inside globular clusters, the use of thermal emission models on X-ray spectra of neutron stars to measure their mass and radius, the combination of several neutron star spectra to measure the radius of neutron stars under the reasonable assumption that all neutron star have the same radius, and finally, the development of a method to reject proposed dense matter equations of state. Chapters 4, 5, and 6 were originally published in three distinct publications, and 7 is an article ready for submission.

Chapter 4 describes the analysis of an *XMM-Newton* observation of the globular cluster NGC 6553. This observation was part of a larger survey designed to identify

possible neutron stars in quiescent low-mass X-ray binary systems inside globular clusters. Chapter 4 relates the discovery of one such source in the core of the NGC 6553. Because of X-ray source confusion in the dense core of the cluster, additional high-spatial resolution observations with the *Chandra X-ray Observatory* were used to validate the classification of the candidate low-mass X-ray binary. This tentatively confirmed the presence of nearby contaminating sources in the *XMM-Newton* observations, but a longer observation with *Chandra* is necessary to firmly confirm the identification of the quiescent low-mass X-ray binary in the core of NGC 6553.

Chapter 5 presents a spectral analysis of archived observations of the quiescent low-mass X-ray binary in the core of the globular cluster NGC 6397. This work relies on the widely accepted description of quiescent low-mass X-ray binaries in which the thermal emission from the surface can be modeled by a neutron star hydrogen atmosphere. Using a publicly accessible spectral model, the long observations available ($\sim 350,000\,\mathrm{sec}$ in total) led to precise measurements of the mass and radius of the neutron star in this quiescent low-mass X-ray binary system inside NGC 6397.

Chapter 6 proposes a radically different approach. Instead of performing individual mass and radius measurements of neutron stars in quiescent low-mass X-ray binaries, a different procedure, which consists in the combination of several neutron star spectra, is present. In this joint simultaneous analysis, it is assumed – based on observational evidence – that all neutron stars have the same radius. Combining the X-ray spectra of several neutron stars led to constraints otherwise unattainable when treating the neutron stars independently. The simultaneous spectral analysis in Chapter 6 was performed with a careful inclusion of various sources of uncertainties that can be quantified. The neutron star radius, assuming it is the same for all neutron stars, is lower ($R_{\mathrm{NS}} < 11\,\mathrm{km}$) that previously expected. Such result is difficult to reconcile with most proposed dense matter equations of state.

Chapter 7 first presents an update to the analysis of Chapter 6, with new data added to the sample. As expected, the results remain unchanged. More importantly,

Chapter 7 contains a modification to the analysis of Chapter 6 which now allows to use the spectral data to observationally confirm or reject, with a quantitative level of certainty, any proposed dense matter equation of state. This method is used to test a selection of dense matter equations of state.

2

Neutron Stars and Neutron Star Matter

This chapter first provides a general introduction to neutron stars (NSs), their interior structure, and the different classes of NSs. Then, a section explains the processes leading to the surface emission that is observed from the NSs in quiescent low-mass X-ray binaries (qLMXBs), the sources of interest in this thesis. This is followed by a discussion of dense nuclear matter such as that found in the core of NSs, and of the constraints on the equation of state (EoS) that can be obtained from astrophysical sources. Finally, this chapter will finish with an overview of globular clusters (GCs) since this thesis makes use of NS qLMXBs hosted inside GCs to constrain the dense matter EoS.

2.1 An Overview of Neutron Stars

NSs are compact objects created during the supernova explosions of massive stars (see Section 2.1.1). They appear to us with a wide variety of observational behaviours, and historically, they have been classified phenomenologically. As the understanding of the physical processes at hand improved, there have been propositions to unify the various classes of NSs (Kaspi, 2010; Viganò et al., 2013, see Section 2.1.3).

NSs present some of the most extreme properties in the Universe. For example, they have been observed having a wide range of rotational periods. The subclass of millisecond pulsars includes the fastest spinning objects known. The pulsar PSR J1748−2446ad is the current record holder with a precisely measured spin frequency

$\mu_{\rm spin} = 716.35556(3)\,{\rm Hz}$ [1] (Hessels et al., 2006). At the other end of the range of rotational periods are NSs with $P = 10 - 12\,{\rm sec}$, representing a possible upper limit of NS spin periods (Pons et al., 2013; Gusakov et al., 2013).

Another sub-class of NSs, the so-called magnetars, have surface dipolar magnetic field of the order of $10^{13-15}\,{\rm G}$, in excess of the electron critical magnetic field $B_{\rm crit} = 4.4{\times}10^{13}\,{\rm G}$, at which the cyclotron energy of electrons is equal to 511 keV, the rest mass of the electron (for a review, see Mereghetti, 2008). The dipolar magnetic field of NSs is estimated from $B_{\rm d} = 3.2{\times}10^{19}\left(P\dot{P}\right)^{1/2}$ G, where P and $\dot{P}$ are the measured period and period derivative, respectively. The magnetar model has been developed to reconcile the observational properties of soft gamma-ray repeaters and anomalous X-ray pulsars, two different manifestations of highly-magnetized NSs (Duncan and Thompson, 1992; Thompson and Duncan, 1993; Thompson et al., 2002; Woods and Thompson, 2006). Twenty-six magnetars (and candidates) are known to date, with dipolar magnetic fields in the range $6{\times}10^{12}$–$2.4{\times}10^{15}\,{\rm G}$ (Olausen and Kaspi, 2014).

In addition to the extreme spin periods or extreme magnetic fields observed in some NSs, they are composed of the densest matter in the Universe. A small variety of observational methods permits probing the outer layers of NSs. For example, some understanding of the NS crust, at densities between $\rho \sim 10^{11}\,{\rm g\,cm^{-3}}$ and $\rho \gtrsim 10^{14}\,{\rm g\,cm^{-3}}$, can be obtained from observations of the cooling rate of NSs (Heinke and Ho, 2010; Newton et al., 2013). However, the composition of NSs and the behaviour of matter in their core, at densities above the normal nuclear density $\rho = 2.8{\times}10^{14}\,{\rm g\,cm^{-3}}$ (also called saturation density), are still largely unknown. The goal of this thesis work is to provide observational measurements to improve the constraints on the EoS of dense matter. But prior to providing the necessary background about the sub-class of NSs studied to this purpose, it is important to introduce to the fascinating objects that are NSs, including, their formation mechanism, their internal structure, and the various classes of the NS population.

[1] the number in parentheses represent the uncertainties in the last digit

2.1.1 Formation

As mentioned in Chapter 1, it had been suggested early on that NSs resulted from the core-collapse supernova explosions of massive stars, long before the supernova phenomenon could be properly explained:

> *With all reserve, we advance the view that a super-nova represents the transition of an ordinary star into a neutron star, consisting mainly of neutrons. Such a star may possess a very small radius and an extremely high density. As neutrons can be packed much more closely than ordinary nuclei and electrons, the "gravitational packing" energy in a cold neutron star may become very large, and, under certain circumstances, may far exceed the ordinary packing fractions.*
>
> Baade and Zwicky (1934)

This initial prediction has remained the general consensus, and, since then, theoretical justifications and observational evidences have provided further support to it. However, there still lack direct observations of the presence of a NS following a supernova explosion for which the progenitor star was observed. NSs associated with supernova remnants have been observed (e.g., Cassiopeia A, Pavlov et al., 2000) and there are examples of supernovae for which the progenitor star was known and its mass estimated but none of these have detected NSs associated with them such as Supernova 1987A in the Large Magellanic Cloud (West et al., 1987), or supernovae in other galaxies (e.g., in M74, Smartt et al., 2004).

To a first order, the type of compact object resulting from a core-collapse supernova depends on the mass of the progenitor star (Carroll and Ostlie, 1996). A main-sequence (MS) star with $M < 9\,M_{\odot}$ will expel its hydrogen envelope into a planetary nebula, leaving behind a white dwarf (WD) resulting from the compression of the star's inner portion. Stars with masses in range $9 - 25\,M_{\odot}$ undergo supernova explosions leading to NSs. Finally, when the initial mass is above $25\,M_{\odot}$, the core of the progenitor star collapses completely to a black hole (Woosley and Weaver, 1986).

However, recent studies have complicated this general picture. It became evident that the initial composition of the progenitor star plays a role on the amount of mass lost during the star lifetime (Heger et al., 2003). High stellar metallicities are believed to enhance the mass loss during the MS lifetime. This mass loss is due to opacity-driven pulsations causing stellar winds. Consequently, massive stars with metallicities comparable to that of the Sun – a high-metallicity star – can form NSs even if their initial masses were larger then $25\,M_{\odot}$. This is summarized in Figure 2.1. In addition, rapid stellar rotation can also increase mass loss and further complicate the simple picture relating the progenitor mass and the compact object resulting from the supernova (Heger et al., 2003).

The basic scenario of core-collapse supernova is described in the next few paragraphs, for which the following reviews have been used: Woosley and Weaver (1986); Burrows (2000); Lattimer and Prakash (2004); Burrows (2013).

As a massive star runs out of hydrogen to fuse in its core, it contracts leading to a temperature increase allowing the helium component to ignite. Once the helium is depleted, and after a short phase of hydrogen-shell burning (in a layer surrounding the core), the carbon and oxygen ashes in the core sequentially burn into heavier elements, up to the most stable element, ^{56}Fe, through a succession of core and shell burning phases. As a result, the elements in the dying star are stratified by atomic mass with the lightest in the outer shells, down to iron in the core. The nuclear fusion reactions increase the mass of the stellar core, up to a maximum defined by the Chandrasekhar limit. In the density conditions encountered in the dying star before the supernova explosion, the matter is supported against collapse by electron degeneracy pressure (due to highly relativistic electron with an EoS of the form $P \propto \rho^{4/3}$). However, as the mass exceeds the Chandrasekhar limit, the inward force of gravity overcomes the electron degeneracy pressure.

Within less than a second, the inner core collapses from a sphere with a radius of $\sim 10^4\,\mathrm{km}$ to a compacted core with radius $\sim 10\,\mathrm{km}$. Consequently, the core

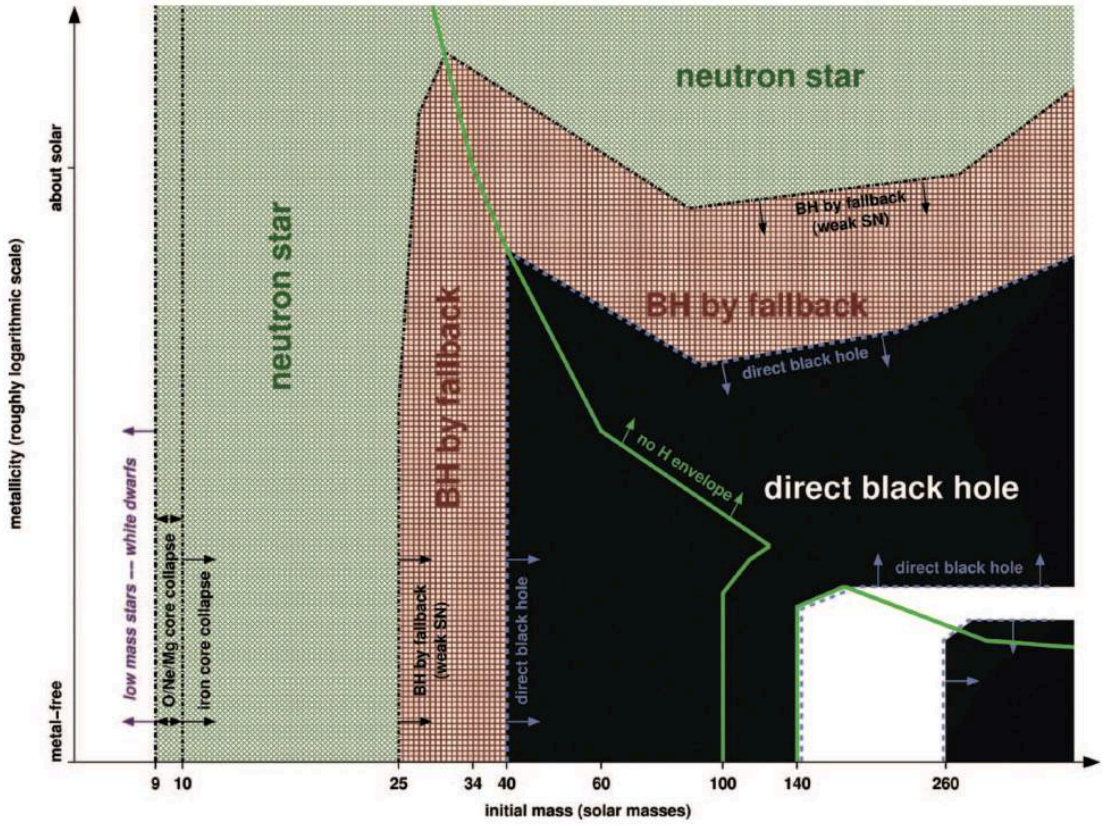

Figure 2.1 – This schematic diagram shows the final evolutionary state of a star as a function of its initial mass and metallicity. Neutron stars are the remnants from the supernova explosion of stars with initial masses in the $\sim 9 - 25\,M_{\odot}$ range, with metallicities lower than that of the Sun. Above $\sim 25\,M_{\odot}$, a star will collapse to a black-hole, either directly or by fallback of the material. However, at high-metallicity, neutron stars can be formed from stars with initial masses larger than $25\,M_{\odot}$. This is due to enhanced mass loss during the star's lifetime, induced by the high metallicity. Figure adopted Heger et al. (2003).

density becomes larger than the density of an atomic nucleus, $\rho \gtrsim 10^{14}\,\mathrm{g\,cm^{-3}}$. In these conditions, the practically incompressible collapsed core is supported by neutron degeneracy pressure. Because the retraction of the inner core is so sudden, the outer core infalls supersonically while the stellar mantle remains unaffected for the first few seconds of the core collapse. The supernova explosion begins when the infalling outer core reaches the $\sim 10\,\mathrm{km}$ incompressible inner core and bounces off the surface of the proto-NS. This triggers an outward shock-wave at a radius of $\sim 20\,\mathrm{km}$ colliding with the many solar masses of stellar material from the outer region of the star that began infalling.

Supernova remnants, consisting of ejected material, are clear observational evidence of the existence of supernova explosions. However, theory and supernova simulations predict the stalling of the outward shock front, and it remains unclear what resuscitates the shock and drives the whole supernova explosion. Specifically, the outgoing shock front stalls within $\sim 20\,\mathrm{ms}$, at a radius of $\sim 100\,\mathrm{km}$. Several mechanisms are invoked to resuscitate the shock within a few seconds and create the observed supernova explosions. These mechanisms include a neutrino-driven wind (Burrows, 2013), or standing accretion instabilities (Ott et al., 2013). However, none of these succeeds at explaining all observables of supernova explosions.

Once restored, the shock litters heavy elements freshly formed during the explosion. The ejected gas composing the outer mantle of the dead star carry $\sim 10^{51}\,\mathrm{erg\ s^{-1}}$ of kinetic energy. However, this represents a negligible fraction of the total energy released, dominated by the neutrino luminosity; up to $\sim 10^{54}\,\mathrm{erg\ s^{-1}}$ or $0.5\ M_\odot\,\mathrm{c^2\,s^{-1}}$. Following the supernova explosion, the expelled material forming the supernova remnant surrounds the newly formed NS, with core densities $\rho \gtrsim \rho_0$, supported by neutron degeneracy pressure, and surrounded by a crystalline crust. The structure of NSs is now briefly presented.

2.1.2 Structure

While this section provides an overview of the NS structure, it is important to understand that a lot of unknowns still remain regarding the deepest layers. In fact, the goal of this thesis work is to make a step closer to the understanding of the dense matter, and therefore the internal structure of NSs. This section briefly describes in a qualitative manner the current knowledge of the NS structure, from the atmosphere to the interior.

The Neutron Star Atmosphere

The atmosphere surrounding a NS represents a negligible fraction of the total mass. However, the large surface gravity ($g \sim 10^{13} - 10^{15}\,\mathrm{cm\,s^{-2}}$) of the NS implies that the atmosphere is compressed up to densities ($\rho \sim 10^{2}\,\mathrm{g\,cm^{-3}}$, Zavlin and Pavlov, 2002), and as a result, extends over $< 10\,\mathrm{cm}$ only. Another consequence of the large surface gravity is the gravitational settling of elements in the outer layers of the NS on short time scales of $\sim$ few seconds (Alcock and Illarionov, 1980; Bildsten et al., 1992), leaving only the lightest element in the atmosphere while the heavier ones sink to the layer below. The composition of the atmosphere directly affects the emission of the NS by shaping the observed photon spectrum via radiative transfer. The composition of the atmosphere and the resulting emergent spectrum are further discussed in Section 2.2.2.

The Neutron Star Envelope

The envelope surrounding the crust also has a negligible contribution ($\ll 1\%$) to the total mass of the NS. Its density increases from $\rho \sim 10^{6}\,\mathrm{g\,cm^{-3}}$ to roughly $\rho \sim 10^{9}\,\mathrm{g\,cm^{-3}}$ at the boundary with the crust. As the density rises, the envelope is composed of heavier and heavier elements in a stratified structure, up to ^{56}Fe at the boundary with the crust. In the literature, the envelope is sometimes considered as part of the crust.

The Neutron Star Crust

The crust ($\sim 1-2\,\mathrm{km}$ thick) has densities in the range $\rho \sim 10^9-10^{14}\,\mathrm{g\,cm^{-3}}$, increasing with depth. The high pressure at densities $\rho > 10^9\,\mathrm{g\,cm^{-3}}$ causes the nuclei to be fully ionized and therefore to exist in a degenerate electron gas (Page and Reddy, 2012). Just like the envelope, the outer part of the crust also experiences a stratification of its composition. Additionally, the rate of electron-capture reactions – transforming protons into neutrons inside nuclei via the weak interaction – increases with density, leading to more neutron-rich nuclei, from ^{56}Fe at the top of the layer, to nuclei with over 100 nucleons at the interface with the inner crust.

At $\rho_{\mathrm{drip}} \sim 5\times10^{11}\,\mathrm{g\,cm^{-3}}$, the neutron-drip density, neutrons start to leak out of nuclei. This is a consequence of the chemical potential of neutrons inside those nuclei dropping to zero, therefore "dripping" out of the nuclei. As a result, at this density, one finds neutron-rich nuclei immersed in a neutron fluid. In addition, observations of the cooling of NSs suggest that these neutrons are in a superfluid state (Heinke and Ho, 2010; Page and Reddy, 2012; Turlione et al., 2013; Newton et al., 2013).

The nuclei in the crust are arranged in a crystalline lattice. At greater densities, this crystalline lattice of nuclei is thought to reorganize to form what are commonly called the "pasta phases" (Ravenhall et al., 1983; Horowitz et al., 2005), resulting from the competition between the Coulomb repulsion and the attractive nuclear force. These phases represent the transition from the inhomogeneous matter in the outer crust to the homogeneous matter found in the core. Specifically, it is thought that the nuclei become progressively more elongated ("spaghetti phase"), eventually forming planar structures ("lasagna phase"), surrounded by the superfluid neutrons. As the density keeps increasing, these structures thicken to form a bulky phase with bubbles of superfluid neutrons ("swiss cheese phase"). The depth where these neutron bubbles disappear marks the transition to the core. Evidence of the "pasta phase" structure comes from semi-classical molecular dynamic simulations of matter at those densities (Schneider et al., 2013). For a review of NS crusts, see Chamel and Haensel (2008).

The crust amounts to about 1% of the total NS mass. Nonetheless the envelope and the crust play a crucial role for the release of the thermal energy as well as for the transport of energy through the surface layers. For example, the crust can be affected by accreted matter. During episodes of accretion onto the NS, energy is deposited in the crust. More details of the crustal heating are provided in Section 2.2.1.

The Neutron Star Core

The core accounts for about $\sim 99\%$ of the mass and has densities of $\rho \gtrsim \rho_0$. At such densities, individual nuclei do not exist as such. Instead, matter subsists in the form of an homogeneous neutron-proton fluid, with likely some electrons to neutralize the superconducting proton charges. In the inner part of the core, a fraction of nucleons can be changed into exotic hyperons, provided the Fermi energies of the nucleons are large enough. However, observations have not confirmed this hypothesis. Other types of exotic matter like pions and kaons may also exist. Finally, quarks might also be present in the core of NS, in the form of deconfined strange quark matter. All of these hypotheses lead to a variety of theoretical models attempting to describe matter at nuclear densities, but experimental and observational measurements so far have not been able to discriminate between them. A description of the various proposed compositions of the NS core can be found later on in this thesis (Section 2.3.1).

2.1.3 Population

The various known sub-classes of NSs originate from a phenomenological classification stemming from observational properties of NSs. However, since the initial discoveries of those different observational signatures, a clearer picture has emerged linking them to physical characteristics. Much remains to be done to construct a fully unified picture. NSs are usually sorted into two categories, the isolated neutron stars (INSs), and those in binary systems[2]. This section describes the various subclasses of NSs.

[2]A radio pulsar in a triple system (with two WDs) was even detected recently (Ransom et al., 2014).

Isolated Neutron Stars

As was mentioned in the historical review, the first identified NS (different from the first observed NS) was a radio rotation-powered pulsar. Over 2000 of these are now known, largely dominating the total known population of INSs and NSs in general (Manchester et al., 2005). The radio emission of the objects in this subclass of NSs is powered by the loss of angular momentum caused by their large magnetic fields, although the emission mechanism is not clearly understood (Melrose, 1995; Hankins et al., 2009). The measurement of their spin down ($\dot{P} \equiv dP/dt$) is routinely used to quantify the strength of the NS surface dipolar magnetic field, which are observed to be in the range $\sim 10^8 - 10^{14}\,\mathrm{G}$. The spin periods of rotation-powered pulsars also cover a wide range of values, from $\sim 1\,\mathrm{ms}$ to $\sim 8\,\mathrm{sec}$. However, objects with the shortest spin periods $P \lesssim 20\,\mathrm{ms}$, usually referred to as millisecond pulsars, are thought to be spun up by the accretion of infalling material from a binary companion (Bhattacharya and van den Heuvel, 1991). These are therefore discussed later on.

Estimating the total population of radio pulsars in the Galaxy is a difficult problem which depends on a wide variety of selection effects (Lorimer, 2010). Radio surveys have sensitivities limited by sky coverage, noise and radio sky backgrounds. In addition, the beaming of the radio pulses as well as the dispersion by free electrons in the interstellar medium limit the detection of pulsars. Finally, the detection of radio pulsars could also hampered by the interruption of the pulses, an effect called "nulling" (Ritchings, 1976). A fraction of pulsars are showing intermittent pulses, alternating on and off states, which affects their detection. Recently discovered, the rotating radio transients exhibit only individual radio pulses, which are not detected in standard pulsars searches (McLaughlin et al., 2006b).

NSs with high magnetic fields, the so-called magnetars, have been discussed above in Section 2.1. They are thought to be powered by the decay of their magnetic field. However, the recent discovery of magnetar-like activity from known high-magnetic field pulsars (Olausen et al., 2013), as well as the evidence of the low dipolar magnetic

field of some magnetars (e.g., Rea et al., 2010, 2012), suggests a continuity between the populations of radio pulsars and magnetars. A possible evolution mechanism has been suggested to reconcile these observations (Viganò et al., 2013).

Finally, a small population of nearby ($< 500\,\mathrm{pc}$) radio-quiet X-ray emitting NS has been discovered by the *ROSAT* All-sky survey (Haberl, 2007). These sources exihibit dim X-ray emission with surface temperatures in the range 40–50 eV originating from the thermally-cooling of their surface. Timing observations have revealed periods in the range 3–11 sec, and spin-down inferred dipolar magnetic fields $B > 10^{13}\,\mathrm{G}$ (Haberl, 2007; van Kerkwijk and Kaplan, 2008). In the magneto-thermal evolution models reconciling the various types of INSs, these radio-quiet X-ray-dim sources tend to corresponds to the older populations (Viganò et al., 2013). Seven INSs are known but over 200 are expected[3] to be discovered with the high-sensitivity of the upcoming all-sky survey X-ray mission *eRosita* (Merloni et al., 2012).

Neutron stars in binary systems

When a NS belongs to a binary system, its observational properties strongly depend on the characteristics of the binary companion as well as the physical processes involved in the emission of electromagnetic radiation. Whether thermal or non-thermal, the emission processes provide valuable information for the understanding of the binary systems and NSs in general, including the determination of their masses or the radii.

A fraction of radio pulsars exists inside binary systems, with MS star companions (e.g., PSR J1903+0337, Freire et al., 2011), with WD companions (e.g., PSR J0348+0432, Antoniadis et al., 2013), or even with a NS companion (e.g., PSR J0737–3039, Burgay et al., 2003). No NS/black hole system has been detected yet. Because the orbital configuration and the electromagnetic emission of the components of a binary system are affected by various effects (including general relativistic effects), precise timing of

[3] R. Rutledge, 2011, *eROSITA: Factory of Gravitational Wave Source Candidates*, at the First *eROSITA* International Conference, Oct. 2011, Garmisch-Partenkirchen, Germany. Available at `http://www2011.mpe.mpg.de/erosita/erosita2011/program/PDF/rutledge.pdf`.

radio pulsars in binary systems allows for precise measurements of orbital parameters. This can prove useful to measure NS masses with high precisions. This is further discussed in Section 2.3.2.

Often, binary systems containing a NS emit X-rays as a consequence of the high-energy processes resulting from the interaction between the two objects. Accretion of material from the companion onto the NS is a common process observed in a variety of binary systems. NS high-mass X-ray binaries are usually defined as a NS accreting matter from a massive star with $M_\star > 10\,M_\odot$. Such stars lose mass via strong stellar winds, a fraction of which is accreted onto the NS. Alternatively, accretion onto the NS can be intermittent if the system is in an eccentric orbit. In that case, accretion and the resulting X-ray emission happen as the NS crosses the circumstellar disk of its companion. Extensive reviews of high mass X-ray binaries systems exist in the literature (e.g., Chaty, 2011).

If the companion to the NS is a low-mass star ($M_\star < 1\,M_\odot$), the binary system is simply called low-mass X-ray binary (LMXB). These low-mass stars do not experience mass-loss via stellar wind and the transfer of mass onto the NSs happens via Roche-lobe overflow. The Roche-Lobe is defined by the limiting region of space where matter is gravitationally bound to the star. In LMXBs, material outside the tear-shaped Roche lobe escapes the gravitationally attraction of the star, and can be transferred onto the companion via the first Lagrange point, the point of contact between the Roche lobes of the two components (see Figure 2.2). Measuring the orbital period of the system informs on the orbital separation and therefore, on the size of the Roche lobe. For example, in ultra-compact X-ray binaries, the short orbital period ($\lesssim 1\,\mathrm{h}$) implies such a small Roche lobe that the companion to the NS must be a WD, or maybe a hydrogen-depleted star (Nelemans and Jonker, 2010).

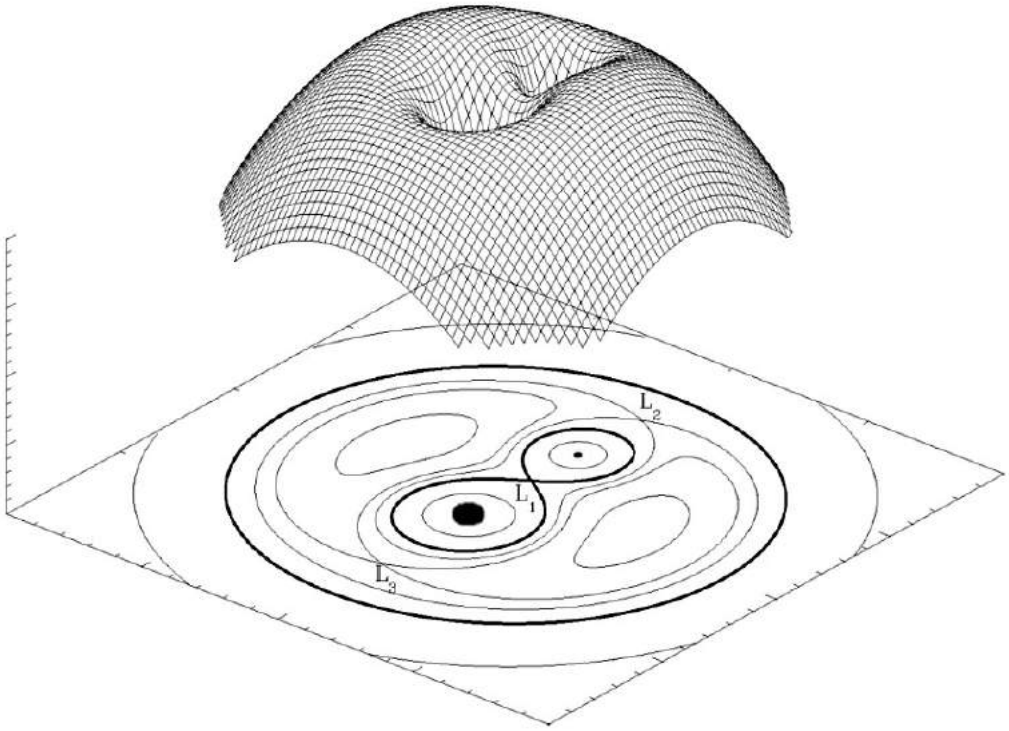

Figure 2.2 – This figure depicts the Roche potential of a binary system, in 3-dimensions. The 2-dimensional projection shows the line of equipotential of the two components, called Roche lobes (tear-shaped dark line). Mass transfer from one object to the other through point L1 (Lagrange point 1) occurs when the donor star fills its Roche lobe. Figure adopted from (van der Sluys, 2006).

LMXBs are either transient or persistent systems, a characteristic that depends on the constancy of the accretion. Persistent LMXBs go through prolonged periods of accretion, and their high-energy emission originates from the disk of matter heated up to X-ray emitting temperatures. In transient LMXBs, the observed emission alternates between periods of X-ray bright outbursts and periods of X-ray dim phase of low or halted accretion, called quiescence. The behaviour of transient LMXBs is explained by the thermal-viscous instability model (Lasota, 2001, 2008). During outbursts, lasting days to months, the disc is in a hot ionized state, transfering matter onto the NS surface. During quiescence, matter accumulates in the disc of accretion, which resides in a cold neutral state. During accretion, thermal instabilities on the

surface of the NS sometimes trigger fast-spreading runaway nuclear reactions causing a sudden increase of the X-ray luminosities up to $L_{\rm X} \sim 10^{38}\,{\rm erg\,s^{-1}}$, called X-ray bursts. In some cases, the burst luminosities become larger than the Eddington luminosity of the NS, i.e., the outward radiative pressure of the nuclear reactions overcomes the inward gravitational pull of the NS, therefore temporarily lifting the NS surface (Lewin et al., 1984; Kuulkers et al., 2003). These so-called photospheric radius expansion (PRE) bursts are further discussed in Section 2.3.2. A LMXB returns to quiescence when the transfer of mass onto the NS stops or decreases to low mass-accretion rates ($\dot{M} \lesssim 10^{-10}\ M_{\odot}\,{\rm yr^{-1}}$). In quiescence, the X-ray luminosity drops below $L_{\rm X} \lesssim 10^{34}\,{\rm erg\,s^{-1}}$, and the X-ray emission mainly comes from the surface of the thermally cooling NS.

Two long-term consequences emerge from the accretion of mass onto a NS. First, transfer of angular momentum from the infalling matter to the NS leads to the accumulation of mechanical rotation energy, causing an increase of the NS spin up to millisecond periods (Bhattacharya and van den Heuvel, 1991; Tauris and van den Heuvel, 2006). This mechanism of "recycling" received observational support from the discovery of the first X-ray pulsar with a period of 2.49 ms in a LMXB (SAX J1808.4−3658, Wijnands and van der Klis, 1998), as well as from the discovery of two systems transitioning between an X-ray emitting LMXB phase and a radio-emitting millisecond pulsar phase (PSR J1023+0038, Archibald et al. 2009, and IGR J182452452, Papitto et al. 2013). Second, the accretion of matter can bury the initial magnetic field of NSs (Romani, 1990), resulting in low magnetic fields $B \sim 10^8 - 10^{10}\,{\rm G}$, compared to the values measured for standard "non-recycled" pulsars. Furthermore, the accretion of matter onto the NSs in binary systems results in a bimodal distribution of NSs masses, clearly differentiating INSs from accreting NSs (Özel et al., 2012b)

Because the work in this thesis uses observations of LMXBs in quiescence, these objects and the origin of their X-ray emission are discussed in greater detail in the next section.

2.2 Quiescent Low-Mass X-Ray Binaries and their Thermal Emission

It is first necessary to clarify that the compact object in qLMXB systems can either be a NS or a black hole. In this thesis, only NSs are considered, and further references to qLMXBs will mean "NS qLMXBs" for conciseness, unless specified otherwise.

The quiescent emission of LMXBs was first detected during the post-outburst periods of historical transiently accreting LMXBs. In those historical X-ray sources, the presence of a NS as the compact object of the binary system had been evidenced by the observation of bright X-ray bursts, indicative of surface thermonuclear burning (Koyama et al., 1981), which does not exist in black hole LMXBs. During quiescence, the detected thermal spectra of LMXBs also indicate a surface emission, much fainter ($L_{\rm X} \sim 10^{32} - 10^{33}\,{\rm erg\ s^{-1}}$) however than the X-ray bursts observed during the active periods ($L_{\rm X} \sim 10^{36} - 10^{38}\,{\rm erg\ s^{-1}}$). The faint quiescent X-ray emission was originally interpreted as blackbody emission. However, the emission area measured under the blackbody assumption was a factor of $\sim$100 smaller than implied by the projected area of a 10 km NS. Observations of historical X-ray transient in quiescence confirmed these observational properties of the class of qLMXBs. At that time, it was suggested that some low-level mass accretion onto the compact object was required to power the observed luminosity, although what set the low-mass accretion rate was unclear (van Paradijs et al., 1987; Verbunt et al., 1994).

This tentative scenario was then replaced with the suggestion that the source of the quiescent thermal emission is internal, coming from the deep crust, and reprocessed in the NS atmosphere. Now follows a description of the *deep crustal heating* theory (DCH) which explains the origin of the thermal emission of qLMXBs, the hydrogen atmosphere models describing the NS surface emission that naturally arise in the DCH framework (Brown et al., 1998), and then provide additional information about qLMXBs in GCs.

2.2.1 Deep Crustal Heating

In the DCH interpretation of the quiescent thermal emission of LMXBs, the luminosity is provided not by accretion onto the compact object, but by heat deposited in the NS crust by pressure-sensitive nuclear reactions happening during the outburst episodes (Brown et al., 1998). As matter is piled on top of the NS surface, it forces the column below to greater density and larger electron Fermi energies. This causes a series of nuclear reactions, including electron captures, neutron emission, and pycnonuclear reactions (e.g., Haensel and Zdunik, 1990, 2003, 2008; Gupta et al., 2007). The latter occur when the Coulomb barrier has been lowered by preceding electron captures, allowing for a density-dependent fusion reactions (Harrison, 1964). Pycnonuclear reactions are to be differentiated from thermonuclear reactions which rates are temperature-dependent.

The series of reactions encountered by elements at the base of the envelope (ashes from thermonuclear burning occuring during X-ray bursts, e.g., ^{56}Fe) and in the crust create more and more neutron-rich elements being pushed to larger and larger densities. For example, beginning with pure ^{56}Fe at the top of the crust, the increasing electron Fermi energy, caused by the increasing densities, induces electron capture at $\rho = 1.494\times10^{9}\,\mathrm{g\,cm^{-3}}$. Then, because of the odd-even staggering of nuclear masses, a second electron capture follows to produce ^{56}Cr. These two electron-capture reactions release a total of 0.041 MeV per accreted nucleon. At a density $\rho = 1.114\times10^{10}\,\mathrm{g\,cm^{-3}}$ the electron Fermi energy is again above the threshold for capture on to ^{56}Cr, and ^{56}Ti is produced with 0.036 MeV of energy deposited at that depth. This process continues with a series of electron captures, neutron emission, and pycnonuclear reactions (see Table 2.1), through the depth of the crust, until the matter reaches the density of undifferentiated equilibrium nuclear matter, at which point it is no longer constituted of differentiable nuclei. In doing so, this reaction chain deposits 1.9 MeV per accreted nucleon, distributed throughout the crust, and relatively insensitive to the nuclear history of the accreted matter (Haensel and Zdunik, 2008).

Table 2.1 – Nuclear reactions heating the neutron star deep crust during accretion, beginning with ^{56}Fe at the top of the crust. Table adapted from Haensel and Zdunik (2008).

ρ[a] (g cm^{-3})	Process	Type of reaction	X_n[b]	Q[c] (keV)
1.49×10^{9}	$^{56}\mathrm{Fe} \rightarrow {}^{56}\mathrm{Cr} - 2e^- + 2\nu_e$	e^- capture	0.00	40.7
1.11×10^{10}	$^{56}\mathrm{Cr} \rightarrow {}^{56}\mathrm{Ti} - 2e^- + 2\nu_e$	e^- capture	0.00	35.8
7.85×10^{10}	$^{56}\mathrm{Ti} \rightarrow {}^{56}\mathrm{Ca} - 2e^- + 2\nu_e$	e^- capture	0.00	47.3
2.50×10^{11}	$^{56}\mathrm{Ca} \rightarrow {}^{56}\mathrm{Ar} - 2e^- + 2\nu_e$	e^- capture	0.00	46.1
6.11×10^{11}	$^{56}\mathrm{Ar} \rightarrow {}^{52}\mathrm{S} + 4n - 2e^- + 2\nu_e$	n emission	0.00	59.8
9.075×10^{11}	$^{52}\mathrm{S} \rightarrow {}^{46}\mathrm{Si} + 6n - 2e^- + 2\nu_e$	n emission	0.07	128.0
1.131×10^{12}	$^{46}\mathrm{Si} \rightarrow {}^{40}\mathrm{Mg} + 6n - 2e^- + 2\nu_e$	n emission	0.18	143.5
1.455×10^{12}	$^{40}\mathrm{Mg} \rightarrow {}^{34}\mathrm{Ne} + 6n - 2e^- + 2\nu_e$ $^{34}\mathrm{Ne} + {}^{34}\mathrm{Ne} \rightarrow {}^{68}\mathrm{Ca}$	n emission pycnonuclear	0.39	507.9
1.766×10^{12}	$^{68}\mathrm{Ca} \rightarrow {}^{62}\mathrm{Ar} + 6n - 2e^- + 2\nu_e$	n emission	0.45	65.8
2.134×10^{12}	$^{62}\mathrm{Ar} \rightarrow {}^{56}\mathrm{S} + 6n - 2e^- + 2\nu_e$	n emission	0.45	71.6
2.634×10^{12}	$^{56}\mathrm{S} \rightarrow {}^{50}\mathrm{Si} + 6n - 2e^- + 2\nu_e$	n emission	0.50	77.9
3.338×10^{12}	$^{50}\mathrm{Si} \rightarrow {}^{44}\mathrm{Mg} + 6n - 2e^- + 2\nu_e$	n emission	0.55	84.6
4.379×10^{12}	$^{44}\mathrm{Mg} \rightarrow {}^{36}\mathrm{Ne} + 8n - 2e^- + 2\nu_e$ $^{36}\mathrm{Ne} + {}^{36}\mathrm{Ne} \rightarrow {}^{72}\mathrm{Ca}$ $^{72}\mathrm{Ca} \rightarrow {}^{66}\mathrm{Ar} + 6n - 2e^- + 2\nu_e$	n emission pycnonuclear n emission	0.61	308.8
5.839×10^{12}	$^{66}\mathrm{Ar} \rightarrow {}^{60}\mathrm{S} + 6n - 2e^- + 2\nu_e$	n emission	0.70	29.5
7.041×10^{12}	$^{60}\mathrm{S} \rightarrow {}^{54}\mathrm{Si} + 6n - 2e^- + 2\nu_e$	n emission	0.73	31.0
8.980×10^{12}	$^{54}\mathrm{Si} \rightarrow {}^{48}\mathrm{Mg} + 6n - 2e^- + 2\nu_e$ $^{48}\mathrm{Mg} + {}^{48}\mathrm{Mg} \rightarrow {}^{96}\mathrm{Cr}$ $^{96}\mathrm{Cr} \rightarrow {}^{94}\mathrm{Cr} + 2n$	n emission pycnonuclear n emission	0.80	135.1
1.057×10^{13}	$^{94}\mathrm{Cr} \rightarrow {}^{88}\mathrm{Ti} + 6n - 2e^- + 2\nu_e$	n emission	0.81	11.5
1.254×10^{13}	$^{88}\mathrm{Ti} \rightarrow {}^{82}\mathrm{Ca} + 6n - 2e^- + 2\nu_e$	n emission	0.82	11.3
1.506×10^{13}	$^{82}\mathrm{Ca} \rightarrow {}^{76}\mathrm{Ar} + 6n - 2e^- + 2\nu_e$	n emission	0.84	10.9
1.838×10^{13}	$^{76}\mathrm{Ar} \rightarrow {}^{70}\mathrm{S} + 6n - 2e^- + 2\nu_e$	n emission	0.85	10.0
2.287×10^{13}	$^{70}\mathrm{S} \rightarrow {}^{64}\mathrm{Si} + 6n - 2e^- + 2\nu_e$ $^{64}\mathrm{Si} + {}^{64}\mathrm{Si} \rightarrow {}^{128}\mathrm{Ni}$ $^{128}\mathrm{Ni} \rightarrow {}^{126}\mathrm{Ni} + 2n$	n emission pycnonuclear n emission	0.87	67.3
2.784×10^{13}	$^{126}\mathrm{Ni} \rightarrow {}^{124}\mathrm{Fe} + 2n - 2e^- + 2\nu_e$	n emission	0.88	2.5
3.493×10^{13}	$^{124}\mathrm{Fe} \rightarrow {}^{122}\mathrm{Cr} + 2n - 2e^- + 2\nu_e$	n emission	0.89	2.4

NOTES: This chain of reactions assumes X-ray burst ashes consisting of pure ^{56}Fe at the top of the crust.
[a] ρ is the density at which the reaction takes place.
[b] X_n is the fraction of free neutrons among nucleons.
[c] Q is the heat deposited in the matter at that density.

During an accretion episode, the largest fraction of the heat is released in the crust, at densities $\rho \sim 10^{12}\,\mathrm{g\,cm^{-3}}$, causing the crust to become hotter than the envelope and the core. As a result, when the accretion episode stops, the crust thermally relaxes with its surrounding. A fraction of the heat deposited in the crust diffuses inward, and the remainding fraction diffuses outward (Brown et al., 1998). Because the LMXB lifetime far exceeds the heating time scale of the NS core, the crust reaches a thermal equilibrium in which the inward-diffusing heat during outbursts balances the core heat loss during quiescent periods. Overall, the crustal reactions resulting from accretion are releasing inward-diffusing heat maintaining the core temperature at $T_\mathrm{c} \sim 10^8\,\mathrm{K}$ (Brown et al., 1998). In a steady-state, these reactions give rise to a time-average luminosity, which is directly proportional to $\langle \dot{M} \rangle$, the time-average mass accretion rate:

$$L = 9{\times}10^{32}\,\frac{\langle \dot{M} \rangle}{10^{-11}\ M_\odot\ \mathrm{yr}^{-1}}\,\frac{Q}{1.5\,\mathrm{MeV/amu}}\,\mathrm{erg\ s^{-1}}. \tag{2.1}$$

where Q is the average heat deposited in the NS crust per accreted nucleon (Brown et al., 1998; Brown, 2000). The DCH theory is now widely accepted as the source of energy responsible for the luminosity of LMXBs in quiescence. However, attempts to test the DCH interpretation (using very-fast X-ray transients in quiescence) have been inconclusive due to the large uncertainties in the estimated mass-accretion rates (Wijnands et al., 2013).

Because the source of the luminosity in qLMXBs is internal, the emergent X-ray spectrum is shaped by the radiative transfer through the outer layers of the NS. This thermal emission is therefore expected to be isotropic and stable on various time scales. However, recent outburst episodes can generate variations in the quiescent thermal luminosity on days to years time scales, as observed for the LMXB KS 1731-260 (Rutledge et al. 2002c, following the models described in Ushomirsky and Rutledge 2001, see also Brown and Cumming 2009). In addition to the surface thermal radiation dominating the X-ray spectrum, non-thermal emission have been observed

in the spectra of some qLMXBs in the field of the Galaxy (e.g., Cen X-4, Rutledge et al. 2001a, and Aql X-1, Rutledge et al. 2001b). Unrelated to the DCH-powered thermal luminosity, this non-thermal emission dominates the spectrum above 2 keV is generally modeled with a additional power-law (PL) spectral component[4]. Proposed interpretations of this PL tail include residual accretion onto the NS magnetosphere (Grindlay et al., 2001a; Cackett et al., 2005), shock emission via the emergence of a magnetic field (Campana and Stella, 2000), or an intrabinary shock between the winds from the NS and its companion star (Campana et al., 2004). However, further analyses of the quiescent emission of some field LMXBs have shown that variations in the non-thermal component are correlated to the variations in the thermal component. This suggests the presence of a variable low-level accretion on the NS (for the LMXB XTE J1701−462, Fridriksson et al. 2010, and for the LMXB Cen X-4, Cackett et al. 2010).

In the following subsection, the modeling of the surface thermal emission of qLMXBs powered by DCH is described.

2.2.2 Neutron Star Hydrogen Atmosphere Models

The thermal spectrum from the NS surface in qLMXBs can be explained as due to realistic NS hydrogen atmosphere models (Romani, 1987; Zavlin et al., 1996; Rajagopal and Romani, 1996; Heinke et al., 2006a; Haakonsen et al., 2012). The NS atmosphere in qLMXB systems has been accreted from the low-mass MS stellar companion, whose envelope are generally composed of about $\sim 70\%$ hydrogen (Carroll and Ostlie, 1996). When accretion shuts off and the binary system enters the quiescent phase, heavier elements such as helium and metals settle gravitationally on a time scale of several seconds (Alcock and Illarionov, 1980; Bildsten et al., 1992), leaving a pure H-atmosphere.

[4] A power law is defined by $A(E) = KE^{-\Gamma}$, with the dimensionless photon index Γ, and the normalization K, in photons $\mathrm{cm}^{-2}\,\mathrm{s}^{-1}\,\mathrm{keV}^{-1}$, at 1 keV.

While providing appropriate fits to the spectra of qLMXBs, the blackbody approximation fails to reproduce the expected derived emission area radius. Specifically, the NS radius deduced from the spectral analysis of the quiescent emission of historical transient LMXBs was $< 1\,\mathrm{km}$, assuming a blackbody emission (e.g., for Cen X-4 and 4U 1608−522, Asai et al. 1996; for 4U 2129+47, Garcia 1994). The emergent photon spectra of H-atmosphere NSs, in the framework of the DCH theory, dramatically changed the derived emission area radii to values consistent with the entire area of the NS (Rutledge et al., 1999). Since then, this interpretation has been applied in the detection of a large number of historically transient LMXBs in quiescence, including: Cen X-4 (Campana et al., 2000; Rutledge et al., 2001a); Aql X-1 (Rutledge et al., 2001b) 4U 1608-522 (Rutledge et al., 1999); 4U 2129+47 (Rutledge et al., 2000); the transient in NGC 6440, SAX J1748−2021 (in't Zand et al., 2001); X1732-304 in Terzan 1 (Wijnands et al., 2002); XTE J2123−058 (Tomsick et al., 2004); EXO 1747−214 (Tomsick et al., 2005); MXB 1659−29 (Cackett et al., 2006); 1M 1716−315 (Jonker et al., 2007a); 2S 1803−245 (Cornelisse et al., 2007); 4U 1730−22 (Tomsick et al., 2007); 1H 1905+000 (Jonker et al., 2007b).

Models of H-atmosphere for NSs are now commonly used for qLMXBs, but also for other sub-classes of NSs, such as millisecond pulsars (e.g., Bogdanov, 2013), or cooling INSs (e.g., Pons et al., 2002). Such models are calculated by solving the radiative transfer through an atmosphere in local thermal equilibrium (e.g., Mihalas, 1978). Due to the large surface gravity ($g \sim 10^{14}\,\mathrm{cm\,s^{-2}}$) of NSs, the atmosphere reaches densities $\rho \sim 10^{2}\,\mathrm{g\,cm^{-3}}$, and becomes optically thick to soft X-ray at $T \sim 10^{6}\,\mathrm{K}$ at a depth of $\sim 1\,\mathrm{cm}$ (Romani, 1987). In addition, the thickness of the atmosphere ($\sim 1\,\mathrm{cm}$) compared to the NS radius ($\sim 10^{6}\,\mathrm{cm}$) warrants the use of the plane-parallel approximation, simplifying the calculations to one dimension. Other assumptions common to all current public models of NS atmosphere include the assumptions of radiative equilibrium (i.e., in steady state) and hydrostatic equilibrium, as well as the assumption of isotropic and coherent scattering (Haakonsen et al., 2012).

These models also assume that the atmospheres are non-magnetic. Specifically, surface magnetic fields below $B \ll 10^{10}\,\mathrm{G}$ do not significantly affect the emergent spectrum since the opacities of free-free processes remain unaffected when the photon frequency is larger than the electron cyclotron energy, i.e., when $h\nu \gg h\nu_B$ or $kT \gg heB/m_e c$, since $h\nu \sim kT$ (Kaminker et al., 1983; Zavlin et al., 1996). For temperatures $T \sim 10^6\,\mathrm{K}$, this relation corresponds to $B \ll 10^{10}\,\mathrm{G}$. The `nsa` model is also calculated for non-magnetic atmospheres, with three different magnetic field strengths $B = 0, 10^{12}, 10^{13}\,\mathrm{G}$ (Zavlin et al., 1996), but only the $B = 0\,\mathrm{G}$ model is relevant for NSs in qLMXBs.

At the temperature encountered in the atmosphere, hydrogen is fully ionized, resulting in absorption (i.e., the opacities) dominantly caused by bound-free and free-free processes. In this situation, the atmosphere highly deviates from the gray-atmosphere approximation used for simple radiative transfer solutions in which the opacities are frequency-independent. In the fully ionized atmosphere of NSs in qLMXBs, the opacities of free-free processes strongly depend on the photon energy, such as $\kappa \propto E^{-3}$ (Romani, 1987). In other words, the atmosphere is less opaque to photons with higher energy, and, as a consequence, they emerge from deeper and hotter layers of the atmosphere. The direct observational consequence of this dependence is a distortion from the blackbody spectrum to a spectrum with higher flux at larger energy (see Figure 2.3).

The physics of the radiative transfer aside, the effects of the large surface gravity of a NS are also accounted for in the calculation of the observed flux, by including the gravitational redshift, time-dilation, and light bending. In the Schwarzschild metric, appropriate for slowly rotating NSs ($\lesssim 300\,\mathrm{Hz}$, Bauböck et al. 2013; Psaltis and Ozel 2013), the redshift factor z is given as a function of the mass M_{NS} and the radius R_{NS} of the NS, such that:

$$(1+z) = \left(1 - \frac{R_{\mathrm{sw}}}{R_{\mathrm{NS}}}\right)^{-1/2} = \left(1 - \frac{2GM_{\mathrm{NS}}}{R_{\mathrm{NS}}\,c^2}\right)^{-1/2}, \tag{2.2}$$

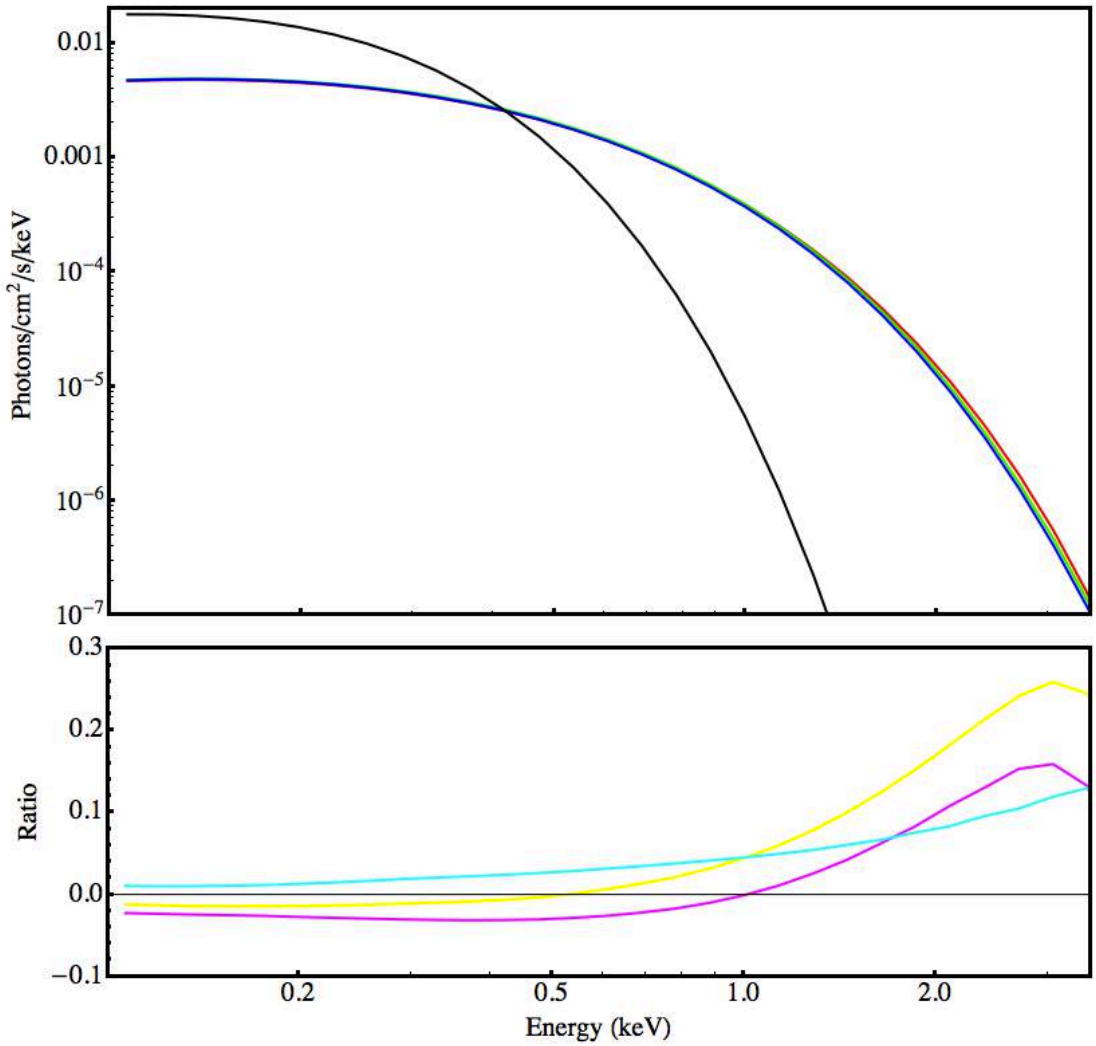

Figure 2.3 – (*top*) The graph compares the spectrum of blackbody emission (black) and spectra of neutron star hydrogen atmosphere models at the same temperature (10^6 K or 86.2 eV), distance (2 kpc), and size of the emission area (corresponding to a neutron star with $R_{\rm NS} = 12$ km and $M_{\rm NS} = 1.4\,M_\odot$). The `nsa` (Zavlin et al., 1996), `nsagrav` (Zavlin et al., 1996), and `nsatmos` (Heinke et al., 2006a) models, available in the X-ray analysis package *XSPEC* (Arnaud, 1996), are shown in red, green and blue, respectively. (*bottom*) The graph shows the fractional differences between the three atmosphere models: `nsa` and `nsagrav` (magenta), `nsa` and `nsatmos` (yellow), `nsagrav` and `nsatmos` (cyan). The differences are less than a few percent below 1 keV, but the models quickly diverge at larger energies.

with G, the gravitational constant, c, the speed of light, and $R_{\rm sw} = 2GM_{\rm NS}/c^2$, the Schwarzschild radius of the NS. The observed flux $F_{\rm obs}$, at a distance $D \gg R_{sw}$ from the source, as a function of the emergent spectrum $F_{\rm em}$, is given by :

$$F_{\rm obs}\left(D, \nu_{\rm obs}\right) = \frac{1}{1+z}\frac{{R_{\rm NS}}^2}{D^2} F_{\rm em}\left[R_{\rm NS}, (1+z)\,\nu_{\rm obs}\right], \tag{2.3}$$

where the photon frequency ν is also redshifted, such that $\nu = (1+z)\,\nu_{\rm obs}$ (for a full derivation, see McClintock et al., 2004). Another consequence of the large surface gravity is the light bending causing the apparent size of the NS (i.e., the apparent radius R_∞, also called projected radius) to be larger than the actual physical size (see Figure 2.4). In other words, an observer at a distance $D \gg R_{sw}$, i.e., at infinity, measures the apparent radius such that:

$$R_\infty = R_{\rm NS}\,(1+z) = R_{\rm NS}\left(1 - \frac{2GM_{\rm NS}}{R_{\rm NS}\;c^2}\right)^{-1/2}. \tag{2.4}$$

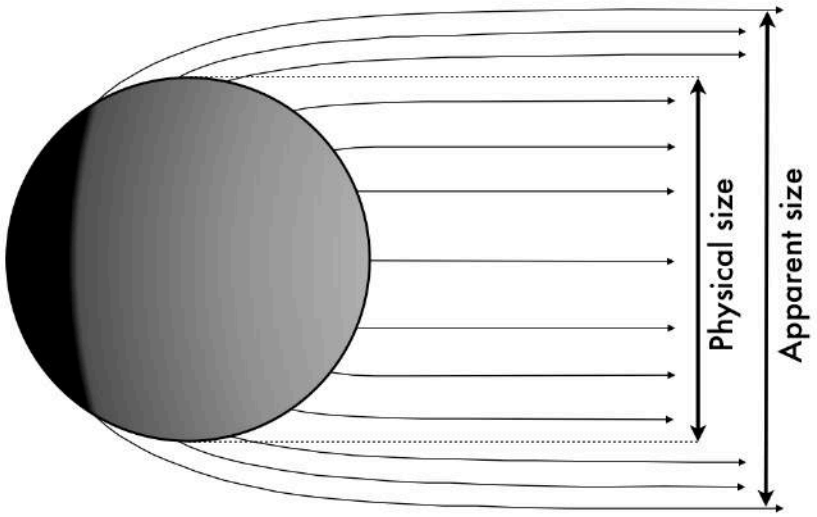

Figure 2.4 – This schematic diagram shows the effect of light bending of photons from the neutron star surface (thin arrows). The visible fraction of the neutron star (gray area) is larger than the hemisphere facing the observer, and as a result, the apparent size is larger than the actual physical size.

The effective temperature is also affected by the gravitational redshift through the relation: $T_{\rm eff,\infty} = T_{\rm eff}\,(1+z)^{-1}$. Therefore, the observed flux at a distance D can be written as:

$$F_{\rm obs}\,(D,\nu_{\rm obs}) = \frac{{R_\infty}^2}{D^2}\,T^3_{\rm eff,\infty}\,\phi\,(\nu_{\rm obs}/T_{\rm eff,\infty})\,, \tag{2.5}$$

where the emergent spectrum is defined by $F_{\rm em} = T^3_{\rm eff}\,\phi\,(\nu/T_{\rm eff})$, with ϕ, a fixed function of temperature and photon frequency, resulting from the radiative transfer calculations (Heinke et al., 2006a).

Among the publicly available models, the major difference resides in the values of the surface gravity g used to calculate the model:

$$g = \frac{GM_{\rm NS}}{{R_{\rm NS}}^2}\,(1+z) = \frac{GM_{\rm NS}}{{R_{\rm NS}}^2}\left(1-\frac{2GM_{\rm NS}}{R_{\rm NS}\,c^2}\right)^{-1/2}. \tag{2.6}$$

The model `nsa` has been implemented for a fixed value $g = 2.43{\times}10^{14}\,{\rm cm\,s^{-2}}$ (Zavlin et al., 1996), i.e., for the values $R_{\rm NS} = 10\,{\rm km}$ and $M_{\rm NS} = 1.4\,M_\odot$. More recently, two more realistic models have been calculated for a range of surface gravity values. The model `nsagrav` has been computed for a range $g = (0.1\text{–}10){\times}10^{14}\,{\rm cm\,s^{-2}}$, as an extension of the `nsa` model, and finally the model `nsatmos` in the range $g = (0.63\text{–}6.3){\times}10^{14}\,{\rm cm\,s^{-2}}$ (Heinke et al., 2006a). Because the models `nsagrav` and `nsatmos` rely on a range of surface gravity values and not a single assumed value, they are more physically accurate than the `nsa` model, and they are therefore preferred for the spectral analyses of qLMXBs. Figure 2.3 shows the small but non-negligible differences between these three publicly available models. They are also compared to a blackbody model of the same temperature and emission area, and at the same distance. Section 6.3.2 also presents a comparison between `nsatmos` and `nsagrav`, when applied to spectral data of qLMXBs.

For the analysis of thermal spectra with the H-atmosphere models described above, the temperature $T_{\rm eff,\infty}$ and the ratio $(R_\infty/D)^2$ are the two parameters adjusted to fit the model to the data (see Equation 2.5). These two measurable parameters

both depend on the physical NS mass $M_{\rm NS}$ and radius $R_{\rm NS}$, which can therefore be deduced from the spectral analysis, assuming a distance to the source. Specifically, the spectral parameters of the `nsatmos` model are $kT_{\rm eff}$, $M_{\rm NS}$, $R_{\rm NS}$, d, and a normalization parameter defining the fraction of the NS surface emitting.

To achieve the precision on the $M_{\rm NS}$ and $R_{\rm NS}$ measurements necessary to constrain the dense matter EoS, it is important to know the distance to the qLMXBs. The 20–50% uncertainty in the distance to qLMXBs in the field of the Galaxy[5] directly contributes to an uncertainty of equal proportions in the radius measurement. Therefore, the large systematic uncertainties on R_∞ resulting from the spectral analysis of field qLMXBs hamper the possibility of obtaining useful constraints on the dense matter EoS until their distances are known with higher precision. One of the observational solutions to obtain precise NS radius measurements lies in the use of qLMXBs located inside GCs, for which the distances are measured from independent methods with uncertainties of $\lesssim 10\%$ (see Section 2.4.2 and 6.2.7 for detailed discussions of GC distance measurements methods and their uncertainties). These systems are chosen to achieve the goals presented in this thesis. The following section presents the matter inside NSs and describes the various proposed dense matter EoS, as well as the constraints that can be obtained from astrophysical sources, such as NSs in LMXBs exhibiting photospheric radius expansion bursts.

2.3 Neutron Star Matter and its Equation of State

NS matter is described by the EoS of cold nuclear matter, i.e., the relation between pressure and density at and above ρ_0. Many EoSs exist to describe matter in all sorts of physical conditions, and under a variety of assumptions. One of the simplest EoSs is the ideal gas law, relating the pressure P, the density ρ and temperature T of an hypothetical ideal gas of randomly moving, non-interacting particles, at low densities $\rho \ll \rho_0$ and relatively low temperatures: $P = \rho R_{\rm sp} T$, where $R_{\rm sp}$ is the

[5]See list of historical transient LMXBs observed in quiescence, at the beginning of Section 2.2.2.

specific gas constant. Cold nuclear matter is far from the ideal gas conditions, and its unique EoS is therefore more complicated than the ideal gas law. It is important to note that EoSs are generally depend on temperature. However, matter at nuclear densities is expected to be in a highly degenerate state (i.e., fermions filling up all energy levels from the lowest level). Consequently, the temperature dependence can be safely neglected.

As mentioned earlier in this thesis, the densities above ρ_0 cannot currently be stably reproduced in Earth laboratory, making it impossible, at the moment, to determine the behaviour of matter at such densities. From a theoretical point of view, various models attempt to determine the EoS of matter above ρ_0 from known interactions between particles. However, the effective forces in neutron-rich matter are unknown, and it is difficult to predict the many-body highly-relativistic interactions such as those happening inside the core of NSs. In addition, it is unclear whether the ground state of matter is composed of deconfined quarks or of hadronic matter. These uncertainties lead to a wide variety of proposed EoSs to describe cold nuclear matter. However, only one EoS describes matter at the densities encountered in the core of NSs, and it is the goal of this thesis to make a step toward the determination of which of the proposed EoSs best describes bulk nuclear matter.

One of parameters playing an important role in the dense matter EoS is the symmetry energy, specifically, how it varies with density. It has numerous implications in astrophysics, including for the radius of NSs. In the low-density regime, at densities between $\rho_{\rm drip}$ and ρ_0 such at those encountered in the crust of NSs, there has been experimental attempts to determine the symmetry energy $S(n)$ and its derivative at ρ_0 (for a review, Newton et al., 2011; Horowitz et al., 2012). At densities over ρ_0, the symmetry energy remains largely unknown. In the following subsections, the three main families of dense matter EoSs that have been proposed in the last 10–20 years are first introduced. This is followed by a short review of the various methods of obtaining observational constraints on the dense matter EoS from NSs.

2.3.1 The High-Density Regime: Description of the Various Equations of State

By solving the equations of stellar structure in a relativistic regime, called Tolman-Oppenheimer-Volkoff (TOV) equations (Tolman, 1939; Oppenheimer and Volkoff, 1939), together with a theoretical EoS $P(\rho)$ describing dense matter, a mass-radius relation ($M_{\rm NS}$–$R_{\rm NS}$) can be obtained for NSs. Conversely, measurements of $M_{\rm NS}$–$R_{\rm NS}$ can be used to determine the corresponding $P(\rho)$. Because NS physical properties are sensitive to the interior physics, this one-to-one correspondence between the EoS and the $M_{\rm NS}$–$R_{\rm NS}$ relation (see Figure 2.5) provides a unique way to determine the EoS in the high-density regime from the observations of NSs (see Section 2.3.2).

Proposed dense matter EoSs can be separated into three main groups (for an extensive review, see Lattimer and Prakash, 2001). The first family of EoSs regroups the so-called "normal" dense matter EoSs. At densities above ρ_0, nuclei dissolve and merge, leaving undifferentiated nuclear matter in β-equilibrium. In this type of matter, the pressure is neutron-dominated via the strong force, with a small proton fraction. In other words, NSs are pressure supported against gravity by neutron degeneracy. The "normal" dense matter EoSs are calculated with a relativistic treatment of nucleon-nucleon interactions, leading to a relation between pressure and density, with the pressure vanishing at zero densities (Lattimer and Prakash, 2001). For NSs, such dense matter EoSs lead to $M_{\rm NS}$–$R_{\rm NS}$ relations composed of two parts. One corresponds to quasi-constant low $M_{\rm NS}$ at large $R_{\rm NS}$ values. Then, as the density increases, the $M_{\rm NS}$–$R_{\rm NS}$ relation for "normal" dense matter EoSs quickly evolves to "quasi-constant" $R_{\rm NS}$ as $M_{\rm NS}$ increases. The EoS then reaches a maximum mass, above which the NS collapses to a black-hole. Examples of these EoSs include AP3-AP4 (Akmal and Pandharipande, 1997), ENG (Engvik et al., 1996), MPA1 (Müther et al., 1987), MS0 and MS2 (Müller and Serot, 1996), and LS (Lattimer and Swesty, 1991). They produce maximum $M_{\rm NS}$ of up to $2.5\,M_\odot$ (Lattimer and Prakash, 2001). This maximum mass increases for "stiffer" EoSs (by opposition to soft EoSs); the stiff-

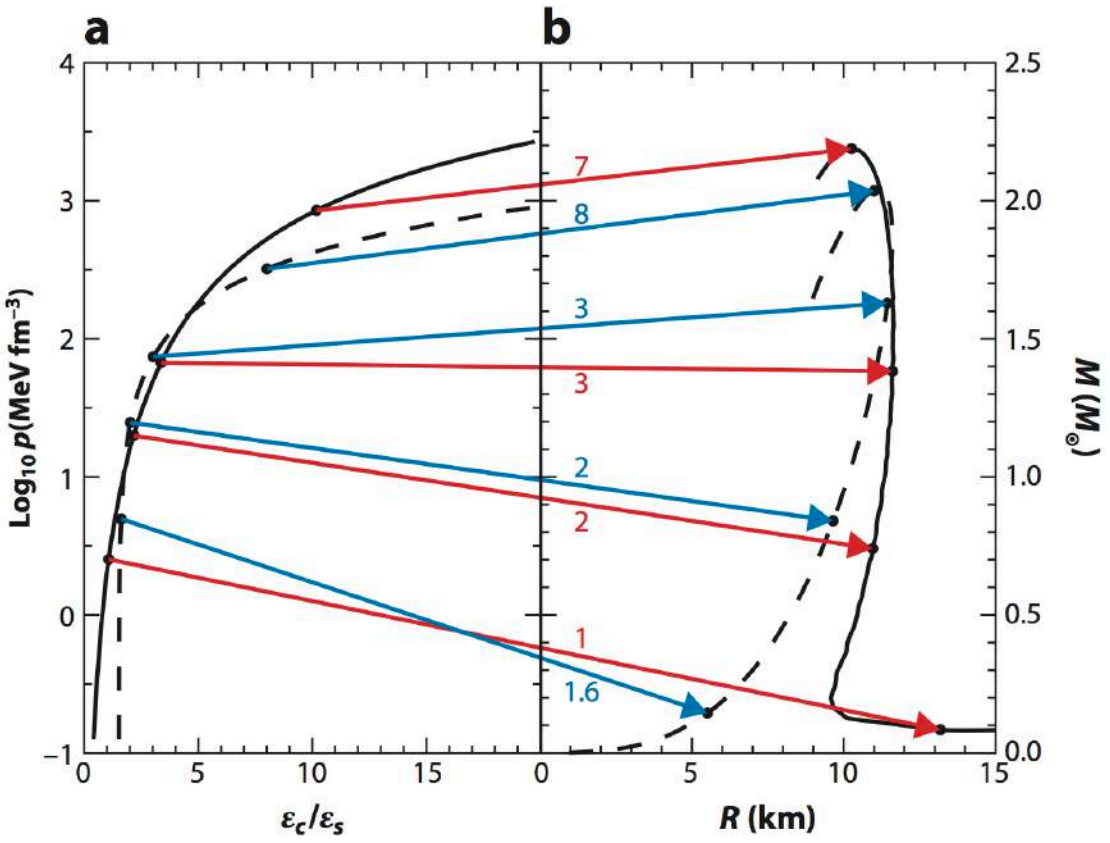

Figure 2.5 – This figure shows the one-to-one correspondence between two equations of state and their respective $M_{\rm NS}$–$R_{\rm NS}$ curves for neutron stars, obtained from solving the Tolman-Oppenheimer-Volkoff equations. The solid (dashed) curve represents a hadronic (pure quark matter) equation of state and the corresponding $M_{\rm NS}$–$R_{\rm NS}$ relation, respectively. The red (blue) arrows connects points on the hadronic (pure quark matter) equation of to the corresponding $M_{\rm NS}$–$R_{\rm NS}$ relations, with the red (blue) numbers providing the central baryon densities n_c/n_s (central energy density ϵ_c/ϵ_s), respectively. Figure adopted from Lattimer (2012)

ness describes how fast the pressure increases with density. For $M_{\rm NS}$–$R_{\rm NS}$ relations, a larger stiffness translates into higher average radii (over $0.5\,M_\odot$).

The second family of dense matter EoSs relies on the assumption that strange quarks compose matter in its ground state. One characteristic of such matter is that the pressure vanishes at a non-zero density, compared to hadronic matter, i.e., they have solid surfaces. In $M_{\rm NS}$–$R_{\rm NS}$ space, these quark star EoSs follow lines of increasing $M_{\rm NS}$ with increasing radius, up to a maximum radius. Above this value, $R_{\rm NS}$ begins decreasing as $M_{\rm NS}$ keeps increasing, until it reaches a maximum, where the object collapses to a black-hole. The maximum $R_{\rm NS}$ varies between $\sim 9\,$km and $\sim 11\,$km, depending on the model parameters used, namely, the strange quark mass m_s and the quantum chromodynamic coupling α_c (Prakash et al., 1995). Note that hadronic compact stars do not have a maximum radius constraint, and their radii can theoretically be as large as $\sim 100\,$km, at masses $M_{\rm NS} < 0.5\,M_\odot$ (Lattimer and Prakash, 2001). Finally, the maximum $M_{\rm NS}$ for strange quark matter (SQM) EoSs is typically in the vicinity of $2\,M_\odot$, at most (Lattimer and Prakash, 2001).

A third family of dense matter EoSs is characterized by matter in which a significant amount of softening (i.e., less pressure) is included at high densities. This emerges from the inclusion of additional degrees of freedom (DOF) resulting from exotic particles at high density. At a critical density of a few ρ_0, a phase transition from nucleons to these exoticas introduces the additional component in the NS "inner core". Such exotic particles include populations of hyperons at large densities (GM3, Glendenning and Moszkowski 1991), or kaon (GS1, GS2, Glendenning and Schaffner-Bielich 1999) or pion condensates (PS, Pandharipande and Smith 1975). These EoSs are referred to as "hybrid" dense matter EoSs. Because of this phase-transition leading to a softer EoS, the maximum $M_{\rm NS}$ is rather low ($M_{\rm NS} < 1.7\,M_\odot$). This also results in $M_{\rm NS}$–$R_{\rm NS}$ curves with a smooth decrease in $M_{\rm NS}$ from the maximum to the minimum $M_{\rm NS}$, as $R_{\rm NS}$ increases. This family of EoSs also includes the possibility of a second phase transition from hyperons to quark matter in the central-most parts

of the core (Weber, 2006). Some of the "hybrid" EoSs are MS1 (Müller and Serot, 1996), FSU (Shen et al., 2010a,b), GM3 (Glendenning and Moszkowski, 1991), GS1 (Glendenning and Schaffner-Bielich, 1999), and PAL6 (Prakash et al., 1988).

Figure 2.6 presents a schematic view of the various proposed structures of NSs, and a selection of $M_{\rm NS}$–$R_{\rm NS}$ relations of dense matter EoSs from the three families are displayed in Figure 2.7.

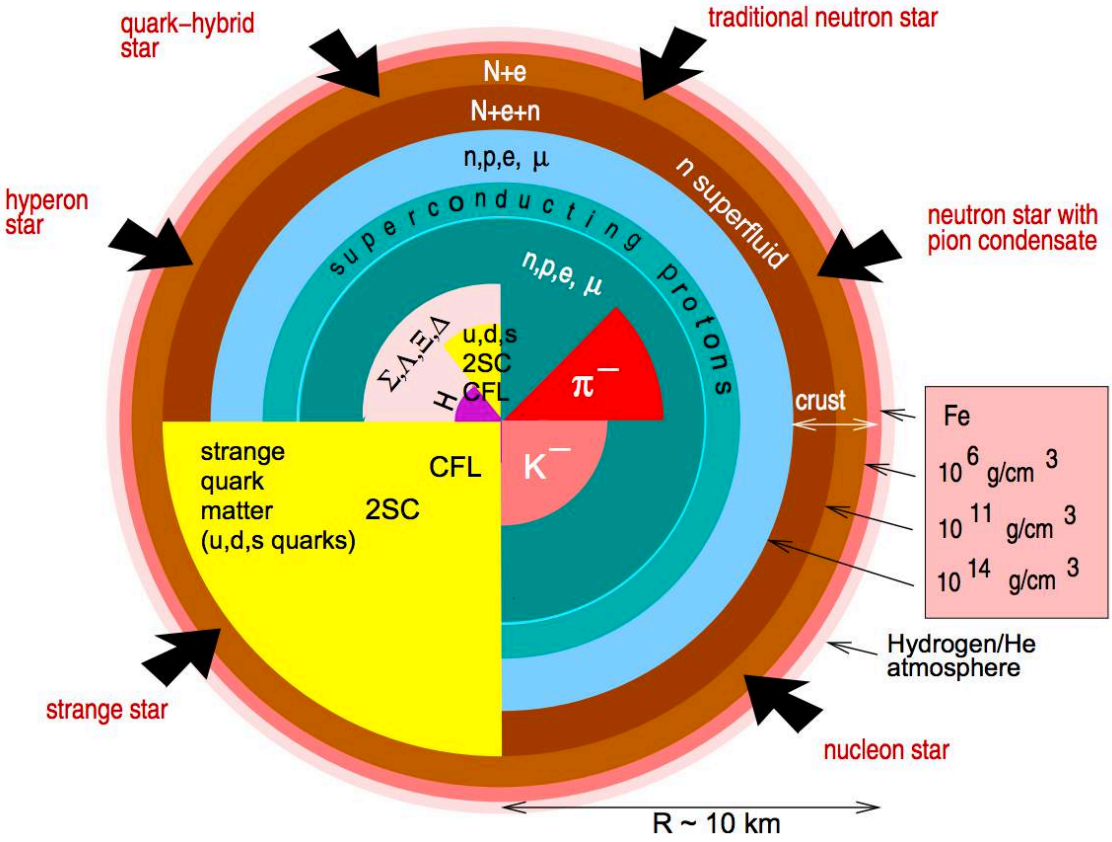

Figure 2.6 – This schematic view presents the different compositions of NSs as predicted by nuclear physics theory. The various letters abbreviate the different particles: nucleons (N), neutrons (n), protons (p), electrons (e), muons (μ), pions (π^-), kaons (K^-), hyperons (Σ, Λ, Ξ, Δ), quarks (u,d,s). CFL and 2SC refer to two superconducting phases of quark matter. Figure adopted from Weber et al. (2007).

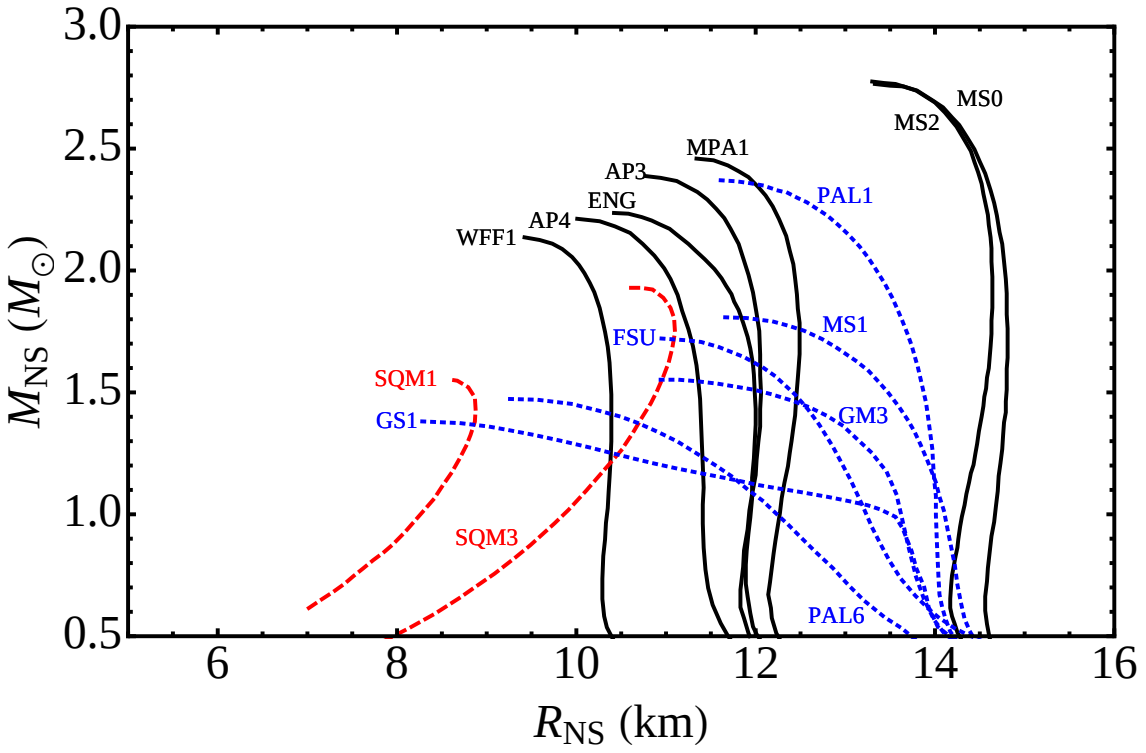

Figure 2.7 – This figure displays the M_{NS}–R_{NS} relations of a selection of dense matter equations of state: *solid black* for "normal" matter equation of state, *dotted blue* for the hybrid matter equation of state, and *dashed red* for the strange quark matter equations of state. These M_{NS}–R_{NS} curves were kindly provided by J. Lattimer, private communication.

2.3.2 Equation of State Constraints from Neutron Stars Observations

This section describes some of the astrophysical constraints on the dense matter EoS that have been obtained from observations of NSs within various scenarios, starting with $M_{\rm NS}$ measurements, before discussing methods leading to measurements of $R_{\rm NS}$.

Measuring $M_{\rm NS}$

NSs in binary systems are not only extremely useful as test beds for general relativity, but also for providing the possibility to measure precisely the masses of NSs. The orbital parameters of a binary system can be obtained from the timing observations of radio or X-ray pulsars in those systems. Indeed, these NSs emit pulses of electromagnetic radiation at regular intervals, which are then used to trace the position of the NS during an orbit. A careful modeling of the times of arrival of these pulses allows reconstruction of the orbital solution of the system. Non-relativistic ("Keplerian") orbital parameters include the orbital period, the eccentricity, the projected semi-major axis of the orbit (which depends on the system's inclination), and the epoch of periastron. Additionally, general relativistic ("post-Keplerian") orbital parameters can also be measured in some specific cases and with sufficently high-S/N timing (for a review of pulsar timing, see Kramer 2008).

With two or more measured relativistic effects such as the rate of advance of the periastron (i.e., precession), the orbital period derivative or/and the gravitational redshift causing time delays, one can break the degeneracy between the masses and the system inclination, and therefore deduce the two masses of the system. Double NS systems are useful for that purpose since their eccentric orbit ($e \gtrsim 0.1$) permits precise measurements of the advance of periastron and the orbital period derivative, both particularly sensitive to non-circular orbits. This method was first used to measure the masses of the two NSs of the Hulse-Taylor pulsar: $m_{\rm psr} = 1.42 \pm 0.06\, M_\odot$ and $m_{\rm comp} = 1.41 \pm 0.06\, M_\odot$ (Taylor and Weisberg, 1982). Twenty-years of additional pulsar timing refined the measurement to make it the most precisely measured NS mass to date: $m_p = 1.4414 \pm 0.0002\, M_\odot$ (Weisberg and Taylor, 2005).

In the case where the companion is not a NS but a WD or a MS star, these two post-Keplerian parameters are more difficult to measure precisely since the orbits tend to be circularized during the evolutionary steps leading to such systems. Consequently, additional relativistic effects, or independent measurements of the companion mass are necessary to break the degeneracy between the mass ratio and the inclination of the system. The Shapiro delay is one such relativistic effect that led to NS mass measurements (e.g., Deneva et al., 2012). Shapiro delay manifests itself as a time delay of the radio pulses traveling near the massive companion (e.g., a WD), due to its gravitational field. It is the strongest and most easily observable for edge-on binary systems ($i \sim 90°$), in which electromagnetic pulses from the NS travel close to the companion during orbital conjunction (alignment with the line of sight). This method was used to measure the mass of a massive NS in orbit with a WD ($m_{\rm psr} = 1.96 \pm 0.04\,M_\odot$, Demorest et al., 2010). Finally, if the mass of the companion can be measured from an independent method, no additional relativistic effects are necessary. For example, in the binary system hosting the radio pulsar PSR J0348+0432, optical observations of the WD companion lead to its mass estimate using WD atmosphere models. With this additional constraint, the mass of the NS was calculated: $m_{\rm psr} = 2.01 \pm 0.04\,M_\odot$ (Antoniadis et al., 2013).

As shown in Figure 2.5, the NS maximum mass is dependent on the dense matter EoS. This is a direct consequence of general relativity and the TOV equations (Lattimer and Prakash, 2007). A NS with a mass larger than the maximum mass of a proposed EoS brings direct observational evidence that this particular EoS does not appropriately describe the matter inside NSs. Historically, $M_{\rm NS}$ measurements were in the 1.3–1.5 $M_\odot$ range (Lattimer, 2012). While they confirmed theoretical predictions about NSs (e.g., Taylor and Weisberg, 1989), subsequent measurements at and below previous values did not place any new constraints on the dense matter EoS. Only a $M_{\rm NS}$ measurement larger than all previous NS masses measurements brings new constraints on the dense matter EoS.

The two high-mass measurements ($\sim 2\,M_\odot$) mentioned above are currently the highest precisely measured masses of NSs. Such high masses exclude previously proposed hybrid models of EoSs, although they do not rule out any specific form of exotica. SQM EoSs also seem to be disfavoured, since their predicted maximum $M_{\rm NS}$ approaches the $2\,M_\odot$ limit for only some of the models within the parameter spaces permitted by nuclear physics constraints. Nonetheless, fine tuning of models may allow these disfavoured EoSs to be marginally consistent with the $M_{\rm NS}$ measured in PSR J1614−2230 and PSR J0348+0432 (e.g., Bednarek et al. 2012; Weissenborn et al. 2012, for hybrid models, and Lai and Xu 2011, for SQM models). Overall, the two high-$M_{\rm NS}$ measurements seem to favour "normal matter" hadronic EoSs. For a review of $M_{\rm NS}$ measurements and their implications for nuclear physics, see Lattimer (2012). It is important to note that a mass of $m_{\rm psr} = 2.40\pm0.12\,M_\odot$ has been measured for PSR B1957+20 (van Kerkwijk et al., 2011), which would place much more stringent constraints on the dense matter EoS. However, the large uncertainties and model dependencies involved with this mass measurement preclude drawing any firm conclusions yet.

Measuring $R_{\rm NS}$

In addition to the NS mass deduced from orbital parameters, several observational methods exist to extract the radius of NSs. However, while they make use of different phenomenology, these methods, described below, often measure the ratio $M_{\rm NS}/R_{\rm NS}$, instead of just $R_{\rm NS}$. Independent observables are therefore needed to break the degeneracies.

As was discussed in Section 2.2, measuring radiation radius R_∞ (Equation 2.4), which depends on $M_{\rm NS}/R_{\rm NS}$, using the surface emission from the NS in qLMXB systems, can place constraints on the dense matter EoS. In a similar fashion, the surface emission from nearby ($< 0.5\,$kpc) cooling INSs can be compared to models of emission from a H-atmosphere of NS to extract R_∞. However, for INSs, this method is only constraining enough when the distance to the NS is known accurately enough.

None of the known INSs are located in the core of GCs which would facilitate the determination of their distance. Only one INS, RX J185635−3754, has a known distance allowing for R_∞ to be measured. For this source, difficulties arise because of the high magnetic field affecting the thermal emission (see Section 6.4.3, for more details about this particular measurement).

Another class of NSs has been studied to attempt to constrain the dense matter EoS. During the active accretion periods in transient LMXBs, surface thermonuclear instabilities can develop leading to a sudden brightening, called a Type-I X-ray burst. While many such bursts occur during an outburst episode in a LMXB, only a small fraction of bursts are powerful enough that the energy released by the surface nuclear burning temporarily lifts the NS photosphere. Following these PRE bursts, the Eddington flux, measured when the flux and the temperature are the highest (called touchdown), provides an additional observable (Özel, 2006):

$$F_{\mathrm{Edd},\infty} = \frac{cGM}{\kappa d^2}\sqrt{1-2GM/Rc^2} \tag{2.7}$$

where κ is a composition-dependent opacity, and d the distance to the source. At touchdown, it is assumed that the photosphere relaxes to the NS surface. If this is the case, the surface emission can be analyzed to deduce the value of R_∞, as is done for qLMXBs (see Section 2.2). Combining $F_{\mathrm{Edd},\infty}$ at touchdown to R_∞ in the post-burst phase breaks the degeneracy between R_{NS} and M_{NS}. However, the degeneracy of M_{NS} and R_{NS} with the distance persists, with two options to solve it: Either observing a PRE burst source with an independently known distance, or measuring an additional observable with a $M_{\mathrm{NS}}/R_{\mathrm{NS}}$ dependence. For the latter, obtaining the gravitational redshift z (Equation 2.2) in an independent manner (not from R_∞) proves useful. This can be achieved from the observation of gravitationally redshifted lines in the spectra of X-ray bursts. In that case, the three observables ($F_{\mathrm{Edd},\infty}$, R_∞, and z) lead

to the determination of $M_{\rm NS}$, $R_{\rm NS}$ and d, such that (Özel, 2006):

$$\begin{aligned} M_{\rm NS} &= \frac{c^5}{4G\kappa}\left(\frac{R_\infty}{d}\right)^2 \frac{1}{F_{\rm Edd,\infty}} \frac{1}{(1+z)^3}\left[1-(1+z)^{-2}\right]^2 \\ R_{\rm NS} &= \frac{c^3}{2\kappa}\left(\frac{R_\infty}{d}\right)^2 \frac{1}{F_{\rm Edd,\infty}} \frac{1}{(1+z)^3}\left[1-(1+z)^{-2}\right]^2 \\ d &= \frac{c^3}{2G\kappa}\left(\frac{R_\infty}{d}\right) \frac{1}{F_{\rm Edd,\infty}} \frac{1}{(1+z)^2}\left[1-(1+z)^{-2}\right]. \end{aligned} \tag{2.8}$$

$M_{\rm NS}$, $R_{\rm NS}$ and d of the type-I X-ray burst LMXB EXO 0748−676 were determined using an independent measurement of $z = 0.35$ (Özel, 2006). However, the original identification of the iron and oxygen lines leading to this z measurement (Cottam et al., 2002) were shown to be controversial (Sidoli et al., 2005), and deeper observations with *XMM* did not confirm the existence of such spectral features (Cottam et al., 2008).

If a measurement of z is not available, the distance must be obtained from an independent method, or assumed. Instances of dense matter EoS constraints from X-ray bursting sources in GCs, or for X-ray bursting sources with alternate distance measurements include:

- EXO 1745−248 in the GC Terzan 5 (Özel et al., 2009),
- 4U 1820−30 in the GC NGC 6624 (Güver et al., 2010b),
- SAX J1748.9−2021 in the GC NGC 6440 (Güver and Özel, 2013),
- 4U 1608−52, using a distance estimated from red clump stars (Güver et al., 2010a),
- KS 1731−260, using a distance estimated from the surrounding stellar density, and a stellar distribution model (Özel et al., 2012a),
- MXB 1730−335, with a range of assumed distances (5–10 kpc, Sala et al., 2012).

The PRE burst scenario still requires assuming a value or range of values for the composition to determine κ. In addition, the post-PRE measurement of R_∞ also depends on an assumption, namely the colour-correction factor $f \equiv T_{\rm eff}/T_\infty$, which can be assumed or modeled (for a discussion of the colour-correction and burst atmosphere modeling, see Suleimanov et al., 2011a; Zamfir et al., 2012).

Some of the results obtained from this method placed stringent constraints on the dense matter EoS, by measuring a radius $R_{\rm NS} < 11\,{\rm km}$, with uncertainties on $R_{\rm NS}$ of the order of 10% (Özel et al., 2009; Güver et al., 2010a), and as good as 4% (Güver et al., 2010b). However, the claimed results were called into question on several fronts. First, some of the assumptions made regarding the composition, and in some cases, the distance were too constraining (Steiner et al., 2010; Suleimanov et al., 2011a). Then, it was pointed out that the photosphere might not fully retract down to the NS surface, which caused these analyses to be internally inconsistent; a large fraction of the Monte Carlo (MC) samples led to complex values of $M_{\rm NS}$ and $R_{\rm NS}$, resulting in low MC acceptance rates ($< 1\%$, as demonstrated by Steiner et al., 2010). Finally, it has been discussed that the short bursts from the LMXBs listed above might not appropriately match the theory of passively cooling NSs (Suleimanov et al., 2011a). These authors proposed a study of the long Type-I X-ray burst from the LMXB 4U 1724−307, in which they fit the flux in the entire cooling tail to theoretical predictions, instead of simply measuring F_∞ at touchdown, when the photosphere touches the NS surface, as previously done. This proposed method, applied to 4U 1724−307, resulted in a radius $R_{\rm NS} > 11\,{\rm km}$, considering a variety of possible atmospheric compositions (Suleimanov et al., 2011a).

A different class of X-ray emitting NSs, the accretion-powered millisecond pulsars, has also been used for $M_{\rm NS}$-$R_{\rm NS}$ measurements. The accretion, channeled by the NS magnetic field, creates hot spots at the magnetic poles of the NS. Because these hot spots dominate the X-ray emission, they induce intensity variation as they move in and out of the line of sight, depending of the angle geometry, while the NS is spinning.

However, gravitational light bending increases the visible fraction of the NS surface, which causes a smearing of the pulses. This effect is related to the compactness of the NS, i.e., $M_{\rm NS}/R_{\rm NS}$. Therefore, modeling of the observed X-ray pulse profile of such sources allows to reconstruct the angle geometry, and more importantly to extract $M_{\rm NS}/R_{\rm NS}$. This method has attempted to place constraints on the dense matter EoS (Leahy et al., 2008, 2009; Morsink and Leahy, 2011). For X-ray pulsars with spin frequencies $> 300\,$Hz, relativistic effects (such as Doppler shifts and time delays) of emitted photons results in pulse profile assymetries (Cadeau et al., 2007). At spin frequencies $> 500\,$Hz, the NS shape deviates from a purely spherical object, and alternative general relativistic space-time metric must be employed (Bauböck et al., 2013; Psaltis and Ozel, 2013). With all these considerations, the pulse profile of X-ray emitting pulsars can be fitted to extract NS properties such as $R_{\rm NS}$, $M_{\rm NS}$, and $M_{\rm NS}/R_{\rm NS}$. Nevertheless, degeneracies persist between the NS properties, the system geometry, or the number of spots visible. The currently available S/N from the pulse profiles of accreting millisecond pulsars prevents placing tight constraints on the NS compactness. Recently, using a method combining pulse profile analysis to X-ray spectroscopy (phase-resolved spectroscopy) of the surface emission, the radius of the millisecond pulsar PSR J0437−4715 was constrained to be $R_{\rm NS} > 11.1\,$km (Bogdanov, 2013).

Alternatively, the spin period of rotating NSs also places limits on the behaviour of matter at high densities. Specifically, the mass-shedding limit defines the absolute maximum spin of NSs, which depends on their mass and radius. This limit is defined by the rotational frequency at which the velocity of a particle orbiting just above the surface of the NS equals the velocity of the NS surface (Lattimer and Prakash, 2004). This is defined by the Keplerian velocity $v_{\rm K} = (2\pi)^{-1}\sqrt{GM/R^3}$, in the case of a Newtonian sphere, which constraints $R_{\rm NS}$ in the following way:

$$R_{\rm NS} < 10.4 \left(\frac{1000\,{\rm Hz}}{\nu_{\rm K}}\right)^{2/3} \left(\frac{M_{\rm NS}}{M_\odot}\right)^{1/3} {\rm km}. \tag{2.9}$$

Thus far, the fastest spinning NS observed, PSR J1748−2446ad, does not exclude any proposed dense matter EoS (Lattimer and Prakash, 2007). In addition, twin kHz quasi-periodic oscillations (QPOs) observed during the bursting X-ray emission of active X-ray binaries, can provide limits on $M_{\rm NS}$ and $R_{\rm NS}$ (Miller et al., 1998). While the origin of the QPOs is not firmly identified, it is generally accepted that the high-frequency component of the kHz QPOs is linked to the innermost stable circular orbit of the accretion disk (defined by $R_{\rm ISCO} = 6GM/c^2$ in a Schwarzschild metric) inside which accreted matter does not orbit the NS anymore but quickly spirals onto it. By measuring this upper kHz QPO frequency $\nu_{\rm ISCO}$, limits on $M_{\rm NS}$ and $R_{\rm NS}$ follow, such that:

$$\begin{aligned} M &\leq \left(\frac{2200\,\mathrm{Hz}}{\nu_{\rm ISCO}}\right)\left(1+0.75\frac{2\pi c f_{\rm spin} I}{GM^2}\right)\,M_\odot \\ R &\leq \left(\frac{1950\,\mathrm{Hz}}{\nu_{\rm ISCO}}\right)\left(1+0.20\frac{2\pi c f_{\rm spin} I}{GM^2}\right)\,\mathrm{km}, \end{aligned} \tag{2.10}$$

where $f_{\rm spin}$ is the spin frequency of the NS (also measured during X-ray bursts), and $I \sim MR^2$ is the moment of inertia of the NS (Miller et al., 1998). These two equations however only place upper limits on $R_{\rm NS}$ and $M_{\rm NS}$ which become more constraining for larger kHz ISCO frequencies, or for smaller NS spin frequencies. This method has not yet generated constraining limits on $M_{\rm NS}$ and $R_{\rm NS}$ to be useful for the determination of the dense matter EoS (Miller, 2013).

Measuring $I_{\rm NS}$

Directly measuring the moment of inertia from NSs in binary systems could constrain $R_{\rm NS}$ if the mass $M_{\rm NS}$ is known. A value of $I_{\rm NS}$ known to $\sim 10\%$ accuracy would permit measurements of the pressure above nuclear density, therefore providing constraints on the dense matter EOS. It is claimed that such accuracy on $I_{\rm NS}$ could be obtained with several years of timing observations of the double-pulsar system PSR J0737−3039A/B (Lattimer and Schutz, 2005). Specifically, measuring the effect of spin-orbit coupling from the rate of advance of the periastron and the orbital

period derivative in this system could lead to an estimation of $I_{\rm NS}$ (Lyne et al., 2004; Kramer, 2008). However, it is claimed that because the acceleration in the potential of the Galaxy is not precisely known, a constraining measurement of $I_{\rm NS}$ might be difficult to obtain (Miller, 2013). This issue could be solved with the discovery of a pulsar, PSR J0337+1715, in a triple system with two WDs (Ransom et al., 2014). In this system, the acceleration in the potential of the third component (one of the WD) is known, and dominates over the gravitational potential of the Galaxy. However, the measurements of the post-Keplerian parameters needed to deduce the spin-orbit coupling will be difficult since the orbits are highly circular, i.e., the eccentricities of the inner and outer orbits are close to zero.

Summary of Astrophysical Constraints

Model ambiguities and other systematics often render difficult the precise measurements of R_∞ (or $R_{\rm NS}$) with the methods described above. Because various methods have their own sets of systematic uncertainties, it is therefore of value to pursue each method independently. This will permit intercomparison of their various NS radius measurements.

Furthermore, the sources of studied in this thesis, namely the qLMXBs inside GCs, are non-variable systems with a well-modeled surface thermal emission. The non-thermal contribution to their observed spectra amounts to less than $\lesssim 3\%$ of the total flux, compared to historical transient LMXBs in quiescence located in the field of the Galaxy. In addition, qLMXBs inside GCs present the advantage of having indenpendently measured distances with uncertainties on the order of $\sim 10\%$. An overview of GCs is now presented in the following section, as well as a description of the various distance measurement methods.

2.4 Globular Clusters

GCs consist of a large set of gravitationally bound stars (up to 10^6 stars), orbiting the centre of a galaxy. In the Milky Way Galaxy, there are 157 GCs catalogued (Harris, 1996, last update in 2010). The closest GC, M4, is located at a distance of 2.2 kpc, while the most distant lies at 123 kpc from the Sun. Because they are composed of a large sample of stars all located at the same distance – modulo their line-of-sight extent (~ 50 pc, i.e., less than a few percent of the total distance) – GCs have been extensively observed at optical wavelengths for their usefulness to study stellar evolution. From these studies, astronomers have been able to estimate the ages, distances, or metallicities of GCs.

For the purpose of the work presented in this thesis, GCs are useful for their well measured distances, and their abundances of X-ray binaries. These reasons, as well as some background information about GCs, are discussed in the following subsections. Also presented here is a list of known qLMXBs in GCs.

2.4.1 Properties of Globular Clusters

Typical GCs are thought to be composed of a single population of stars formed from the gravitational collapse of the same gaseous molecular cloud (Caputo, 1985). As a consequence, the member stars of a GC have essentially the same metallicity and age. Only the initial masses of stars differed at formation, leading to a variety of stellar lifetimes within a GC. Metallicity is a stellar property related to composition, i.e., the abundance of elements heavier than hydrogen and helium. It is defined by:

$$[\mathrm{Fe/H}] = \log_{10}\left(\frac{N_{\mathrm{Fe}}}{N_{\mathrm{H}}}\right)_{\star} - \log_{10}\left(\frac{N_{\mathrm{Fe}}}{N_{\mathrm{H}}}\right)_{\odot}, \tag{2.11}$$

the difference of the log-ratios of abundances of iron with respect to hydrogen between a star and the Sun. All GCs have metallicities lower than that of the Sun, i.e., $[\mathrm{Fe/H}] < 0$. GC stars therefore correspond to an older generation of stars (population II) that formed from material less metallic than the Sun, which is a population I star

(Baade, 1944). GCs are among the oldest objects in our Galaxy. Historically, they have been used to place a lower limit on the age of the Universe. The average age of GCs has been estimated to $12.9 \pm 2.9\,\mathrm{Gyr}$ (Carretta et al., 2000).

In the last decade or so, high-precision photometric studies of GCs, in particular with the *Hubble Space Telescope* (*HST*), have exposed two or three generations of stars previously concealed in the MS of some GCs. For example, the GC $\omega\,\mathrm{Cen}$ has two distinct populations (Bedin et al., 2004), while NGC 2808 appears to have three populations (Piotto et al., 2007). This paints a more complicated picture of GCs were the different populations of stars were not formed from the same initial cloud. One possible explanation is that the GC first generation of stars, presumably massive, quickly evolved, therefore enriching the GC with heavier elements resulting from the nuclear burning within hot massive stars (Gratton et al., 2012). A second generation of stars with higher metallicity then formed from this enriched material.

The easiest observable to obtain from GC stars is their stellar magnitudes. Using different photometric bands, one can produce a colour-magnitude diagram (CMD), where the colour is a difference of magnitudes (for example, $m_B - m_V$). The colour is a distance independent parameter linked to the effective temperature of a star. Thus, a CMD describes the distribution of GC stars in a Luminosity-Temperature space (see Figure 2.8). The first CMD data calibrated with photoelectric measurements were obtained for the GCs M92 and M3, more than 60 years ago (Arp et al., 1952, 1953). In a CMD, a single population should follow a particular theoretical curve of stellar evolution (called isochrones, from *iso-*, same, and *chronos*, time). Because stars evolve differently depending on their composition, some properties of individual populations of stars in a GCs, such as the metallicity, can be deduced from the fitting of theoretical isochrones to the observable distribution of stars in a CMDs (Caputo, 1985). The age of the cluster can also be deduced from theoretical isochrones by identifying the stars that have evolved passed the MS.

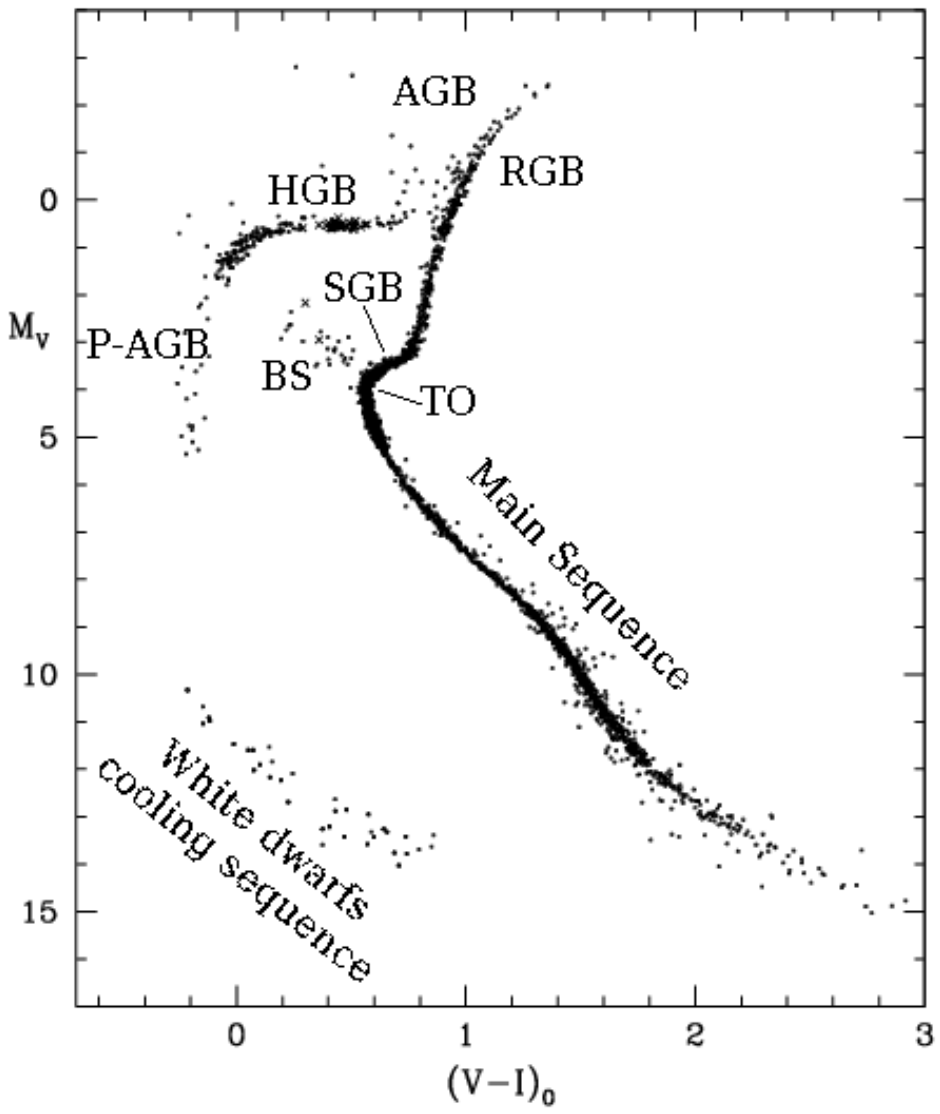

Figure 2.8 – This figure shows a template colour-magnitude diagram made, for illustrative purposes, with data from six globular clusters (Harris, 2003). The different stages of stellar evolution are labeled: `TO`, for Turn-off point, `BS`, for Blue stragglers, `SGB`, for Sub-giant branch, `RGB`, for Red-giant branch, `AGB`, for Asymptotic giant branch, `HGB` for Horizontal giant branch, and `P-AGB` for Post-asymptotic giant branch. Figure adapted from Harris (2003). Original figure available at `http://www.physics.mcmaster.ca/Fac_Harris/Astropics.html`, and labeled for the purpose of this section.

GCs can also be described by their morphology, deduced from star counting and luminosity density profiles of the clusters. The luminosity radial profile $f(r)$ of most GCs can be represented by a King profile (King, 1962):

$$f(r) = k\left(\frac{1}{\left(1+(r/r_c)^2\right)^{1/2}} - \frac{1}{\left(1+(r_t/r_c)^2\right)^{1/2}}\right)^2, \tag{2.12}$$

where r_c defines the core radius (the full width at half maximum FWHM of the King profile), r_t defines the tidal radius, where the Galactic tidal force balances the GC gravitational attraction, and k is the normalization of the profile. The half-mass radius r_h, corresponding to the radius of the sphere enclosing half of the GC mass, can also be used to characterize a cluster. The typical morphological characteristics of GCs are central densities of the order $\rho_{\rm GC} = 10^3 - 10^4\ L_\odot\,{\rm pc}^{-3}$ (Harris, 1996), masses of $\sim 10^4 - 10^6\,M_\odot$ (Caputo, 1985) and sizes of $r_h \lesssim 10\,{\rm pc}$ (van den Bergh, 2008). For core-collapsed GC, with $r_c \to 0$, the luminosity profile diverges from King profile since the central density increased to $\rho_{\rm GC} = 10^{4.5} - 10^{5.5}\ L_\odot\,{\rm pc}^{-3}$ (Harris, 1996) after several relaxation times (Hénon, 1965; Joshi et al., 2000). The sizes of GCs are converted from angular to physical sizes using the distances estimated for each clusters, which are measured with a variety of methods. These methods are now described since the distances to GCs and their uncertainties play an important role in the analyses of this thesis.

2.4.2 Distance Determination

Since the first GC distance estimations performed in 1918 (Shapley, 1918) using a Period-Luminosity relation for RR Lyrae stars[6] established empirically (Leavitt and Pickering, 1912), a wide variety of methods have been developed to determine the distances to GCs. RR Lyrae, named after the prototype of the class, are stars of the horizontal branch (HB) exhibiting regular pulsations; their observed period of

[6] Although, these were thought to be Cepheids variables at the time.

intensity variation is related to the average luminosity (Smith, 1995, for a review). This theoretically well-understood relation is calibrated in absolute luminosity with nearby RR Lyrae stars for which an accurate parallax distance measurement is possible (Popowski and Gould, 1999). With such calibration, and because of the abundance of RR Lyrae in GCs, the distances to these collection of stars can be estimated (e.g., Bono et al., 2007, 2008).

Other GC distance determination techniques rely on observations in various photometric bands to obtain colour information, i.e., stellar temperature. Some methods require, for example, fitting parts of the CMD (in apparent magnitudes) with theoretical isochrones (with given ages and metallicities) calibrated in absolute magnitude to allow for measurements of the distance modulus μ. The physical distance of the GC can then be calculated with $\mu = M - m = 5 \log_{10} (d_{\rm GC})$, where M and m are the absolute and apparent magnitudes. This can be done with the MS stars of a cluster (e.g., Gratton et al., 2003), the HB stars (e.g., Salaris et al., 2007), or the stars at the tip of the red giant branch (RGB, e.g., Ferraro et al., 2000). Distance measurement from MS fitting can be complicated by the presence of multiple stellar populations with different metallicities (Gratton et al., 2012). HB and RGB stars have the advantage of being brighter than MS stars, although they are generally less numerous. In a similar manner, the cooling sequence of WDs can be compared to theoretical cooling models to extract the distance modulus of a GC (e.g., Hansen et al., 2007; Strickler et al., 2009). This method is generally restricted to nearby GCs because of the low luminosity of WDs. An alternative method involves fitting the spectral energy distribution of WDs in a GC to theoretical models of WDs with hydrogen atmosphere to calibrate the apparent magnitudes and deduce the distance modulus (e.g., Woodley et al., 2012).

Another method of GC distance determination requires the presence of eclipsing binaries inside the GC. When a star transits in front of its companion, analysis of the eclipse light curve can lead to precise measurements of the stellar radii. When

combined with temperature measurements and stellar evolution models, estimates of the luminosity and distance modulus are obtained, and therefore the distance of the host cluster is deduced (e.g., Thompson et al., 2010).

Finally, the last method discussed here does not depend on the photometric properties of stars (colour and magnitudes). Instead, by studying the kinematics of GCs, i.e., how the stars move within, distance estimates can be extracted. Briefly, such methods require measuring the proper motion of GC stars (projected displacement over an extended period of time), as well as the radial velocities of GC stars (line of sight velocities, measured from spectral analysis). Proper motions provide a velocity dispersion in milliarcseconds per year while the radial velocities lead to a velocity dispersion in kilometer per second (in the radial direction). The "dynamical" distance of the host cluster is then obtained by combining these two velocity dispersion measurements (e.g., McLaughlin et al., 2006a; Watkins et al., 2013). While earlier work made use of catalogued distances of GCs obtained from photometric measurements (in Chapters 4 and 5), dynamical distance measurements were prefered later on (Chapters 6 and 7). The reasons for this choice are detailed in Section 6.2.7.

2.4.3 Abundance of X-ray Binaries

As early as the mid-1970s, it was evident from observations of the X-ray sky by *UHURU* that GCs held an excess of bright X-ray variable sources compared to the field of the Galaxy (Katz, 1975). Four out of the 70 bright X-ray sources known at the time were located in four of the 119 GCs known. Because GCs represent only 0.02% of the total mass of the Galaxy, the abundance of X-ray binaries per unit mass is two orders of magnitude larger in GCs than in the field of the Galaxy (Clark, 1975). Follow-up observations with other X-ray satellites have made this observational excess more dramatic (Hut et al., 1992). Deeper searches with the *Einstein Observatory* led to the detection of a fainter class of X-ray sources, with $L_{\rm X} \lesssim 10^{34.5}\,{\rm erg\ s^{-1}}$ (Hertz and Grindlay, 1983). These X-ray sources have been labeled as X-ray binaries because

it was recognized early that the variability of the observed X-ray sources stemmed from accretion of matter from a companion onto a compact object (Blumenthal and Tucker, 1974; Koyama et al., 1981).

GCs are the hosts of many stellar interactions because of their high stellar densities. This naturally leads to the formation of an excess of binary systems (Verbunt and Bassa, 2003). This population of dynamically-formed binaries, created in the densest parts of the GCs, is distinct from the primordial binaries. A correlation exists between the GC encounter rate and the number of accreting NS binary systems (Heinke et al., 2003d). More generally, there is a correlation between the encounter rate and the number of X-ray sources (Pooley et al., 2003). However, core-collapsed GCs, such as NGC 6397, seem to deviate from this relation (Pooley et al., 2003). The encounter rate is related to the physical properties of GCs, size and central density, so that the high stellar density in their core creates a propitious environment for large encounter rates (Verbunt and Bassa, 2003). In addition to that, cluster metallicity can play a significant role in the abundance of LMXBs in GCs (e.g., Ivanova, 2006). An extended review of X-ray sources in GCs can be found elsewhere (Verbunt and Bassa, 2003). The populations of X-ray binaries observed in GCs include:

- Cataclysmic Variables (CVs): These systems consist of a WD accreting matter from a companion star via Roche-Lobe overflow. The term *variable* originates from the historical variability observed. They were initially called *novae*, because their outbursts appeared as new stars to the unaided eyes of the ancient astronomers. They are believed to represent the largest portion of X-ray binaries in GCs (Di Stefano and Rappaport, 1994). Their X-ray emission (with luminosity $L_{\rm X} = 10^{31} - 10^{32}\,{\rm erg\ s^{-1}}$) usually comes from the accretion disk, with a hard spectrum having a PL photon index $\Gamma \sim 1 - 2$, which depends on the accretion rate (Verbunt and Bassa, 2003). Their spectrum can also be described by thermal bremsstrahlung emission (Webb et al., 2006).

- Millisecond pulsars: These are NSs that have been spun-up by accretion of matter from a companion star. The observed X-ray emission is composed of a thermal component (from a hot spot, near the magnetic pole) and a hard non-thermal emission from relativistic electrons in the magnetosphere. The typical luminosity of millisecond pulsars is up to $L_{\rm X} \sim 10^{32}\,{\rm erg\ s^{-1}}$ (Verbunt and Bassa, 2003). There is now observational evidence that these objects are the evolutionary stage following that of LMXBs (see discussion is Section 2.1.3).

- Magnetically active binaries: These are close binaries composed of two stars in co-rotation, but no compact object. Their rapid rotation and the convection in low-mass stars ($M_\star \lesssim 0.8\,M_\odot$ as found in GCs) create a dynamo effect that increases the magnetic field. The X-ray emission emerges from the magnetic loops containing hot gas (Verbunt and Bassa, 2003). Their typical luminosities range from $L_{\rm X} \sim 10^{28}\,{\rm erg\ s^{-1}}$ for BY Dra systems to $L_{\rm X} \sim 10^{32}\,{\rm erg\ s^{-1}}$ for RS CVn systems (van den Berg et al., 2004).

- LMXBs: These systems are composed of a NS in orbit with a stellar companion, which has a low mass $M_\star \lesssim 1\,M_\odot$. They were discussed in greater detail in Section 2.2. Eighteen bright X-ray sources ($L_{\rm X} \gtrsim 10^{35}\,{\rm erg\ s^{-1}}$, persistently bright or exhibiting bright outbursts) are known to belong to Galactic GCs (Bahramian et al., 2014).

This thesis focuses on qLMXBs inside GCs, and in particular, those that have not shown any bright X-ray outbursts. They are listed in the following section.

2.4.4 Quiescent Low-Mass X-ray Binaries in Globular Clusters

QLMXB inside GCs are identified based on the similarities of their X-ray spectra with those of field transient LMXBs observed during their quiescent phase. In other words, the X-ray spectra of GC qLMXBs is consistent with H-atmosphere models of NS, at the distance of the host GC. None of the currently known GC qLMXBs

spectrally identified have exhibited any outburst activity since the first discovery about a decade ago. The lack of observed active periods of accretion results in a stable long-term quiescent X-ray emission. This lack of variability has been confirmed for several qLMXBs in GCs, such as in M28 (Servillat et al., 2012), or in NGC 6397 (see Section 5.2.3).

A few historical transient X-ray binaries in the core of GCs have been observed and analyzed in quiescence, such as SAX J1748−2021 in NGC 6440, (in't Zand et al., 2001), or EXO 1745−248 in Terzan 5 (Wijnands et al., 2005). The presence of strong non-thermal emission ($> 90\%$ contribution to the total flux in the case of EXO 1745−248) complicates the analysis of the surface emission from the surface, making these sources less useful for the purpose of measuring NS properties. In addition, some recently discovered GC bursting sources have been associated with quiescent counterparts detected in earlier observations, such as Terzan 5 X-2 (Pooley et al., 2010) corresponding to Terzan 5 CX-25, a faint soft X-ray source tentatively classified as a qLMXB (Heinke et al., 2006b). A list of persistent and transient LMXBs in GCs is available in a recent work (Bahramian et al., 2014).

The first firmly-identified GC qLMXB is located in the GC Omega Centauri (ω Cen), from observations obtained with *Chandra* (Rutledge et al., 2002b), and later confirmed with an *XMM* observation (Gendre et al., 2003a). Since then, the population of spectrally identified qLMXBs inside GCs have grown and now counts 25 objects (see Table 2.2). This list only includes GC qLMXBs that have been spectrally identified, and have not been observed in outburst, i.e., those with the potential of measuring the NS radius R_∞ using the method described in this thesis. However, because of the low signal-to-noise ratio (S/N) available, some of the qLMXBs listed in Table 2.2 have unconstrained R_∞, or were identified assuming some values of $M_{\rm NS}$ and $R_{\rm NS}$.

Table 2.2 – List of Known Quiescent Low-Mass X-ray Binaries in Globular Clusters.

Host Globular Cluster [a]	R_∞ (km)	$kT_{\rm eff}$ (eV)	$N_{H,22}$ [b]	$d_{\rm GC}$ (kpc)	Reference (discovery)
ω Cen	14.3±2.1	66^{+4}_{-5}	(0.09)	5.0	Rutledge et al. (2002b)
M13	12.8±0.4	76^{+3}_{-3}	(0.011)	7.7	Gendre et al. (2003b)
M28	$14.5^{+6.9}_{-3.8}$	90^{+30}_{-10}	0.26±0.04	5.5	Becker et al. (2003)
M30	$16.1^{+5.3}_{-3.2}{}^{\star}$	94^{+17}_{-12}	$0.029^{+0.017}_{-0.012}$	9.0	Lugger et al. (2007)
M80 CX2	$(13.1)^{\dagger}$	89±2	$0.094^{+0.025}_{-0.000}$	10.3	Heinke et al. (2003b)
M80 CX6	$(13.1)^{\dagger}$	76^{+4}_{-5}	$0.220^{+0.080}_{-0.070}$	10.3	Heinke et al. (2003b)
NGC 362	$11.3^{+3.7}_{-2.6}$	99^{+100}_{-19}	(0.028)	8.6	Margon et al. (2010)
NGC 2808	$(14.8)^{\ddagger}$	89±4	0.098±0.004	9.6	Servillat et al. (2008)
NGC 3201	$(14.8)^{\ddagger}$	172±48	(0.117)	5.0	Webb et al. (2006)
NGC 6304	$11.6^{+6.3}_{-4.6}{}^{\star}$	122^{+31}_{-45}	(0.266)	5.97	Guillot et al. (2009a)
NGC 6397	5^{+14}_{-1}	57–92	0.1–0.26	2.5	Grindlay et al. (2001b)
NGC 6440 CX3	$12.8^{+16.9}_{-2.4}$	108^{+39}_{-15}	(0.59)	8.5	Heinke et al. (2003d)
NGC 6440 CX5	$12.4^{+0.3}_{-6.4}$	109^{+30}_{-26}	(0.59)	8.5	Heinke et al. (2003d)
NGC 6819 [c]	$(13.1)^{\dagger}$	62.8±0.5	(0.083)	2.3	Gosnell et al. (2012)
47Tuc X4	$13.7^{+10.0}_{-6.3}{}^{\star}$	53^{+13}_{-8}	$0.050^{+0.007}_{-0.014}$	4.85	Heinke et al. (2005)
47Tuc X5	$14.5^{+9.7}_{-4.5}{}^{\star}$	119^{+21}_{-18}	0.09±0.05	4.5	Heinke et al. (2003c)
47Tuc X7	$17.1^{+2.2}_{-1.9}{}^{\star}$	$105^{+5.6}_{-5.6}$	$0.042^{+0.018}_{-0.016}$	4.85	Heinke et al. (2006a)[d]
47Tuc W17	$17.6^{+17.9}_{-6.3}{}^{\star}$	46^{+11}_{-12}	$0.041^{+0.017}_{-0.013}$	4.85	Heinke et al. (2005)
47Tuc W37	$15.1^{+7.3}_{-4.4}{}^{\star}$	82^{+10}_{-9}	0.059–2.48[e]	4.85	Heinke et al. (2005)
Terzan 5 W2	$(13.1)^{\dagger}$	98^{+5}_{-6}	(1.2)	8.7	Heinke et al. (2003a)
Terzan 5 W3	$(13.1)^{\dagger}$	104±5	(1.2)	8.7	Heinke et al. (2003a)
Terzan 5 W4	$(13.1)^{\dagger}$	90^{+9}_{-17}	(1.2)	8.7	Heinke et al. (2003a)
Terzan 5 W8	$(13.1)^{\dagger}$	92^{+6}_{-9}	(1.2)	8.7	Heinke et al. (2003a)

Notes: Numbers in parentheses indicate parameters held fixed during the spectral analysis.
[a] The ID name of the qLMXB is provided when there are more than one per GC.
[b] $N_{H,22}$ is the column density of hydrogen $N_{\rm H}$ in units of $10^{22}\,{\rm atoms\,cm^{-2}}$.
[c] NGC 6819 is an open cluster. Candidate quiescent low-mass X-ray binary to be confirmed.
[d] 47Tuc X7 was reported in Heinke et al. (2003c), but re-analyzed in Heinke et al. (2006a).
[e] For NGC 6440 W37, the column density $N_{\rm H}$ varied dramatically between observations.
* R_∞ is obtained assuming a fixed $M_{\rm NS} = 1.4\,M_\odot$.
† R_∞ is obtained assuming fixed $R_{\rm NS} = 10\,{\rm km}$ and fixed $M_{\rm NS} = 1.4\,M_\odot$.
‡ R_∞ is obtained assuming fixed $R_{\rm NS} = 12\,{\rm km}$ and fixed $M_{\rm NS} = 1.4\,M_\odot$.

Additional qLMXBs are tentatively identified and not listed in Table 2.2 (8 in the GC Terzan 5, and 4 in NGC 6440). However, the X-ray spectra of these sources have $\lesssim 50$ counts, a number too low to firmly identify the sources as qLMXBs. The faint candidates were tentatively classified based on their position on an X-ray colour-luminosity diagram (e.g., Heinke et al., 2006b). The effects of the large distances of the host GCs (8.5 kpc for NGC 6440, and 8.7 kpc for Terzan 5), and the large amount of Galactic absorption ($N_{\rm H} = 0.59\times10^{22}\,{\rm cm^{-2}}$ for NGC 6440, and $N_{\rm H} = 1.2\times10^{22}\,{\rm cm^{-2}}$ for Terzan 5) combined to the relatively low-luminosity of these sources ($L_{\rm X} \lesssim 5\times10^{32}\,{\rm erg\ s^{-1}}$) are responsible for the low number of counts of these sources.

Specifically, dust and heavy elements of the interstellar medium of the Galaxy absorb photons from X-ray sources. During spectral analyses, the effects of absorption are modeled with models, such as `wabs` in the X-ray spectral analysis package *XSPEC* (Arnaud, 1996), in which the amount of absorbing material is represented by the column density of hydrogen $N_{\rm H}$, assuming a particular composition of the interstellar medium (e.g., Morrison and McCammon, 1983, for `wabs`). However, the column density of hydrogen is solely used as a proxy for the absorption of soft X-rays by other elements. In the remainder of this thesis, $N_{\rm H}$ will be provided in units of $10^{22}\,\mathrm{atoms\,cm^{-2}}$, noted as $N_{H,22}$. The effects of absorption are dominant in the soft X-ray band (0.2–1 keV), where the spectra of qLMXBs peak. Therefore, large amounts of absorption impede the spectral analysis of soft X-ray sources such as qLMXBs by reducing the S/N where it is the largest. Figure 2.9 shows the attenuating effect of increasing amount of absorbing material on a NS H-atmosphere model.

Overall, qLMXBs inside GCs represent an improvement over field qLMXBs since GC distances are known to better than $\sim 10\%$, while field qLMXBs have distance uncertainties of the order of 20–50%. The lack of variability due to the absence of recent accretion episodes, their low surface magnetic field not affecting the emergent spectrum, and the pure composition of their atmosphere, make them useful systems for R_∞ measurements, compared to NSs in rapidly evolving systems such as transient LMXBs (which often show residual accretion as discussed above), or compared to NSs with high magnetic fields such as X-ray-dim INS. These R_∞ measurements required the use of X-ray observatories which are presented in the next chapter.

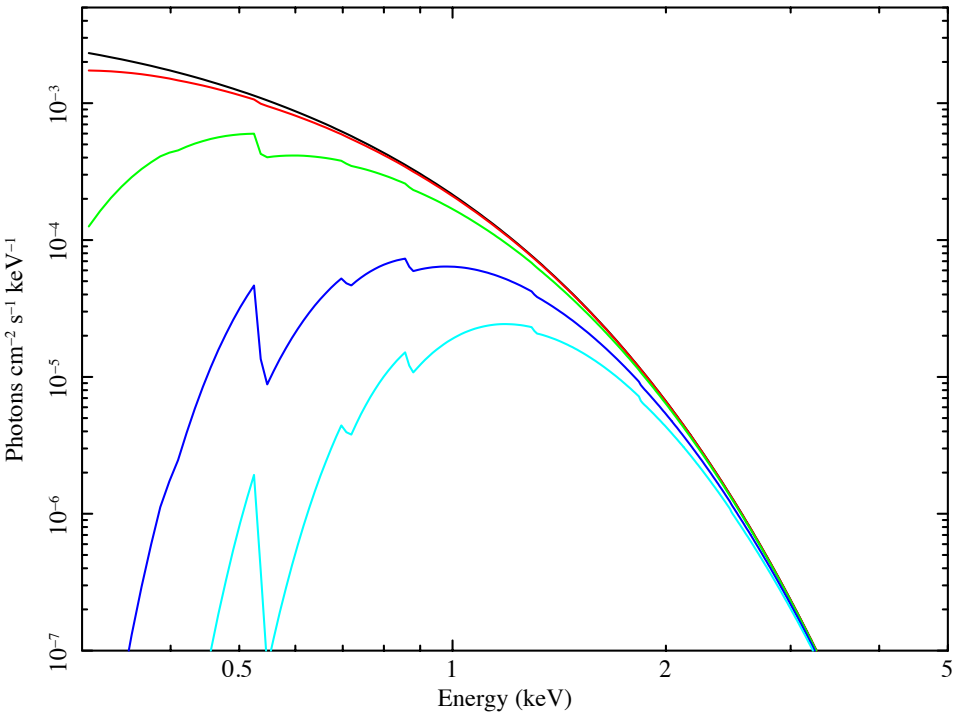

Figure 2.9 – The figure shows the `nsatmos` spectral model, with $T_{\rm eff} = 10^6\,{\rm K}$, $M_{\rm NS} = 1.4\,M_\odot$, $R_{\rm NS} = 12\,{\rm km}$, and a distance of 2 kpc, combined to absorption models with varying amounts of absorbing materials. The values of $N_{\rm H}$ used were: $N_{H,22}$=0.0 (black), $N_{H,22}$=0.01 (red), $N_{H,22}$=0.1 (green), $N_{H,22}$=0.5 (blue), and $N_{H,22}$=1.0 (cyan), in units of $10^{22}\,{\rm atoms\,cm^{-2}}$. Absorption edges start to appear at hydrogen column densities $N_{H,22} \sim 0.1$.

3

X-ray Observations of Neutron Stars

Since the discovery of NSs in the 1960s, their study have relied on X-ray observations. While radio observations have produced the largest number of detections of NSs (as radio-emitting rotation-powered pulsars), X-ray astronomy probes the high-energy physics involved and led to the discovery of exotic phenomena.

From the first X-ray detectors in sounding rockets to the highly sensitive charge-coupled device (CCD) detectors at the focal plane of X-ray focusing satellite-borne telescopes, X-ray astronomy instrumentation underwent tremendous progress in terms of sensitivity, spectral and angular resolutions, and in terms of the limitation of background noise. Section 3.1 presents a short historical review of X-ray instrumentation.

The remainder of this chapter is a technical discussion of the X-ray astronomy relevant to this thesis, including CCD detectors, X-ray focusing optics, as well as the two observatories used in this work (*Chandra* and *XMM*). Since the emission of the NSs studied in this thesis peaks in the soft X-ray band (0.5–2 keV, corresponding to the wavelength range 0.62–2.5 nm, or to the frequency range 1.2×10^8–5×10^8 GHz), the discussions in Sections 3.2 to 3.4 will be limited to X-ray astronomy in the soft X-ray band.

3.1 Brief History of X-ray Astronomy

The study of NSs is intimately tied to the developments and progress of X-ray astronomy. This short historical review of X-ray astronomy is presented in the context of NS observations.

Because X-rays are absorbed by photo-ionization of inner-shell electron of oxygen or nitrogen in the Earth's atmosphere, the development of X-ray astronomy required the advancement of rocket and satellite technology. A sub-orbital sounding rocket, an Aerobee rocket, detected in 1949 the first astronomical X-ray source, our Sun (Garmire, 1966). Later on, in 1962, an Aerobee 150 rocket, with a Geiger counter in its nose cone, led to the discovery of Scorpius X-1 (see Section 1.2.2). Because photons of hard (high-energy) X-rays penetrate the atmosphere more than the soft (low-energy) X-rays, they can be detected from lower altitudes. For example, in 1964, a balloon-borne scintillation counter discovered the hard X-ray emission (15–60 keV) from the Crab Nebula (Clark, 1965).

In the past four decades, technological advancements rapidly revolutionized the field of X-ray astrophysics, improving the angular resolution, the spectral resolution and eventually permitting all-sky surveys in the X-ray band. Some highlights are listed below and do not represent an exhaustive list[1].

In 1970, the first astronomy-dedicated X-ray satellite – *SAS-1* for *Small Astronomical Satellite*, also called *UHURU* – was launched. Equipped with two proportional counter arrays for an effective area of $\sim 0.084\,\mathrm{m}^2$ in the 2–20 keV range, this satellite performed an all-sky survey and detected 339 X-ray sources, including X-ray binaries, supernova remnants, and other galaxies (Giacconi et al., 1971). Later, the *Astronomische Nederlandse Satelliet* (launch in 1974), with its single parabolic mirror working on the principle of grazing incidence (see Section 3.3), with effective area $\sim 0.014\,\mathrm{m}^2$, marked the first use of grazing-incidence reflection of soft X-rays (Brinkman et al., 1974). This satellite detected the first X-ray burst (a sudden increase of the X-ray flux) located in the globular cluster NGC 6624 (Grindlay et al., 1976). *SAS-3* (1975-1979) was designed to precisely locate (within $\sim 15''$) bright sources of the X-ray sky with a system of collimators (e.g., Jernigan et al., 1977), and to detected transient X-ray sources (Lewin et al., 1976a,b,c). In 1975, the 8$^{\mathrm{th}}$ *Orbiting*

[1] A complete time line of all X-ray observatories can be found here `https://heasarc.gsfc.nasa.gov/docs/heasarc/missions/time.html`.

Solar Observatory measured the blackbody-like spectral shape of X-ray bursts with the detectors of its Cosmic X-ray Spectroscopy Experiment (Swank et al., 1977).

In 1977, the first *High Energy Astronomy Observatory* (*HEAO-1*) was a large size survey mission with instruments covering the 0.2 keV to 10 MeV energy range (Bradt et al., 1992). Together, the four instruments with various effective areas (between $0.0045\,\mathrm{m}^2$ and $0.19\,\mathrm{m}^2$) and energy ranges produced a comprehensive study of the high-energy sky with spectral and temporal resolution (Wood et al., 1984; Piccinotti et al., 1982; Levine et al., 1984). Other highlights of *HEAO-1* include the monitoring of the variability of X-ray binaries, and the discovery of the first eclipse in a LMXB.

With the *Einstein Observatory* (*HEAO-2*) launched in 1978, the *National Aeronautics and Space Administration* (*NASA*) pioneered X-ray imager telescopes. The Wolter type I grazing incidence X-ray focusing optics of the *Einstein Observatory* (Giacconi et al., 1979), together with imaging detectors, allowed for angular resolutions of a few arcseconds. Its instruments (the High Resolution Imager, the Imaging Proportional Counter, the Solid State Spectrometer and the Focal Place Crystal Spectrometer) were designed for various needs, including high imaging sensitivity ($\sim 100\times$ higher than any previous mission), and high-resolution spectroscopy ($E/\Delta E \sim 100$ at 0.4 keV). Among the many scientific highlights, the angular and spectral resolutions capabilities of *HEAO-2* permitted the morphological study of supernova remnants for the first time (e.g., Fabbiano et al., 1980; Fabbiano, 1980). Finally, with its innovative Guest Observer program, the *Einstein Observatory* transformed X-ray astrophysics into a field accessible to all astrophysicists.

In 1983, the *European Space Agency* launched *EXOSAT*, its first X-ray satellite. The two Wolter type I grazing incidence telescopes working at energies in the 0.05–2 keV range (de Korte et al., 1981) led to the observations of various X-ray sources, including X-ray binaries and X-ray pulsars, cataclysmic variables, and active galactic nuclei. For the first time, an iron spectral line was observed in Galactic and extragalactic sources (White and Peacock, 1988).

A series of Japanese X-ray satellites launched between 1979 and 1987 (*Hakucho*, Miyamoto 1982; *Tenma*, Tanaka et al. 1984; and *Ginga*, Turner et al. 1989) significantly contributed to rapidly growing field X-ray astrophysics both by their technological advancements, specifically in the spectral resolution, and by their exploration of the X-ray sky, including the low-mass X-ray binaries Cen X-4 and Aql X-1 (Matsuoka et al., 1980; Koyama et al., 1981), a large number of bursting sources (Makishima et al., 1983), and the discovery of spectral features (iron or cyclotron lines, Clark et al., 1990).

Launched in 1990, *ROSAT* (for *Roentgen Satellite*, Snowden and Schmitt 1990), was the first to use the nested mirror Wolter type I X-ray focusing optics technology for an all-sky survey. The $\sim 0.024\,\mathrm{m}^2$ effective area Position Sensitive Proportional Counter catalogued $\sim$ 105 000 sources compared to a few hundreds known X-ray sources before (Voges et al., 2000). Following its all-sky survey, *ROSAT* performed pointed observations with the High-Resolution Imager, an instrument with a $2''$ spatial resolution. During the nine years of its lifetime, *ROSAT* detected thermally emitting nearby INSs (Treves et al., 2001), pulsations from the enigmatic gamma-ray source Geminga twenty years after its discovery (Halpern and Holt, 1992), and even the X-ray emission following the collision of the comet Shoemaker-Levy 9 with Jupiter (Waite et al., 1995).

The fourth Japanese X-ray satellite, *ASCA*, introduced the use of charge coupled devices for the detection of X-ray photons, which permitted a spatial resolution of $30''$ and an energy resolution of 2% at 5.9 keV (Tanaka et al., 1994).

The *Rossi X-ray Timing Explorer* (*RXTE*), in operation between 1995 and 2012, was designed to observe the rapidly-changing X-ray sky (Swank, 1999). It was equipped with an All-Sky Monitor scanning 80% of the sky every 90 minutes, and an array of five proportional counters (PCA) with a collecting area of $0.65\,\mathrm{m}^2$ working at a time resolution of $1\,\mu$s. *RXTE* provided a revolutionary view of the variable X-ray sky, observing star quakes inside NSs (Palmer et al., 2005), providing estimates of

the NS radius from measurements of a NS spin frequency (Villarreal and Strohmayer, 2004), but more importantly, allowing for a frequent monitoring (every several days) of variable X-ray sources, such as magnetars (e.g., Kaspi et al., 2001).

The design of *Swift*, launched in 2004, allows it to detect bursts of gamma-ray emission with a wide-field monitor, and to automatically slew within 90 sec to observe the location of the burst with narrow-field X-ray and ultraviolet telescopes, making the precise location of the source public within minutes (Gehrels et al., 2004). The Japanese satellite *Suzaku* was designed to observe simultaneously over the energy range 0.3–600 keV with high spectral resolution ($\sim$ 1% in the 0.3–12 keV, and 10% above 20 keV). Unfortunately, a failure of the cryogenic system of the X-Ray Spectrometer (XRS), left this instrument unusable[2]. Since 2012, the satellite *NuSTAR* observes the high-energy X-ray sky (up to 79 keV) through the first telescope focusing hard X-rays (Harrison et al., 2013), instead of the usual coded-mask instruments used for hard X-rays. *NuSTAR* provides a new window on the high-energy X-ray sky, significantly increasing the sensitivity to X-ray sources above 10 keV.

Some of the planned X-ray telescopes will be mentioned at the end of the thesis in the context of the discussion of future work (Chaper 8).

All soft X-ray telescopes onboard currently operating X-ray observatories use focusing X-ray telescopes (Wolter type I systems), with the exception of the Monitor of All-Sky X-ray Image onboard the International Space Station (Matsuoka et al., 2007, 2009). Their instrumentation covers a wide range of time and angular resolutions. The two major soft X-ray missions *XMM-Newton* and the *Chandra X-ray Observatory* launched in 1999, both used for the work of this thesis, are described in detail in Section 3.4. The following presents the detectors at the focal plane of X-ray focusing telescopes which are then presented in Section 3.3.

[2] `http://heasarc.gsfc.nasa.gov/docs/suzaku/news/xrsend.html`

3.2 Charge-Coupled Devices for X-ray Astronomy

Depending on the science objective requirements, a variety of X-ray detectors with various capabilities are available, including:

- proportional counters (detecting the showers of particles ionized by X-rays),
- scintillators (using scintillation of crystals hit by X-rays),
- microcalorimeters (measuring temperature variations of materials hit by X-rays),
- charge-coupled device detectors (measuring electrons deposited by the absorption of X-rays).

Proportional counter arrays offer large collecting areas with modest spectral resolution, and they are affected by large background count rates. CCD detectors represent a reasonable compromise between the various characteristics of other X-ray detectors, but their small physical size require they be placed at the focal place of X-ray-focusing optics. Reviews of CCD detectors used in X-ray astronomy can be found in the following publications: Lumb et al. (1991); Grant (2011), which were used to write this section.

Invented in the late 1960s by Willard S. Boyle and George E. Smith (both recipients of the Physics Nobel Prize in 2009), CCD detectors quickly gained in popularity among astronomers, originally for the visible band, because of their quantum efficiency far superior to that of photographic plates. CCDs are now used at all major infrared/optical astronomical observatories. The application of CCDs to X-ray astronomy was realized early on, and used on the first X-ray observatories in the late 1980s, after adaptation of the technology, notably for the read-out registers. CCDs consist of a photosensitive semiconductor substrate (usually silicon) and an array of electrodes with different potentials, defining a line of pixels in one direction. In the other direction, pixels are separated by channel stops (thickening of the insulator material). As photons photoelectrically react with the semiconductor substrate,

a number of electrons proportional to the energy of the X-ray photon is released[3]. Each cloud of charges created remains in the pixel where it appeared, before being transferred to the read-out.

After an exposure time frame (from tens of milliseconds to a few seconds, at most), the pixels are transfered to the output register. This is done by applying clock-pulsed voltages to the electrodes, to sequentially shifts the charges along a channel, pixel by pixel. The 2D pixel map is reconstructed in the output register, while the pixels of the CCD are exposed to X-ray photons for the next time frame. Because the number of electrons directly informs the energy accumulated in a pixel, problems arise when two or more photons interact with a single pixel in the semiconductor substrate within a single read-out time frame. When this happens, the output register, which only measures the amount of charge in each pixel, will consider only one X-ray photon with an energy equal to the sum of the energies of the incident photons on that particular pixel. This is the reason why short time frames are preferable. This effect, called pile-up, is further discussed in Section 6.2.4, in the context of the spectral analysis of qLMXBs. Despite this difficulty, the advantage of CCDs in X-ray astronomy is that they can be used as photon counting detectors.

In summary, the long exposures from X-ray observatories with CCD detectors are obtained by the accumulation of a large number of short read-out time frames, during which ideally only one incident X-ray photon was detected on each pixel in each individual time frame. By contrast, the individual electrons released by photons in the visible band are accumulated during long exposures (up to several minutes) before being amplified and converted to a brightness value.

Because the data rate of the output register exceeds the telemetry resources of current X-ray satellites, an onboard pre-processing must be performed before transmission of the exposure data to ground stations. For that reason, events in a 3×3 pixel island are assigned a grade (or pattern) depending on the event shape. Dur-

[3]By contrast, a photon in the visible light energy range releases only one electron.

ing its photoelectric interaction with the substrate, an X-ray photon can result in a charge cloud that overlaps with a few pixels surrounding a central pixel. X-ray photons events are usually defined by a single pixel event, or a simple pattern. By comparison, charged particles such as cosmic rays have more complex event grades. The assignment of event grades allows for an on-board pre-filtering that reduces the data rate (Grant, 2011). *Chandra*'s telemetry mode can be varied depending on the expected full-chip count rate during the observation. These modes include "VERY FAINT" (VFAINT), "FAINT", and "GRADED FORMAT", with decreasing amount of information telemetered. For the observations of interest in this thesis, the VFAINT or FAINT modes can be safely used without risks of saturating the telemetry.

A modification to CCD detectors can be implemented to improve the sensitivity at low-energies, $E < 1\,\mathrm{keV}$. Indeed, standard CCD, called "front-illuminated" (FI) CCD, highly absorb low-energy photons in the dead layers (e.g., channel stops, gates of the electrodes). To increase the quantum efficiency at low-energies, the CCD can be flipped upside-down. As a consequence, in back-illuminated (BI) CCDs, the dead layers lie behind the photosensitive substrate. Additionally, part of the substrate can be removed to ensure that the charge clouds form close enough to the electrodes. A negative consequence of a thinner active region is the lower sensitivity to high-energy photons above 4 keV, which will be more likely to traverse the photosensitive part without interacting. BI CCDs also suffer from larger noise and therefore have poorer spectral resolution (about 50 eV wider at FWHM). A comparison between the effective areas of FI and BI detectors onboard *XMM* and *Chandra* is presented in Figure 3.1.

Overall, X-ray CCDs simultaneously offer imaging, timing and spectral capabilities. Such a feature is unique to high-energy astrophysics and does not exist in optical or infrared astrophysical observations. Finally, when a CCD is placed at the focal plane of an X-ray focusing telescope, precise spatial information also becomes available. The optical design of such telescopes is now presented.

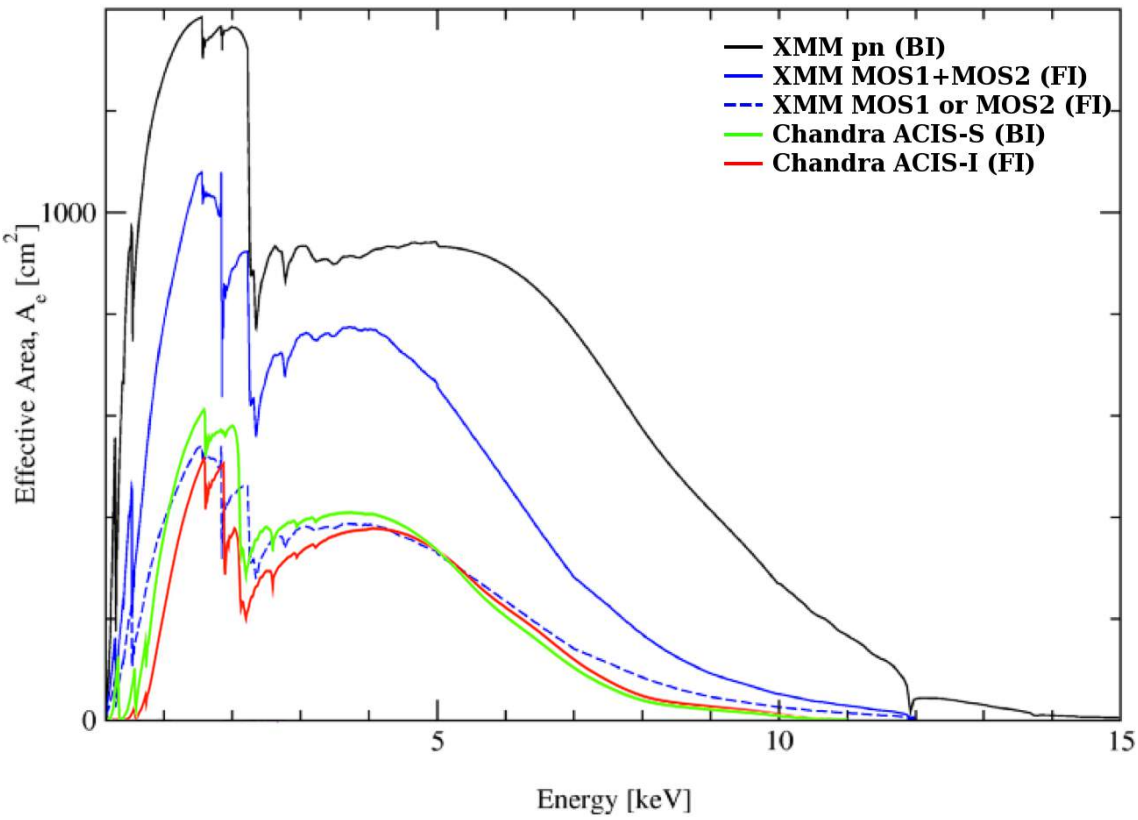

Figure 3.1 – This graphs compares the effective areas of the front-illuminated (FI) and back-illuminated (BI) detectors onboard *Chandra* and *XMM*. The value of effective area depends on the combined effects of the collective area of the X-ray optics systems and the quantum efficiency of each detector. Figure adapted from data available in the *XMM* proposer guide (`http://xmm.esac.esa.int/external/xmm_user_support/documentation/`) and the *Chandra* PIMMS tools (`http://cxc.harvard.edu/cgi-bin/prop_viewer/build_viewer.cgi?ea`).

3.3 Focusing X-ray photons

Historically, collimators placed in front the detectors provided spatial information by restricting stray X-ray photons from hitting the detectors. The spatial origin of high-energy photons (X-rays and Gamma-rays) can also be determined using coded-aperture masks. By placing a patterned mask opaque to high-energy photons (e.g., made of Tungsten) in front of the detector, the spatial information can be computationally reconstructed by analyzing the multiple images from the various apertures of the coded mask. However, greater angular resolution can only be obtained by using the concentrating power of focusing X-ray optics systems, which basic principles are described here.

At wavelength less than a few nanometers, X-ray photons generally do not penetrate materials, or, in the case of sufficient thickness, they are absorbed. In other words, reflecting X-ray photons in a "standard" optical system (spherical, parabolic or hyperbolic mirrors) is difficult the because incident angles $\theta_{\rm inc}$ are small. However, reflection of X-rays is possible at grazing-incidence angles, i.e., at angles $\theta_{\rm inc}$ at most a few degrees away from 90°. This is analogous to "skipping" stones on water. Specifically, for X-rays, the index of the refraction $n_{\rm mirror}$ of the mirror is smaller than that of vacuum, i.e., unity. This allows for total external reflection to happen below a critical grazing angle $\theta_{\rm g} = \pi/2 - \theta_{\rm inc}$ of a few degrees, defined by:

$$\cos\left(\theta_{\rm g,crit}\right) = n_{\rm mirror} \tag{3.1}$$

At X-ray wavelengths, the indices of refraction[4] of most materials slightly deviates from unity by only 1 part in $\sim 10^3 - 10^5$, leading to values of $\theta_{\rm g,crit} < 1°$. It is important to note that the critical grazing angle is material-dependent, but it also inversely proportional to the photon energy. Therefore, higher-energy photons are reflected at shallower angles.

[4]Indices of refraction for various materials are available here: `http://henke.lbl.gov/optical_constants/`

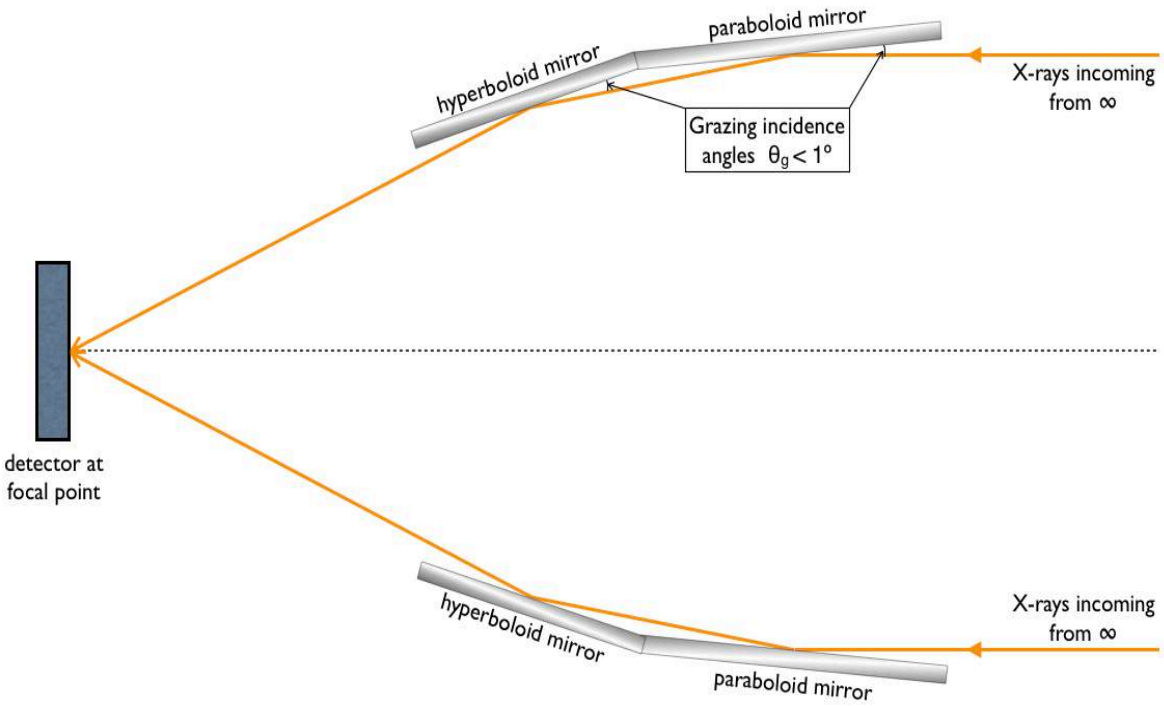

Figure 3.2 – This schematic diagram shows how X-rays are focused by paraboloid and hyperboloid mirrors, using the grazing incidence principle, in Wolter type I X-ray focusing systems.

Within the restriction imposed by the small grazing angles, X-ray focusing systems were designed to maximize the collecting area and to minimize the focal length. Because the optical path of each photon must be equal to obtain a sharp image, it was demonstrated that paired conic sections of revolution would form an image free of coma aberrations (Wolter, 1952). Based on this demonstration, three Wolter-type design were deduced and later introduced in X-ray astronomy. The Wolter type-I design is the most commonly used optical system to focus X-rays since it offers the possibility to nest mirrors for an increased collecting area, and since it has a shorter focal length than the other two designs (Wolter, 1952).

To focus X-rays toward the focal plane, the Wolter-I design uses confocal paraboloid and hyperboloid mirrors (see Figure 3.2). The effective area of a single mirror used at grazing incidence represents a small fraction of the actual surface area of the mirror:

$$A_{\text{eff}} \approx \cos\left(90^\circ - \theta_g\right) A_{\text{surface}}. \tag{3.2}$$

Therefore, multiple thin nested concentric mirrors are used to increase the total effective area of the telescope. However, the performance of this optical design is highly dependent on the number of mirrors. Adding more mirrors increases the effective area but becomes prohibitive for space missions, due to the extra mass. Similarly, reducing the thickness of each mirror shell permits the addition of mirror shells, resulting in a gain of effective area, but leads to significant mirror deformations, altering the point spread function (PSF). The PSF is the impulse response of the focusing system and can be thought of as the figure of merit for the focusing quality of the telescope. The PSF depends on the energy of incoming X-ray photons, and on the distance from the aim point (i.e., the focal point of the optical system), called the off-axis angle. Specifically, the FWHM of the PSF is usually provided to quantify the angular resolution power of an X-ray telescope.

PSF and effective area calibrations of X-ray telescopes requires a careful treatment of many factors. They are usually performed on the ground, as well as after the deployment in space since the mirror alignment can be altered by the launch. As mentioned above, the grazing angle depends on the photon energy. Therefore, the effective area is also energy-dependent (see Figure 3.1). In addition, X-ray sources away from the optical axis are blocked by self-shadowing of the nested mirror shells, causing a decrease of the effective area toward the edge of the field of view, an effect called vignetting. The work presented in this thesis requires a compromise between high sensitivity, high angular and spectral resolution, which is obtained with the X-ray focusing telescopes and the CCD detectors onboard the observatories *Chandra* and *XMM-Newton*, both described in the following subsections.

3.4 The Two X-ray Telescopes Used in the Thesis

Chandra and *XMM-Newton* are often presented as two complementary observatories. For example, the superior collective area of *XMM-Newton* allows for the accumulation of more X-ray counts, and therefore the possibility to obtain higher S/N data for spectral analyses. On the other hand, *Chandra* has the angular resolution necessary to spatially resolve different X-ray sources in the crowded core of GCs, which *XMM* may not succesfully differentiate otherwise. Some details relevant to this thesis are presented for *Chandra* and *XMM* in the following two sections.

3.4.1 *Chandra*

Most of the spectra used in this work were obtained from observations with the *Chandra X-ray Observatory*[5] (Weisskopf et al., 2000), one of *NASA*'s Great Observatories, launched in July 1999 (Figure 3.3). This 13 m-long observatory is equipped with a single Wolter-I X-ray telescope, called the High Resolution Mirror Assembly (HRMA) and two science instruments at the focal plane. The four concentric 2-cm thick iridium-coated glass elements of the HRMA have diameters from 0.8 m to 1.2 m, resulting in a collecting area of 600 cm^2 at 1.5 keV, for a focal length of 10.1 m. The small number of mirrors offers mechanical stability of the optical system and provides an unmatched angular resolution ($\sim 0.5''$), at the expense of the collecting area. Because *Chandra* has only 4 concentric pairs of mirrors, the field of view is affected by a vignetting of $\sim 20\%$ decrease in effective area at 1.5 keV (compared to a decrease of $\sim 70\%$ for *XMM*, due to its 58 concentric mirrors, see Section 3.4.2). The reduction of the illumination of the geometric collecting area when moving off-axis is caused by the loss of X-ray photons, hitting the edges of the mirrors or the non-reflective surface. This effect increases with the number of mirrors and the thickness of each mirror shell. Finally, the PSF on *Chandra* rapidly degrades for increasing off-axis angles: $0\farcs5$ FWHM at the aimpoint compared to $\sim 10''$ at a distance of $\sim 10'$ off-axis.

[5]The following description was compiled from the *Chandra* X-ray Centre website at http://cxc.harvard.edu.

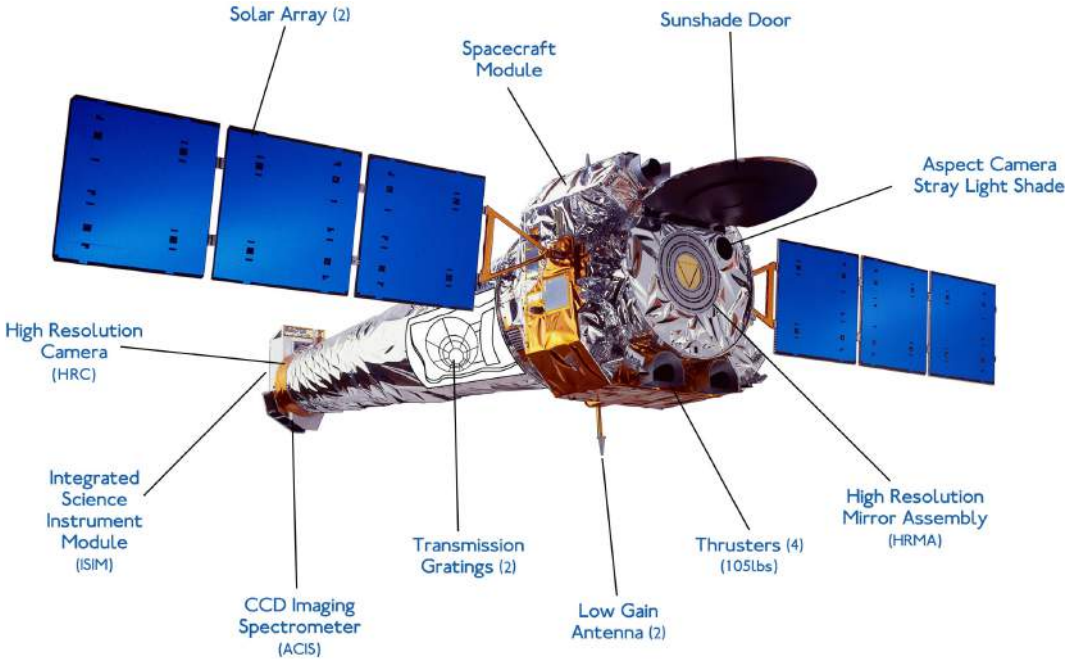

Figure 3.3 – This labeled figure shows the different components of the *Chandra* telescope. Source: The *Chandra* X-ray Center. `http://cxc.harvard.edu/`

The instruments on-board *Chandra* are designed for imaging and spectroscopy. The focal plane is equipped with the Advanced CCD Imaging Spectrometer (ACIS) and the High Resolution Camera (HRC). The choice of instrumentation for a planned observation is made possible by the mobile focal plane, allowing to move the detector of interest to the focal point (Figure 3.4). Two optional transmission gratings, the High Energy Transmission Grating (HETG) and the Low Energy Transmission Grating (LETG), can also be used for high resolution spectroscopy if placed in the optical path.

The ACIS instrument was used for all the observations analyzed in this work. It is composed of two groups of CCDs. The ACIS-I (for imager) instrument has four FI CCDs arranged in a square pattern for a $16\farcm9 \times 16\farcm9$ field of view, off-centred by $23'' \times 38''$ to move the aim point away from the central chip gap. The ACIS-S (for spectrometer) is arranged as line of 6 CCD to form an $8\farcm3 \times 50\farcm6$ field of view. Two

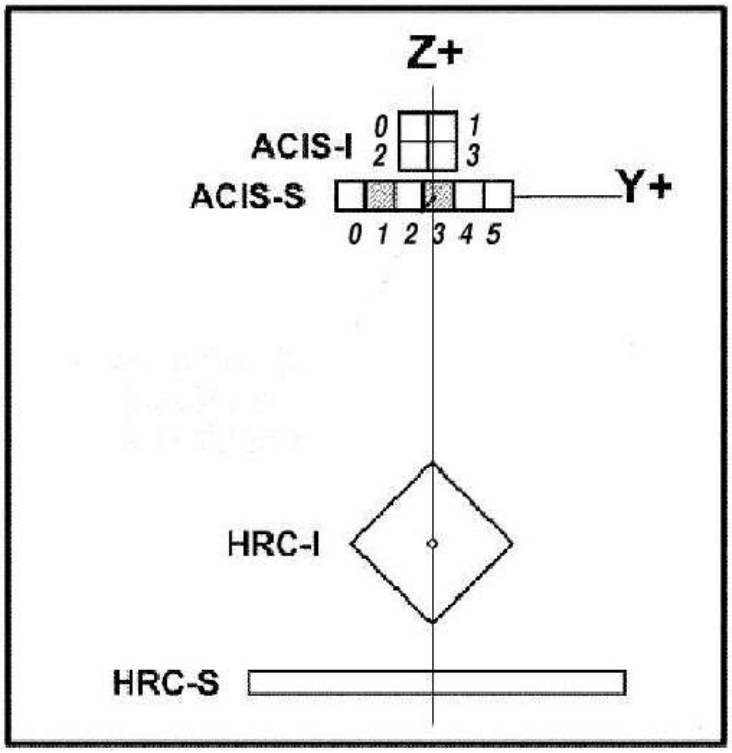

Figure 3.4 – This diagram shows the arrangement of the different instruments available on-board the *Chandra X-ray Observatory*. Here, the labels `I` and `S` following ACIS and HRC indicate that the charge-coupled device detectors are designed for imaging and spectroscopy, respectively. The shaded squares on ACIS correspond to the two back-illuminated chips. The Science Instrument Module is moved along the Z-axis to place the detector of interest at the focal point. Source: The *Chandra* X-ray Center. `http://cxc.harvard.edu/`

of the ACIS-S CCDs are BI, and the aim point is near the centre of one of the two BI chips (Figure 3.4). All CCDs of the ACIS-I and ACIS-S instruments are metal-oxide-superconductor and offer spectral resolutions of $E/\Delta E \sim 10 - 60$ for the FI chips, and $E/\Delta E \sim 5 - 45$ for the BI chips. As explained in Section 3.2, the BI chips are more sensitive than the FI chips, especially in the low-energy range below 1 keV (see Figure 3.1). The ACIS instrument allows to spatially and spectrally resolve X-ray sources in crowded environments, such as the core of GCs. Finally, during observations, *Chandra* dithers by $\sim 1''$ on the target to partially avoid large chip gaps.

The HRC instrument has a smaller pixel size than ACIS allowing an angular resolution of $0.4''$. However, its spectral resolution is rather poor (~ 1 keV at 1 keV) which prohibits its use for the spectral analysis required in this thesis. The HETG and LETG instruments, inserted in the focused X-ray beam, allow for high spectral resolution (up to $E/\Delta E \sim 800$ at 1.5 keV for HETG, and $E/\Delta E > 1000$ below 0.2 keV for LETG). However, grating spectrometers disperse the incident light, decreasing the photon throughtput by a factor of ~ 10. The low effective areas of grating spectrometers makes them less useful to observe the faint qLMXBs which are the subject of this thesis.

Chandra's ACIS camera can be operated in a various modes, with different field of view sizes and time resolutions. The time resolution of a CCD can be improved by reducing the physical portion of the detector read-out after each time frame. The imaging modes of ACIS (*Timed Exposure* modes) have time resolutions from 0.4 sec to 3.8 sec, depending on the number of CCD chips used and the fraction of the CCDs that is read-out (1/8, 1/4, 1/2 or full frame).

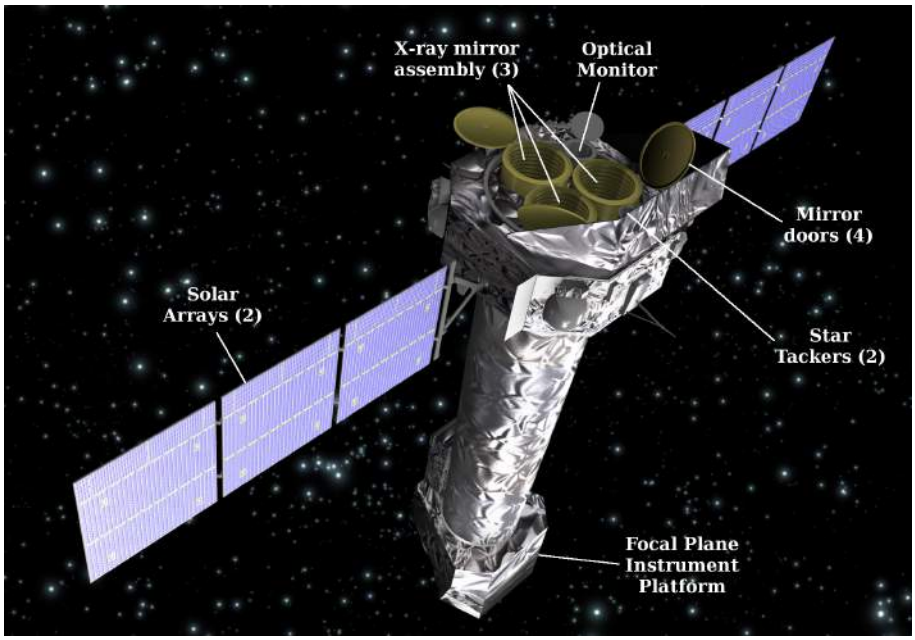

Figure 3.5 – This labeled figure shows the different components of the *XMM* observatory. Source: The *XMM-Newton* Science Operation Center. `http://xmm.esac.esa.int/`; Figure labeled for the purpose of this section.

3.4.2 *XMM-Newton*

The *European Space Agency* launched the *X-ray Multi-Mirror* satellite[6] in December 1999 (Jansen et al., 2001), as one of the corner stones of the Horizon 2000 program. It is in an orbit similar to that of *Chandra*, a highly elliptical orbit which allows for long continuous exposures of X-ray sources, up to ~ 135 ks. The focusing of the X-ray photons is obtained with three identical Wolter type-I telescopes (focal length of 7.5 m, Figure 3.5), each composed of 58 gold-coated concentric shells of thickness in the $0.4 - 1.1$ mm range, and with diameters from 31 cm to 70 cm. The large number of concentric shells allows for a large collective area (1400 cm^2 at 1.5 keV for each telescope), at the expense of the angular resolution ($\sim 5''$), poorer than *Chandra*'s ($\sim 0.5''$). A CCD detector lies at the focal point of each telescopes, and records X-ray photons in the 0.15–15.0 keV energy range.

[6]The description of *XMM-Newton* and its instruments is based on information available on the *XMM-Newton* Science Operation Centre website available at http://xmm.esac.esa.int/.

The European Photon Imaging Camera (EPIC, Strüder et al., 2001) instrument consists of the three CCDs, all with a field of view of $\sim 30'$ in diameter. Two of the three CCDs are Metal Oxide Semi-conductor (MOS) arrays, made of seven FI CCD chips, for a total of 600×600 pixels. The pixel size of $40\,\mu$m corresponds to $1.1''$ on the sky allowing the camera to fully sample the PSF of the telescope (PSF $= 6''$ FWHM). The spectral resolution of the MOS cameras is $E/\Delta E \sim 13$ at 1 keV. They share their respective focal paths with the two Reflection Grating Spectrometer (RGS) detectors, and, as a result, collect only 44% of the incoming flux, the remainder being deflected and dispersed by gratings to the RGS detectors. These are used for high-resolution spectrometry with $E/\Delta E \sim 800$, over the low-energy range 0.33–2.5 keV (den Herder et al., 2001). Due to the presence of the RGS gratings, the MOS CCDs have lower sensitivity, compared to the third EPIC CCD detector: a p-n junction CCD (pn hereafter). A full diagram of the focal plane instrumentation of *XMM* is shown in Figure 3.6.

The pn camera is at the focal plane of the third telescope, but without any intercepting grating instrument, therefore receiving the full photon flux from the X-ray telescope. It is composed of two rows of six rectangular BI pn-CCD chips for a total of 400×384 pixels. Its spectral resolution ($E/\Delta E \sim 12$ at 1 keV) is slightly worse than the MOS detectors, but its sensitivity is significantly better, by a factor $\times 2$ at 1 keV (see Figure 3.1). Each $150\,\mu$m pixels cover $4.1''$ on the sky and therefore slightly under-sampling the PSF. The detector is slightly shifted off-centre to move the optimal PSF position away from a chip gap. The major drawback of the pn-camera is the mediocre pixel quality. The large quantity of hot pixels and dead columns (which number has increased since launch) can prevent the thorough analysis of crowded fields. In addition, because of the large number of concentric mirrors, the imaging capabilities of *XMM* are strongly affected by vignetting, decreasing the sensitivity by a factor of ~ 2 between the aimpoint and the edges of the detector, as can be readily noticed on an exposure map (Figure 3.7). Regarding the modes of *XMM*-

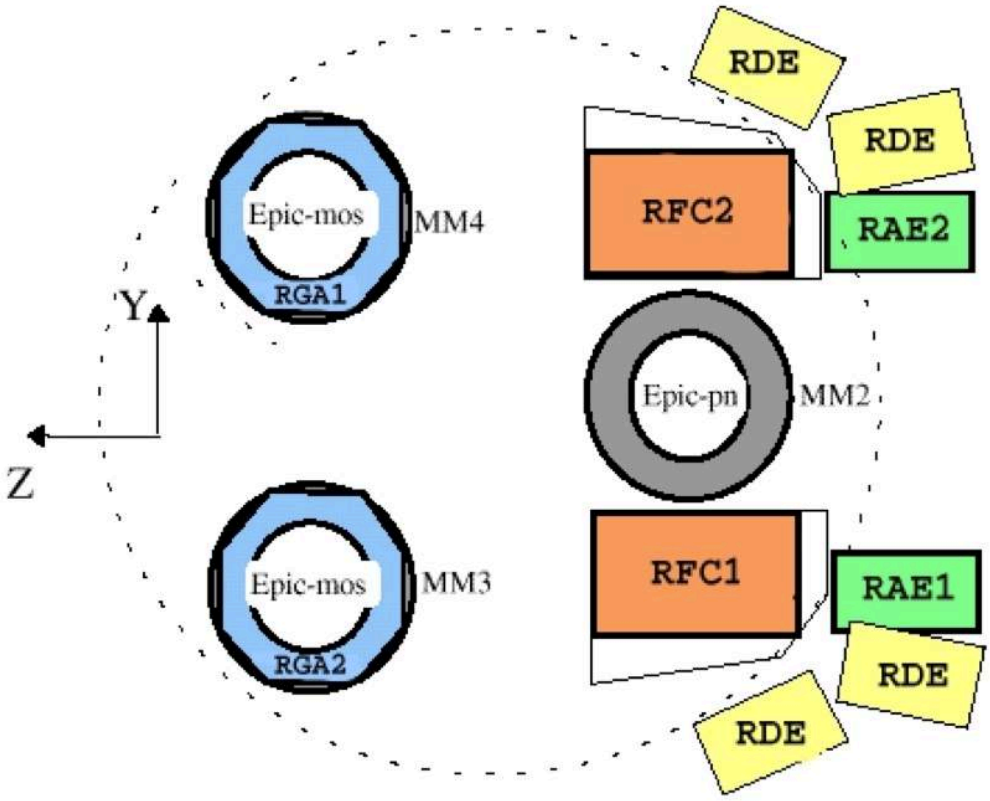

Figure 3.6 – This diagram shows the focal plane instrumentation of *XMM-Newton*. The three charge-coupled devices, the pn and the two MOS cameras, are each located at the focal points of the three X-ray telescopes MM2, MM3 and MM3, respectively. The modules RFCs, RDEs and RAEs belong to the RGS detectors, and record the light dispersed by the gratings RGA1 and RGA2. Source: The *XMM-Newton* Science Operation Center. `http://xmm.esac.esa.int/`

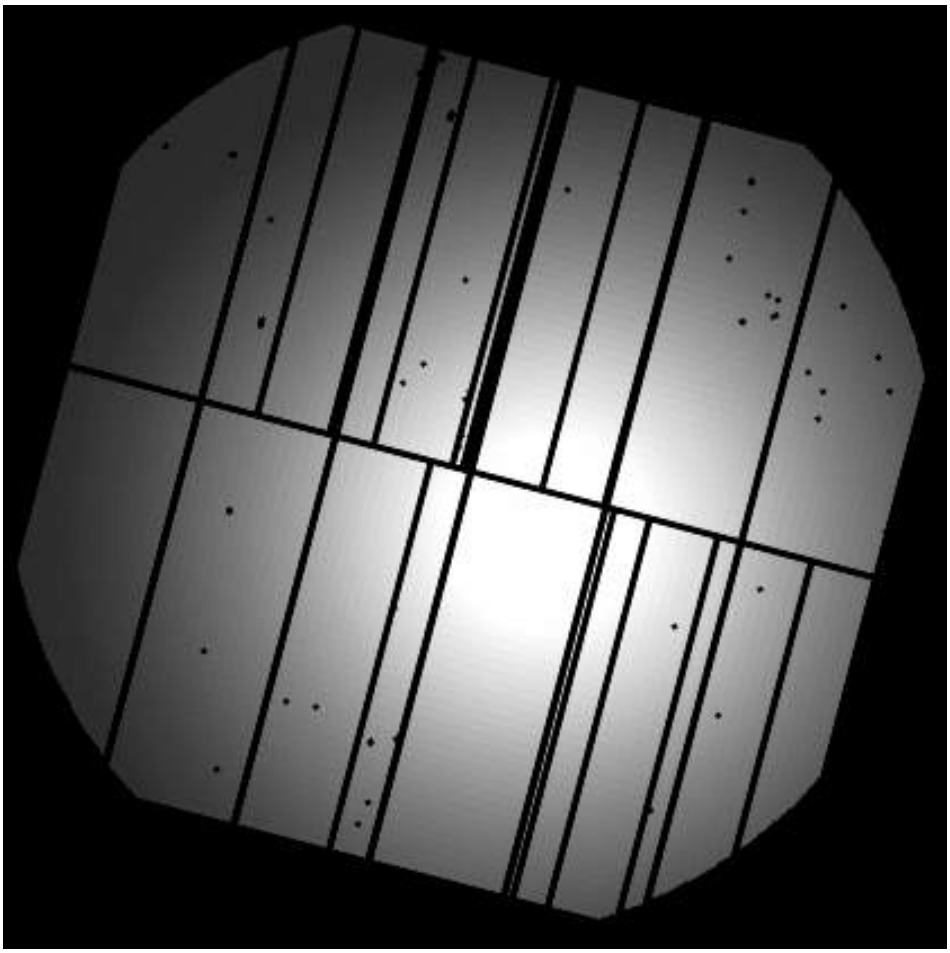

Figure 3.7 – This exposure map of the *XMM*-pn camera shows the numerous unusable columns because of dead pixels and gaps between chips. The black dots corresponds to cosmic rays hitting pixels during this particular exposure. The effect of vignetting is clearly visible on this exposure (Guillot, 2009).

EPIC, the *full-frame* mode, designed for imaging, has a time resolution of 2.6 sec for MOS and 73.4 ms for pn. Finally, three filters blocking optical light (thin, medium, and thick) can be placed in front of the *XMM* telescopes to prevent contamination from bright optical/ultra-violet sources. However, the thicker the filter, the more it absorpbs low-energy X-ray photons. For the GCs environments studied in this thesis, the "medium" filter is generally used, minimizing contamination from stars with apparent magnitudes up to $m_V = 8 - 10$.

3.4.3 *Chandra* and *XMM* for the Work in this Thesis

As mentioned above, both the *Chandra* and *XMM* observatories are being used in this work because of their complementarity. Nonetheless, most of the spectra were obtained with *Chandra* since qlMXBs in the core of GCs, such as the core of NGC 6397 (Chapter 5), can only be resolved by the superior angular resolution of *Chandra*. Spatially unresolved sources complicates the spectral identification of sources and their analyses (see Chapter 4.

Another difference between *Chandra* and *XMM* is the level of background recorded during observations. The p-n junction detector of *XMM*-EPIC is much more sensitive than the *Chandra*/ACIS (BI or FI) detectors. This results in a more significant background on *XMM*-pn spectra than in those of *Chandra*/ACIS. In addition, *XMM*-pn is much more sensitive to background flares than *Chandra*'s detectors, which usually results in larger fractions of observations that have to be discarded.

Regarding the spectral resolution, the detectors of both observatories have similar performances: $E/\Delta E = 8$ for *Chandra*/ACIS-S, $E/\Delta E = 20$ for *Chandra*/ACIS-I, $E/\Delta E \sim 13$ for *XMM*-pn or MOS1/2, all at 1 keV. And finally, because the time resolution of *XMM*-pn (73.4 ms in full-frame mode) is significantly smaller than that of *Chandra*/ACIS (3.2 sec in full-frame mode), and because of the larger PSF of *XMM* spreading photons over more pixels, the detectors of *XMM*-pn are much less subject to the effects of pile-up than those of *Chandra* for bright X-ray sources (see Section 6.2.4).

In conclusion, the *XMM-Newton* obervatory was prefered for the search of qLMXB located in GCs (Chapter 4), but the *Chandra X-ray Observatory* was used when required by the crowded environment of some targeted GCs (such as NGC 6397, see Chapter 5). For the simultaneous analyses of Chapters 6 and 7, spectral data from both *Chandra* and *XMM* were used and combined to place constraints on the dense matter EoS.

4

A New Quiescent Low-Mass X-ray Binary in NGC 6553

This chapter presents the result of the search for qLMXBs in the GC NGC 6553 using an *XMM-Newton* observation designed specifically for that purpose. One candidate qLMXB in the core of the cluster was spectrally identified based on the consistency of the spectrum with a NS H-atmosphere model at the distance of NGC 6553. The PSF of the X-ray source with *XMM*, as well as the detection of a strong non-thermal component in its spectrum, are indicative of the presence of nearby contaminated sources in the core of the cluster, unresolved with *XMM*. The analysis of an archived *Chandra* observation provides marginal additional support to this hypothesis.

This chapter was published as: S. Guillot, R. E. Rutledge, E. F. Brown, G. G. Pavlov, and V. E. Zavlin. *Discovery of a Candidate Quiescent Low-mass X-Ray Binary in the Globular Cluster NGC 6553*. ApJ, 738:129, Sept. 2011. The introduction of the original article has been edited to remove redundant information already provided in Chapter 2. The last sentence in the conclusion of this chapter (Section 4.4) was added for this thesis, to serve as a transition.

4.1 Introduction

Twenty-six GC qLMXBs, including the more recent candidates, have been discovered so far (see Heinke et al., 2003c; Guillot et al., 2009a, for complementary lists, and Table 2.2). However, for some of them, the poorly constrained $R_{\rm NS}$ and $kT_{\rm eff}$ measurements, as well as the high Galactic absorption in their direction (for example, $N_{H,22} \sim 1.2$ in the direction of Terzan 5), affects the certainty of their identification.

To increase the list of known GC qLMXBs, a program of short observations using the EPIC instrument onboard *XMM-Newton* has been undertaken to survey GCs and search for qLMXBs. This chapter reports the discovery via spectral identification of a candidate qLMXB in the core of NGC 6553. A short archived *Chandra* observation targeted at this GC was also analyzed to provide more accurate positions and tentatively confirm the source classification.

The targeted cluster, NGC 6553, is a low-Galactic latitude GC located at the position R.A.=$18^{\rm h}09^{\rm m}17.6^{\rm s}$ and decl. = $-25°54'31\farcs3$ (J2000), approximately 2.2 kpc from the Galactic centre, corresponding to a heliocentric distance of $d = 6.0$ kpc. It is a GC of moderate core compactness and moderate size: core radius $r_{\rm c} = 0\farcm55$, half mass radius $r_{\rm HM} = 1\farcm55$ and tidal radius $r_{\rm t} = 8\farcm16$. Its metallicity [M/H] = −0.09 (Valenti et al., 2007) makes it one of the most metallic clusters in the Galaxy. The foreground reddening $E\,(B-V) = 0.63$ corresponds to a moderately high hydrogen column density $N_{H,22} = 0.35$ (Predehl and Schmitt, 1995), which will be assumed for the X-ray spectral fits. Note that the published relation between $N_{\rm H}$ and $E\,(B-V)$ does not provide any uncertainties. Different values of $N_{\rm H}$ would affect the spectral fits (see Section 6.4.2 for more details). The value $N_{H,22} = 0.35$ is similar to the value found from NRAO data[1] (Dickey and Lockman, 1990), which accounts for the atomic hydrogen $N_{\rm HI}$ through the entire Galaxy. The GC properties come from the catalog of GCs (Harris, 1996, update Dec. 2010), except when other references are provided.

The organization of this chapter is as follows. Section 4.2 describes the data reduction and analysis of the *XMM-Newton* and *Chandra* observations. In Section 4.3, the results are presented. Section 4.4 contains a discussion and a conclusion.

4.2 Data Reduction and Analysis

NGC 6553 was observed with *XMM-Newton* on 2006 October 6 at 01:41:44 UT, using the three EPIC cameras, for an exposure time of 20.4 ks, with the medium filter. The

[1]From `http://cxc.harvard.edu/toolkit/colden.jsp`

Chandra X-ray Observatory observed the GC for 5.25 ks, on 2008 October 30 at 01:38:12 UT, with the ACIS-S detector (Garmire et al., 2003) in VFAINT mode.

4.2.1 Data Reduction

Reduction of *XMM-Newton* data is performed with the *XMM-Newton* Science Analysis Software (SAS) v8.0.0, using the standard procedures[2]. More specifically, `epchain` and `emchain` are used for the preliminary reduction of the raw pn and MOS data files, respectively. Single and double patterns are used for pn data and single, double and quadruple patterns for the MOS cameras, both in the 0.3–10 keV range. Prior to the source detection, the data are checked for background flares by looking for $> 3\sigma$ deviation from the mean count rate of the entire detector. None are found and the whole integration time is used. Also, an exposure map is created to correct for the effect of vignetting. The script `wavdetect` from CIAO v4.2 (Fruscione et al., 2006) is then run on the pn image in the 0.3–10 keV range, with the following parameters: minimum relative exposure of 0.1, the wavelet scales *"1.0 2.0 4.0 8.0"* and a significance threshold 3×10^{-6} (inverse of the total number of pixels in the detector), allowing for $\sim$ one spurious detection in the entire image. Sources with detection significance $\sigma > 4$ are retained for analysis.

The reduction and analysis of the *Chandra* data are accomplished with the CIAO v4.2 package (Fruscione et al., 2006). The level-1 event file is first reprocessed using the public script *chandra_repro* which performs the steps recommended by the data preparation analysis thread[3] (corrections for charge transfer inefficiency, destreaking, bad pixel removal, etc, if needed) making use of the latest effective area maps, quantum efficiency maps, and gain maps of CALDB v4.3 (Graessle et al., 2007). The newly created level-2 event file is then checked for background flares, but there are none detected.

[2]User Guide to the *XMM-Newton* Science Analysis System, Issue 5.0, 2008 (ESA: *XMM* SOC).
[3]`http://cxc.harvard.edu/ciao/threads/data.html`

4.2.2 Count Extraction

The command `evselect` from the SAS is used for source and background count extraction of the *XMM* data. A radius of 30″ around each source is chosen, accounting for 88% of the total energy from an on-axis source at 1.5 keV with the pn detector[4]. The background counts, used for background subtraction, are extracted from a larger region (100″) around the source of interest, excluding the source itself and other detected sources in close proximity with a circular region of 40″ around each of them, ensuring that 92% of the overlapping source counts (at 1.5 keV on the pn detector) are excluded. In some cases, the close proximity of the detected sources requires adapting the exclusion radii of nearby sources. Those few cases are discussed in Section 4.3. The tasks `rmfgen` and `arfgen` generate the response matrix files (RMF) and the ancillary response files (ARF) for each observations. The *XMM-Newton* extracted counts are binned using `grppha` into energy bins between 0.3 and 10 keV with a minimum of 20 counts per bin. This criterion ensures having approximate Gaussian statistics in each spectral bin.

For *Chandra* data, the script `psextract` is used to extract the counts of the X-ray sources, in the energy range 0.5–8 keV. The extraction region depends on the off-axis angle since the PSF degrades at large off-axis angles. Since the analyzed observation of NGC 6553 was performed with the ACIS-S instrument and a focal plane temperature of -120 °C, the RMFs have to be recalculated, according to the recommendations of the CIAO Science Thread *"Creating ACIS RMFs with mkacisrmf"*. It is also crucial to recalculate the ARFs using the new RMFs in order to match the energy grids between the two files.

In both the *XMM-Newton* and *Chandra* observations, the count rates are low enough for the effects of pile-up to be ignored. Specifically, for the *Chandra* data, the count rate was 0.031 photons per detector frame (3.24 sec), and therefore the effect of pile-up can be safely neglected.

[4]From *XMM-Newton* Users Handbook, Figure 3.7, July 2010

4.2.3 Spectral Analysis

The identification of candidate qLMXBs in this analysis is based on the spectral identification with the models that empirically describe the spectra of previously known qLMXBs. Spectra from the pn camera are first extracted and analyzed, since its superior efficiency facilitates spectral analysis with an improved S/N over the two MOS cameras. H-atmosphere models are available in *XSPEC*, including `nsa` and `nsagrav` (Zavlin et al., 1996) and `nsatmos` (McClintock et al., 2004; Heinke et al., 2006a). The major difference between the models resides in the surface gravity values g used to calculate the model: `nsa` has been implemented with a fixed value $g = 2.43{\times}10^{14}\,\mathrm{cm\,s^{-2}}$, `nsagrav` has been computed for a range $g = (0.1\text{–}10){\times}10^{14}\,\mathrm{cm\,s^{-2}}$ and `nsatmos` for the range $g = (0.63\text{–}6.3){\times}10^{14}\,\mathrm{cm\,s^{-2}}$. Models with calculated for multiple values of g are therefore preferred, and the model `nsatmos` is chosen here for the spectral identification of qLMXBs.

The identification of candidate qLMXBs is based on the statistical consistency (null hypothesis probability, NHP hereafter, $p_{\mathrm{null}} \gtrsim 0.01$) with the `nsatmos` model at the distance of the host GC, with the Galactic absorption taken into account using the multiplicative model `wabs`. Additional conditions impose that the best-fit effective temperature and projected radius are within the range of previously observed GC qLMXBs, i.e., $kT_{\mathrm{eff}} \sim 50\text{–}180\,\mathrm{eV}$ and $R_{\infty} \sim 5\text{–}20\,\mathrm{km}$ (see Heinke et al., 2003d; Guillot et al., 2009a, for complementary lists of GC qLMXBs). For identified candidate qLMXBs, the pn, MOS1 and MOS2 extracted spectra are then fit simultaneously to improve statistics and diminish the uncertainties on the best-fit parameters.

In some cases, an excess of counts at high energy is modeled with an additional PL component. This is empirically justified by the fact that qLMXBs sometimes display a hard PL which dominates the spectrum above 2 keV. Most qLMXBs in the field of the Galaxy have spectra best fitted with H-atmosphere models combined with a hard-photon PL (for example, Cen X-4, Asai et al. 1996; Rutledge et al. 2001a, Aql X-1, Asai et al. 1998; Campana et al. 1998; Rutledge et al. 2001b). It has been claimed

that some GC qLMXBs also displayed significant PL contributions (between $\sim 10\%$ and $\sim 50\%$ of the total flux), for example, in NGC 6440 (Cackett et al., 2005), and in Ter 5 (Heinke et al., 2006b). Proposed interpretations of the observed PL tail include residual accretion onto the NS magnetosphere (Grindlay et al., 2001a; Cackett et al., 2005), shock emission via the emergence of a magnetic field (Campana and Stella, 2000), or an intrabinary shock between the winds from the NS and its companion star (Campana et al., 2004). However, analyses of the quiescent emission of LMXBs have shown evidence of the presence of a variable low-level accretion on the NS; for the LMXB Aql X-1 (Rutledge et al., 2002a), for XTE J1701−462, (Fridriksson et al., 2010), and for the LMXB Cen X-4 (Cackett et al., 2010).

Such an additional spectral component for qLMXBs in the core of GCs might not necessarily originate from one of the interpretations listed above. For example, a PL component was required in addition to the H-atmosphere model for the spectral fit of the candidate qLMXB XMMU J171433−292747 in NGC 6304 observed with *XMM* (Guillot et al., 2009a). However, a short 5 ks archived *Chandra* observation demonstrated that the high energy excess of counts noticed for this source originated from another close by X-ray source (possibly a CV) unresolved in the *XMM* data (Guillot et al., 2009b). Then, a longer 100 ks *Chandra* exposure confirmed the NS radius measurement and the initially reported results (see Section 6.3.1).

The main focus of this chapter is the discovery of candidate qLMXBs in NGC 6553, but as part of the systematic analysis of *XMM* data, a simple spectral analysis is performed for all other X-ray sources that are not consistent with NS H-atmosphere models at the distance of the host GC. Specifically, a simple absorbed PL model is used and their best-fit photon indices, as well as their unabsorbed flux (0.5–10 keV) are reported. In some cases, the X-ray spectra cannot be fit adequately with either an NS H-atmosphere model or a PL model. In those cases, the use of other models is attempted for completeness and the details are provided in Section 4.3. Finally, sources with an $S/N < 3$ are fit with a fixed ($\Gamma = 1.5$) photon index.

In all cases, the Galactic absorption is taken into account with the model `wabs`, keeping the value of $N_{\rm H}$ fixed at the value in the direction of the GC, i.e., $N_{H,22} = 0.35$. Also, all quoted uncertainties on the spectral parameters are 90% confidence level in the text and the tables. Finally, the quoted fluxes are corrected for the finite aperture (extraction radius).

4.2.4 Astrometric Correction

The uncertainties reported in Table 4.1 on the *XMM* positions are composed of the `wavdetect` statistical error on the pn positions (up to $1''$) and the systematic uncertainty of *XMM* ($2''$at 1σ [5]). An absolute astrometric correction – into the frame of the Two Micron All Sky Survey (2MASS) – is applied through the association of X-ray sources with 2MASS counterparts. Three X-ray sources were firmly associated with 2MASS objects. The sources #5, #2 and #9 have probabilities 0.001%, 0.21% and 0.04%, respectively, that a star as bright or brighter as the stars 2MASS J18093564−25555377, 2MASS J18100723−25511760 and the star 2MASS J18083961−2601203, respectively, lie as close or closer to the three X-ray sources. These probabilities were calculated using all 2MASS stars detected in $2'$ wide annulli, centred at the GC optical centre, and with respective average radii equal to the distances of the respective 2MASS counterparts from the GC centre. This means that sources #5, #2 and #9 have probabilities 99.999%, 99.79% and 99.96% to be associated with the stars 2MASS J18093564−25555377, 2MASS J18100723−25511760 and the star 2MASS J18083961−2601203, respectively. From these three associations, the best-fit required transformation is a shift of -0.″1 in R.A. and 0.″71 in decl. The residual uncertainties are 0.″34 in R.A. and 1.″08 in decl. This is added in quadrature to the 2MASS astrometric uncertainty ($\sim$ 0.″15 [6]) and to the statistical uncertainty of the X-ray source detection.

[5] from *XMM* Science Operations Centre XMM-SOC-CAL-TN-0018, Guainizzi (2012)
[6] Section 2 of `http://www.ipac.caltech.edu/2mass/releases/allsky/doc/`

Table 4.1 – X-ray sources detected in the *XMM* observation of NGC 6553.

Object Name	Right Ascension (J2000)	Declination (J2000)	$\delta_{\mathrm{R.A.}}\backslash\delta_{\mathrm{decl.}}$ [a] ($''$)	S/N[b]	ID[c]
XMMU J180846−260043	272.19551	-26.01220	±0.0\0.0	166.1	01
XMMU J181007−255118	272.53028	-25.85518	±0.3\0.3	28.0	02
XMMU J180916−255425	272.31889	-25.90704	±0.4\0.3	26.2	03
XMMU J180832−255852	272.13472	-25.98135	±0.4\0.4	24.6	04
XMMU J180935−255554	272.39844	-25.93172	±0.4\0.5	22.6	05
XMMU J180845−260035	272.18903	-26.00978	±0.4\0.4	21.4	06
XMMU J180935−255157	272.39592	-25.86605	±0.3\0.3	21.3	07
XMMU J180952−254637	272.46964	-25.77697	±0.7\0.6	16.9	08
XMMU J180839−260118	272.16497	-26.02191	±0.6\0.5	16.7	09
XMMU J180936−255952	272.40357	-25.99803	±0.6\0.5	15.5	10
XMMU J180851−254113	272.21633	-25.68706	±0.6\0.5	14.1	11
XMMU J180910−254125	272.29530	-25.69036	±0.5\0.5	12.1	12
XMMU J180931−254105	272.38234	-25.68474	±0.6\0.4	10.9	13
XMMU J180853−254106	272.22092	-25.68513	±0.6\0.5	9.3	14
XMMU J180934−255549	272.39324	-25.93030	±0.5\0.4	9.2	15
XMMU J180915−255631	272.31424	-25.94212	±0.7\0.5	9.0	16
XMMU J180921−260325	272.34126	-26.05712	±1.0\0.7	8.0	17
XMMU J181002−260135	272.51131	-26.02663	±0.6\0.7	7.9	18
XMMU J180922−255310	272.34343	-25.88638	±0.9\0.6	7.5	19
XMMU J180854−260353	272.22729	-26.06497	±0.6\0.5	7.4	20
XMMU J180937−255408	272.40664	-25.90245	±0.5\0.5	7.3	21
XMMU J180912−255138	272.30407	-25.86082	±0.8\0.8	6.6	22
XMMU J180931−255149	272.38286	-25.86367	±0.8\0.6	6.4	23
XMMU J180915−260127	272.31512	-26.02427	±0.9\0.9	6.3	24
XMMU J180938−260233	272.41026	-26.04259	±1.0\0.6	6.2	25
XMMU J180856−254806	272.23482	-25.80185	±0.9\0.7	6.2	26
XMMU J180921−255731	272.34030	-25.95878	±0.8\0.7	6.2	27
XMMU J180920−255614	272.33388	-25.93725	±0.7\0.6	5.9	28
XMMU J180917−254614	272.32096	-25.77083	±0.9\0.7	5.8	29
XMMU J180941−255048	272.42476	-25.84671	±0.9\0.8	5.7	30
XMMU J180913−254834	272.30522	-25.80972	±0.9\0.8	5.6	31
XMMU J180943−255808	272.42940	-25.96905	±0.7\0.7	5.6	32
XMMU J180950−255531	272.45886	-25.92548	±0.7\0.6	5.5	33
XMMU J180930−260205	272.37870	-26.03489	±0.8\0.8	5.5	34
XMMU J180939−254723	272.41319	-25.78992	±0.0\0.0	5.4	35
XMMU J180950−260307	272.46218	-26.05219	±0.9\0.7	5.4	36
XMMU J180839−254707	272.16615	-25.78536	±0.7\0.6	5.3	37
XMMU J180934−254537	272.39339	-25.76053	±0.6\0.6	5.2	38
XMMU J181003−255636	272.51627	-25.94347	±0.7\0.6	5.0	39
XMMU J180844−254812	272.18444	-25.80336	±0.8\0.7	4.6	40
XMMU J180924−255540	272.35017	-25.92790	±0.7\0.6	4.5	41
XMMU J181007−260503	272.53191	-26.08422	±0.7\1.0	4.4	42
XMMU J181023−254811	272.59968	-25.80325	±0.7\0.7	4.2	43

NOTES: [a] Statistical uncertainty on the position.
[b] Signal-to-noise ratio provided by the source detection algorithm `wavdetect`.
[c] The sources are sorted in order of their detection significance.

4.3 Results

In the reduced image of NGC 6553, the `wavdetect` algorithm detected 43 X-ray sources on the pn camera within the field of the observation. Table 4.1 lists all the sources detected with their positions, their statistical uncertainty and their detection significance, while Table 4.2 provides the results of the spectral fits and the fluxes. The spectral analysis of candidate qLMXBs and of the sources for which a PL model does not describe the data is detailed below.

As can be seen in Figure 4.1, the proximity (17.″5) of source #15 to source #5 requires adapting the extraction radius prior to the spectral analysis. More specifically, instead of excluding the default 40″ around nearby sources, the exclusion radii of source #15 is chosen to be 10″ (59% of encircled energy fraction, EEF) for the count extraction of #5, and the exclusion radii of source #5 is chosen to be 12.″5 (68% of EEF) for the count extraction of source #15. The radii mentioned were determined by visual inspection of the X-ray image. Similarly, the `wavdetect` algorithm detected two sources, #11 and #14, located 16″ apart near the edge of the pn camera. In this case, the exclusion radii of #11 and #14 are set to 15″ and 10.″5, when considering the extraction region of sources #14 and #11, respectively.

4.3.1 Source #1 - XMMU J180846−260043

This X-ray source has the largest pn count rate of the observation, $0.197 \pm 0.004\,\mathrm{cts\,s^{-1}}$. Nevertheless, it is not affected pile-up (accumulation of photon events within a single CCD time frame, 73 ms) since its count rate per detector frame is then ~ 0.014.

The bright X-ray source corresponds to the *ROSAT* source 1RXS J180847.7-260037 (Voges et al., 1999) and to the IR star 2MASS J18084678-2600417 (with probability of association 99.999%). It is also named, HD 315209, as listed in the Tycho Reference Catalog with the proper motion $+14.2 \pm 2.4\,\mathrm{mas\,yr^{-1}}$ in R.A. and $-9.0 \pm 1.7\,\mathrm{mas\,yr^{-1}}$ in decl. (Høg et al., 1998, 2000). The star has a spectral type K5V and is located at a distance of 33 pc, deduced from spectroscopic observations (Riaz et al., 2006).

Table 4.2 – Spectral results of all X-ray sources detected in NGC 6553.

ID	pn Rate (cts ks^{-1})	Γ	$kT_{\rm eff}$ (keV)	$F_{\rm X,-13}$	χ^2_ν/DOF ($p_{\rm null}$)	Model Used
01	197.3±3.8	–	$0.35^{+0.05}_{-0.12}$; $2.80^{+5.75}_{-0.67}$	17.3	1.01/115 (0.44)	RS+RS
02	17.7±1.3	$3.0^{+0.3}_{-0.3}$	–	2.54	1.32/15 (0.18)	PL
03	27.1±1.5 †	$2.1^{+0.5}_{-0.8}$	$0.136^{+0.021}_{-0.034}$	1.29	0.90/54 (0.68)	`nsatmos+PL`
04	18.1±1.4	$1.4^{+0.2}_{-0.2}$	–	2.67	0.79/18 (0.71)	PL
05	15.0±1.3	–	$0.37^{+0.07}_{-0.12}$	0.42	0.75/13 (0.71)	RS
06	8.6±0.9	$3.3^{+0.5}_{-0.4}$	–	5.89	1.50/ 7 (0.16)	PL
07	17.6±1.4	$0.9^{+0.2}_{-0.2}$	–	2.46	0.75/18 (0.76)	PL
08	10.8±1.1	$0.8^{+0.3}_{-0.3}$	–	2.72	0.94/11 (0.50)	PL
09	11.6±1.2	–	$0.873^{+0.145}_{-0.092}$	0.65	1.20/30 (0.21)	RS
10	9.6±1.1	$2.4^{+0.5}_{-0.4}$	–	0.74	0.75/12 (0.70)	PL
11	6.0±0.9	$0.7^{+0.3}_{-0.4}$	–	2.58	0.85/ 6(0.53)	PL
12	4.0±1.0	$-0.3^{+0.7}_{-0.7}$	–	2.44	0.83/ 8 (0.58)	PL
13	3.9±0.9	$1.2^{+0.6}_{-0.6}$	–	1.07	0.92/ 6 (0.48)	PL
14	3.7±0.7	$0.2^{+0.6}_{-0.7}$	–	2.2	0.66/ 3 (0.57)	PL
15	6.7±1.0	$2.8^{+0.8}_{-0.8}$	–	0.44	2.02/ 8 (0.04)	PL
16	4.5±1.0	$4.5^{+1.5}_{-1.3}$	–	0.31	1.27/ 9 (0.25)	PL
17	4.3±0.9	$3.9^{+1.2}_{-1.1}$	–	0.34	2.15/ 7 (0.03)	PL
18	5.1±1.0	$1.5^{+0.5}_{-0.5}$	–	0.96	0.59/ 8 (0.79)	PL
19	3.7±1.0	$1.3^{+0.7}_{-0.7}$	–	0.30	0.86/ 9 (0.56)	PL
20	4.0±0.9	$5.0^{+1.4}_{-1.2}$	–	0.51	1.30/ 7 (0.25)	PL
21	4.4±0.9	$3.5^{+1.0}_{-0.9}$	–	0.31	1.14/ 7 (0.33)	PL
22	2.3±0.9	(1.5)	–	0.13	0.54/ 8 (0.82)	PL
23	4.6±1.0	$2.1^{+0.7}_{-0.6}$	–	1.60	0.65/ 8 (0.74)	PL
24	3.5±0.9	$1.0^{+0.6}_{-0.6}$	–	0.47	1.31/ 7 (0.24)	PL
25	4.4±0.9	$1.4^{+1.7}_{-1.1}$	–	0.44	1.84/ 7 (0.08)	PL
26	2.6±0.9	$1.4^{+1.2}_{-1.4}$	–	0.28	0.52/ 6 (0.79)	PL
27	1.5±0.9	(1.5)	–	0.08	0.95/ 8 (0.37)	PL
28	0.4±0.9	(1.5)	–	0.05	2.26/ 7 (0.03)	PL
29	3.3±0.8	$0.3^{+0.9}_{-1.0}$	–	0.75	0.34/ 5 (0.89)	PL
30	3.0±0.8	$1.8^{+1.3}_{-0.9}$	–	0.29	0.60/ 5 (0.70)	PL
31	3.0±0.9	$1.4^{+0.9}_{-0.8}$	–	0.30	0.36/ 7 (0.93)	PL
32	1.5±0.9	(1.5)	–	0.20	0.39/ 7 (0.91)	PL
33	2.2±0.9	(1.5)	–	0.21	0.47/ 7 (0.86)	PL
34	2.7±0.8	$1.6^{+1.2}_{-1.1}$	–	0.31	0.56/ 5 (0.73)	PL
35	4.1±0.8	$3.8^{+0.7}_{-0.7}$	–	0.51	0.63/ 8 (0.85)	PL
36	3.8±0.9	$2.8^{+0.7}_{-0.7}$	–	0.45	1.66/ 7 (0.11)	PL
37	2.0±0.8	(1.5)	–	0.09	2.25/ 6 (0.04)	PL
38	3.3±0.9	$3.9^{+2.1}_{-2.0}$	–	0.33	1.07/ 6 (0.38)	PL
39	3.0±0.9	$4.3^{+3.4}_{-2.2}$	–	0.33	0.63/ 6 (0.70)	PL
40	1.7±0.8	(1.5)	–	0.20	0.66/ 5 (0.65)	PL
41	0.7±0.9	(1.5)	–	0.01	2.01/ 7 (0.05)	PL
42	0.4±0.7	(1.5)	–	0.24	1.37/ 4 (0.24)	PL
43	1.8±0.8	(1.5)	–	0.49	0.88/ 5 (0.50)	PL

NOTES: The columns of this table are, from left to right: the source ID according to Table 4.1; the background subtracted count rates on the pn camera in the 0.3–10 keV range; the best-fit photon index Γ when a power law was used (values in parentheses were held fixed); the best-fit effective temperature when a thermal model was used; the unabsorbed X-ray flux in unit of 10^{-13} erg cm^{-2} s^{-1} in the 0.5–10 keV energy band (not corrected for the finite aperture); the χ^2-statistic obtained with the model listed; and the model used to fit the spectrum of the source. PL: `powerlaw`, RS: `Raymond-Smith` plasma. Note that the flux is not corrected for the finite aperture in this table. All fits have been performed with a fixed value of the Galactic absorption, $N_{H,22}$=0.35. DOF refers to the number of degrees of freedom.

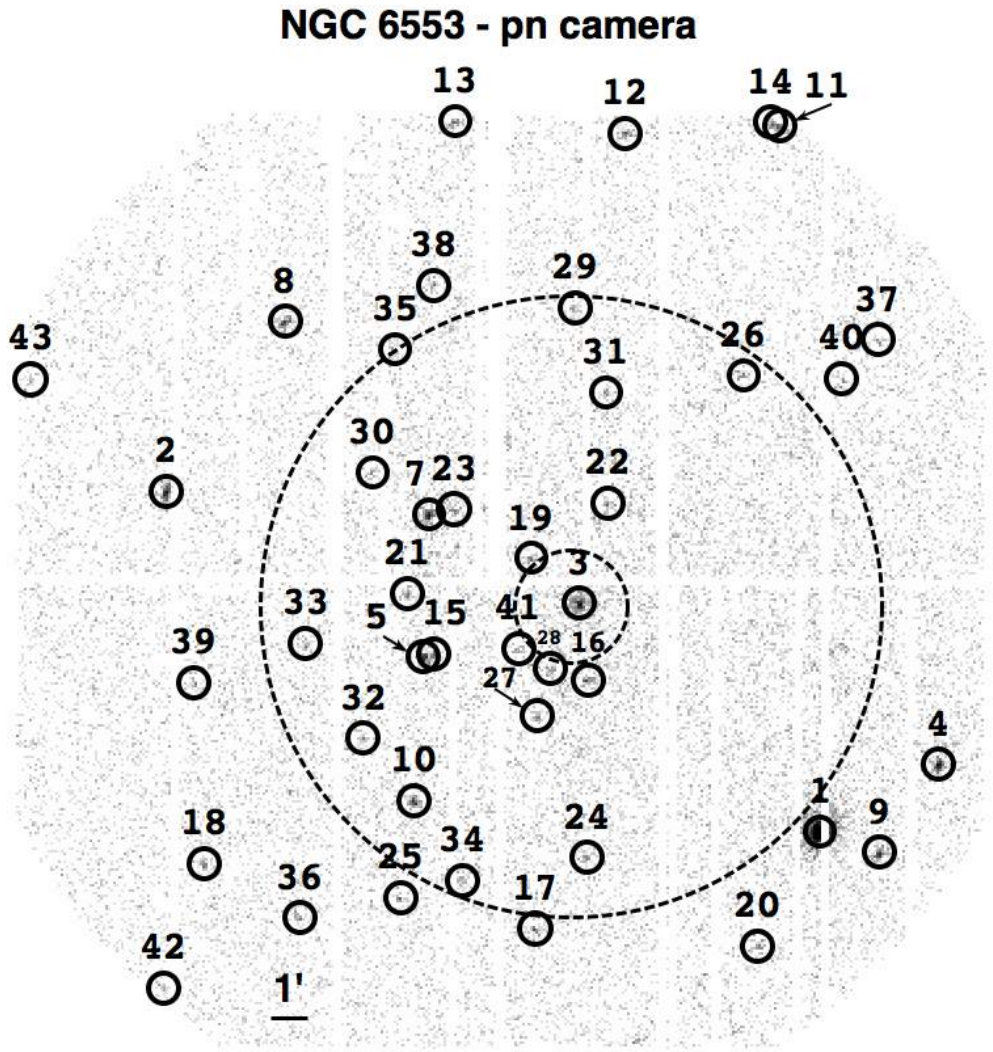

Figure 4.1 – This *XMM*-pn image of NGC 6553 shows the 43 sources detected on the pn camera. The small and large dashed circles respectively represent the half-mass ($r_{\rm HM} = 1\farcm55$) and tidal radii ($r_{\rm t} = 8\farcm16$). A log gray-scale has been used for the image due to the brightness of source #1. In this figure, north is up, and right ascension increases to the left. The candidate quiescent low-mass X-ray binary detected in this globular cluster is the source #3, corresponding to XMMU J180916−255425.

The *XMM* source is adjacent to a bad column on the pn camera. Therefore, the resulting astrometry is likely to be offset in the direction opposite to the bad column, i.e., toward increasing right ascension. Therefore, the position obtained with the MOS2 camera is provided: R.A.=$18^{\rm h}08^{\rm m}46.7^{\rm s}$ and decl. = $-26°00'42\farcs7$.

The high-S/N spectrum of this star is not well described by an absorbed PL: χ^2_ν/DOF ($p_{\rm null}$) = 1.80/120 (1.7×10^{-7}). Removing the absorption, i.e., setting $N_{\rm H}$=0, also leads to a non-acceptable fit with $p_{\rm null} \sim 10^{-60}$. Similarly, NS H-atmosphere, thermal bremsstrahlung and blackbody models do not fit properly the data, leading to $p_{\rm null} < 10^{-10}$, whether or not Galactic absorption is included with the models fitted. A Raymond-Smith (RS) plasma model provides improved fit statistics with $p_{\rm null} \approx 10^{-3}$ but this is still not a statistically acceptable fit. A two-temperature RS model, often used to represent stellar coronal spectra (Dempsey et al., 1993), satisfactorily describes the spectrum, χ^2_ν/DOF ($p_{\rm null}$) = 1.01/11.5 (0.44), with best-fit temperatures $kT_{\rm eff,1} = 0.35^{+0.05}_{-0.12}$ keV and $kT_{\rm eff,2} = 2.80^{+5.75}_{-0.67}$ keV. With this model, the best-fit hydrogen column density is $N_{H,22} = 0.09 \pm 0.04$, consistent with a small distance to this star which lies in the foreground of NGC 6553.

4.3.2 Source #5 - XMMU J180935−255554

This source, located within the GC tidal radius, is likely associated with the star HD 165973 of spectral type G8III (Houk and Smith-Moore, 1988). The 2MASS name of this star is 2MASS J18093564-2555537 (99.999% chance of association with the X-ray source #5). It has a proper motion of $+12.9\pm1.9$ mas yr^{-1} in R.A. and -3.5 ± 1.6 mas yr^{-1} in decl. (Høg et al., 1998, 2000). No parallax measurement is available for this star. The X-ray spectrum cannot be fit with the NS H-atmosphere, PL, blackbody and thermal bremsstrahlung models. All of these models lead to $p_{\rm null} < 0.006$. However, an RS plasma model provides a statistically acceptable fit with χ^2_ν/DOF ($p_{\rm null}$) = 0.75/13 (0.71). The best-fit temperature is $kT_{\rm eff} = 0.37^{+0.07}_{-0.12}$ keV and the best-fit hydrogen column density is $N_{H,22} < 0.26$ (90% confidence).

4.3.3 Source #9 - XMMU J180839−260118

The source #9 has a soft thermal spectrum that is found to be acceptably fit by the `nsatmos` model: $kT_{\rm eff} = 80^{+21}_{-12}\,$eV and $R_{\rm NS} = 15.4^{+6.3}_{-6.0}\,$km for $M_{\rm NS} = 1.4\,M_\odot$, with χ^2_ν/DOF ($p_{\rm null}$) = 1.50/32 (0.03). The spectrum is also acceptably fit with a RS plasma model: $kT_{\rm eff} = 0.87^{+0.15}_{-0.09}\,$keV, $N_{H,22} = 0.19^{+0.07}_{-0.08}$ and $Z = 0.10^{+0.16}_{-0.06}$ with χ^2_ν/DOF ($p_{\rm null}$) = 1.20/30 (0.21). A Kolmogorov-Smirnov test (probability $p_{\rm KS}$ = 0.22) shows no evidence of variability.

The infrared (IR) source, 2MASS J18083961−2601203, is located at a distance of 1.″51 from source #9 (after correction) and is identified as the probable counterpart of the candidate qLMXB, with a probability of association of 99.86%. It has magnitudes in the J, H and K IR bands of $m_J = 10.146\,(15)$, $m_H = 9.796\,(23)$, and $m_K = 9.723\,(31)$, where the numbers in parentheses indicate the uncertainties on the magnitudes. The X-ray to J-band flux ratio of the association is $F_{\rm X}/F_J \approx 2{\times}10^{-3}$ and is consistent with that of a coronally active star. The possibility that source #9 is a qLMXB with a giant star in NGC 6553 cannot be discarded on this basis.

However, in the CMD of NGC 6553 (Ortolani et al., 1995), the V-band magnitude of this star in the NOMAD Catalogue (Zacharias et al., 2005) lies ~ 5 mag above the tip of the RGB. This observation strongly disfavours the giant star hypothesis, since the star is $\sim 100\times$ brighter than the brightest giants in the cluster. In addition, the location of the system outside the tidal radius of the cluster also disfavours the qLMXB classification. Therefore, source #9 is not a candidate qLMXB at the distance of the GC.

4.3.4 Candidate qLMXB, Source #3 - XMMU J180916−255425

XMM-Newton Observation

The X-ray spectrum of this source is acceptably fit (χ^2_ν/DOF ($p_{\rm null}$) = 1.44/33 (0.05)) with `nsatmos`, for which the parameters are: $R_{\rm NS} = 6.7^{+0.9}_{-1.2}\,$km and $kT_{\rm eff} = 137^{+20}_{-18}\,$eV, for $M_{\rm NS} = 1.4\,M_\odot$. However, an additional PL component is required to account

for the high-energy tail of the spectrum, as evidenced by a low f-test probability ($p_{\mathrm{F-test}} = 0.002$). Adding the PL component to `nsatmos` results in the following improved fit : χ^2_ν/DOF (p_{null}) = 0.97/31 (0.52), with $R_{\mathrm{NS}} = 6.3^{+2.9}_{-1.0}\,\mathrm{km}$ ($M_{\mathrm{NS}} = 1.4\,M_\odot$), $kT_{\mathrm{eff}} = 135^{+25}_{-42}\,\mathrm{eV}$ and $\Gamma = 2.1^{+1.5}_{-0.9}$ (Figure 4.2). The best-fit projected radius R_∞ and temperature are consistent with the qLMXB classification. There is no evidence of variability on the time scale of the observation as evidenced by a Kolmogorov-Smirnov test with probability $p_{\mathrm{KS}} = 0.25$.

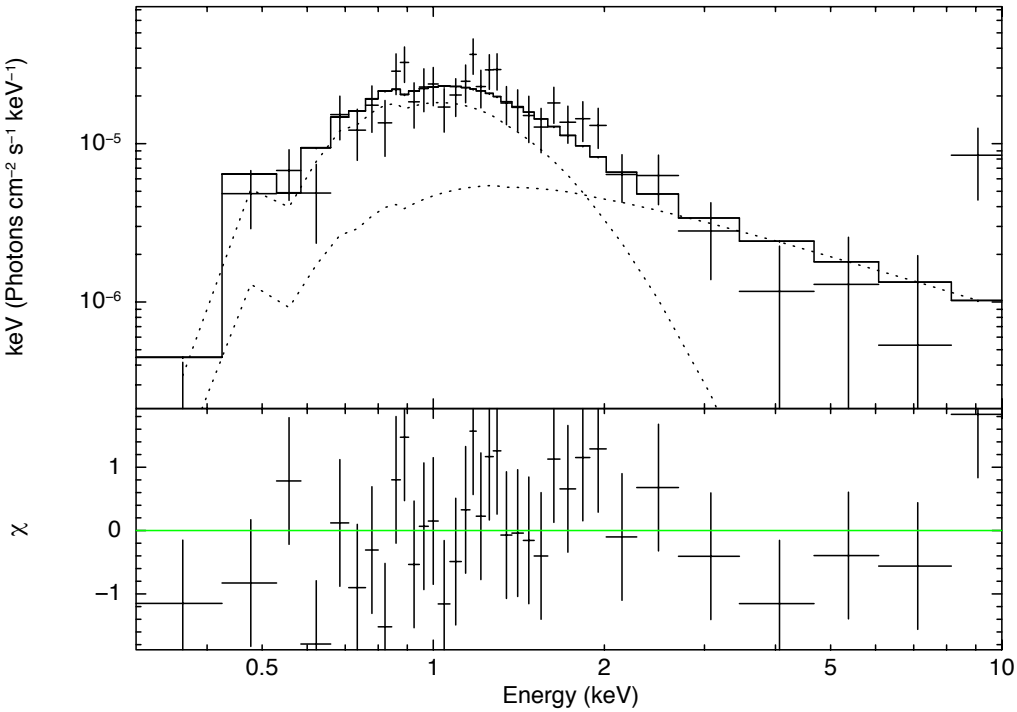

Figure 4.2 – This graph shows the *XMM*-pn spectrum of the candidate quiescent low-mass X-ray binary XMMU J180916−255425 in NGC 6553. The two spectral components (hydrogen atmosphere model `nsatmos` and power law component `powerlaw`) are shown in dashed lines, with `nsatmos` dominating at 1 keV, and the `powerlaw` dominating the flux above ~ 2 keV. They are both affected by interstellar absorption modeled with `wabs` and the hydrogen column density $N_{H,22}$=0.35.

To improve the statistics, the MOS1 and MOS2 extracted spectra are added and a simultaneous spectral fit is performed. A multiplicative constant is added to the `nsatmos + powerlaw` model to verify that there is no discrepancy between the pn spectrum and the MOS1/2 spectra normalizations. The multiplicative constant is fixed to $c = 1$ for pn and fit for the MOS1/2 data. It is found that $c_{\rm MOS1} = 1.08^{+0.20}_{-0.18}$ and $c_{\rm MOS2} = 0.86^{+0.17}_{-0.16}$, both consistent with unity. Therefore the simultaneous fit is performed with $c = 1$ for all spectra. The best-fit `nsatmos + powerlaw` parameters are listed in Table 4.3. The NS parameters and the unabsorbed luminosity (thermal component $L_{\rm X,th,[0.5-10\,keV]} = 4.2{\times}10^{32}\,{\rm erg\ s^{-1}}$, and PL component $L_{\rm X,PL,[0.5-10\,keV]} = 2.1{\times}10^{32}\,{\rm erg\ s^{-1}}$) are within the expected range of values for qLMXBs.

The PL component accounts for 33% of the total unabsorbed flux. Such a strong PL component, if not intrinsic to the source, could suggest that, as observed for the candidate qLMXB in the core of NGC 6304 (Guillot et al., 2009b), multiple X-ray sources are unresolved in the core. Running the detection algorithm `wavdetect` on the MOS1/2 images (because of the smaller pixel size than the pn camera) does not reveal the presence of multiple resolved sources in the core. Nonetheless, visual inspection of the EPIC images seems to suggest that the spatial count distribution deviates from that of a point source, favouring the hypothesis that nearby sources are unresolved by *XMM-Newton*. A more quantitative analysis is performed using the *XMMSAS* task `eradial`. By comparing the spatial distribution of counts to the telescope PSF at 1.5 keV (Figure 4.3), there is marginal evidence that the source differs from a point source (χ^2=51.5 for 31 DOF, with $p_{\rm null} = 1.2\%$). In other words, there is marginal support to the hypothesis that the qLMXB candidate is confused with nearby sources (at $\sim 15''$–$30''$) in the *XMM* data. For this fit and for Figure 4.3, the radial extent of the PSF is cut off at $100''$, the distance of the next closest X-ray source detected. However, the fit statistics are highly dependent on the radial extent of the PSF. Choosing instead a cut off at $30''$ leads to χ^2=30.1 for 9 DOF, with $p_{\rm null} = 0.04\%$, which is evidence for the presence of nearby unresolved sources.

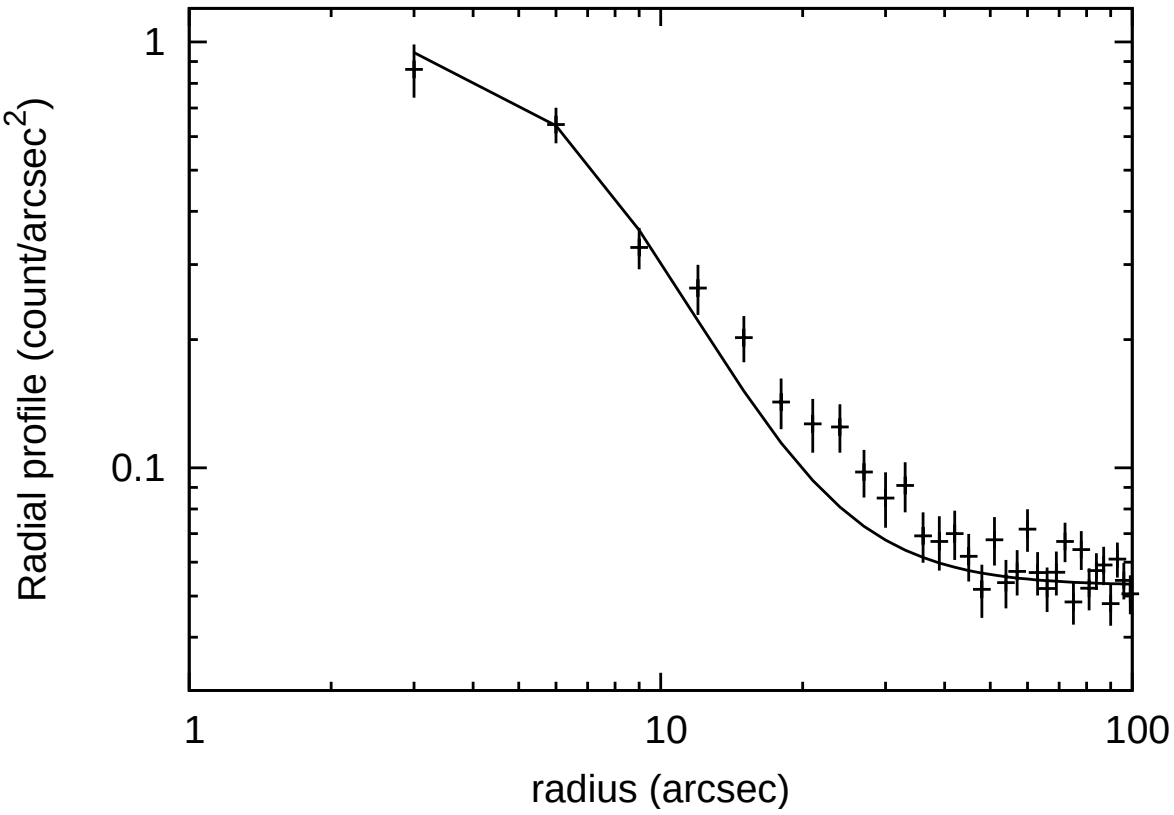

Figure 4.3 – This graph shows the *XMM* surface brightness as a function of radius of the candidate quiescent low-mass X-ray binary in the core of NGC 6553. The line indicates the best-fit pn-camera point-spread function at 1.5 keV at the position of the source. Counts in excess of the telescope point spread function at $\sim 15''$–$30''$ are evidence of the presence of one (or more) unresolved sources. This is marginally supported by the statistic of the point spread function fit: $\chi^2 = 51.5$ for 31 degrees of freedom, with a null hypothesis probability $p_{\rm null} = 1.2\%$.

The hypothesis that the PL component is due to nearby sources is further tested by using a spectrum created from counts located within 12″ of the source centre, therefore decreasing the contamination from possible nearby sources at > 12″, as evidenced by the PSF analysis above. However, this method reduces the S/N since only 62% of the EEF is included within 12″ at 1.5 keV. This spectrum has a count rate of $15\pm1\,\mathrm{cts\,ks^{-1}}$. Using the `nsatmos` model alone, the best-fit parameters, $R_{\rm NS} = 6.4^{+1.8}_{-0.8}\,\mathrm{km}$ (for $M_{\rm NS} = 1.4\,M_{\odot}$) and $kT_{\rm eff} = 135^{+19}_{-27}\,\mathrm{eV}$, are consistent with the best-fit parameters mentioned above, as is the unabsorbed flux $F_{\rm X} = 1.49\times10^{-13}\,\mathrm{erg\ cm^{-2}\ s^{-1}}$. The statistically acceptable fit, χ^2_ν/DOF ($p_{\rm null}$) = 1.73/12 (0.05), does not require a PL component, as demonstrated by the high F-test probability ($p_{\rm F-test} = 0.31$). Adding a PL component leads to consistent NS parameters and flux. Also, the fraction of the PL to the total flux is consistent with zero at the 1σ level. This provides additional support to the claim that the PL component represents the emission of nearby contaminating sources at angular distances > 12″ from the qLMXB candidate in the core of NGC 6553.

Finally, the second *XMM-Newton* serendipitous source catalog (2XMMi; Watson et al., 2009) reports two sources located 20.″7 apart, at the positions R.A.=$18^{\rm h}09^{\rm m}16.5^{\rm s}$ and decl. = −25°54′26.″1 for the brightest one, coincident with the qLMXB and a fainter source at R.A.=$18^{\rm h}09^{\rm m}18.0^{\rm s}$ / decl. = −25°54′27.″5. The discrepancy between 2XMMi and the detections in this work may reside in the algorithm used. While the source detection in this work is performed with `wavdetect`, the 2XMMi sources are detected with a sliding box algorithm. In addition, only the pn data was used in this work, while the 2XMMi catalog is constructed with a pn+MOS1/2 mosaic.

Overall, the present analysis supports the hypothesis that one or more nearby sources produce the observed PL component. However, only the angular resolution of *Chandra* offers the possibility to ascertain that the above claim is correct, by spatially and spectrally differentiating multiple sources. Archived *Chandra* data of NGC 6553 are analyzed and the results are presented in the following subsection.

Chandra Observation of NGC 6553

The following pertains solely to the confirmation of the candidate qLMXB and makes use of *Chandra*'s angular resolution to understand the core-source emission. A systematic detection and spectral analysis of all X-ray sources are not reported here.

Only one source is detected with `wavdetect` in the core of the GC, with a background subtracted count number of 46.8±6.9 cts. The position of the X-ray source CXOU 180916.48−255426.58 is consistent with the corrected *XMM* position of the candidate qLMXB. The difference between the *Chandra* and *XMM* positions, 1.″4, is within the accuracy of the *Chandra* systematic uncertainty (0.″6) and the *XMM* residual error after the correction (1.″1, see Section 4.2.4). Therefore, the *Chandra* source is consistent with being the same X-ray source as XMMU J180916−255425. Figure 4.4 shows the *Chandra* image of the GC core, with *XMM* contours and the two 2XMMi catalog sources.

A second possible source, with a 2.1σ significance (1.28±0.54 cts ks^{-1}), lies 17″ from the core candidate qLMXB, and close ($\sim$ 5″) to the faint 2XMMi source. An additional one, ($\sim$ 4″) away from the faint 2XMMi source and 19.″5 distant from the qLMXB candidate, has a significance of 1.6σ. Other faint possible sources, with low-significance (1.6σ, 1.7σ and 2.2σ) are located at distances 14.″8, 17.″7 and 22.″7, respectively (see Figure 4.4). The extended emission observed in Figure 4.3 could be explained by the presence of other sources in the GC core. Unfortunately, this short *Chandra* observation does not permit a confident detection of all the sources in the core. Furthermore, restricting counts to the 3–10 keV or the 2–10 keV energy ranges in `wavdetect` does not lead to the detection of any nearby source, suggesting that this excess of counts above 2 keV is not due to a single source, but due to multiple fainter sources. A longer high angular resolution observation of the central region of NGC 6553 would certainly shed light on the PL tail observed, and it will be of value to obtain deep *Chandra* observations of the core of this GC.

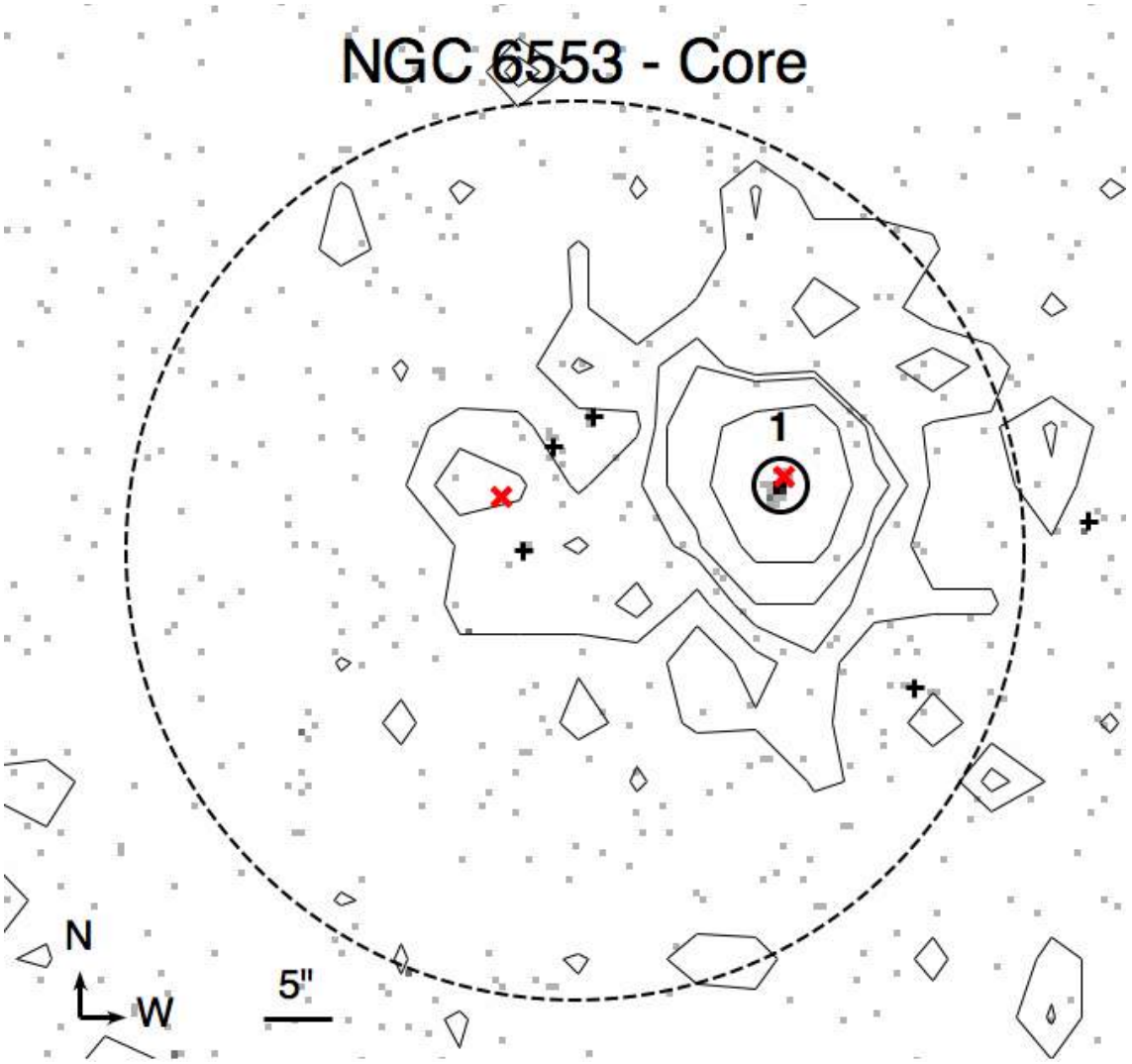

Figure 4.4 – This figure displays *XMM* contours plotted over the *Chandra* ACIS-S3 image. The small circle is the candidate quiescent low-mass X-ray binary detected with *Chandra*. The large dashed circle represents the 0.′55 core radius of the globular cluster. The red crosses '×' show the positions of the two 2XMMi sources. Finally, the five black '+' signs show the possible sources that have low significance in this short ~ 5 ks *Chandra* observations.

The PL component measured with *XMM* has an absorbed flux $F_{\rm X} = 4.9{\times}10^{-14}$ erg cm^{-2} s^{-1} in the 0.5–10 keV range with a photon index $\Gamma = 2.1$. Using *webPIMMs*[7], the expected *Chandra*/ACIS-S3 count rate is 4.7 cts ks^{-1} (0.5–8 keV), which corresponds to 23.5 counts on this short *Chandra* observation. However, the *Chandra* background subtracted count rate of an annulus ($r_{\rm in} = 10''$ and $r_{\rm out} = 30''$) centred around the core source is 7 ± 14 cts. The non-detection on the *Chandra* data of an excess of counts around the core source does not support the possibility that multiple diffuse sources are responsible for the high-energy contamination of the *XMM* spectrum of the candidate qLMXB. This could be explained if these surrounding sources experienced variations of their luminosity between the two observations, as could be expected from CVs.

Alternatively, the detected PL component could be intrinsic to the candidate qLMXB, but display some variability, as has been observed for other LMXBs. This possibility is investigated by extracting counts in the 2–10 keV range. With the pn camera, a count rate of $0.97{\pm}0.31$ cts ks^{-1} is detected, which corresponds to 0.36 cts ks^{-1} expected on the ACIS-S3 detector using *webPIMMs*, assuming a photon index $\Gamma = 2.1$. The detected count rate is $1.13{\pm}0.47$ cts ks^{-1} on the *Chandra* data in the 2–10 keV range. These count rates are consistent and therefore there is no observed variability of the high-energy component (> 2 keV), at the $< 2\sigma$ level.

The *Chandra* spectrum of the candidate qLMXB in the core of NGC 6553, i.e., image on-axis, is extracted from a $2\farcs5$ radius circular region to include more than 95% of the source energy[8]. For the purpose of the count rate calculation only, the background is extracted using a circular region of $25''$ radius around the source, excluding $5''$ around the qLMXB itself, ensuring that $> 99\%$ of the EEF is excluded.

Due to the small numbers of counts, a binning of 10 counts per bin is applied for the candidate qLMXB, which only guarantees marginally Gaussian uncertainty in each bin. The binned spectrum is used simultaneously with the three EPIC spectra

[7] Available via HEASARC, `http://heasarc.gsfc.nasa.gov/Tools/w3pimms.html`
[8] *Chandra* Observatory Proposer Guide, Chap. 6, v11.0, Jan 2009

Table 4.3 – Spectral analysis of the candidate quiescent low-mass X-ray binary in the core of NGC 6553

Instrument	Spectral Model	$R_{\rm NS}$ (km)	$kT_{\rm eff}$ (eV)	Γ	$F_{\rm X}$	PL Flux (%)	χ^2_ν/DOF ($p_{\rm null}$)
EPIC-pn (12″)	`nsatmos+PL`	$6.4^{+3.1}_{-1.1}$	131^{+28}_{-42}	$2.0^{+0.8}_{-3.6}$	$1.6^{+6.9}_{-1.2}$	23^{+48}_{-23}	1.37/10 (0.18)
EPIC-pn+MOS1/2	`nsatmos+PL`	$6.3^{+2.3}_{-0.8}$	136^{+21}_{-34}	$2.1^{+0.5}_{-0.8}$	$1.5^{+4.2}_{-0.7}$	33^{+32}_{-22}	0.90/54 (0.68)
EPIC+ACIS-S3 [a]	`nsatmos+PL`	$6.4^{+2.1}_{-0.8}$	134^{+21}_{-34}	$2.1^{+0.5}_{-0.7}$	$1.5^{+4.3}_{-0.7}$	32^{+35}_{-22}	1.02/58 (0.44)
ACIS-S3	`nsatmos`	$6.6^{+3.2}_{-1.3}$	134^{+35}_{-39}	–	$1.0^{+4.6}_{-0.3}$	–	cstat=146.98

Notes: In all the fits, the Galactic absorption, modeled with `wabs`, is represented by a fixed value of the hydrogen column density $N_{H,22} = 0.35$. Γ represents the photon index of the power-law (PL) model, when applicable. $F_{\rm X}$ is the total unabsorbed flux, in units of 10^{-13} erg cm^{-2} s^{-1}, in the 0.5–10 keV energy range, with 1σ-errors. `PL Flux (%)` represents the power-law contribution to the total flux (1σ-errors). DOF refers to the number of degrees of freedom.
[a] For the ACIS-S3 spectrum, the `powerlaw` normalization is set to zero. The multiplication constant, set free for ACIS-S3, is $c_{\rm ACIS} = 0.85^{+0.43}_{-0.26}$.

to evaluate the consistency of the spectra. All parameters are tied between the four spectra. Only the `powerlaw` normalization is set to zero for the *Chandra* observation. Also, a multiplicative constant is added to the model to quantify the variation between EPIC and ACIS-S3 spectra. The best-fit parameters of the four spectra are consistent with that of the EPIC spectra alone (see Table 4.3 and Figure 4.5). In addition, the multiplication constant, which was left free for the ACIS-S3 spectrum, is statistically consistent with unity, $c_{\rm ACIS} = 0.85^{+0.43}_{-0.26}$. This is evidence that, within the statistics of the observation, the *Chandra* spectrum is consistent with the three EPIC spectra.

Finally, a fit of the *Chandra* unbinned spectrum alone, using Cash-statistic (Cash, 1979), is also performed. The background, representing 2.5% of the extracted counts (1.2 counts out of 48 in the source extraction region) can be neglected. For comparison purposes with the *XMM* spectral fitting, the chosen model here is `nsatmos` alone (with fixed `wabs` absorption, distance and mass as before), which assumes that the PL component observed in the *XMM* spectrum is not intrinsic to the candidate qLMXB, i.e., that in the *XMM* spectrum, the PL tail is due to contaminating nearby sources. The best-fit value are $R_{\rm NS} = 6.6^{+3.2}_{-1.3}$ km ($M_{\rm NS} = 1.4\,M_\odot$) and $kT_{\rm eff} = 134^{+35}_{-39}$ eV, which are in remarkable agreement with the values obtained from the *XMM* observation. The 0.5–10 keV unabsorbed X-ray flux is $F_{\rm X} = 1.0\times10^{-13}$ erg cm^{-2} s^{-1}. These results are also listed in Table 4.3, for a convenient comparison with the *XMM* spectral fits.

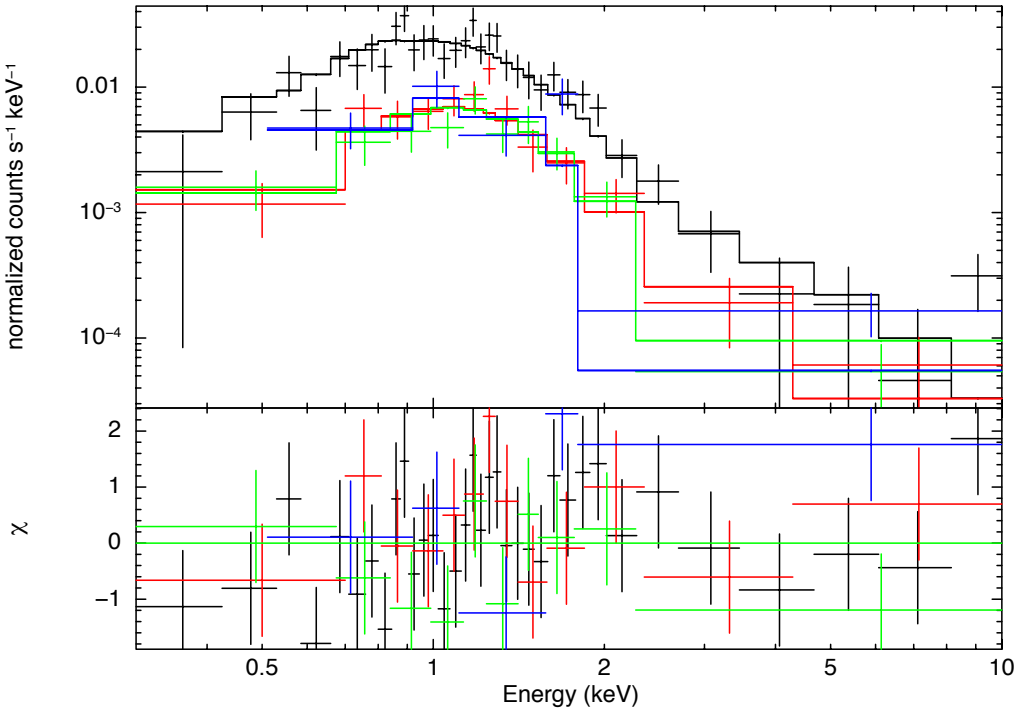

Figure 4.5 – This graph shows the *XMM*-pn (black), MOS1 (red), MOS2 (green) and ACIS-S3 (blue) spectra of the candidate quiescent low-mass X-ray binary of NGC 6553, XMMU J180916−255425, with the best-fit `nsatmos+powerlaw` model with `wabs` Galactic absorption $N_{H,22}$=0.35. The ACIS-S3 counts are grouped with a minimum of 10 cts per bin, due to the small number of counts. The fit statistic χ^2_ν/DOF ($p_{\rm null}$) = 1.02/58 (0.44) and the multiplicative constant applied to the ACIS-S3 spectra $c = 0.85^{+0.43}_{-0.26}$ (consistent with unity) are evidence that the *Chandra* spectrum is consistent with the *XMM* spectra, within the uncertainty. The bottom part displays the residuals between the data and the model.

4.4 Discussion and Conclusion

Using the *XMM* observation of NGC 6553, one candidate qLMXB in the GC has been spectrally identified. The best-fit `nsatmos` parameters found are $R_{\rm NS} = 6.3^{+2.3}_{-0.8}\,$km (for $M_{\rm NS} = 1.4\,M_\odot$) and $kT_{\rm eff} = 136^{+21}_{-34}\,$eV, and the best-fit PL photon index is $\Gamma = 2.1^{+0.5}_{-0.8}$. The low-S/N *Chandra* spectrum finds consistent best-fit values within the statistic permitted by the detected counts. The modest precision of the NS radius measurement obtained with these short exposures does not permit to place constraints on the dense matter EoS. Deeper *Chandra* exposures will provide the S/N necessary to confirm the classification and to produce useful uncertainty on the radius measurement for the determination of the dense matter EoS.

The number of candidates identified in NGC 6553 (only 1) is in agreement with that predicted from the relations $N_{\rm qNS} \sim 0.04 \times \Gamma_{\rm GC} + 0.2$ (Gendre et al., 2003b) and $N = 0.993 \times \Gamma_{\rm GC} - 0.046$ (Heinke et al., 2003d), where the authors used different normalizations for $\Gamma_{\rm GC}$; the encounter rate of the GC is defined by $\Gamma_{\rm GC} \propto \rho_{GC}^{1.5} r_{\rm c}^2$ (Verbunt, 2003). In this last equation, ρ_{GC} is the central luminosity density (in $L_\odot\,{\rm pc}^{-3}$) and $r_{\rm c}$ is the core radius (in pc, not angular distance). Quantitatively, using the same respective normalizations, the number of expected qLMXBs in NGC 6553, given $\rho_{GC,\rm NGC\ 6553} = 3.84\ L_\odot\,{\rm pc}^{-3}$ (Harris, 1996), are 0.43 and 0.34 using the two relations cited above, respectively. Assuming Poisson statistics, the probability of finding one qLMXB when 0.43 (0.34) are expected is 28% (24%). Therefore, the number of qLMXB found in the GC is not in disagreement with these two empirical predictions.

The total unabsorbed *XMM* flux of the candidate qLMXB, $F_{\rm X} = 1.5^{+4.3}_{-0.7} \times 10^{-13}\,{\rm erg\ cm^{-2}\ s^{-1}}$, includes a PL component with a 33^{+35}_{-22}% contribution to the flux. If intrinsic to the source, this PL component has one of the strongest contribution to the total flux ever observed for a qLMXB in a GC (others are in NGC 6440 and 47Tuc, Heinke et al., 2003d, 2005, respectively). However, there is evidence for the presence of nearby contaminating sources. This is tentatively supported by a short archived *Chandra*

observation, but the low-significance detection of the nearby sources does not confirm with certainty the existence of contamination. Only a longer *Chandra* observation would confirm the spectral classification of the bright core source and confirm the detection of the faint neighbouring core sources.

The candidate qLMXB did not display X-ray variability on the time scale of the observation. Specifically, there was no evidence that the *XMM* integrated light curve is significantly different from a linear distribution of counts. Regarding the long time scale variability, there is no significant change of flux between the *XMM* and *Chandra* observations. Search in archived *ROSAT* observation did not reveal any source at the position of XMMU J180916−255425 on the PSPC survey, and no HRI observation at the centre of the GC was performed.

To conclude, the candidate in the core of NGC 6553, with $L_{\rm X,th} = 4.2{\times}10^{32}\,{\rm erg\ s^{-1}}$ ($d = 6\,{\rm kpc}$), adds to the small list of known GC qLMXB. However, only a deeper observation with *Chandra* will allow confirmation with certitude of the spectral classification of the source, and to permit providing and R_∞ measurement capable of constraining the dense matter EoS. Higher S/N spectra, such as the one of the qLMXB located in NGC 6397, allow for more precise measurement of R_∞ or $R_{\rm NS}$, as shown in Chapter 5.

5

The Radius of the Neutron Star in NGC 6397

This chapter reports the spectral and timing analyses of the qLMXB U24 observed during five archived *Chandra*/ACIS exposures of the nearby GC NGC 6397, for a total of 350 ks. The X-ray flux and the parameters of the hydrogen atmosphere spectral model are consistent with those previously published for this source. In addition, no evidence of intensity variability is detected at various time scales, as expected for this class of X-ray sources. The improved NS physical radius measurement is reported here, with statistical accuracy of the order of ∼10%. This makes U24 the third most precisely measured NS radius among qLMXBs, after those in ω Cen, and in M13. The confidence regions in $M_{\rm NS}$–$R_{\rm NS}$ space for this NS are also provided as well as the measured best-fit projected radius R_∞, as seen by an observer at infinity. Finally, the measured effective NS surface temperature is used to estimate the NS core temperature.

The chapter was published as: S. Guillot, R. E. Rutledge, and E. F. Brown. *Neutron Star Radius Measurement with the Quiescent Low-mass X-ray Binary U24 in NGC 6397*. ApJ, 732:88, May 2011. The introduction of the original article has been edited to remove redundant information provided in Chapter 2. The last paragraph in the conclusion of this chapter (Section 5.5) did not appear in the original publication and was added for this thesis, to serve as a transition.

5.1 Introduction

Obtaining precise constraints on the dense matter EoS is the observational motivation for measuring the radii of NSs, requiring $\sim 5\%$ accuracy on R_∞ to be useful for this purpose (Lattimer and Prakash, 2004; Steiner et al., 2010). Most qLMXBs in GCs have low-S/N spectra, and therefore, have rather large uncertainties on their R_∞ measurements ($\sim$ 15% or more), precluding their use for EoS constraints. So far, only a few qLMXBs (in ω Cen, Gendre et al. 2003a, in M13, Gendre et al. 2003b, and X7 in 47 Tuc, Heinke et al. 2006a) have spectra with S/N high enough to provide useful constraints on the dense matter EoS[1] (Webb and Barret, 2007; Steiner et al., 2010).

The close proximity of the GC NGC 6397 ($d \approx 2.5$ kpc, Harris 1996; Hansen et al. 2007; Strickler et al. 2009), the moderately low Galactic absorption[2] ($N_{H,22} = 0.14$) in its direction makes it a useful target for the spectral identification of qLMXBs. The discovery observation of the qLMXB U24[3] in NGC 6397 provided modest constraints on the NS projected radius: $R_\infty = 4.9^{+14}_{-1}$ km (Grindlay et al., 2001b, Gr01 hereafter). The proximity of U24 to the GC core requires the use of the *Chandra X-ray Observatory*'s angular resolution to positionally and spectrally separate the qLMXB from other sources in the crowded GC core. U24 lies at $d_c = 6.8\, r_c \approx 20''$ from the GC centre (core radius $r_c = 0.05'$ and half-mass radius $r_{HM} = 2.33'$, NGC 6397 is a core-collapse cluster). The reported effective temperature of U24 was $kT_{eff} = 57$–92 eV (90% confidence interval, Gr01).

This chapter presents the spectral and timing analyses of five archived deep *Chandra*-ACIS observations of U24, located in GC NGC 6397. These long exposures provide the high-S/N data necessary to confirm the qLMXB classification of U24 by obtaining precise R_{NS} estimation. The lack of variability also supports this classi-

[1] Footnote not present in original article, and added in this thesis: The R_∞ measurements of the NS in ω Cen and M13 have analysis flaws leading to underestimations of the error bars. This is further discussed in Section 6.3.

[2] From http://cxc.harvard.edu/toolkit/colden.jsp using the NRAO data (Dickey and Lockman, 1990).

[3] The source name U24 was used in the discovery article (Gr01) and will be used here.

Table 5.1 – *Chandra* Observations of Globular Cluster NGC 6397.

Obs. ID	Starting Time (TT)[a]	Exposure Time (ks)	Detector[b]	Telemetry Mode
79	2000 July 31 15:31:33	48.34	ACIS-I3 (FI)	FAINT
2668	2002 May 13 19:17:40	28.10	ACIS-S3 (BI)	FAINT
2669	2002 May 15 18:53:27	26.66	ACIS-S3 (BI)	FAINT
7460	2007 July 16 06:21:36	149.61	ACIS-S3 (BI)	VFAINT
7461	2007 June 22 21:44:15	87.87	ACIS-S3 (BI)	VFAINT

Notes: All observations were performed in full-frame mode).
[a] TT refers to terrestrial time.
[b] FI and BI refer to front and back-illuminated detectors, respectively.

fication. The organization of this chapter is as follows. Section 5.2 describes the data reduction and the analyses. Section 5.3 presents the results of the analyses. Section 5.4 provides a discussion of the results and Section 5.5 is a short conclusion.

5.2 Data Reduction and Analysis

5.2.1 Observations, Source Detection, and Count Extraction

One archived *Chandra*/ACIS-I and four archived *Chandra*/ACIS-S observations of NGC 6397 (Table 5.1) are analyzed here. The source detection and the data analysis are performed using the CIAO v4.1.1 package (Fruscione et al., 2006). The event files (level=1) are re-processed with the latest calibration files from CALDB v4.1 (Graessle et al., 2007, with the latest effective area maps, quantum efficiency maps, and gain maps), as recommended in the CIAO Analysis Thread "*Reprocessing Data to Create a New Level=2 Event File*" to include the up-to-date charge transfer inefficiency corrections.

The re-processed event files are analyzed including counts in the 0.5–8.0 keV energy range. The full-chip light curves do not show evidence of background flares in any of the five observations, allowing use of the full exposure time of each observation. The low flux of the source of interest, U24, allows neglecting pile-up; the count rate of ~ 0.06 photons per frame corresponds to a pile-up fraction of less than 2% [4].

[4] *Chandra* Observatory Proposer Guide v12.0, Figure 6.18, December 2009

For each observation (ObsID), the source detection is performed with the CIAO `wavdetect` algorithm. An exposure map is created using the task `mkexpmap` prior to the source detection. The `wavdetect` exposure threshold *expthresh* is set to 0.1 and the wavelet detection scales are set to *scales = "1.0 2.0 4.0 8.0"*. Thirty-five sources are detected ($\sigma > 3$) on the ObsID 2668, 37 sources on ObsID 2669, 66 sources on ObsID 7460, 48 on ObsID 7461, and 37 on the ACIS-I observation ObsID 79.

This chapter is solely focused on radius measurement and timing analysis on the qLMXB U24. While the source detection is performed over the whole ACIS chip, the following analysis pertains only to the source U24.

Counts are extracted with the CIAO script `psextract` around the source position in a circular region of radius $3''$, which ensures that 98% of the EEF at 1 keV is included[5]. The closest detected source, located at $10.6''$ distance from U24, has 21.6 counts (background subtracted) within $1.5''$. It contributes to $\ll 0.04$ contamination counts within the extraction radius of U24 (on the longest observation). The background is extracted from an annulus centred at the qLMXB position with inner radius $5''$, and outer radius $30''$. Other detected sources within the background annulus are excluded with a $5''$ radius region, which eliminate 99.8% of source counts in the background region. For the deepest observation (ObsID 7460), 15 counts from other sources are within the extracted background (which contains 6187 counts). In other words, these constraints ensure that $\lesssim 0.25\%$ of the background counts are due to other sources. Finally, the extraction radius (containing 98% of the ECF) does not require application of a correction to the flux.

Following the CIAO Science Thread *"Creating ACIS RMFs with mkacisrmf"*, the response matrices files (RMFs) are recalculated prior to the spectral analysis since the RMFs obtained from `psextract` are not suited for ACIS observations with focal plane temperature of –120°C (the usual `mkrmf` command does not use the latest calibration available in the case of –120°C ACIS imaging data). In addition, the

[5] *Chandra* Observatory Proposer Guide v12.0, Figure 6.7, December 2009

ancillary response files (ARFs) are also recalculated using the energy grid of the newly obtained RMFs. Overall, the extracted spectra, together with the RMFs and ARFs, are used for the spectral analysis. In those spectra, the effect of background counts can be ignored. Indeed, in the worst case (for ObsID 7460), the number of expected background events accounts for 2.4% of the total number of counts in the extracted region (78.0 background counts out of a total of 3188 counts), so that the background is neglected for the spectral analysis.

5.2.2 Spectral Analysis

For each of the five observations, two spectral files are created, one with unbinned events (for fitting with the Cash-statistics, Cash 1979) and one with binning (for fitting with the χ^2-statistics). For the latter, the bin width in the 0.5–1.5 keV energy range matches the energy resolution of the ACIS-S3 chip, i.e., $\sim$0.15 keV. Above 1.5 keV, four wider bins (0.3 keV, 0.6 keV, and two 3 keV wide spectral bins) are created. In some cases of low count statistics, the last 2 or 3 bins are grouped together to maintain a minimum of 20 counts per bin. The main criterion for the creation of the spectral bins is the energy resolution of the detector, but the 20 counts minimum is imposed to ensure approximate Gaussian uncertainty in each bin. Such a binning avoids an artificially small reduced-χ^2, and conserves the validity of χ^2-statistics.

Spectral fitting is performed with the software *XSPEC* v12.5.1 using the publicly available model of NS H-atmosphere `nsatmos` (McClintock et al., 2004; Heinke et al., 2006a). The model assumes non-magnetic NSs and has been computed for a range of surface gravity $g = (0.1-10)\times10^{14}\,\mathrm{cm\,s^{-2}}$. For the normalization parameter, `nsatmos` uses the emitting fraction of the NS surface. It is kept fixed to unity in this work; in other words, the whole NS surface emits. The distance parameter is held fixed as well at the value of NGC 6397, $d = 2.5$ kpc (Hansen et al., 2007; Strickler et al., 2009). Note that in Chapter 6, for the simultaneous study of qLMXBs, a more complete litterature search of all reported distances to the targeted GCs led us to prefer geometric distance

measurements as they are less affected by systematic uncertainties than photometric distance measurements (see Section 6.2.7). As a result, the distance to NGC 6397 used in Chapter 6 was $d = 2.02 \pm 0.18\,\mathrm{kpc}$, compared to $d = 2.5\,\mathrm{kpc}$ used in the present chapter.

The NS mass is assumed to be $1.4\,M_{\odot}$. Finally, the Galactic absorption is taken into account using the `phabs` multiplicative model, with N_{H}, the hydrogen column density parameter, set to $N_{H,22} = 0.14$. The errors on the best-fit parameters (R_{NS}, kT_{eff}) are calculated using the command `error` in *XSPEC* with 90% confidence or using the command `steppar`. Confidence contours in mass–radius space are obtained with the `steppar` command with both the mass and the radius as free parameters. The results of the spectral analysis are presented in Section 5.3.2.

5.2.3 Variability Analysis

For each of the five observations, two analyses are performed to search for source variability on time scales shorter than the duration of the observations, and one analysis for time scales spanning the time between the first and last observations.

Power Density Spectrum (PDS). The data from each observation were binned into a discrete light curve, with time bin size equal to the time resolution used in the observation ($\Delta T = 3.24104\,\mathrm{sec}$). A standard fast-Fourier transform (FFT) of the discrete data into frequency space was produced (Press et al., 1995), using an open-source FFT algorithm (Frigo and Johnson, 1998). This produced a Fourier transform of the data, covering the frequency range $1/T - 0.15427\,\mathrm{Hz}$, where T is the duration of the observation, and $0.15427\,\mathrm{Hz}$ is the Nyquist frequency, with discrete frequency resolution $1/T$, and a total of $N/2$ frequency bins, where $N = T/\Delta T$ is the number of time bins in the light curve. The resulting Fourier transform was then converted into a PDS, where the power P_j in each frequency bin j is $P_j = a_j^2 + b_j^2$, where a_j and b_j are the real and imaginary parts of the Fourier component associated with a frequency $f_j = j/T$, producing a PDS. The data were then normalized according to a standard prescription for analyses (Leahy et al., 1983).

Short-Time scale (<1 day) Variability. Short-term variability in each ObsID is assessed by visual inspection of the five sources' light curves. In addition, a Kolmogorov–Smirnov (K-S) test (Press et al., 1995) is performed to quantify the consistency of the temporal distribution of counts in each observation with a constant count rate. More specifically, the integrated-count light curve is compared to a linear distribution using a K-S test. A low K-S probability would indicate that the integrated light curve is significantly different from a linear distribution, demonstrating the presence of variability on the time scale of the observation.

Long Time scale (∼months-years) flux variability. Long-term variability is investigated to determine if the flux remained constant over the course of the five observations, between 2000 and 2007. This is performed by adding a multiplicative constant parameter to the spectral model, and by fitting the five spectra simultaneously. The constant is kept fixed at a value $c = 1$ for one spectrum (ObsID 79) and as a free and untied parameter for the remaining four spectra while the remaining spectral parameters ($N_{\rm H}$, $R_{\rm NS}$, $kT_{\rm eff}$) are assumed to be the same across all observations. Best-fit c values statistically consistent with unity would demonstrate that the source flux remained constant on the time scale of the five observations.

5.3 Results

5.3.1 Positional Analysis

The position of the X-ray source reported in the discovery observation (ObsID 79) is R.A.=$17^{\rm h}40^{\rm m}41\overset{\rm s}{.}421$ and decl. = $-53°40'04\overset{''}{.}73$ (Gr01). The authors corrected for the systematic *Chandra* uncertainty in the pointing ($0\overset{''}{.}6$) by cross-identifying CVs on *Chandra* and *HST* observations. The positional uncertainty on the source is subarcseconds and consists of the residual error from the correction and the statistical uncertainty from the detection algorithm.

For comparison, the source detection in all five observations presented here led to the positions listed in Table 5.2. The position of U24 is consistent with that reported

Table 5.2 – Position of U24 in *Chandra* Observations of NGC 6397 .

Observation ID	Right Ascension (J2000)	$\Delta_{\text{R.A.}}$ [a] ($''$)	Declination (J2000)	$\Delta_{\text{Decl.}}$ [a] ($''$)	Detection Significance	Reference
79	$17^{\text{h}}40^{\text{m}}41\overset{\text{s}}{.}421$	0.02[b]	$-53°40'04\overset{''}{.}73$	0.02[b]	–	Gr01
79	$17^{\text{h}}40^{\text{m}}41\overset{\text{s}}{.}459$	0.6	$-53°40'04\overset{''}{.}47$	0.6	128σ	This work
2668	$17^{\text{h}}40^{\text{m}}41\overset{\text{s}}{.}489$	0.6	$-53°40'04\overset{''}{.}38$	0.6	152σ	This work
2669	$17^{\text{h}}40^{\text{m}}41\overset{\text{s}}{.}485$	0.6	$-53°40'04\overset{''}{.}53$	0.6	149σ	This work
7460	$17^{\text{h}}40^{\text{m}}41\overset{\text{s}}{.}486$	0.6	$-53°40'04\overset{''}{.}60$	0.6	302σ	This work
7461	$17^{\text{h}}40^{\text{m}}41\overset{\text{s}}{.}488$	0.6	$-53°40'04\overset{''}{.}54$	0.6	228σ	This work

NOTES: [a] This uncertainties on the position are dominated by the *Chandra* pointing systematic uncertainty.
[b] The positions reported previously in Gr01 (Grindlay et al., 2001b) have been corrected for the *Chandra* systematic uncertainty in the pointing (see details in Section 5.3.1).

previously, within the $0\overset{''}{.}6$ *Chandra* systematic uncertainty. No correction for the systematic uncertainty is performed here since the identification of U24 is free of source confusion and since this chapter focuses on the spectral analysis.

5.3.2 Spectral Analysis

The spectral analysis is performed using the Cash-statistics on the unbinned data (neglecting the background) and using χ^2-statistics on the grouped data. Results are presented in Table 5.3, listing the best-fit parameters for Cash and χ^2-statistics, freezing and thawing N_{H}. All reported errors are 90% confidence. The χ^2-statistics NHP confirms the viability of the fitted model (when $p_{\text{null}} > 0.01$) while the Cash-statistics assumes that the model describes the data. Nonetheless, the use of Cash-statistics provides smaller uncertainties on the best-fit parameters, specifically for the NS radius measurements.

A simultaneous fit is also performed using all five spectra, therefore increasing the count statistics and providing better constraints on the best-fit parameters (Figure 5.1). Prior to that, the source long-term variability is inspected, as described in Section 5.2.3. The best-fit values (with Cash-statistic) for the multiplicative constants described in Section 5.2.3 are $c = 1.02^{+0.09}_{-0.10}$, $c = 1.04^{+0.09}_{-0.10}$, $c = 0.92^{+0.06}_{-0.07}$, and $c = 0.95^{+0.07}_{-0.08}$, for the observations ObsID 2668, ObsID 2669, ObsID 7460, and ObsID 7461, respectively, and $c = 1$ (fixed) for ObsID 79. All best-fit values are statistically

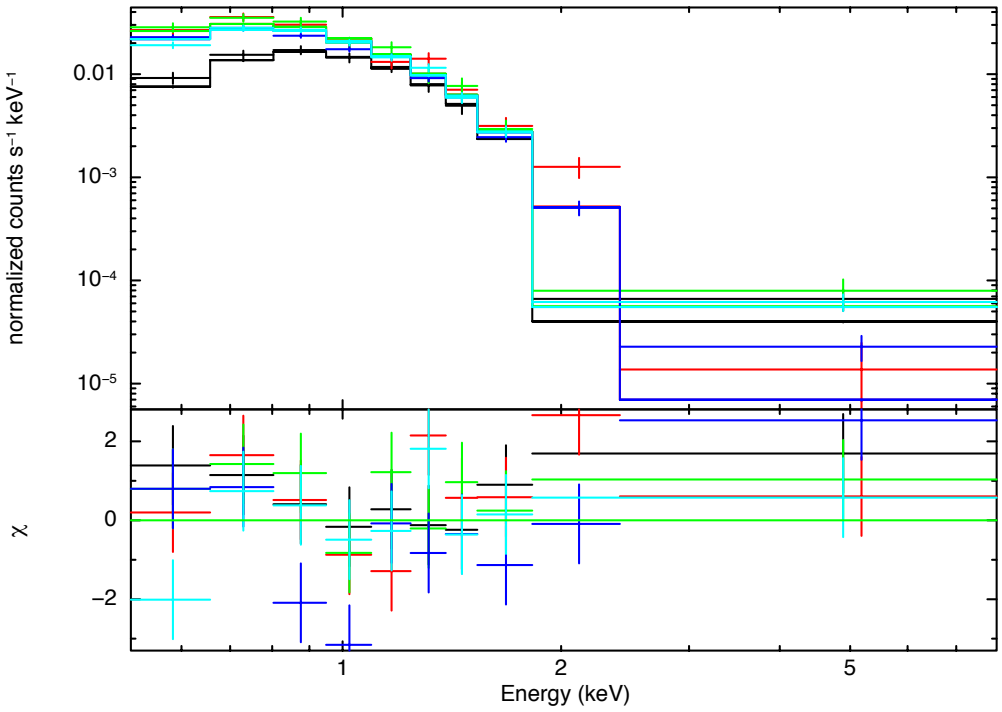

Figure 5.1 – This figure is the folded spectra of all five *Chandra*-ACIS observations of U24 in NGC 6397, in the 0.5–8.0 keV energy range. Each colour corresponds to the spectra of each observations: ObsID 79 in black, ObsID 2668 in red, ObsID 2669 in green, ObsID 7460 in blue, ObsID 7461 in cyan blue. The solid lines are the best-fitting model of an neutron star hydrogen atmosphere model: `nsatmos`, with $N_{H,22} = 0.14$ and $M_{\rm NS} = 1.4\,M_\odot$ kept frozen. The spectral binning was performed in accordance with the *Chandra* energy resolution (see Section 5.2.2). The fit is statistically acceptable with χ^2_ν/DOF ($p_{\rm null}$) = 1.49/45 (0.02). The residuals, shown in the lower part, indicate evidence of a count deficiency between 0.8 keV and 1.2 keV (see Figure 5.2 and Section 5.3.2), as well as an apparent excess of counts at large energy, above 2.5 keV, which is fit with a power-law component with $\Gamma = 1$ to estimate the contribution to the total flux (see Section 5.3.2).

consistent with unity (within 1.5σ), indicating that the source flux did not vary on long-term time scale. This allows for simultaneous spectral fitting with the constant multiplier fixed at the value $c = 1$ for all five spectra.

The upper limit of a PL contribution to the total flux is also estimated, for the individual spectra and the simultaneous fit Table 5.3. To do so, a PL component with fixed photon index $\Gamma = 1$ is added to the NS atmosphere model and the flux of this component using the upper limit of the PL normalization parameter is measured. It is found that the PL contribution accounts for $\leq 3.7\%$ of the total flux (90% confidence upper limit), for the simultaneous fits.

There is some evidence for a count deficiency between 0.8 and 1.2 keV on ObsID 7460 given the assumed spectrum and instrument calibration (see Figure 5.2). This apparent dip in the spectrum is parametrized with a `notch` component. The best-fit `notch` central energy is $E = 0.96^{+0.03}_{-0.02}$ keV, and the best-fit width is $W = 42 \pm 17$ eV. The added component improves the statistics, χ^2_ν/DOF ($p_{\rm null}$) = 1.35/6 (0.23), without altering the best fit NS temperature and radius. The statistical significance of this deficiency is investigated. Using the method described in a previous work (Rutledge and Sako, 2003), the probability of observing such a deviation from a continuum model is estimated. First, the observed spectrum is convolved with the energy redistribution of the ACIS-S detector. Using a MC approach, it is shown that the convolved spectrum does not exceed the 99% confidence limits envelope obtained from 10,000 simulated spectra (Figure 5.3). They were created using the best-fit `nsatmos` model ($R_{\rm NS} = 8.9$ km, $kT_{\rm eff} = 80$ eV, $M_{\rm NS} = 1.4$, $d = 2.5$ kpc, and $N_{H,22} = 0.14$, see Table 5.3). The maximum deviation corresponds to a 98.2% confidence, not a sufficient evidence to claim the detection of an absorption line, but which should be investigated in more details with higher S/N observations.

For completeness, the results of spectral fits with other models are provided. Using an absorbed simple blackbody model, the fit to the spectra (all five binned spectra) is not statistically acceptable: χ^2_ν/DOF ($p_{\rm null}$) = 3.51/45 (2×10^{-14}) with $N_{H,22}$=0.14

Table 5.3 – Spectral Parameters of U24 in *Chandra* Observations of NGC 6397 with the `nsatmos` model.

Obs. ID	$N_{H,22}$	$R_{\rm NS}$ (km)	$kT_{\rm eff}$ (eV)	$F_{\rm X,-13}$	Statistics χ^2 or Cash	PL Contribution
79	(0.14)	$10.7^{+3.3}_{-2.3}$	73^{+10}_{-10}	$1.50^{+0.14}_{-0.22}$	Cash: 256.7 (100%)	–
	$0.09^{+0.03}_{-0.03}$	$6.8^{+5.1}_{-1.8}$	97^{+38}_{-32}	1.27	Cash: 254.2 (0%)	–
	(0.14)	$10.1^{+3.4}_{-5.1p}$	75^{+49}_{-11}	$1.49^{+0.11}_{-0.22}$	χ^2_ν/DOF ($p_{\rm null}$) = 0.76/7 (0.62)	$\leq 8.8\%$
	$0.10^{+0.05}_{-0.03}$	$7.2^{+3.2}_{-2.2p}$	93^{+42}_{-28}	1.30	χ^2_ν/DOF ($p_{\rm null}$) = 0.60/6 (0.73)	–
2668	(0.14)	$7.2^{+2.4}_{-1.8}$	95^{+28}_{-19}	$1.47^{+20}_{-1.34}$	Cash: 213.3 (100%)	–
	$0.13^{+0.03}_{-0.02}$	$7.1^{+2.8}_{-1.6}$	96^{+26}_{-21}	1.44	Cash: 213.1 (0%)	–
	(0.14)	$7.8^{+3.4}_{-2.8}$	88^{+43}_{-19}	$1.44^{+1.20}_{-5.81}$	χ^2_ν/DOF ($p_{\rm null}$) = 1.81/9 (0.61)	$\leq 3.9\%$
	$0.13^{+0.04}_{-0.03}$	$7.2^{+4.6}_{-2.2}$	94^{+41}_{-27}	1.38	χ^2_ν/DOF ($p_{\rm null}$) = 1.97/8 (0.46)	–
2669	(0.14)	$10.0^{+2.6}_{-5.0p}$	76^{+37}_{-9}	$1.52^{+0.06}_{-0.26}$	Cash: 159.0 (98%)	–
	$0.11^{+0.05}_{-0.02}$	$7.0^{+5.4}_{-2.0p}$	96^{+41}_{-32}	1.36	Cash: 157.7 (0%)	–
	(0.14)	$9.9^{+3.0}_{-4.9p}$	77^{+51}_{-10}	$1.51^{+0.05}_{-0.40}$	χ^2_ν/DOF ($p_{\rm null}$) = 0.63/8 (0.74)	$\leq 4.2\%$
	$0.12^{+0.07}_{-0.03}$	$7.2^{+8.8}_{-2.2p}$	93^{+44}_{-31}	1.37	χ^2_ν/DOF ($p_{\rm null}$) = 0.66/7 (0.70)	–
7460	(0.14)	$9.9^{+1.2}_{-1.2}$	75^{+6}_{-5}	$1.35^{+0.04}_{-0.09}$	Cash: 367.0 (100%)	–
	$0.11^{+0.01}_{-0.01}$	$6.9^{+1.4}_{-0.9}$	94^{+13}_{-12}	1.18	Cash: 355.1 (0%)	–
	(0.14)	$10.1^{+1.5}_{-1.5}$	74^{+7}_{-6}	$1.35^{+0.54}_{-0.17}$	χ^2_ν/DOF ($p_{\rm null}$) = 2.32/8 (0.02)	$\leq 4.7\%$
	$0.11^{+0.02}_{-0.01}$	$7.0^{+1.9}_{-1.5}$	93^{+25}_{-21}	1.19	χ^2_ν/DOF ($p_{\rm null}$) = 2.14/7 (0.04)	–
7461	(0.14)	$6.7^{+1.9}_{-1.0}$	100^{+19}_{-17}	$1.37^{+5.29}_{-1.19}$	Cash: 291.0 (0%)	–
	$0.14^{+0.02}_{-0.02}$	$6.6^{+2.6}_{-1.1}$	101^{+20}_{-24}	1.38	Cash: 291.0 (0%)	–
	(0.14)	$6.1^{+3.4}_{-0.9}$	104^{+24}_{-31}	$1.37^{+1.33}_{-1.07}$	χ^2_ν/DOF ($p_{\rm null}$) = 0.97/7 (0.45)	$\leq 3.3\%$
	$0.17^{+0.06}_{-0.04}$	$10.7^{+5.3}_{-5.7p}$	74^{+52}_{-14}	1.57	χ^2_ν/DOF ($p_{\rm null}$) = 1.03/6 (0.41)	–
All 5	(0.14)	$8.9^{+0.9}_{-0.6}$	80^{+4}_{-5}	$1.39^{+0.02}_{-0.06}$	Cash: 1289.9 (100%)	–
	$0.12^{+0.01}_{-0.01}$	$6.9^{+1.0}_{-0.7}$	95^{+9}_{-10}	1.28	Cash: 1276.1 (69.2%)	–
	(0.14)	$9.3^{+1.0}_{-1.0}$	78^{+5}_{-4}	$1.39^{+0.04}_{-0.06}$	χ^2_ν/DOF ($p_{\rm null}$) = 1.49/45 (0.02)	$\leq 3.7\%$
	$0.12^{+0.02}_{-0.01}$	$7.2^{+1.9}_{-1.5}$	92^{+22}_{-14}	1.29	χ^2_ν/DOF ($p_{\rm null}$) = 1.16/44 (0.03)	–

Notes: The model used for all spectral fits presented here is the neutron star H-atmosphere model `nsatmos`, with the distance to the source fixed at the value $d = 2.5\,$kpc and the mass of the neutron star fixed at $M_{\rm NS} = 1.4\,M_\odot$. $N_{H,22}$ is the Galactic absorption $N_{\rm H}$ in units of $10^{22}\,$atoms cm^{-2}. Values in parentheses are held fixed for the spectral fits and quoted uncertainty are 90% confidence . $F_{\rm X}$ is the unabsorbed flux in units of $10^{-13}\,$erg cm^{-2} s^{-1} in the 0.5–10 keV range. The uncertainties on the fluxes were only calculated for the fixed-$N_{\rm H}$ fits. For ObsID 7460, the χ^2 value greater than 2 prevents *XSPEC* to directly estimate the error region. It was obtained using the command `steppar`. "PL contribution" refers to the upper limit of a power-law component contribution to the total flux (see Section 5.3.2). The percent in parenthesis following the Cash-statistic value indicates the goodness-of-fit. The best fit parameters and the statistics information provided do not include the power-law component. DOF refers to the number of degrees of freedom.

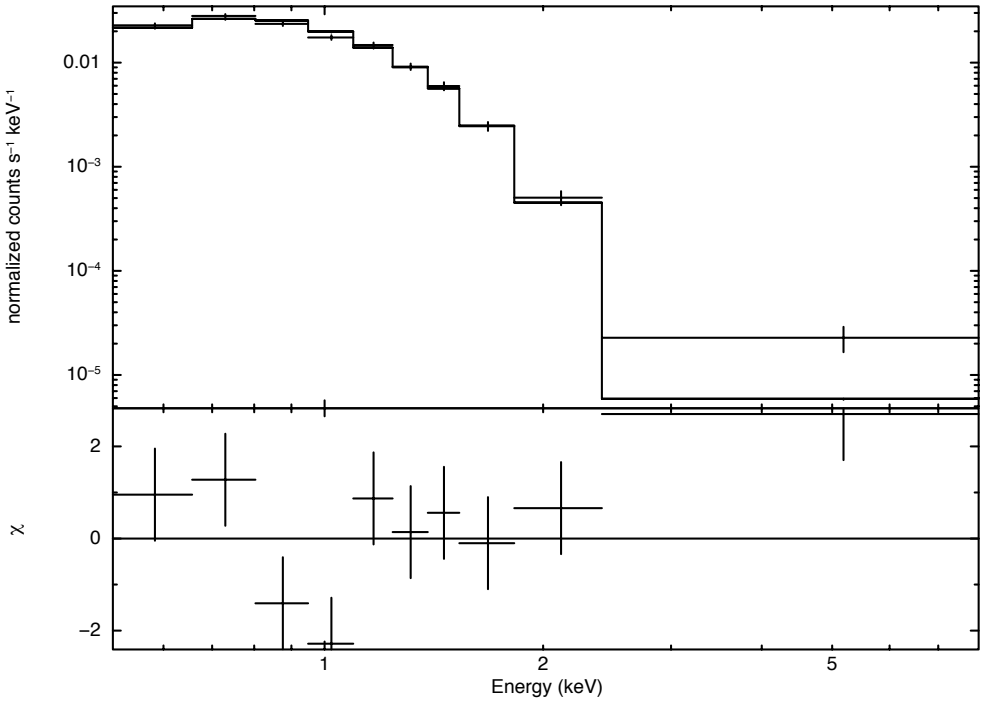

Figure 5.2 – This figure shows the folded spectrum of the ACIS observation 7460. As for Figure 5.1, the solid line shows the best-fitting `nsatmos` model. The count deficiency observed between 0.8 keV and 1.2 keV does not exceed the 99% limit from the Monte Carlo simulations of 10,000 spectra. In other words, the detection is not significant enough to claim the presence of an absorption line (see Section 5.3.2).

fixed, and χ^2_ν/DOF ($p_{\rm null}$) = 1.631/44 ($5{\times}10^{-3}$) with $N_{\rm H}$ allowed to vary. A thermal bremsstrahlung model is also fit to the spectra, leading to a statistically acceptable fit (χ^2_ν/DOF ($p_{\rm null}$) = 1.45/45 (0.03)) with best-fit parameter $kT = 391 \pm 10\,{\rm eV}$.

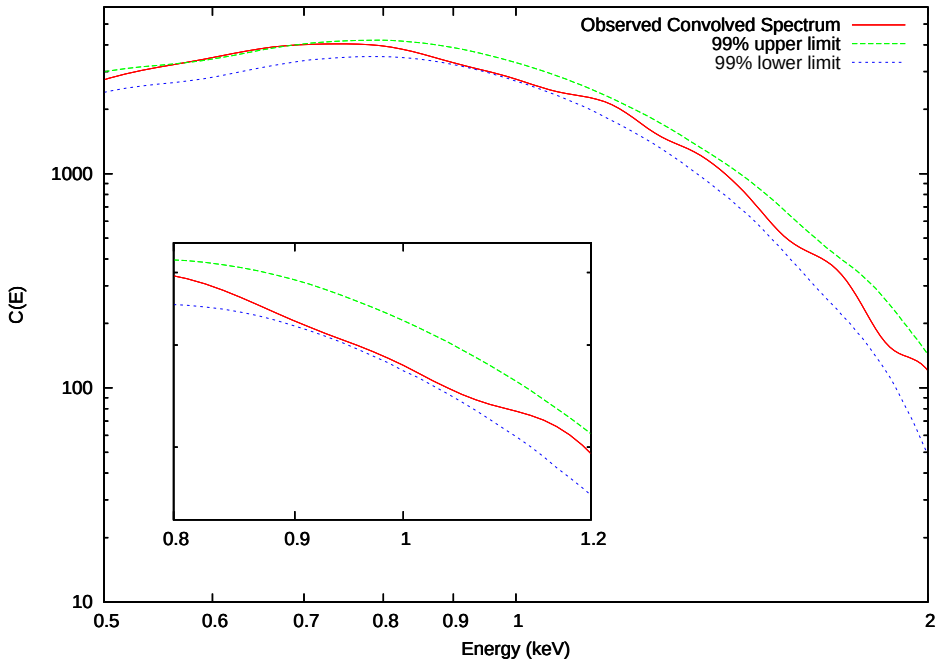

Figure 5.3 – This graph shows the results of the Monte Carlo simulations analyzing the count deficiency observed in Figure 5.2, in the energy range 0.8–1.2 keV. The observed spectrum (solid line) convolved with the *Chandra*-ACIS energy redistribution, $C(E)$, is shown within the 99% upper- and lower-limit envelopes (dashed and dotted lines, respectively) obtained from Monte Carlo simulations (see Section 5.3.2).

5.3.3 Variability Analyses

There is no evidence of broadband variability as a function of frequency in the PDS. For broadband variability, uncertainties were assigned to each frequency bin equal to the square root of the theoretical variance in the power, appropriate to the assumed normalization (Leahy et al., 1983), and derived 90% confidence (2σ) upper-limits on the root-mean-square (rms) variability. The data were then rebinned logarithmically and the resulting PDS were fit with a model of a constant power[6], plus a PL compo-

[6]The constant accounts for the expected Poisson noise power in the PDS, which is approximately 2 in the PDS normalization used; however, the Poisson level for each of the PDS is suppressed, to a

nent in which the power scales $P_j \propto f_j^{-\Gamma}$, and the PL photon index was held fixed at $\Gamma = 1$. This model was fit to the data using a Levenberg–Marquardt χ^2 minimization technique (Press et al., 1995), to find the best-fit model parameters. The resulting 90% confidence upper limits on the broadband variability, in a frequency range 0.0001–0.10 Hz (used for each observation, to ease comparison of limits, although the longer observations are sensitive to variability at frequencies below this range) and across the full *Chandra*/ACIS energy range (0.5–8.0 keV) were : $< 12\%$ (ObsID 79), χ^2_ν=0.63 (26 DOF); $< 19\%$ (ObsID 2668), χ^2_ν=1.5 (27 DOF);$< 11\%$ (ObsID 2669), χ^2_ν=1.32 (26 DOF); <6.4% (ObsID 7460), χ^2_ν=0.98 (15 DOF); <8.6% (ObsID 7461), χ^2_ν=0.98 (9 DOF). There is no evidence of periodic variability. For ObsIDs 79, 2668, 2669, 7460, and 7461 respectively, the maximum (normalized) powers are $P_{\rm max}$ =21.8, 17.0, 15.3, 17.7, and 23.7 which, with a number of frequency bins of 7526, 4383, 4154, 23072, and 13812, correspond to respective probabilities of chance occurrence in all cases of >10%. Neglecting background, the rms variabilities of each observation are calculated with $\sqrt{P_{\rm max}/N_{\rm counts}}$, when $N_{\rm counts}$ is the number of counts in the observation. The upper limits on the rms variabilities are: $< 19\%$ (ObsID 79), $< 16\%$ (ObsID 2668), $< 16\%$ (ObsID 2669), $< 8\%$ (ObsID 7460) and $< 12\%$ (ObsID 7461).

Visual inspection of the light curves did not reveal any variation in the source count rates. Short-term variability was also investigated in a more quantitative way by comparing the integrated light curve with a linear distribution. None of the five observations showed an integrated light curve significantly different from a linear distribution. More specifically, the calculated K-S probabilities were 65% (ObsID 79), 62% (ObsID 2668), 95% (ObsID 2669), 51% (ObsID 7460) and 16% (ObsID 7461). Therefore, no intensity variability is observed on the time scale of the integration times, i.e., $\lesssim 1$ day.

value of ~ 1.9, due to instrumental dead-time effects. To correct for this, on average, in the rms variability upper limits derived here, the measured rms limits were increased by a factor $\langle A \rangle / 2.0$, where $\langle A \rangle$ is the best-fit Poisson power level.

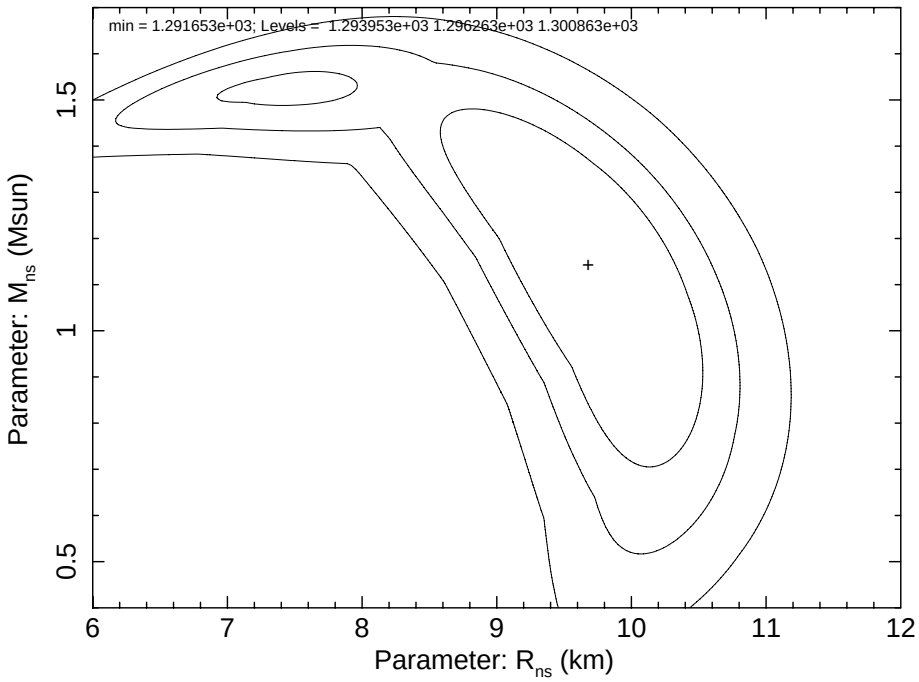

Figure 5.4 – This contour plot in $M_{\rm NS}$–$R_{\rm NS}$ space results from the simultaneous fit of the five data sets with the `nsatmos` model. The 67%, 90%, and 99% contours are shown, and the cross indicates the best fit (when both the mass and the radius are free to vary). For an neutron star mass of $1.4\,M_\odot$, the range of $R_{\rm NS}$ corresponds to that obtained and quoted in Section 5.3.2.

5.4 Discussion

5.4.1 R_∞ Calculation

Producing realistic constraints on the EoS requires obtaining values of R_∞ relying on as few assumptions as possible. Keeping the mass fixed for the model fitting is therefore not appropriate for that purpose. The value of R_∞ is estimated by permitting $M_{\rm NS}$ to vary, and calculating the contours of constant model probability resulting from the fits in a mass–radius space (Figure 5.4). This is done using the `steppar` command in *XSPEC*. The 90% confidence regions of $R_{\rm NS}$ and $M_{\rm NS}$ are

obtained from the 90%-contour in the mass–radius space: $R_{\rm NS} = 9.7^{+0.9}_{-0.8}\,$km and $M_{\rm NS} = 1.13^{+0.47}_{-0.32}\,M_\odot$. The best-fit value of the projected radius is therefore $R_\infty = 11.9\,$km. The calculation of the uncertainties is complicated by the fact that the distribution of $R_{\rm NS}$ and $M_{\rm NS}$ is not symmetric around the best-fit values (i.e., not Gaussian). Moreover, $R_{\rm NS}$ and $M_{\rm NS}$ are highly correlated, as shown by the crescent shape of the contour in M-R space (Figure 5.4). Therefore, the calculation of the uncertainties on R_∞ using Gaussian normal error propagation is not valid. Two methods to obtain the uncertainty on R_∞ are described here.

The projected radius and its uncertainties can be obtained from a tabulated version of the `nsa` spectral model (Zavlin et al., 1996). However, this model (or `nsa`) is less adapted than the `nsatmos` or `nsagrav` models (Webb and Barret, 2007) because it was calculated for a single value of the surface gravity $g = 2.43\times10^{14}\,{\rm cm\,s^{-2}}$ while the other two models consider a range of values. Nevertheless, the best-fit R_∞ value with this model is: $R_\infty = 12.1^{+1.5}_{-0.9}\,$km (consistent with the value calculated in the previous paragraph), for a temperature $kT_{\rm eff} = 76^{+2}_{-3}\,$eV ($\chi^2_\nu$/DOF ($p_{\rm null}$) = 1.54/44 (0.02)).

A second method to estimate the uncertainties involves geometric construction, by reading graphically the error region of R_∞ on the M-R contours (Figure 5.4). For that, a line of constant surface gravity (i.e., constant $M\,(R)$) that goes through the point $(R, M) = (0\,{\rm km}, 0\,M_\odot)$ and the point of best fit in M-R space. This line intersects the 90% contour at the points $(R, M) = (9.048\,{\rm km}, 1.045\,M_\odot)$ and $(R, M) = (10.39\,{\rm km}, 1.245\,M_\odot)$ is used. These two points correspond to the values $R_\infty = 11.15\,$km and $R_\infty = 12.92\,$km which are, respectively, estimates of the lower and upper 90% confidence uncertainties on R_∞, assuming a constant value of the surface gravity.

Therefore, the projected radius and its estimated 90% confidence uncertainties are: $R_\infty = 11.9^{+1.0}_{-0.8}\,$km. With the achieved uncertainty, U24 becomes the third best radius measurement of a NS among the population of GC qLMXBs, after the ones in $\omega\,$Cen (Gendre et al., 2003a) and in M13 (Gendre et al., 2003b).

5.4.2 Error Budget

The high S/N spectra and the precise radius measurements obtained in the work presented here can be used to constrain the EoS of dense matter. A high precision on the NS radius is mandatory to exclude some of the existing nuclear dense matter EoSs and provide the necessary constraints to understand the behaviour of such matter. However, other sources of error come into play in this type of measurements. To quantify the total uncertainty on the radius measurement presented here, the contribution of each source of error into an error budget is estimated, including the distance to the GC NGC 6397, uncertainties intrinsic to the model used, systematic and statistical uncertainties. In those references where these uncertainties are discussed (for example, Heinke et al. 2006a), only two of the three uncertainties discussed here (distance and detector systematics) are addressed. No work in the literature discusses the impact of the uncertainty in the spectral model on derived model parameters; therefore, it is done here.

- The distance to the GC was recently measured using two independent methods. The analysis of the WD sequence from deep observations in an outer field of NGC 6397 led to a distance of 2.54±0.07 kpc (Hansen et al., 2007). More recently, using WDs in central regions of the cluster, the distance was calculated to be 2.34±0.13 kpc (Strickler et al., 2009). The weighted mean of these two measurements is 2.50±0.06 kpc, corresponding to a 2.4% uncertainty. The unknown line-of-sight position of U24 within NGC 6397 accounts for $< 0.1\%$ of the distance uncertainty, which can be neglected compared to the GC distance uncertainty.

- The calculation of spectral model `nsatmos` also contributes to the total uncertainty on the measured radius. However, the previous works describing the model do not provide a discussion on the fractional uncertainties in intensity due to convergence during the calculation of the spectral model (McClintock

et al., 2004; Heinke et al., 2006a). Therefore, it is not possible to evaluate the errors of the resulting spectra. The cited reference for similar models (`nsa` and `nsagrav`, Zavlin et al., 1996) only provides information on the temperature calculation convergence, which does not permit an estimation of the uncertainty error in the modeled intensity as a function of energy.

- The statistical uncertainties are those quoted in Table 5.3 (90% confidence). This includes the 3% systematic uncertainty of the detector calibration, taken into account using the "`systematic 0.03`" command in *XSPEC*.

Consequently, the distance uncertainty (2.4%) is the only quantifiable error not taken into account in the radius measurement obtained from spectral fitting. It is therefore added in quadrature to the systematic and statistical uncertainties to obtain the total quantifiable uncertainty in the radius measurement. For example, the upper bound uncertainty limit of $R_{\rm NS}$ was 10.1% and is 10.4% when accounting for the distance uncertainty. The lower bound uncertainty limit was 6.7% and becomes 7.1%. Consequently, the physical radius is $R_{\rm NS} = 8.9^{+0.9}_{-0.6}$ (for $M_{\rm NS} = 1.4\,M_{\odot}$) while the estimated radiation radius is $R_{\infty} = 11.9^{+1.0}_{-0.8}\,$km, when considering the sources of uncertainty listed above. In conclusion, in NGC 6397, the distance uncertainty of NGC 6397 alone minimally affects the current uncertainty on the radius measurement.

5.4.3 Core Temperature Calculation

The best-fit temperature and physical radius of the NS can be used to determine the interior temperature. This calculation is model dependent and due to the uncertainties in the deep atmosphere composition (the depth of the H/He transition in particular), two different models are considered here. The first one assumes a layer of helium down to a column depth $y = 1{\times}10^{9}\,{\rm g\,cm^{-2}}$ with a pure layer of iron underneath. The second model considers a thin layer of He down to $y = 1{\times}10^{4}\,{\rm g\,cm^{-2}}$ with a mixture dominated by rp-processes. These two alternatives take into account the extremal values for the core temperature, for a fixed effective temperature.

The calculation, described in a previous work (Brown et al., 2002), was performed with a fixed mass $M_{\rm NS} = 1.4\,M_\odot$ and a fixed radius $R_{\rm NS} = 8.9\,{\rm km}$, which corresponds to the best-fit value. The effective temperature used was $kT_{\rm eff} = 80^{+4}_{-5}\,{\rm eV}$. The calculation is performed down to a column depth of $1{\times}10^{14}\,{\rm g\,cm^{-2}}$, since the temperature is nearly isothermal in deeper layers.

For the first model, the resulting interior temperature (at $y = 10^{14}\,{\rm g\,cm^{-2}}$) is $T_{\rm core} = \left(3.37^{+0.36}_{-0.41}\right) {\times}10^7\,{\rm K}$. The second model leads to the value of interior temperature $T_{\rm core} = \left(8.98^{+0.81}_{-0.98}\right) {\times}10^7\,{\rm K}$. Overall, if it is assumed that the H/He transition depth is unknown, the core temperature is in the range of extreme values: $T_{\rm core} = (3.0 - 9.8)\,{\times}10^7\,{\rm K}$.

5.5 Conclusion

In this work, the spectral analysis of five archived *Chandra* observations of the qLMXBs in the GC NGC 6397 was performed. The $\sim 350\,{\rm ks}$ of integration time available permitted to obtain high S/N spectra and improve the radius measurement. More specifically, the simultaneous spectral fitting of all five observations, using an NS H atmosphere, allowed us to provide constraints on the NS radius with $\sim$10% statistical uncertainty (90% confidence). This confirmed the qLMXB nature of the X-ray source. Therefore, the measured NS properties are $R_{\rm NS} = 8.9^{+0.9}_{-0.6}\,{\rm km}$ and $kT_{\rm eff} = 80^{+4}_{-5}\,{\rm eV}$, for $M_{\rm NS} = 1.4\,M_\odot$, and assuming an NS with an atmosphere composed of pure hydrogen. The estimated interior temperature lies in the range $T_{\rm core} = (3.0 - 9.8)\,{\times}10^7\,{\rm K}$. In the 0.5–10 keV range, the flux corresponding to these best-fit parameters is $F_{\rm X} = \left(1.39^{+0.02}_{-0.06}\right) {\times}10^{-13}\,{\rm erg\ cm^{-2}\ s^{-1}}$, equivalent to a luminosity of $L_{\rm X} = \left(1.04^{+0.01}_{-0.05}\right) {\times}10^{32}\,{\rm erg\ s^{-1}}$ at a distance of 2.5 kpc. The spectra did not show evidence for a PL component as inferred by the upper limit on the contribution to the total flux of 3.7%.

The results of this analysis were consistent with those of the discovery observation (Gr01); the reported NS radius and temperature were $R_\infty = 4.9^{+14}_{-1}$ km and $kT_{\rm eff} =$ 57–92 eV. No optical counterpart was detected on the *HST* observations, with a limiting magnitude of $M_V > 11$ (Gr01).

No variability was observed on long time scales. Therefore, unless an outburst (for which there is no evidence) happened between the observations–between 2000 and 2002, or between 2002 and 2007–the source remained in its quiescent stage since the discovery observation. It is worth noting that none of the GC qLMXBs discovered in quiescence so far have been seen in outburst. Moreover, an outburst happening between the available observations would have had an impact on the observed luminosity and intensity variability would have been detected (Ushomirsky and Rutledge, 2001; Rutledge et al., 2002c). The search of short time scale variability (< 1 day) did not reveal any such variability. Finally, a PDS analysis was performed and did not demonstrate evidence of periodic variability in the frequency range 0.0001–0.10 Hz. The lack of intensity variability on various time scales further supports the classification of the source. In conclusion, the qLMXB U24 in the GC NGC 6397 adds to the list of qLMXBs suitable to place constraints on the dense matter EoSs with a best-fit projected radius of $R_\infty = 11.9^{+1.0}_{-0.8}$ km.

However, this R_∞ measurement was obtained while assuming a value of the absorption, $N_{H,22}$=0.14. As argued in Section 6.4, the systematics linked with assumed values of $N_{\rm H}$ can be large and skew the R_∞ measurement. Relaxing this assumption leads to a more conservative much a less constrained measurement of R_∞, which individually, cannot place useful constraints on the dense matter EoS. Chapter 6 presents a novel method – superior to individual analyses of qLMXBs – which combines the spectra from multiple qLMXBs to obtain more stringent constraints on the dense matter EoS.

6

Measuring the Radius of Neutron Stars

This chapter presents the measurement of the NS radius using the thermal spectra from qLMXBs inside GCs. The present work assumes, based on observational evidence, that the radii of NSs are quasi-constant (constant within measurement errors) for astrophysically relevant masses. This framework is used to constrain a single $R_{\rm NS}$ value from five qLMXB targets with available high S/N X-ray spectroscopic data. A MCMC approach results in the marginalized posterior distribution for $R_{\rm NS}$, constrained to be the same value for all five NSs in the sample. An effort was made to include all quantifiable sources of uncertainty into the uncertainty of the quoted radius measurement. Using conservative assumptions, the radius, common to the five qLMXBs and constant for a wide range of masses, lies in the low range of possible NS radii. Such a value is consistent with low-$R_{\rm NS}$ dense matter EoSs. This result is compared to previous radius measurements of NSs from various analyses of different types of systems. In addition, the spectral analyses of individual qLMXBs is also compared to previous works.

The chapter was published as: S. Guillot, M. Servillat, N. A. Webb, and R. E. Rutledge. *Measurement of the Radius of Neutron Stars with High Signal-to-noise Quiescent Low-mass X-Ray Binaries in Globular Clusters.* ApJ, 772:7, July 2013. The introduction of the original article has been edited to remove redundant information provided in Chapter 2. The last paragraph in the conclusion of this chapter (Section 6.5) did not appear in the original publication and was added for this thesis.

6.1 Introduction

Recent mass measurements of pulsars have placed some constraints on the dense matter EoS. In particular, the high-$M_{\rm NS}$ measuresurements of the pulsar PSR 1614−2230, $M_{\rm NS} = 1.97 \pm 0.04\,M_{\odot}$ (Demorest et al., 2010), and PSR J0348+0432, $M_{\rm NS} = 2.01 \pm 0.04\,M_{\odot}$ (Antoniadis et al., 2013), seem to favour "normal matter" hadronic EoSs. If such EoSs desbribe dense nuclear matter, this means that the radius of astrophysical NSs should be observed to be within a narrow ($\lesssim 10\%$) range of values for $M_{\rm NS} > 0.5\,M_{\odot}$, since "normal matter" EoSs follow lines of quasi-constant radius in $M_{\rm NS}$–$R_{\rm NS}$-space at such masses (Lattimer and Prakash, 2001). Here, the term "quasi-constant" means constant within measurement precision, $\sim 10\%$. This should be differentiated from a value which is constant when measured with infinite precision, or a value which is constant according to theory. It is important to notice that the spread in $R_{\rm NS}$ increases for stiff EoSs, especially close to the maximum $M_{\rm NS}$ of the compact object (e.g., up to a 2-km difference in $R_{\rm NS}$ for the EoS PAL1, Prakash et al. 1988).

The empirical dense matter EoS obtained from $M_{\rm NS}$–$R_{\rm NS}$ confidence regions from type-I X-ray bursts and from the thermal spectra of qLMXBs combined also favours this conclusion (Steiner et al., 2010, 2013). Using a Bayesian approach, the most probable dense matter EoS was calculated, resulting in a EoS approaching the behaviour of theoretical hadronic dense matter EoSs, with predicted radii in the range $R_{\rm NS} \sim 10-13\,$km. Such radii suggest that soft hadronic EoSs are describing the dense matter inside NSs. However, different analyses of other NSs found radii consistent with stiff EoSs. These include the qLMXB X7 in 47Tuc (Heinke et al., 2006a), or the type I X-ray burster 4U 1724-307 (Suleimanov et al., 2011a). Nonetheless, these results are not inconsistent with the observation that the $R_{\rm NS}$ is almost constant for a large range of $M_{\rm NS}$, since they are consistent with stiff "normal matter" EoSs, such as MS0/2 (Müller and Serot, 1996)

Given the evidence supporting the "normal matter" hadronic EoSs, it therefore becomes a natural assumption – to be tested against data – that observed NSs have radii which occupy only a small range of $R_{\rm NS}$ values ($\lesssim 10\%$). Using the thermal spectra of five qLMXBs, fitted with a H-atmosphere model[1], a single $R_{\rm NS}$ value is assumed and measured, as well as its uncertainty. Furthermore, under this assumption, the best-fit $M_{\rm NS}$ and surface effective temperature $kT_{\rm eff}$ for these qLMXBs and their uncertainties are extracted. The various sources of uncertainty involved in this spectral analysis are addressed, including, the distances to the qLMXBs, the amount of Galactic absorption in their direction, and the possibility of an excess of high-energy photons as observed for other qLMXBs (and modeled with a PL component). The goal is to place the best possible constraints on $R_{\rm NS}$ accounting for all known uncertainties, and to discuss other unquantifiable systematic uncertainties.

The organization of this chapter is as follows: Section 6.2 explains the analysis of the X-ray data. Section 6.3 contains the results of the spectral analysis. A discussion of the results is in Section 6.4 and a summary is provided in Section 6.5.

6.2 Data Reduction and Analysis

6.2.1 Targets

The targets used in this work are chosen among the qLMXBs located in GCs that produced the best $R_{\rm NS}$ measurements, i.e., with R_∞ uncertainties of $\lesssim 15\%$ in the previous works. The GCs ω Cen (Rutledge et al., 2002b; Gendre et al., 2003a) and M13 (Gendre et al., 2003b; Catuneanu et al., 2013) each have one qLMXB that was used in previous work to place moderate constraints on the dense matter EoS (Webb and Barret, 2007). The projected radius measurements R_∞ reported in the original works are within 2–3% uncertainty. However, there is evidence that these uncertainties are highly under-estimated (Section 6.3).

[1]NSs atmosphere composed of pure helium have been studied, and applied to qLMXBs (see Section 6.4).

The qLMXB in the core of NGC 6304, discovered recently with the *XMM-Newton* observatory (*XMM*, hereafter) and confirmed with a short *Chandra X-ray Observatory* exposure (Guillot et al., 2009a,b), was then observed for 100 ks with ACIS-I onboard *Chandra* (Advanced CCD Imaging Spectrometer). Here, only the long *Chandra* exposure is used since, in the *XMM* observation, the core source is contaminated by nearby sources, mostly one spectrally hard source (Guillot et al., 2009b).

The qLMXB in NGC 6397 (named U24 in the discovery observation, Grindlay et al. 2001b) has a $R_{\rm NS}$ value measured with $\sim 8\%$ uncertainty, obtained from a total of 350 ks of *Chandra X-ray Observatory* archived observations (Chapter 5). The spectra for this target were re-analyzed in this work, for a more uniform analysis.

Finally, the R_∞ measurement of the NS qLMXB in the core of M28 reported in the discovery observation does not place useful constraints on the dense matter EoS: $R_\infty = 14.5^{+6.9}_{-3.8}$ (Becker et al., 2003). However, an additional 200 ks of archived observations with *Chandra* have been analyzed in a recent work, finding $R_{\rm NS} = 9 \pm 3$ km and $M_{\rm NS} = 1.4^{+0.4}_{-0.9}\,M_\odot$ for a H-atmosphere, and $R_{\rm NS} = 14^{+3}_{-8}$ and $M_{\rm NS} = 2.0^{+0.5}_{-1.5}\,M_\odot$ for a pure He-atmosphere (Servillat et al., 2012, and their Figures 3 and 4, for the $M_{\rm NS}$–$R_{\rm NS}$ confidence regions). The same data sets are used in the present work. This source is moderately piled-up ($\sim 4\%$ pile-up fraction) and necessitates the inclusion of a pile-up model component (Davis, 2001, see Section 6.2.4 for details). All uncertainties for values obtained from a X-ray spectral analysis with *XSPEC* are quoted at the 90% confidence level, unless noted otherwise.

The qLMXB X7 in 47 Tuc has also been observed with the high S/N that could provide constraints on the dense matter EoS. However, it suffers from a significant amount of pile-up (pile-up fraction $\sim 10 - 15\%$). While the effects of pile-up can be estimated and corrected for by the inclusion of a pile-up model (Heinke et al., 2003c, 2006a), the uncertainties involved with such a large amount of pile-up are not quantified in this model[2]. It was chosen not to include this target in the present

[2]See "The Chandra ABC Guide to Pile-Up" available at `http://cxc.harvard.edu/ciao/download/doc/pileup_abc.pdf`

Table 6.1 – X-ray Exposures of the Targeted Clusters.

Target	Obs. ID	Starting Time (TT)	Time (ksec)	S/N	Telescope and detector	Filter or Mode	Refs.
M28	2683	2002 July 04 18:02:19	14.0	23.85	*Chandra* ACIS-S3 (BI)	VFAINT	2
M28	2684	2002 Aug. 04 23:46:25	13.9	23.54	*Chandra* ACIS-S3 (BI)	VFAINT	2
M28	2685	2002 Sep. 09 16:55:03	14.3	23.90	*Chandra* ACIS-S3 (BI)	VFAINT	2
M28	9132	2008 Aug. 07 20:45:43	144.4	78.75	*Chandra* ACIS-S3 (BI)	VFAINT	1, 3
M28	9133	2008 Aug. 10 23:50:24	55.2	48.46	*Chandra* ACIS-S3 (BI)	VFAINT	1, 3
NGC 6397	79	2000 July 31 15:31:33	48.34	25.03	*Chandra* ACIS-I3 (FI)	FAINT	4, 5
NGC 6397	2668	2002 May 13 19:17:40	28.10	25.47	*Chandra* ACIS-S3 (BI)	FAINT	5
NGC 6397	2669	2002 May 15 18:53:27	26.66	24.97	*Chandra* ACIS-S3 (BI)	FAINT	5
NGC 6397	7460	2007 July 16 06:21:36	149.61	52.31	*Chandra* ACIS-S3 (BI)	VFAINT	5
NGC 6397	7461	2007 June 22 21:44:15	87.87	41.40	*Chandra* ACIS-S3 (BI)	VFAINT	5
M13	0085280301	2002 Jan. 28 01:52:41	18.8	14.25	*XMM* pn, MOS1, MOS2	Medium	6,7
M13	0085280801	2002 Jan. 30 02:21:33	17.2	12.10	*XMM* pn, MOS1, MOS2	Medium	6,7
M13	5436	2006 Mar. 11 06:19:34	27.1	16.07	*Chandra* ACIS-S3 (BI)	FAINT	1,8
M13	7290	2006 Mar. 09 23:01:13	28.2	16.01	*Chandra* ACIS-S3 (BI)	FAINT	1,8
ω Cen	653	2000 Jan. 24 02:13:28	25.3	13.33	*Chandra* ACIS-I3 (FI)	VFAINT	9
ω Cen	1519	2000 Jan. 25 04:32:36	44.1	16.45	*Chandra* ACIS-I3 (FI)	VFAINT	9
ω Cen	0112220101	2001 Aug. 12 23:34:44	33.9	24.35	*XMM* pn, MOS1, MOS2	Medium	7,10
NGC 6304	11074	2010 July 31 15:31:33	98.7	27.94	*Chandra* ACIS-I3 (FI)	VFAINT	1

Notes: TT refers to Terrestrial Time. FI and BI refer to front and back illuminated detectors. S/N indicates the signal-to-noise ratio of each individual exposure. The column "Filter or Mode" refers to the *XMM* optical-blocking filter used or the telemetry mode used on *Chandra* observations. All observations have been re-processed and re-analyzed in this work. The references solely indicate the previously published analyses of the data.
References: (1) This work; (2) Becker et al. (2003); (3) Servillat et al. (2012); (4) Grindlay et al. (2001b); (5) Chapter 5; (6) Gendre et al. (2003b); (7) Webb and Barret (2007); (8) Catuneanu et al. (2013), (9) Rutledge et al. (2002b); (10) Gendre et al. (2003a).

analysis, in an effort to limit the sources of uncertainties that are not quantified (see Section 6.2.4).

The list of targets and their usable observations with *XMM* and *Chandra* is presented in Table 6.1, along with the usable exposure time and other relevant parameters of the observations.

6.2.2 Data Processing

The processing of raw data sets is performed according to the standard reduction procedures, described briefly below.

Chandra X-ray Observatory Data Sets

The reduction and analysis of *Chandra* data sets (ACIS-I or ACIS-S) is done using `CIAO v4.4`. The level-1 event files were first reprocessed using the public script *chandra_repro* which performs the steps recommended in the data preparation analysis thread[3] (charge transfer inefficiency corrections, destreaking, bad pixel removal, etc, if needed) making use of the latest effective area maps, quantum efficiency maps and gain maps of CALDB v4.4.8 (Graessle et al., 2007). The newly created level-2 event files are then systematically checked for background flares. Such flares were only found in the middle and at the end of an observation of M28 (ObsID 2683), for a total of 3 ks. These two flares caused an increase by a factor of 2.4, at most, of the background count level. Given the extraction radius chosen here (see below), this period of high background contaminates the source region with < 1 count. Therefore, the entire exposure of the ObsID is included in the present analysis.

To account for the uncertainties of the absolute flux calibration, systematics are added to each spectral bin using the `heasoft` tool `grppha`: 3% systematics in the 0.5–10 keV range (Table 2 in Chandra X-Ray Center Calibration Memo by Edgar and Vikhlinin, 2004). This document (Table 2) provides the uncertainties on the ACIS detector quantum efficiency at various energies, which are 3% at most. In the 0.3–0.5 keV range, the uncertainty in the calibration is affected by the molecular contamination affecting ACIS observations. The recent version of CALDB contains an improved model for this contamination. The RMS residuals are now limited to 10% in the 0.3–0.5 keV range (Figure 15 of document "Update to ACIS Contamination Model", Jan 8, 2010, ACIS Calibration Memo[4]). To account for the variations in the residuals of contamination model, 10% systematics are added to spectral bins below 0.5 keV.

[3] `http://cxc.harvard.edu/ciao/threads/data.html`
[4] available at `http://cxc.harvard.edu/cal/memos/contam_memo.pdf`

XMM-Newton Data Sets

The reduction of *XMM* data sets is completed using the *XMM* `Science Analysis System v10.0.0` with standard procedures. The command *epchain* performs the preliminary data reduction and creates the event files for the pn camera in the 0.4–10.0 keV energy range, with 3% systematic uncertainties included, accounting for the uncertainties in the flux calibration of the pn camera on *XMM* (Guainizzi, 2012). The data sets are checked for flares and time intervals with large background flares are removed. The total usable time (after flare removal) for each observation is listed in Table 6.1. MOS1 and MOS2 data are not used in the present work to minimize the effects of cross-calibration uncertainties between detectors.

6.2.3 Count Extraction

On *Chandra X-ray Observatory* Data Sets

The count extraction of the source and background spectra is performed with the task `specextract`, as well as the calculation of the response matrices and ancillary response files (RMFs and ARFs). The centroid position is chosen using the reported source positions from previous works. The extraction radii are chosen to correspond to a 99% EEF, and therefore depend on the off-axis angle of the targets. For on-axis qLMXBs (M13, M28, NGC 6397 and NGC 6304), counts within a 3.4″ radius are extracted to create the spectrum. This ensures that 99% of the EEF at 1 keV is included[5]. The qLMXB in ω Cen is at a large off-axis angle ($\sim 4.4'$) which requires an extraction radius of 6″ to contain 99% of the EEF. This is due to the degradation of the PSF of the *Chandra* mirror with increasing off-axis angle. Background counts were taken from an annulus centred around the qLMXB, with an inner radius of 5″ (9″ for ω Cen) and an outer radius of 50″. Regions surrounding other point sources detected in the qLMXB extraction regions or in the background regions are also excluded (radius of 5″ or more). For NGC 6304, the background region is off-centred

[5] *Chandra* Observatory Proposer Guide v15.0, Figure 6.7, December 2012

with respect to the source region, to ensure that the background lies on the same CCD chip as the source.

Figures 6.1a–e show the regions used to extract the counts and create the spectra of each target. When several observations are available for a target, the largest-S/N observation was used to create the figure.

On *XMM-Newton* Data Sets

For the three *XMM* data sets, the extraction method was the same as that described above. Only the source extraction radii were different and determined using the XMM SAS task `eregionanalyse` which provides the optimum extraction radius that maximizes the S/N given the source position and the surrounding background. The optimum radius is 19″ for ObsID 01122 of ω Cen. The encircled energy of the source is therefore 79% at 1.5 keV.

For the *XMM* observations of M13, the close proximity of a CV complicates the task. A 25″ extraction radius and a 12.5″ exclusion radius for the nearby source are used to create the spectra. It ensures that 84% of the total energy from the qLMXB at 1.5 keV is encircled[6].

Similar to the *Chandra* data, the background is an annulus around the source, restricted to remain on the same CCD chip as the source. `rmfgen` and `arfgen` are then used to generate the response matrices files (RMF) and the ancillary response file (ARF) for each observations.

Contamination from Nearby Sources

As mentioned above, some qLMXBs lie in close proximity of other contaminating sources. The most evident case is that of M13, observed with *XMM* (Figure 6.1e), in which part of the counts from a nearby CV still overlaps with the qLMXB extraction region even after excluding 10″ around the CV. In M28, three sources in the proximity of the qLMXB require parts of the extraction region to be excluded (Figure 6.1a),

[6]From *XMM* Users Handbook, Figure 3.7, July 2010

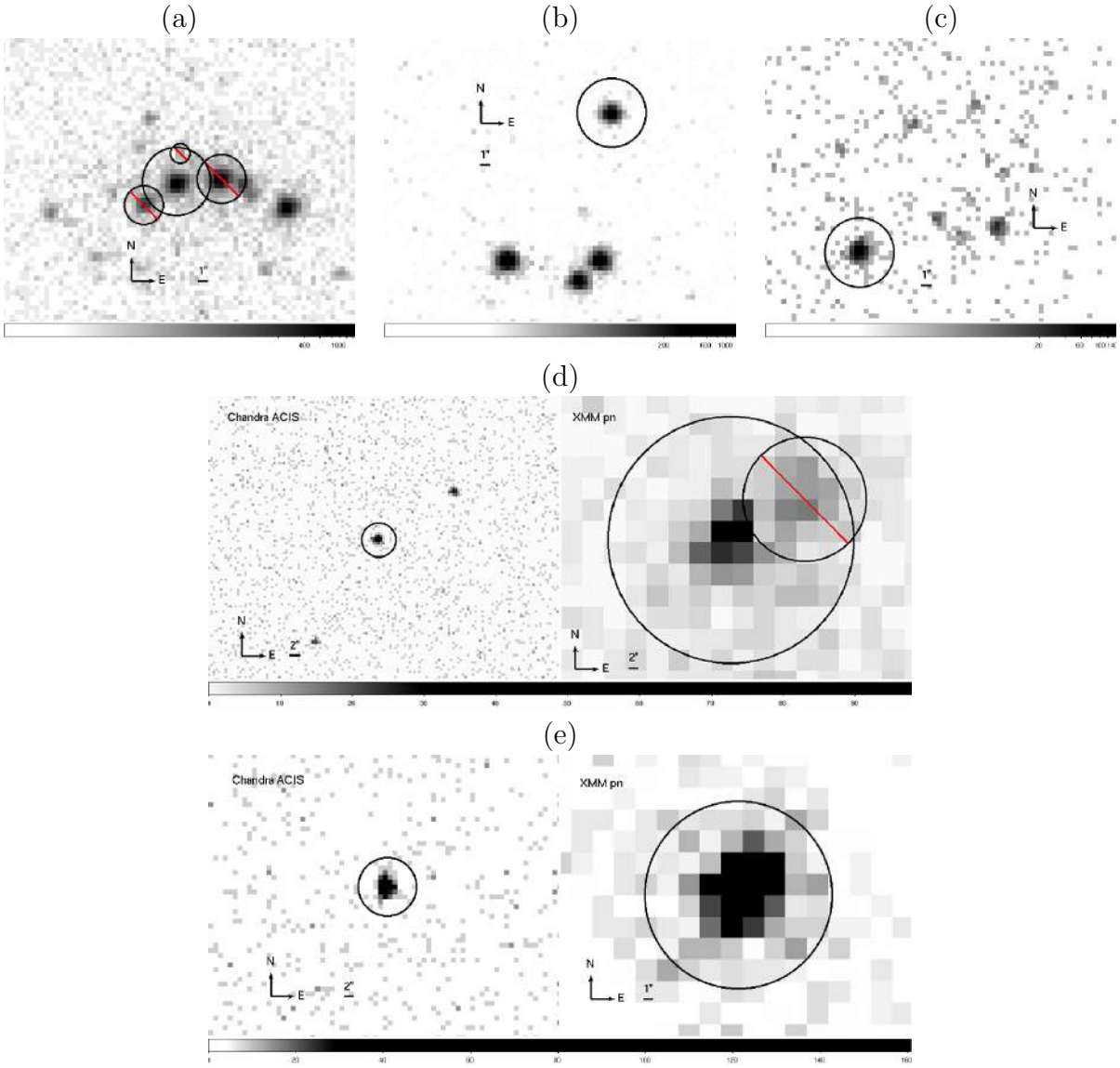

Figure 6.1 – These figures show the extraction regions for the five quiescent low-mass X-ray binaries. *(a)* For M28, ObsID 9132, the three nearby sources are excluded, limiting contamination to $< 1\%$ within the extraction region (see Table 6.2). *(b)* For NGC 6397, ObsID 7460, no counts from nearby sources fall within the extraction region. *(c)* For NGC 6304, ObsID 11074, the nearby sources are not contaminating the extraction region. *(d)* For M13, *Chandra* data are on the left, ObsID 7290, and *XMM* data are on the right, ObsID 0085280301. The nearby cataclysmic variable is excluded. *(e)* For ω Cen, *Chandra* data are on the left, ObsID 1519, and *XMM* data are on the right, ObsID 0112220101. There is no contamination from nearby sources.

Table 6.2 – Count Contamination from Nearby Sources

Target	ObsID (detector)	Number of contaminating counts source 1	source 2	source 3	Sum	Total (%)
M28	2693 (ACIS)	0.16	0.11	0.16	0.43	0.08%
	2684 (ACIS)	0	0.15	0.32	0.47	0.08%
	2685 (ACIS)	0.05	0.19	0.17	0.37	0.06%
	9132 (ACIS)	1.7	38.9	6.3	46.9	0.75%
	9133 (ACIS)	1.0	11.7	2.7	15.4	0.65%
M13	0085280301 (pn)	27	–	–	27	8.7%
	0085280801 (pn)	34	–	–	34	6.2%

NOTES: The columns "source1", "source2" and "source3" indicate the absolute numbers of counts falling within the quiescent low-mass X-ray binary extraction region, and "Sum" is the simple sum of contaminating counts. For M13, there is only one nearby source, not fully resolved with *XMM*. The last column provides the amount of contamination as a percent of the total number of counts within the quiescent low-mass X-ray binary extraction region.

with a minor contamination from the nearby sources. For the observations of M28 and M13, the fraction of contaminating counts present within the extraction region of the qLMXBs is estimated using a MC sampler which draws counts from the radial distribution of encircled energy of ACIS or pn at 1 keV (see footnotes in previous subsections). Table 6.2 lists the amount of contamination for each observation of M28 and for the *XMM*-pn observations of M13. The contamination over the M28 qLMXB region can be neglected, since, in the worst case (ObsID 9132) only 47 counts out of 6250 are contamination from nearby sources. The CV close to the qLMXB in M13 causes a contamination of 6% and 9% of the counts in each of the *XMM* spectra, or 4% of the total counts available for the qLMXB in M13 (*XMM* and *Chandra* spectra combined). Overall, contamination for nearby sources represents 0.5% of the total count number, all sources combined. This contamination can be safely neglected, since it will not significantly affect the radius measurement.

6.2.4 Pile-Up

Observations of bright X-ray sources may be subject to an instrumental effect known as pile-up. When two or more photons strike a pixel on an X-ray detector within a single time frame (3.24 sec for *Chandra*-ACIS observations and 73.4 ms for *XMM*-pn observations), the pile-up effect causes degradation of the PSF and, more importantly

for the analysis presented here, a degradation of the spectral response. Specifically, the recorded energy of the event will be the sum of the two (or more) piled-up photon energies. In addition, grade migration (also called photon pattern distortion for *XMM*) also occurs. Although a pile-up model exists in *XSPEC* to take into account these effects (Davis, 2001), it is chosen here to restrict the analysis to mildly piled-up observations.

None the *XMM* observations of qLMXBs are piled-up, given the short duration of a single time frame on *XMM*-pn (73.4 ms). Quantitatively, the count rates of the qLMXBs in ω Cen and M13 (2.6×10^{-2} and 2.7×10^{-2} counts per seconds, respectively) correspond to $\sim 10^{-3}$ counts per frame. At those rates, the pile-up is negligible. The frame time of *Chandra*-ACIS in full-frame mode, however, is significantly longer than that of *XMM*-pn (compensated by the smaller effective area). The *Chandra* observations of the qLMXB in M28 are moderately piled-up because of a count rate of ~ 0.043 counts per seconds (~ 0.14 counts per frame) which corresponds to a pile-up fraction of $\sim 5\%$ [7]. Such amount of pile-up cannot be neglected and is taken into account using the `pileup` model in *XSPEC* (Davis, 2001). Other *Chandra* observations of the qLMXBs studied in this work have smaller count rates which do not necessitate a pile-up correction.

As stated before, the correction of pile-up fractions $\sim 10\%$ and above (such as that of the qLMXB in 47Tuc, observed in full-frame mode on *Chandra*/ACIS) comes with unquantified uncertainties. This is tested by simulating piled-up spectra of 47Tuc (10–15% pileup fraction) and M28 (5% pileup fraction) with their respective `nsatmos` parameters, and then by fitting the spectra with the `nsatmos` model without the pile-up component. The best-fit radii of each spectrum is affected by systematics: $\sim 10\%$ for M28 and $\sim 50\%$ for 47Tuc. The systematic error involved with the pile-up of M28 is smaller than the measurement error of $R_{\rm NS}$ in the present analysis, while for 47Tuc, the systematic bias caused by pileup is substantially larger than the $R_{\rm NS}$

[7] *Chandra* Observatory Proposer Guide v12.0, Figure 6.18, December 2009

measurement uncertainty. Therefore, the qLMXB in 47Tuc is not used in this analysis to avoid introducing a systematic uncertainty which may be comparable in size to the total statistical uncertainty[8].

6.2.5 Spectral Analysis

The spectral analysis is composed of two parts. In the first one, the five targets are analyzed individually and the results are compared to previously published results. The second part of the analysis in the present work pertains to the simultaneous fitting of the targets, with a $R_{\rm NS}$ value common to all five qLMXBs. Prior to the discussion of these two parts, the analysis techniques common to the two analyses are described.

Counts Binning, Data Groups and Model Used

Once the spectra and the respective response files of each observation are extracted, the energy channels are grouped with a minimum of 20 counts per bin to ensure that the Gaussian approximation is valid in each bin. For observations with a large number of counts (>2000 counts, in ObsID 9132 and 9133 of M28 and ObsID 7460 of NGC 6397), the binning is performed with a minimum of 40 counts per bin. In all cases, when the last bin (at high energy, up to 10 keV) contains less than 20 counts, the events are merged into the previous bin.

The spectral fitting is performed using the "data group" feature of *XSPEC*. The spectra of each target are grouped together, and each group (corresponding to each qLMXB) is assigned the same set of parameters. The spectral model used is the `nsatmos` model (Heinke et al., 2006a), together with Galactic absorption taken into account with the multiplicative model `wabs`. The amounts of Galactic absorption, parameterized by $N_{\rm H}$, are fitted during the spectral analysis, and compared to those

[8]Inclusion of 47Tuc X7 in this analysis does not significantly affect the best-fit $R_{\rm NS}$ value; nonetheless, this qLMXB is not included, since the effect of including it on the error region of $R_{\rm NS}$ cannot be estimated (Section 6.4.2).

obtained from a HI Galactic survey from NRAO data[9] (Dickey and Lockman, 1990). The $N_{\rm H}$ values used in the present analysis are shown in Table 6.3. The results obtained with `nsatmos` are also compared with the best-fit results using the model `nsagrav` (Zavlin et al., 1996) for completeness.

As mentioned before, the `pileup` model (Davis, 2001) is necessary for the spectral fitting of M28 spectra. In *XSPEC*, multiple groups cannot be fitted with different models, so a single model is applied to all groups, namely, `pileup*wabs*nsatmos`. For the spectra of the qLMXB in M28, the α parameter of the `pileup` model, called "good grade morphing parameter" is left free. The frame time parameter is fixed at 3.10 sec. This value corresponds to the `TIMEDEL` parameter of the header (3.14104 sec for the observations of M28) where the readout time (41.04 ms) is subtracted. All the other parameters of the `pileup` model are held fixed at their default values, as recommended in the document "The Chandra ABC Guide to Pile-Up v.2.2"[10]. Since the targets in M13, ω Cen, NGC 6397 and NGC 6304 do not require to account for pile-up, the time frame for these four groups is set to a value small enough so that the `pileup` model has essentially no effect and the α parameters of the four non piled-up sources are kept fixed at the default value, $\alpha = 1$. A quick test is performed to demonstrate that the `pileup` model with a small frame time has no effect on the spectral fit using the non piled-up spectra of the qLMXB in NGC 6304. Specifically, the best-fit `nsatmos` parameters and the χ^2-statistic do not change when the `pileup` model (with a frame time of 0.001 sec) is added, as expected.

Individual Targets

Prior to the spectral analysis, it is important to verify that the qLMXBs do not present signs of spectral variability. This is done by considering each target individually (without the other targets) and by demonstrating that the `nsatmos` spectral model

[9] obtained from the *HEASARC* $N_{\rm H}$ tools available at `http://heasarc.nasa.gov/cgi-bin/Tools/w3nh/w3nh.pl`

[10] from the Chandra X-ray Science Center (June 2010), available at `http://cxc.harvard.edu/ciao/download/doc/pileup_abc.pdf`

fits adequately, with the same parameters, all the observations of the given target. More precisely, for each target, all the parameters are tied together and it is verified that the fit is statistically acceptable.

In Section 6.3.1, the results of the spectral fits of individual targets are presented. In order to provide the full correlation matrix for all the parameters in the fit, a Markov-Chain Monte-Carlo (MCMC) simulation is implemented (described in Section 6.2.6) and the resulting posterior distributions are used as the best-fit confidence intervals, including the $M_{\rm NS}$–$R_{\rm NS}$ confidence region. These spectral fitting simulations are performed with the Galactic absorption parameters $N_{\rm H}$ left free. This allows us to obtain best-fit X-ray-measured values of the absorption in the direction of each of the targeted GCs. These best-fit values are compared to HI-deduced values (from neutral hydrogen surveys), and are also used for the remainder of the work, when $N_{\rm H}$ is kept fixed. Finally, the results of the individual spectral fits are compared to previously published results.

Simultaneous Spectral Analysis of the Five Targets

The main goal of this chapter is the simultaneous spectral fit of five qLMXBs assuming an $R_{\rm NS}$ common to all qLMXBs. Therefore, $R_{\rm NS}$ is a free parameter constrained to be the same for all data sets, while each NS targeted has its own free $M_{\rm NS}$ and $kT_{\rm eff}$ parameters. In addition, the spectra of M28 require an extra free parameter α for the modeling of pile-up. This leads to a total of 12 free parameters.

In an effort to include all possible uncertainties in the production of the $M_{\rm NS}$–$R_{\rm NS}$ confidence regions, Gaussian Bayesian priors for the source distances parameters are included, instead of keeping the parameter values fixed[11]. Since, additional systematic uncertainties can arise when keeping the $N_{\rm H}$ parameters fixed, this assumption is also relaxed in the spectral analysis. Finally, the spectra of some qLMXBs display excess flux above 2 keV, which is not due to the H-atmosphere thermal emission. This is accounted for by adding a PL spectral component to the model, where the photon

[11]For a review on Bayesian analysis, see Gregory (2005)

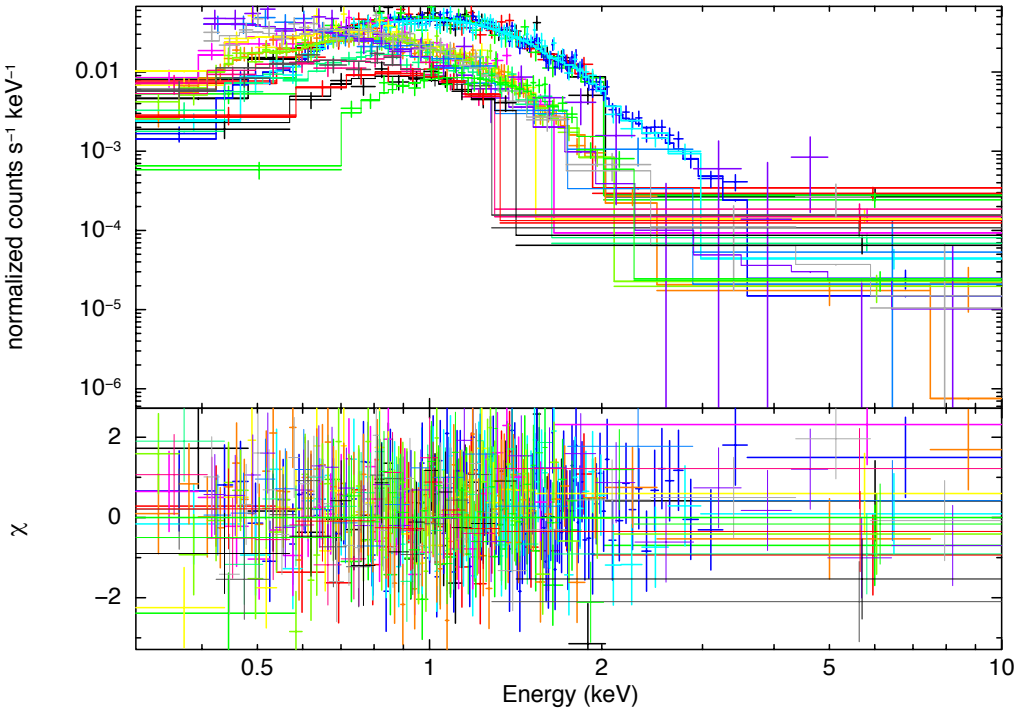

Figure 6.2 – This figure shows the spectral fit resulting from Run #7, obtained with the model `wabs*(nsatmos+powerlaw)`, for which the best-fit statistic is χ^2_ν/DOF ($p_{\rm null}$) = 0.98/628 (0.64).

index is fixed at $\Gamma = 1.0$ but the PL normalizations are free to vary. Such PL index is the hardest observed for a transient LMXB in quiescence (Cen X-4 Cackett et al., 2010). The spectra resulting from this analysis (with all five qLMXBs, and with all assumptions relaxed) are shown in Figure 6.2.

Relaxing the assumptions mentioned above adds 15 free parameters, for a total of 27, which increases the complexity of the χ^2-space. Because of that, in *XSPEC*, the estimation of the confidence region for each parameter proves difficult. The command `steppar` iteratively calculates the χ^2-value for fixed values of a parameter in the range provided by the user. However, this grid-search procedure is highly dependent on the

starting point of the parameter of interest and on the number of steps. Such a problem is particularly evident in the case of highly covariant sets of parameters. This can result in 1D or 2D $\Delta\chi^2$ contours that are not reliable to estimate the uncertainties. A solution to this issue relies in using the posterior distributions from MCMC simulations (described in Section 6.2.6). With those, one can quantify the uncertainties of each parameters. The need to include Bayesian priors also brings forward the use of MCMC simulations.

The simultaneous spectral fitting of all five targets using MCMC simulations was performed in seven separate runs, during which the assumptions on the spectral model are progressively relaxed. The characteristics of each run are described in Section 6.3.2. Another run is also performed with the `nsagrav` model for purposes of comparison with the `nsatmos` model. The following subsection describes the MCMC analysis performed.

6.2.6 Markov-Chain Monte Carlo Analysis

As described above, the main advantage of using an MCMC simulation resides in a complete understanding of the posterior probability density functions of each parameter. It also allows one to marginalize over the so-called nuisance parameters, i.e., those that are an important part of the modeling but which are of little physical interest to the problem at hand. Because of the curved parameter distributions obtained with the `nsatmos` model, in particular the $M_{\rm NS}$–$R_{\rm NS}$ contours, an MCMC algorithm different from the typically used Metropolis-Hasting algorithm (MH) is chosen. Indeed, the MH algorithm is not efficient at exploring skewed parameter spaces. The next few paragraphs are dedicated to a brief description of the Stretch-Move algorithm used.

The Stretch-Move algorithm (Goodman and Weare, 2010) is particularly useful for elongated and curved distributions (e.g., $M_{\rm NS}$–$R_{\rm NS}$ with `nsatmos`), as demonstrated in previous works (e.g., Wang et al., 2013); the implementation used here generally follows that work. Other analyses have used the Stretch-Move algorithm (Bovy et al.

2012; Olofsson et al. 2012, using another implementation, by Foreman-Mackey et al. 2013). The algorithm consists in running several simultaneous chains, also called walkers, where the next iteration for each chain is chosen along the line connecting the current point of the chain and the current point of another randomly selected chain. The amount of "stretching" is defined by a random number z from an affine-invariant distribution (Goodman and Weare, 2010):

$$g(z) \propto \begin{cases} \frac{1}{\sqrt{z}} & \text{if } z \in \left[\frac{1}{a}, a\right] \\ 0 & \text{otherwise} \end{cases} \tag{6.1}$$

In this work, each individual chain starts from a randomly selected point in the parameter space, within the typical hard limits defined for `nsatmos` in *XSPEC*.

The parameter a is used as a scaling factor and is adjusted to improve performance. A larger value of a increases the "stretching" of the chains, i.e., the algorithm will better explore the elongated parts of the parameter space, but it decreases the likelihood that the next step is accepted. A smaller value of a only produces small excursions from the previous value but increases the likelihood that the next step is accepted. Efficiency is optimized at an intermediate value of a. The Stretch-Move algorithm can be fine-tuned with only two parameters: a and the number of simultaneous chains. By comparison, the MH algorithm requires $N(N+1)/2$ tuning variables, where N is the number of free parameters.

The validity of this MCMC algorithm is assessed by performing a test run with a single source (U24 in NGC 6397, with fixed distance) and comparing the resulting $M_{\rm NS}$–$R_{\rm NS}$ contours with those obtained from a simple grid-search method (`steppar` in *XSPEC*). Specifically, the obtained $M_{\rm NS}$–$R_{\rm NS}$ contours as well as other posterior distributions match those obtained from a `steppar` grid-search in *XSPEC*. The addition of Gaussian Bayesian priors on the distance is also tested with U24, which results in $M_{\rm NS}$–$R_{\rm NS}$ contours broadened in the R_∞ direction. This is because the normalization of the thermal spectrum is approximately $\propto (R_\infty/d)^2$.

For the Stretch-Move algorithm, the minimum number of simultaneous chains is equal to N + 1, where N is the number of free parameters. However, increasing the number of simultaneous chains ensures a more complete coverage of the parameter space, when comparing the results of the Stretch-Move algorithm to contours obtained with `steppar`. In addition, it reduces the chances of having the N + 1 walkers collapsing to a N – 1 dimensional space, i.e., one of the parameters has the same value within all the chains causing all following steps to evolve in the same plane. However, increasing the number of walkers also increases the convergence time.

The resulting posterior distributions are then marginalized over nuisance parameters. While necessary for the spectral fitting, these parameters do not provide physical information (e.g., α, the pile-up parameter). The results are presented in Section 6.3, where the values quoted correspond to the median value (i.e., 50% quantile) of each parameter. The results are also presented in the Figures 6.3–6.8 and 6.9–6.16, as one- and two- dimensional posterior probability density distributions. For each 1D probability density distributions, the 68%, 90%, and 99% confidence regions are calculated using quantiles, and delimited by the solid, dashed and dotted lines in the 1D probability density distribution of each figure (Figures 6.3–6.8 and 6.9–6.16). This ensures that the integrated probabities on each side of the median are equal (i.e., equal areas under the probability density curves). In addition, the median value of some parameters are different from the most probable value, especially in the case of highly skewed parameter posterior distributions. In some cases, the normalized probability of a parameter posterior distribution does not converge to zero within the parameter's hard limits in *XSPEC*. This is indicated by a '*p*' in the tables listing the parameters. The 2D posterior distributions are normalized to unity and the colour bars indicate the probability density in each bin. The 68%, 90%, and 99% contours are obtained by calculating the lines of constant probability density that enclose 68%, 90%, and 99% of the accepted MCMC steps, respectively.

6.2.7 Distances to the Globular Clusters and their Uncertainties

While most GCs have distances estimated from photometry – using RR Lyrae variable stars (Marconi et al., 2003; Bono et al., 2007), HB stars (Valenti et al., 2007; Gratton et al., 2010), or the WD sequence (Hansen et al., 2007) – these methods suffer from systematic uncertainties that are difficult to quantify. In fact, many recent photometric studies of GCs do not quote the amount of uncertainty in the measured distance (Rosenberg et al., 2000; Bica et al., 2006; Gratton et al., 2010).

While some references discuss systematic uncertainties related to the correction of extinction (e.g. McDonald et al., 2009, for ω Cen), other sources of systematic errors can affect the results, including errors related to the metallicity of cluster members (see dispersion in Figure 1 of Harris 2010), to a possible differential reddening in the direction of GCs (as observed for ω Cen, Law et al. 2003), to variations in the modeling of extinction with $R(V) \sim 3.1-3.6$ (adding $\sim 10\%$ of uncertainty, Grebel and Roberts 1995), or to the stellar evolution/atmosphere models used. As an example for the latter, distance determination methods to NGC 6397 using WDs may be affected by uncertainties in the evolutionary code models (Hansen et al., 2007; Strickler et al., 2009), which are not easily quantifiable.

Therefore, whenever possible, dynamical distance measurements are used – distances estimated from proper motion and radial velocities of cluster members. These purely geometrical methods produce well-understood uncertainties, although they are at the moment larger than reported uncertainties from photometric methods. This is consistent with the goal of this chapter which is to estimate $R_{\rm NS}$ and its uncertainties, minimizing systematic uncertainties. The upcoming mission GAIA from the *European Space Agency*, launched in 2013, is expected to produce GC distance measurements, to an accuracy of few percent, by determining the parallax of cluster members (Baumgardt and Kroupa, 2005; Baumgardt, 2008). The adopted distance values are discussed below and are summarized in Table 6.3, with uncertainties of $\lesssim 9\%$, keeping in mind that the photometric distances measurement uncertainties are

Table 6.3 – Globular Cluster Relevant Parameters

Name	$d_{\rm GC}$ (kpc)	Method	$N_{H,22}$ (X-ray)	$N_{H,22}$ (HI)	Reference
M28	5.5±0.3	HB fitting	$0.256^{+0.024}_{-0.024}$	0.24	Testa et al. (2001)
NGC 6397	2.02±0.18	Dynamical	$0.096^{+0.017}_{-0.014}$	0.14	Rees (1996)
M13	6.5±0.6	Dynamical	$0.008^{+0.044}_{-0.007}$	0.011	Rees (1996)
ω Cen	4.8±0.3	Dynamical	$0.182^{+0.045}_{-0.042}$	0.09	van de Ven et al. (2006)
NGC 6304	6.22±0.26	HB fitting	$0.346^{+0.105}_{-0.084}$	0.266	Recio-Blanco et al. (2005)

NOTES: The selection of the distance values is described in Section 6.2.7, and the quoted uncertainties are 1σ. The values of the hydrogen column densities $N_{\rm H}$ are given in units of 10^{22} atoms cm^{-2}, with 90%-confidence uncertainties from X-ray spectral fitting. The $N_{\rm H}$ (HI) column corresponds to value in the direction of globular clusters, from the HI survey of (Dickey and Lockman, 1990). The X-ray values are deduced from the best-fit $N_{\rm H}$ obtained from X-ray spectral fitting of each target in this work. Only the $N_{\rm H}$ values for NGC 6397 and ω Cen are not consistent with the HI values (see Section 6.3.1 for details). $N_{\rm H}$ values deduced from the present X-ray spectral analysis are used in the present work. HB refers to the horizontal branch of the globular clusters.

systematically underestimated. In the following list, uncertainties are quoted at the 1σ level (for GC distances, distance modulii, etc.).

- The GC M28 does not have a dynamical distance measurement, but its distance has been estimated in different works: 5.1±0.5 kpc (Rees and Cudworth, 1991), 4.8–5.0 kpc (Davidge et al., 1996) and 5.5 kpc (Harris, 1996; Testa et al., 2001), all using photometric methods. For the most recent result, uncertainties can be estimated from the uncertainties in the magnitude of the HB. Specifically, the uncertainty in $V_{\rm HB} = 15.55 \pm 0.1$, translates into the uncertainty in the distance: $d_{\rm M28} = 5.5 \pm 0.3$ kpc (Servillat et al., 2012). This measured value and its uncertainties were used here.

- The distance to NGC 6397 has been reported from a dynamical study to be $d_{\rm NGC\ 6397} = 2.02\pm0.18$ kpc (Rees, 1996). More recent photometric studies (WD sequence) have been performed, with $d = 2.54\pm0.07$ kpc (Hansen et al., 2007), or $d = 2.34\pm0.13$ kpc (Strickler et al., 2009), and the weighted mean $d = 2.50\pm0.06$ kpc was used in Chapter 5. However, since those results are model-dependent, they are not used in this Chapeter, in an effort to minimize unquantified systematics. When the present analysis was at an advanced

near-completion stage, recent results reporting a dynamical measurement of the distance was published: $d_{\mathrm{NGC\ 6397}} = 2.2^{+0.5}_{-0.7}\,\mathrm{kpc}$ (Heyl et al., 2012), consistent with $d_{\mathrm{NGC\ 6397}} = 2.02\pm0.18\,\mathrm{kpc}$, the value used in the present work.

- For M13, the dynamical distance has been measured: $d_{\mathrm{M13}} = 6.5\pm0.6\,\mathrm{kpc}$ (Rees, 1996). No other paper in the literature reports a distance measurement with quantified uncertainty. This dynamical measurement is consistent with the value $d_{\mathrm{M13}} = 7.1\,\mathrm{kpc}$ obtained form photometry (Harris, 1996; Sandquist et al., 2010). While uncertainties could be estimated for this measurement like as done for M28, the dynamical measurement is preferred to limit the effect of systematic uncertainties, as explained above.

- $\omega\,$Cen's distance was measured in a dynamical study, $d_{\omega\,\mathrm{Cen}} = 4.8\pm0.3\,\mathrm{kpc}$ (van de Ven et al., 2006), and no other reference provides a distance with its measurement uncertainty. This measurement is consistent with other estimates (e.g. $d_{\omega\,\mathrm{Cen}} = 5.2\,\mathrm{kpc}$, Harris 1996, update 2010).

- The GC NGC 6304 lacks a dynamical distance measurement. However, results from a previous work (Recio-Blanco et al., 2005, using photometric data from Piotto et al. 2002) are available. In that work, the distance modulus in the F555W filter (*HST* filter) is $(m-M)_{F555W} = 15.58\pm0.09$. The reddening in this band for NGC 6304 was not provided in the published work, but the value $E\,(B-V) = 0.52$ (Piotto et al., 2002) can be used instead. This is acceptable because the average difference between $E\,$(HST) and $E\,(B-V)$ in the Recio-Blanco et al. (2005) catalogue is $\Delta E = 0.005$, which has a negligible effect on the absolute distance modulus. Therefore, $(m-M)_0 = 13.97\pm0.09$, assuming $A_V = 3.1\times E\,(B-V)$, give $d_{\mathrm{NGC\ 6304}} = 6.22\pm0.26\,\mathrm{kpc}$.

6.3 Results

In this section, the results of the spectral analyses of each target individually, with their R_∞ measurements, are first presented. These include comparisons with previously published results. In particular, some issues regarding the reported spectral analyses for the qLMXBs in ω Cen and M13 are raised. Following this, the results of the $R_{\rm NS}$ measurement from the simultaneous fit are detailed.

6.3.1 Individual R_∞ Measurements of Neutron Stars

The analysis of the targeted qLMXBs is performed with the spectral model detailed above (Section 6.2.5). For each target, analyzed individually, the fits are statistically acceptable (i.e., with a NHP $nhp > 0.01$), which demonstrates that, within the statistics of the observations, the sources did not experience any significant spectral variability over the time scale between the observations. The resulting values and 90% confidence uncertainties, along with the χ^2-statistic obtained, are provided in Table 6.4. The spectral results obtained with $N_{\rm H}$ fixed at the X-ray-deduced values, instead of the usual HI survey values, are also provided. Discrepancies between the X-ray-deduced and HI survey values of $N_{\rm H}$, if any, are discussed for each individual target. Table 6.4 also shows the best-fit R_∞ values, calculated using Equation 2.4 from each accepted points of the MCMC runs. Uncertainties in R_∞ are then obtained from the calculated posterior distributions of R_∞ resulting for the MCMC runs. The use of MCMC simulations has the advantage of avoiding geometrical construction to calculate the uncertainties of R_∞ from the $M_{\rm NS}$–$R_{\rm NS}$ contours as performed in Chapter 5.

In the following subsections, the previously published results are compared to those obtained here. To do so, the R_∞ measurements are renormalized to the distance used in the present analysis.

Table 6.4 – Spectral Fit Results of Individual Sources

Target	$kT_{\rm eff}$ (eV)	$R_{\rm NS}$ (km)	$M_{\rm NS}$ ($M_\odot$)	R_∞ (km)	$N_{H,22}$	χ^2_ν/DOF ($p_{\rm null}$)
M28	120^{+44}_{-12}	$10.5^{+2.0}_{-2.9}$	$1.25^{+0.54}_{-0.63p}$	$13.0^{+2.3}_{-1.9}$	$0.252^{+0.025}_{-0.024}$	0.94 / 269 (0.76)
NGC 6397	76^{+14}_{-7}	$6.6^{+1.2}_{-1.1p}$	$0.84^{+0.30}_{-0.28p}$	$8.4^{+1.3}_{-1.1}$	$0.096^{+0.017}_{-0.015}$	1.06 / 223 (0.25)
M13	83^{+26}_{-11}	$10.1^{+3.7}_{-2.8p}$	$1.27^{+0.71}_{-0.63p}$	$12.8^{+4.7}_{-2.4}$	$0.008^{+0.044}_{-0.007p}$	0.94 / 63 (0.62)
ω Cen	64^{+17}_{-7}	$20.1^{+7.4p}_{-7.2}$	$1.78^{+1.03p}_{-1.07p}$	$23.6^{+7.6}_{-7.1}$	$0.182^{+0.041}_{-0.047}$	0.83 / 50 (0.80)
NGC 6304	107^{+32}_{-17}	$9.6^{+4.9}_{-3.4p}$	$1.16^{+0.90}_{-0.56p}$	$12.2^{+6.1}_{-3.8}$	$0.346^{+0.099}_{-0.093}$	1.07 / 29 (0.36)
M28	119^{+39}_{-9}	$10.6^{+0.9}_{-2.6}$	$1.17^{+0.51}_{-0.56p}$	$12.9^{+0.9}_{-0.9}$	(0.252)	0.94 / 270 (0.77)
NGC 6397	76^{+15}_{-6}	$6.6^{+0.7}_{-1.1p}$	$0.84^{+0.24}_{-0.28p}$	$8.4^{+0.5}_{-0.5}$	(0.096)	1.06 / 224 (0.26)
M13	86^{+27}_{-10}	$9.2^{+1.7}_{-2.3p}$	$1.15^{+0.42}_{-0.53p}$	$11.6^{+1.8}_{-1.5}$	(0.008)	0.93 / 64 (0.63)
ω Cen	64^{+13}_{-5}	$19.6^{+3.3}_{-3.8}$	$1.84^{+0.98p}_{-1.10p}$	$23.2^{+3.6}_{-3.3}$	(0.182)	0.82 / 51 (0.82)
NGC 6304	106^{+31}_{-13}	$9.4^{+2.4}_{-2.4p}$	$1.12^{+0.52}_{-0.51p}$	$11.8^{+2.5}_{-2.0}$	(0.346)	1.05 / 30 (0.39)

NOTES: The targets were fit individually with fixed distances. The top part shows the results of fits obtained with free values of the hydrogen column density $N_{\rm H}$, while the bottom shows results obtained with fixed $N_{\rm H}$ (indicated in parenthesis). For M28, the `pileup` model is included (see Section 6.2.5 for details), and a value $\alpha = 0.45^{+0.13}_{-0.13}$ is obtained. The posterior distribution of R_∞ was obtained by calculating the value of R_∞ from $R_{\rm NS}$ and $M_{\rm NS}$ at each accepted Marko-Chain Monte Carlo iteration. Quoted uncertainties are 90% confidence. "p" indicates that the posterior distribution did not converge to zero probability within the hard limits of the model. DOF refers to the number of degrees of freedom.

Comparison with Published Results - M28

Using the 2002 *Chandra* data, the reported R_∞ value of the qLMXB in M28 was $R_\infty = 14.5^{+6.9}_{-3.8}\,{\rm km}\ \ (D/5.5\,{\rm kpc})$ (Becker et al., 2003). An additional 200 ks of observations obtained with *Chandra*-ACIS in 2008 was used to produce a refined radius measurement: $R_{\rm NS} = 9{\pm}3\,{\rm km}$ and $M_{\rm NS} = 1.4^{+0.4}_{-0.9}\,M_\odot$, with an H-atmosphere model (Servillat et al., 2012), corresponding to $R_\infty = 12.2^{+2.6}_{-1.4}\,{\rm km}$ for $d_{\rm M28} = 5.5\,{\rm kpc}$, consistent with the discovery work (Becker et al., 2003).

All the NS parameters resulting from the present analysis (Table 6.4, Figure 6.3, $R_\infty = 13.0^{+2.3}_{-1.9}\,{\rm km}\ \ (D/5.5\,{\rm kpc})$, for $N_{H,22} = 0.252^{+0.025}_{-0.024}$) are also consistent with the previously published results. In addition, the previous work also performed a careful variability analysis (Servillat et al., 2012), confirming the findings that the qLMXB in M28 is not variable.

The best-fit $N_{\rm H}$ found here is consistent with the value from an HI survey: $N_{H,22} = 0.24$ (Dickey and Lockman, 1990), but the X-ray-measured $N_{\rm H}$ value is preferred in the rest of the present work, for the MCMC runs with fixed $N_{\rm H}$.

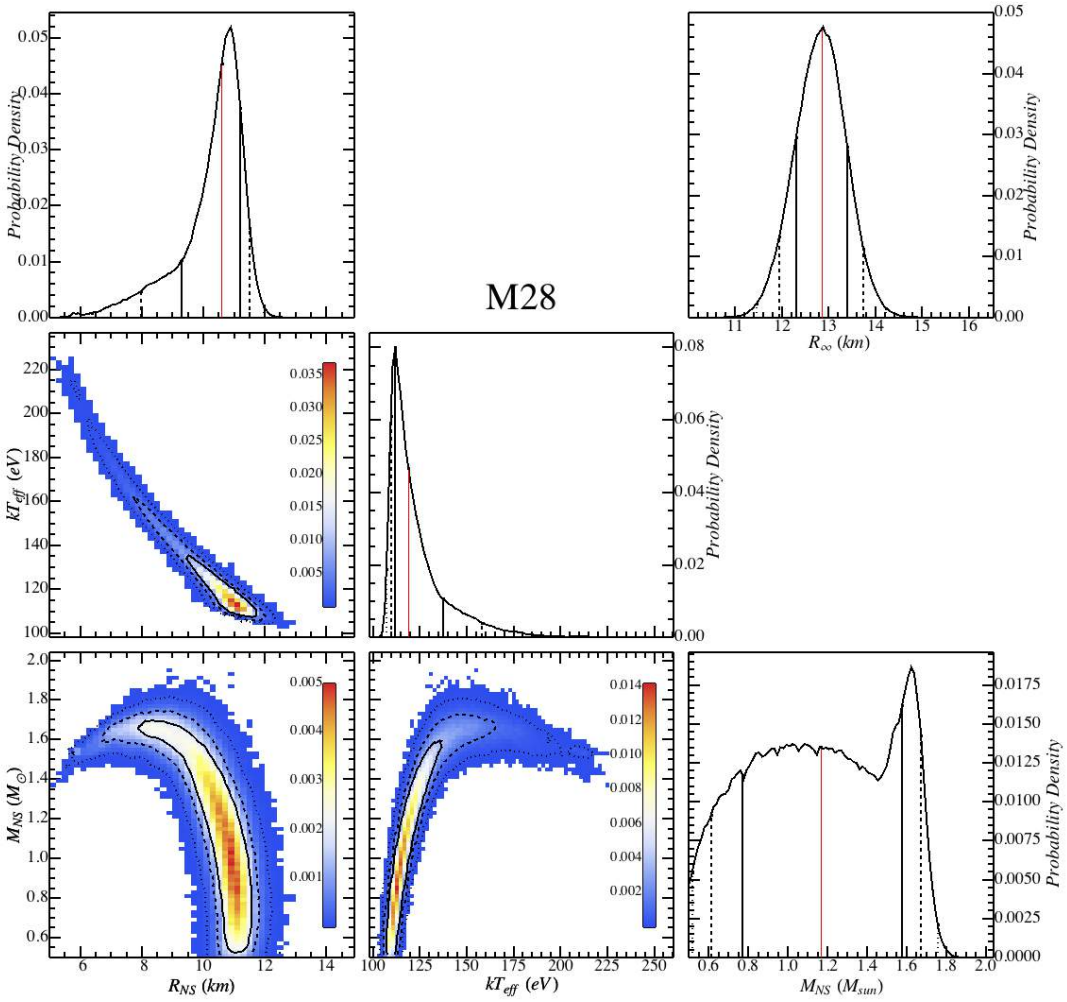

Figure 6.3 – This figure displays the one- and two- dimensional marginalized posterior distributions for the neutron star properties (radius, temperature and mass) obtained from the Markov-Chain Monte Carlo run for the quiescent low-mass X-ray binary in M28, for fixed distance and fixed $N_{\rm H}$, i.e., corresponding to the lower part of Table 6.4. The 1-dimension and 2-dimensions posterior probability density distributions are normalized to unity. The top-right plot shows the 1-dimension posterior distribution of R_∞ values. The 68%, 90% and 99% confidence intervals or regions are shown with solid, dashed, and dotted lines, respectively. In the 1-dimension distributions, the median value is shown as a red line, the 99% region is not always visible. The physical radius of the neutron star in M28 is $R_{\rm NS} = 10.6^{+0.9}_{-2.6}$ km. This corresponds to a projected radius of $R_\infty = 12.9^{+0.9}_{-0.9}$ km, for $N_{H,22} = 0.252$. The double-peaked 1-dimension distribution of $M_{\rm NS}$ is due to the strongly curved nature of the $M_{\rm NS}$–$R_{\rm NS}$ and $M_{\rm NS}$–$kT_{\rm eff}$ 2-dimensions distributions, i.e., the strong correlation between these parameters. The colour scale in each 2-dimensions distribution represents the probability density in each bin. This figure and the following Figures 6.4–6.16 were created with the Mathematica package LevelSchemes (Caprio, 2005).

Comparison with Published Results - NGC 6397

The data sets used in this work are the same as the ones used in Chapter 5. There are however minor differences in the data reduction, namely, the extraction radius used (99% EEF in this work compared to 98% EEF at 1 keV previously), the calibration files used (latest version of CALDB v4.4.8), the distance used for the spectral fit, and the energy range (0.5–8 keV in Chapter 5). After re-normalizing to the distance used in the present work, the previous R_∞ result, $R_\infty = 9.6^{+0.8}_{-0.6}$ km $(D/2.02\,\mathrm{kpc})$, is consistent with the one obtained from the MCMC run: $R_\infty = 8.4^{+1.3}_{-1.1}$ km $(D/2.02\,\mathrm{kpc})$, for $N_{H,22} = 0.096^{+0.017}_{-0.015}$ (Figure 6.4). This best-fit value of N_H is however, inconsistent with the fixed HI value ($N_\mathrm{H} = 0.14$, Dickey and Lockman 1990) used in Chapter 5 [12]. This puts into question the R_NS measurement and M_NS–R_NS contours previously published with the value $N_{H,22}$=0.14 (Chapter 5). When fixing $N_{H,22}$=0.14 in the present work, the resulting R_∞ value is $R_\infty = 11.9^{+0.8}_{-0.8}$ km $(D/2.02\,\mathrm{kpc})$, marginally consistent with the result of Chapter 5. Nonetheless, one notices that the different value of N_H causes a significantly different resulting R_NS value. Increasing the assumed value of N_H for a given target leads to a larger R_∞. This is further discussed in Section 6.4. In the rest of this chapter, the best-fit X-ray deduced N_H value $N_{H,22} = 0.096$ is used.

Comparison with Published Results - ω Cen

The original R_∞ measurement from the *Chandra* discovery observations was $R_\infty = 14.3\pm2.1$ km $(D/5.0\,\mathrm{kpc})$ for $N_{H,22} = 0.09$ (Rutledge et al., 2002b), or, when renormalized, $R_\infty = 13.7\pm2.0$ km $(D/4.8\,\mathrm{kpc})$. Another work measured the radius $R_\infty = 13.6\pm0.3$ km $(D/5.3\,\mathrm{kpc})$ with $N_{H,22} = 0.09 \pm 0.025$, equivalent to the renormalized value $R_\infty = 12.3\pm0.3$ km $(D/4.8\,\mathrm{kpc})$, using the *XMM* observation of ω Cen (Gendre et al., 2003a). Results from both analyses are consistent with the radius measurement performed in this work, with the value of Galactic absorption $N_{H,22}$=0.09, i.e.,

[12] The X-ray deduced value of N_H found here is nonetheless consistent with the N_H value from a different survey of Galactic HI (Kalberla et al., 2005), $N_{H,22}$=0.11, and with the N_H value calculated from the reddening in the direction of NGC 6397 (Harris, 1996) with a linear relation between N_H and the extinction A_V (Predehl and Schmitt, 1995).

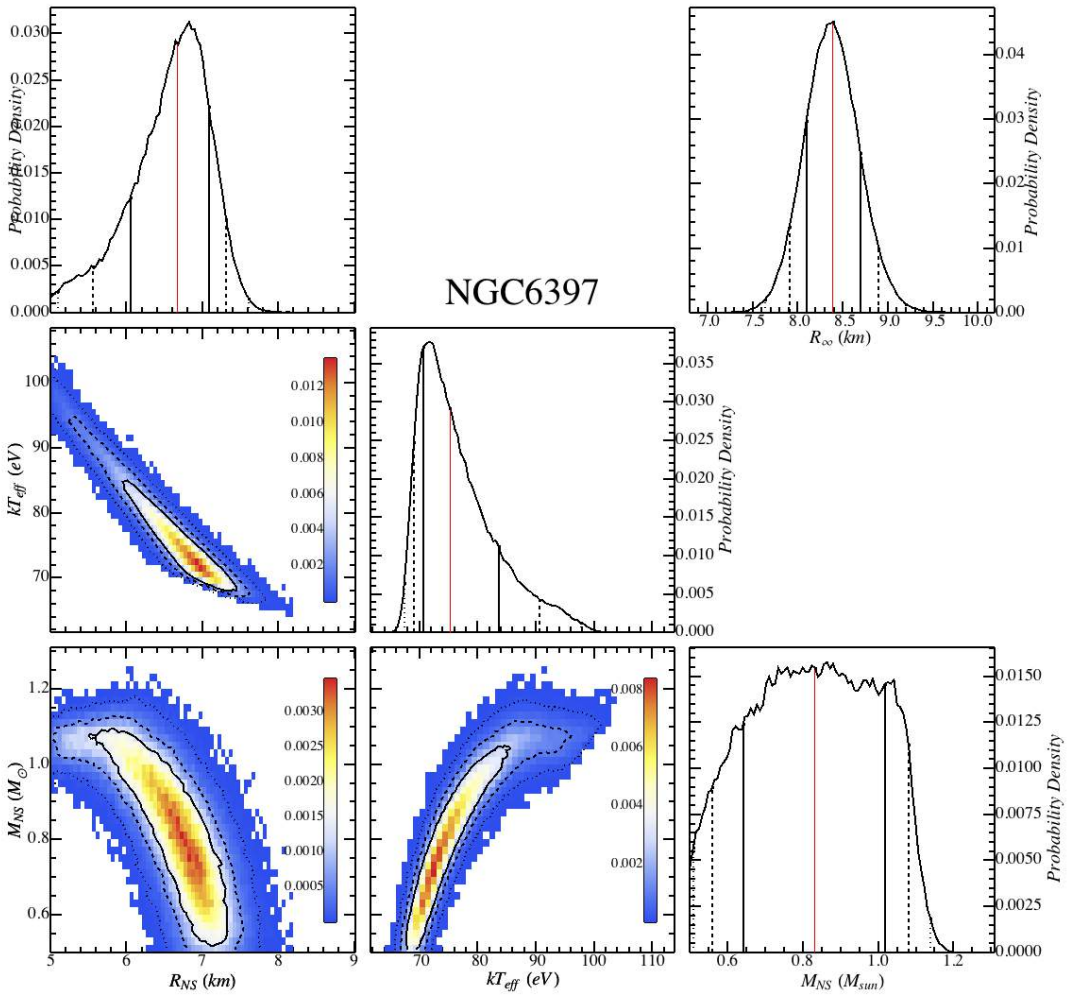

Figure 6.4 – This figure is similar to the precedent (Figure 6.3), but for the quiescent low-mass X-ray binary in NGC 6397. The physical radius of the neutron star is $R_{\rm NS} = 6.6^{+0.7}_{-1.1p}$ km which corresponds to $R_\infty = 8.4^{+0.5}_{-0.5}$ km, for $N_{H,22} = 0.096$.

$R_\infty = 11.9^{+1.6}_{-1.4}\,\mathrm{km}\ (D/4.8\,\mathrm{kpc})$. However, when removing the constraint on N_H, the best-fit R_∞ and N_H become inconsistent with the previously reported values. Specifically, $R_\infty = 23.6^{+7.6}_{-7.1}\,\mathrm{km}\ (D/4.8\,\mathrm{kpc})$ for $N_{H,22} = 0.182^{+0.041}_{-0.047}$. This value of N_H, not consistent with the HI survey value (Dickey and Lockman, 1990), was used in the remainder of the present work. The present results (best-fit R_NS, M_NS, kT_eff, and N_H) are also consistent with those previously published (Webb and Barret, 2007).

The results presented in Table 6.4 and Figure 6.5 should be treated as more realistic than the initially reported one since they make use of more recent calibrations of *XMM* and *Chandra*, as well as an improved method. In particular, the small uncertainties ($\sim 2\%$) on R_∞ previously published (Gendre et al., 2003a) are particularly intriguing. It has also been shown in another reference that the S/N obtained with 50 ks exposure of ω Cen is not sufficient to constrain the radius with $\sim 2\%$ uncertainty (Webb and Barret, 2007), but the cause of this discrepancy was not discussed. The constrained R_NS measurement with $\sim 2\%$ uncertainties (Gendre et al., 2003a) was not reproduced in the later work (Webb and Barret, 2007, $R_\mathrm{NS} = 11.7^{+7.0}_{-5.0}\,\mathrm{km}$, using the same *XMM* data), nor in the present work. Using the same model as the one initially used (Gendre et al., 2003a), similar uncertainties ($\sim 2\%$) can only be obtained when keeping the NS surface temperature fixed, leaving the normalization (i.e., the projected radius R_∞) as the sole free parameter. Specifically, with the same model and analysis procedure, the uncertainties on R_∞ are $\sigma_{R_\infty} \sim 3\%$ with the temperature fixed and becomes $\sigma_{R_\infty} \sim 15\%$ when the temperature is a free parameter. If this is the method used in Gendre et al. (2003a), the uncertainties of R_∞ only represent the statistical uncertainties and are therefore highly underestimated. It is inappropriate to keep the temperature fixed because there is no known prior on the NS surface temperature, and therefore it must remain free during the spectral fitting. In addition, the *XMM*-pn observations suffer from periods of high-background activity which need to be removed (see Figure 6.6). This leads to 34 ks of usable exposure time of the 41 ks available. No such background flares were originally reported (Gendre et al., 2003a; Webb and Barret, 2007).

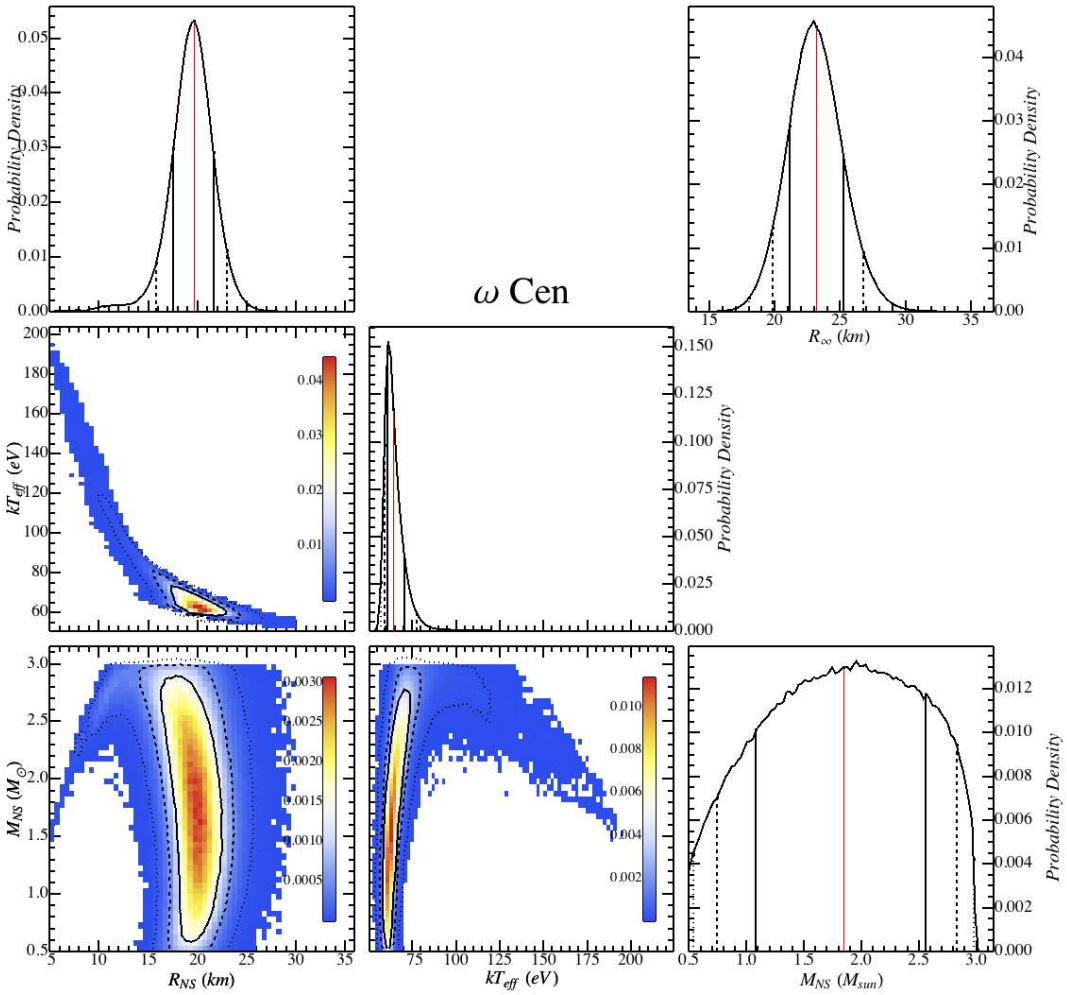

Figure 6.5 – This figure is similar to Figure 6.3, but for the quiescent low-mass X-ray binary in ω Cen. The physical radius of the neutron star is $R_{\rm NS} = 19.6^{+3.3}_{-3.8}$ km which corresponds to $R_\infty = 23.2^{+3.6}_{-3.3}$ km, for $N_{H,22} = 0.182$.

This note about the amount of uncertainty for ω Cen is of crucial importance since this source has often been used (e.g. Lattimer and Prakash, 2007) as the qLMXB with the best radius measurement available, citing the underestimated $\sim 2\%$ uncertainties on $R_{\rm NS}$. Deeper exposures of ω Cen are needed to provide constraints that will be useful for determination of the dense matter EoS. Moreover, this discussion also points out the importance of reporting $M_{\rm NS}$–$R_{\rm NS}$ contours (instead of simple $R_{\rm NS}$ measurements) for the measurements of NS properties using the thermal emission from qLMXBs.

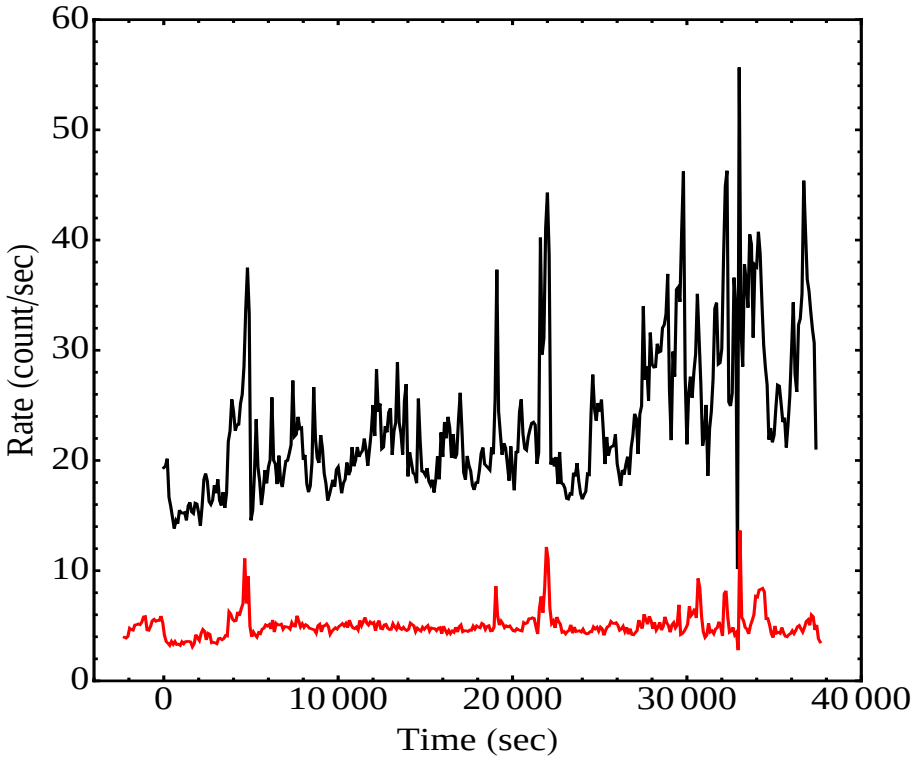

Figure 6.6 – This graph represents the *XMM*-pn full-detector light curves of ω Cen, ObsID 0112220101, with bins of 100 sec. The black (top) line corresponds to the pn camera light curve. The $t = 0$ sec time is the beginning of the pn exposure, on 2001 Aug. 12, 23:34:44. The MOS1 light curve, in red (bottom), is shown for completeness and because periods of flaring are more readily visible. The time intervals with large background flaring are excluded from the analyzed data set.

Comparison with Published Results - M13

The R_∞ value of the qLMXB in M13 reported in the discovery paper (Gendre et al., 2003b), $R_\infty = 12.8 \pm 0.4\,\mathrm{km}$ $(D/7.7\,\mathrm{kpc})$, corresponds to $R_\infty = 10.8 \pm 0.3\,\mathrm{km}$ $(D/6.5\,\mathrm{kpc})$. This value is consistent with the value presented in the present work, given the uncertainties: $R_\infty = 12.8^{+4.7}_{-2.4}\,\mathrm{km}$ $(D/6.5\,\mathrm{kpc})$, for $N_{H,22} = 0.008^{+0.044}_{-0.007p}$. The best fit N_H is consistent with HI survey values ($N_\mathrm{H} = 0.011$, Dickey and Lockman 1990), but $N_{H,22} = 0.008$ is used in the remainder of the present analysis.

Once again, the uncertainties reported in the original work are small and can only be reproduced when fixing the temperature. Similarly to ω Cen, the M13 discovery analysis was likely performed keeping the temperature frozen to estimate the uncertainty on the radius, and the $\pm 0.3\,\mathrm{km}$ uncertainties cited (Gendre et al., 2003b) are only systematic uncertainties. In summary, the results found in this work for M13 are consistent with the existing ones (Gendre et al., 2003b; Webb and Barret, 2007), and while the radius measurement uncertainties obtained here are not as constraining as those previously reported, they are considered more realistic given the S/N available for the observations, and given that more recent calibrations have been used. Similarly to ω Cen, deeper exposures of M13 would provide the necessary S/N to constrain the dense matter EoS. A recent analysis of this qLMXB found results consistent with those present when (Catuneanu et al., 2013).

Comparison with Published Results - NGC 6304

This analysis presents a new 100 ks observation of NGC 6304. The R_∞ value of the qLMXB, $R_\infty = 12.2^{+6.1}_{-3.8}\,\mathrm{km}$ $(D/6.22\,\mathrm{kpc})$, for $N_{H,22} = 0.346^{+0.099}_{-0.093}$), is consistent with that obtained from the *XMM* observation (Guillot et al., 2009a), $R_\infty = 12.1^{+6.6}_{-4.8}\,\mathrm{km}$ $(D/6.22\,\mathrm{kpc})$, and with that from a short *Chandra* observation (Guillot et al., 2009b), $R_\infty = 7.8^{+8.6}_{-3.8}\,\mathrm{km}$ $(D/6.22\,\mathrm{kpc})$, after re-normalizing the 2009 measurement to the distance used in the present work. The best-fit X-ray deduced value is also consistent with the value used in the original work, obtained from HI surveys. Nonetheless, the X-ray measured N_H value is used in the remainder of this work.

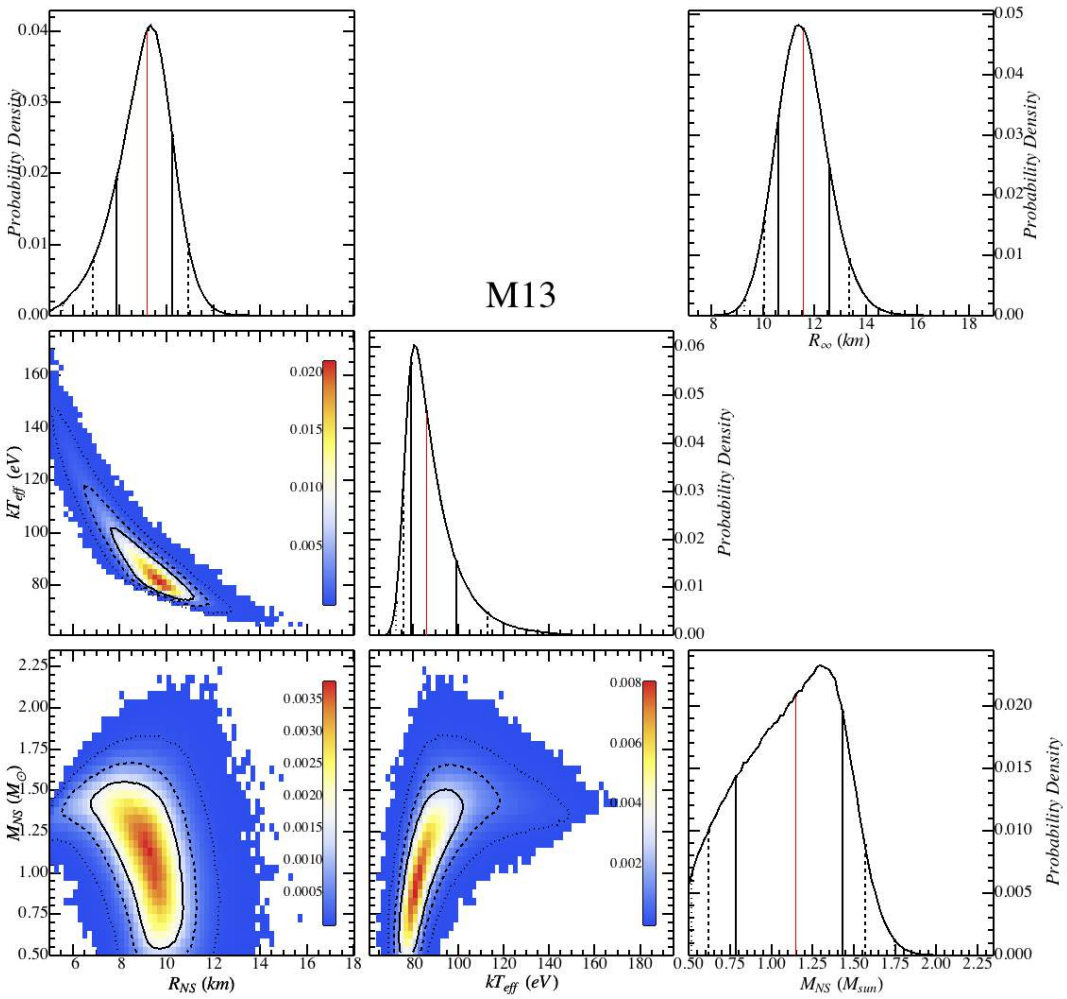

Figure 6.7 – This figure is similar to Figure 6.3, but for the quiescent low-mass X-ray binary in M13. The physical radius of the neutron star is $R_{\rm NS} = 9.2^{+1.7}_{-2.3p}$ km which corresponds to $R_\infty = 11.6^{+1.8}_{-1.5}$ km, for $N_{H,22} = 0.008$.

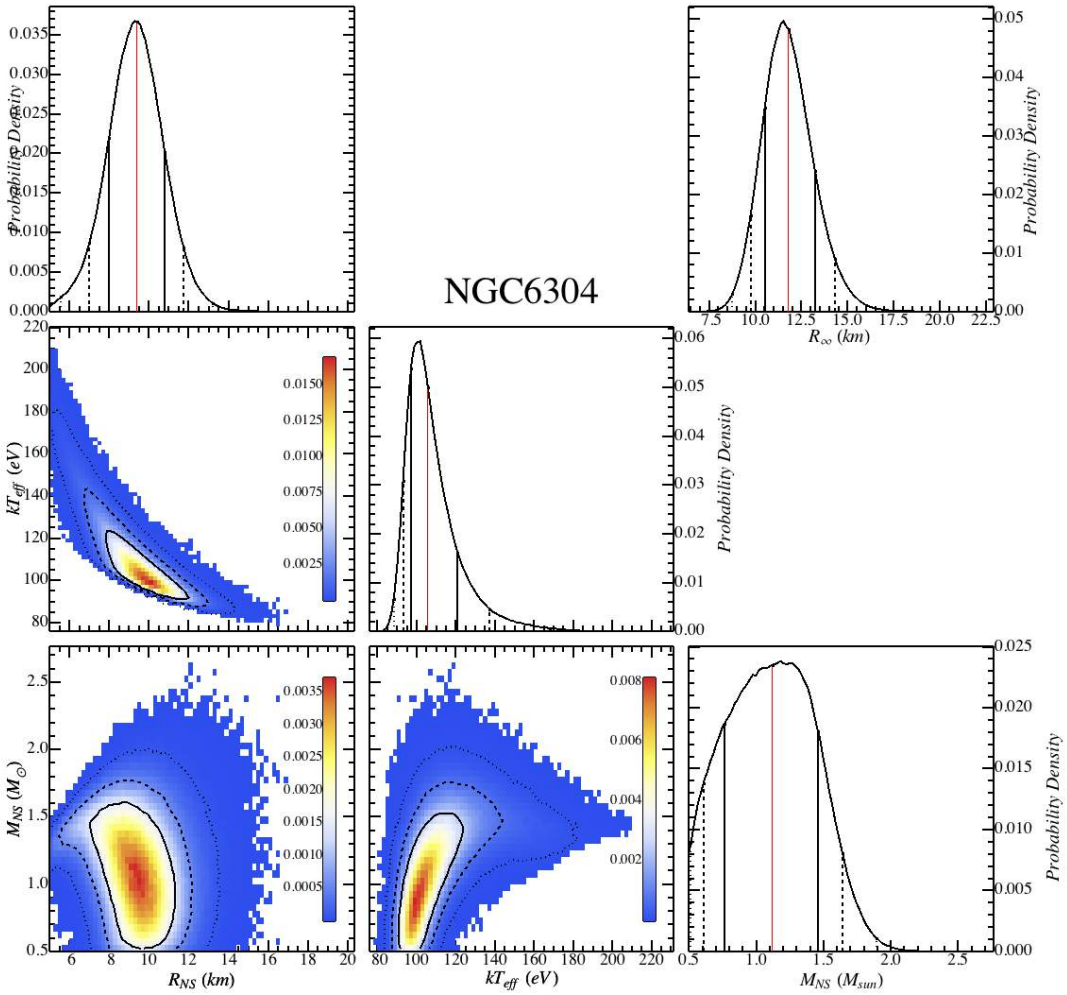

Figure 6.8 – This figure is similar to Figure 6.3, but for the quiescent low-mass X-ray binary in NGC 6304. The physical radius of the neutron star is $R_{\rm NS} = 9.5^{+2.4}_{-2.4p}$ km. The corresponding projected radius is $R_\infty = 11.8^{+2.5}_{-2.0}$ km, for $N_{H,22} = 0.346$.

6.3.2 The Measurement of $R_{\rm NS}$, the Radius of Neutron Stars

In this section, the results of the simultaneous spectral fits with the parameter posterior distributions obtained from the MCMC simulations are presented. The following distinct MCMC runs are performed:

- Run #1: Model `nsatmos` with fixed $N_{\rm H}$ values and fixed distances: 12 free parameters, 25 Stretch-Move walkers.
- Run #2: Model `nsatmos` with fixed $N_{\rm H}$ values and Gaussian Bayesian priors for the distances: 17 free parameters, 30 Stretch-Move walkers.
- Run #3: Model `nsatmos` with fixed $N_{\rm H}$ values and fixed distances, and an additional PL component: 17 free parameters, 30 Stretch-Move walkers.
- Run #4: Model `nsatmos` with fixed $N_{\rm H}$ values, Gaussian Bayesian priors for the distances, and an additional PL component (with fixed index $\Gamma = 1.0$, but free normalizations): 22 free parameters, 35 Stretch-Move walkers.
- Run #5: Model `nsatmos` with free $N_{\rm H}$ values and fixed distances: 17 free parameters, 30 Stretch-Move walkers.
- Run #6: Model `nsatmos` with free $N_{\rm H}$ values and Gausssian Bayesian priors for the distances: 22 free parameters, 35 Stretch-Move walkers.
- Run #7: Model `nsatmos` with free $N_{\rm H}$ values, Gaussian Bayesian priors for the distances, and an additional PL component: 27 free parameters, 40 Stretch-Move walkers. The spectra resulting from this run are shown in Figure 6.2.
- Run #8: Model `nsagrav` with fixed $N_{\rm H}$ values and fixed distances: 12 free parameters, 25 Stretch-Move walkers. This model is used for comparison with the `nsatmos` model.

All the runs converged to a statistically acceptable point in the parameter space, with $\chi^2_\nu \sim 1$ and $p_{\rm null} > 0.01$. In addition, the acceptance rate of each run is large

enough ($> 5\%$) that the model used and the assumptions are adequate for the data. From the accepted steps of each run, the marginalized posterior distributions of all parameters and the median values with 90% confidence regions are quoted in the tables. In addition, $M_{\rm NS}$–$R_{\rm NS}$ posterior distributions for each of the five qLMXBs are obtained.

Run #1 was performed with the maximum constraints imposed on the model. With the assumptions imposed on the parameters, this run leads to the most constrained $M_{\rm NS}$–$R_{\rm NS}$ contours of this work, resulting in $R_{\rm NS} = 7.1^{+0.5}_{-0.6}$ km (90%-confidence), and the minimum χ^2_ν/DOF ($p_{\rm null}$) = 0.97/643 (0.70). Detailed information for other parameters is shown in Table 6.5.

The possible effect of auto-correlation between the steps of the MCMC simulation is investigated by selecting every other 10 accepted point, a method called thinning (MacEachern and Berliner, 1994). The resulting confidence regions for all parameters are not affected by thinning and it can be safely concluded that the steps in the MCMC runs are not subject to auto-correlation. All the accepted steps of each run are therefore used to create the posterior distributions.

Following the first run, all assumptions (on distance, $N_{\rm H}$ and the presence of a PL) are progressively relaxed in the MCMC Runs #2 through #7, with the last one producing the $R_{\rm NS}$ measurement with the fewest assumptions. The $M_{\rm NS}$–$R_{\rm NS}$ contours and $R_{\rm NS}$ distribution of each of these are displayed in Figures 6.9–6.15 and the results are listed in Tables 6.5 and 6.6. In the process of relaxing assumptions, one confirms that the results remain consistent between each run and such process does not significantly bias the results. The effects of relaxing each assumption are briefly described below.

Using Gaussian Bayesian Priors for Distances

When adding Gaussian Bayesian priors in place of the fixed distance parameters, the $M_{\rm NS}$–$R_{\rm NS}$ contours are, as expected, broader in the R_∞ direction. Because the normalization of a thermal spectrum such a `nsatmos` is $\propto (R_\infty/d)^2$, relaxing the

Table 6.5 – Results from Simultaneous Spectral Fits, with Fixed $N_{\rm H}$

Target	$\alpha_{\rm pileup}$	$kT_{\rm eff}$ (eV)	$M_{\rm NS}$ ($M_\odot$)	R_∞ (km)	$N_{H,22}$	PL Norm $\times 10^{-7}$ keV^{-1} s^{-1} cm^{-2}
Run #1: `Fixed` $N_{\rm H}$, `Fixed` $d_{\rm GC}$, `No PL included`, $R_{\rm NS}$=$7.1^{+0.5}_{-0.6}$ km χ^2_ν/DOF ($p_{\rm null}$) = 0.97/643 (0.70), 18% accept. rate						
M28	$0.44^{+0.11}_{-0.11}$	176^{+14}_{-11}	$1.62^{+0.08}_{-0.08}$	$12.5^{+0.6}_{-0.6}$	(0.252)	–
NGC 6397	–	71^{+7}_{-3}	$0.69^{+0.26}_{-0.16p}$	$8.4^{+0.5}_{-0.5}$	(0.096)	–
M13	–	110^{+12}_{-10}	$1.41^{+0.21}_{-0.29}$	$11.0^{+1.4}_{-1.3}$	(0.008)	–
ω Cen	–	164^{+14}_{-14}	$2.05^{+0.13}_{-0.15}$	$18.9^{+1.7}_{-1.7}$	(0.182)	–
NGC 6304	–	136^{+18}_{-17}	$1.41^{+0.25}_{-0.43p}$	$11.0^{+1.8}_{-1.8}$	(0.346)	–
Run #2: `Fixed` $N_{\rm H}$, `Gaussian Bayesian priors for` $d_{\rm GC}$, `No PL included`, $R_{\rm NS}$=$7.6^{+0.9}_{-0.9}$ km χ^2_ν/DOF ($p_{\rm null}$) = 0.98/638 (0.64), 11% accept. rate						
M28	$0.44^{+0.11}_{-0.10}$	165^{+22}_{-20}	$1.63^{+0.14}_{-0.15}$	$12.6^{+1.}_{-1.0}$	(0.252)	–
NGC 6397	–	71^{+8}_{-3}	$0.73^{+0.33}_{-0.20p}$	$9.0^{+1.1}_{-0.9}$	(0.096)	–
M13	–	101^{+20}_{-16}	$1.34^{+0.33}_{-0.53p}$	$11.0^{+1.9}_{-1.7}$	(0.008)	–
ω Cen	–	154^{+21}_{-22}	$2.16^{+0.22}_{-0.21}$	$19.3^{+2.3}_{-2.1}$	(0.182)	–
NGC 6304	–	127^{+23}_{-19}	$1.36^{+0.34}_{-0.59p}$	$11.0^{+2.1}_{-1.8}$	(0.346)	–
Run #3: `Fixed` $N_{\rm H}$, `Fixed` $d_{\rm GC}$, `PL included`, $R_{\rm NS}$=$7.3^{+0.5}_{-0.6}$ km χ^2_ν/DOF ($p_{\rm null}$) = 0.96/638 (0.78), 15% accept. rate						
M28	$0.35^{+0.12}_{-0.12}$	170^{+14}_{-11}	$1.63^{+0.08}_{-0.08}$	$12.6^{+0.6}_{-0.6}$	(0.252)	$5.1^{+3.7}_{-3.4p}$
NGC 6397	–	70^{+7}_{-3}	$0.68^{+0.28}_{-0.15p}$	$8.6^{+0.5}_{-0.5}$	(0.096)	$2.2^{+1.3}_{-1.3p}$
M13	–	109^{+12}_{-11}	$1.50^{+0.24}_{-0.32}$	$11.7^{+1.8}_{-1.5}$	(0.008)	$2.2^{+4.2}_{-2.0p}$
ω Cen	–	163^{+13}_{-14}	$2.14^{+0.14}_{-0.16}$	$19.9^{+1.9}_{-1.9}$	(0.182)	$2.9^{+3.7}_{-2.4p}$
NGC 6304	–	136^{+18}_{-17}	$1.51^{+0.26}_{-0.44p}$	$11.7^{+2.0}_{-2.0}$	(0.346)	$1.7^{+2.5}_{-1.5p}$
Run #4: `Fixed` $N_{\rm H}$, `Gaussian Bayesian priors for` $d_{\rm GC}$, `PL included`, $R_{\rm NS}$=$8.0^{+1.0}_{-1.0}$ km χ^2_ν/DOF ($p_{\rm null}$) = 0.97/633 (0.72), 11% accept. rate						
M28	$0.35^{+0.12}_{-0.12}$	157^{+24}_{-20}	$1.64^{+0.15}_{-0.18}$	$12.8^{+1.0}_{-1.0}$	(0.252)	$5.0^{+3.8}_{-3.4p}$
NGC 6397	–	70^{+8}_{-3}	$0.72^{+0.37}_{-0.19p}$	$9.4^{+1.1}_{-1.0}$	(0.096)	$2.2^{+1.3}_{-1.3p}$
M13	–	99^{+22}_{-17}	$1.43^{+0.37}_{-0.61p}$	$11.7^{+2.3}_{-1.9}$	(0.008)	$2.2^{+4.0}_{-1.9p}$
ω Cen	–	151^{+21}_{-21}	$2.28^{+0.25}_{-0.25}$	$20.4^{+2.6}_{-2.4}$	(0.182)	$3.0^{+3.8}_{-2.5p}$
NGC 6304	–	125^{+24}_{-20}	$1.46^{+0.36}_{-0.69p}$	$11.8^{+2.2}_{-2.1}$	(0.346)	$1.7^{+2.4}_{-1.5p}$

NOTES: $\alpha_{\rm pileup}$ corresponds to the parameter of the `pileup` model. "PL Norm." refers to the value of the normalization of the power-law (PL) component, when used. For each run, the characteristics are described: whether or not the absorption $N_{\rm H}$ was fixed; whether the globular cluster distances $d_{\rm GC}$ were fixed or if a Bayesian prior was imposed; whether or not a additional power-law component was included in the model. For each run, the best χ^2_ν value is provided, as well as the null hypothesis probability $p_{\rm null}$. Finally, the acceptance rate (not including the burn-in period) is provided. All quoted uncertainties are 90% confidence. Values in parentheses are kept fixed in the analysis. "p" indicates that the posterior distribution did not converge to zero probability within the hard limit of the model. DOF refers to the number of degrees of freedom.

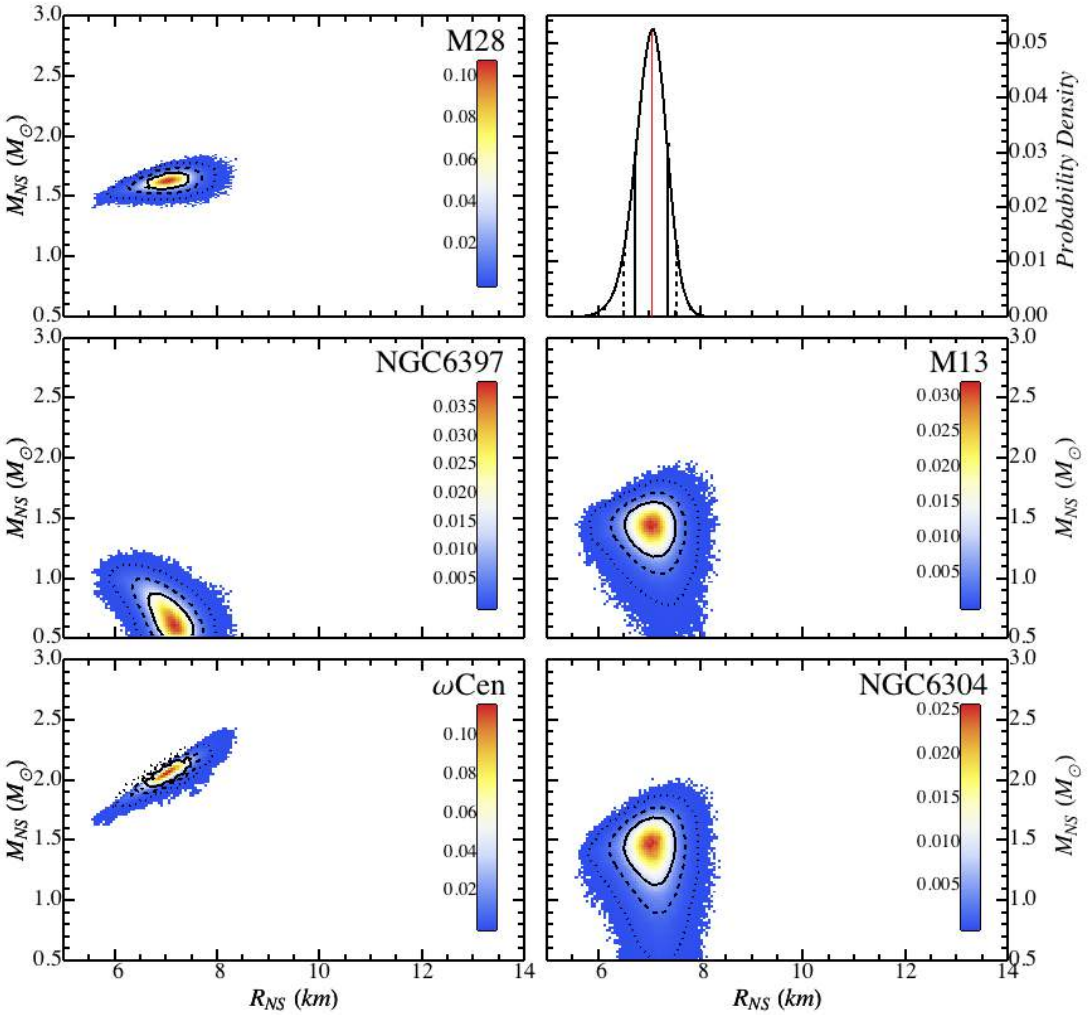

Figure 6.9 – This figure displays the marginalized posterior distribution in $M_{\rm NS}$–$R_{\rm NS}$ space for the five quiescent low-mass X-ray binaries, in the first Markov-Chain Monte Carlo run, where the distance and the hydrogen column density $N_{\rm H}$ are fixed, and where no power-law component is added, corresponding to Run #1. The 1-dimension and 2-dimensions posterior probability distributions are normalized to unity. The colour scale in the 2-dimensions distributions represents the probability density in each bin. The 68%, 90% and 99%-confidence contours are shown with solid, dashed and dotted lines on the $M_{\rm NS}$–$R_{\rm NS}$ density plots, respectively. The top-right graph is the resulting normalized probability distribution of $R_{\rm NS}$, common to the five quiescent low-mass X-ray binaries, with the 68%, 90% and 99%-confidence regions represented by the solid, dashed and dotted vertical lines. The median value is shown by the red line. The measured radius is $R_{\rm NS} = 7.1^{+0.5}_{-0.6}$ km (90% confidence).

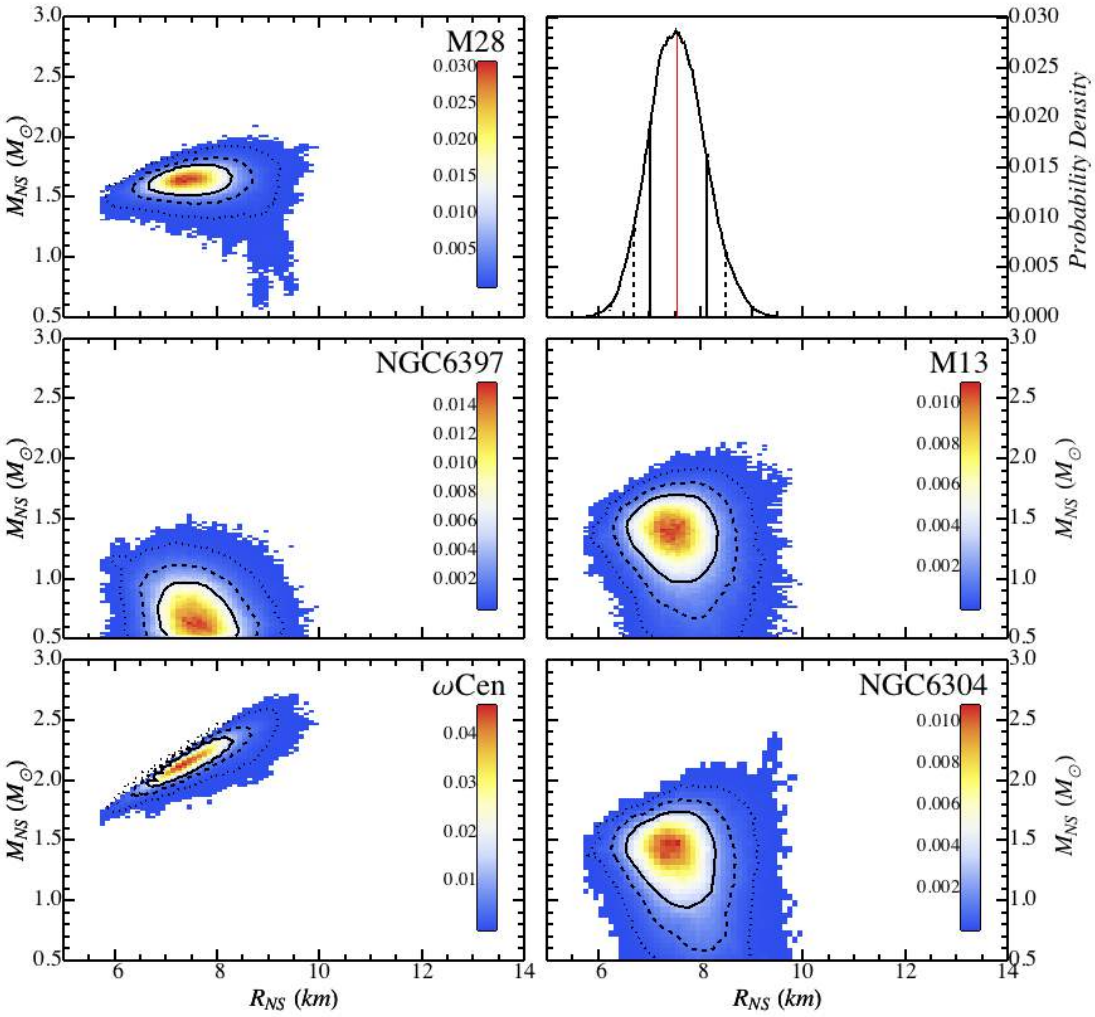

Figure 6.10 – This figure is similar to the previous one, Fig 6.9, but for the Markov-Chain Monte Carlo Run #2, where Gaussian Bayesian priors were used for the distances to the five quiescent low-mass X-ray binaries (see Table 6.3). The resulting radius measurement is $R_{\rm NS} = 7.6^{+0.9}_{-0.9}$ km.

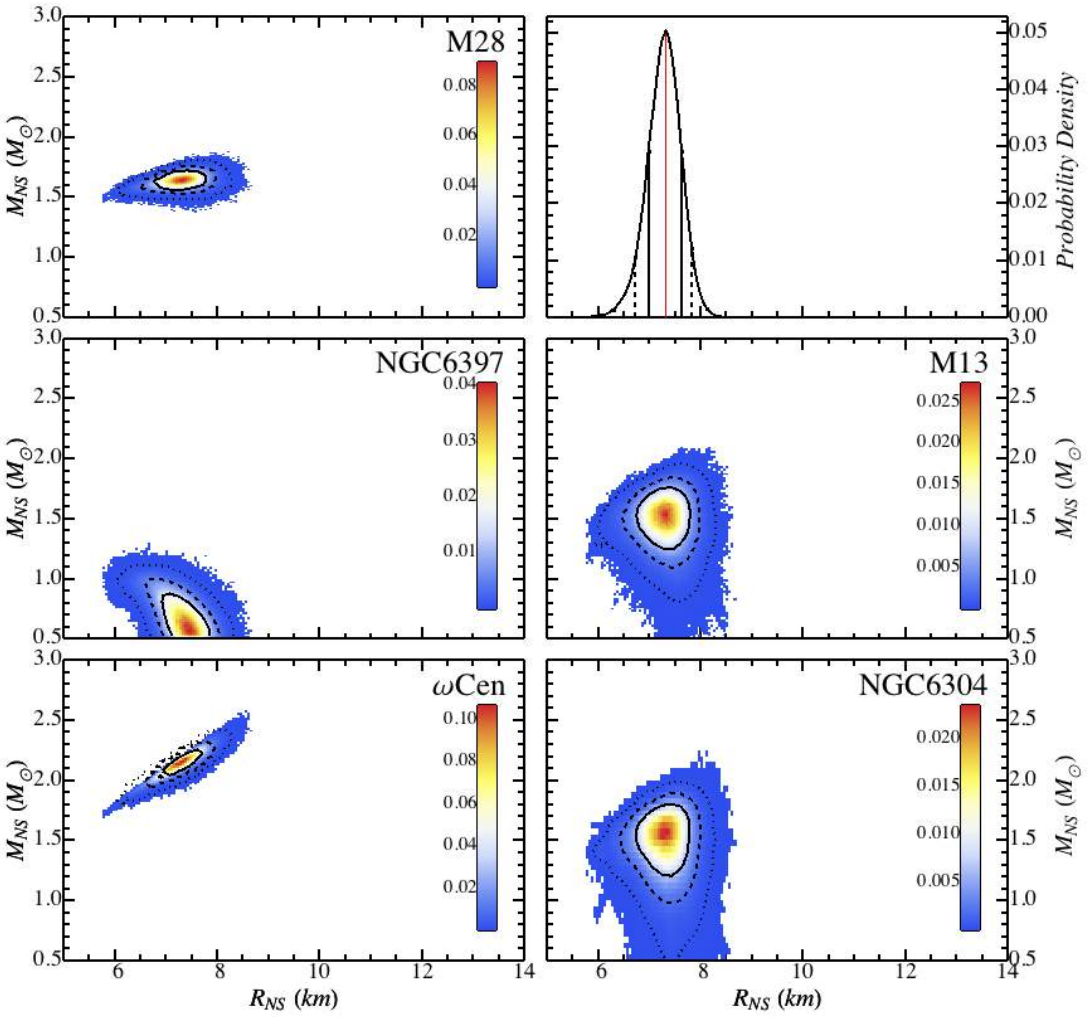

Figure 6.11 – This figure, similar to Figure 6.9, corresponds to the results of Run #3. In this run, the distances are fixed (no priors included), but a power-law component (with fixed photon index $\Gamma = 1$) is added to the spectral model, leading to $R_{\rm NS} = 7.3^{+0.5}_{-0.6}$ km.

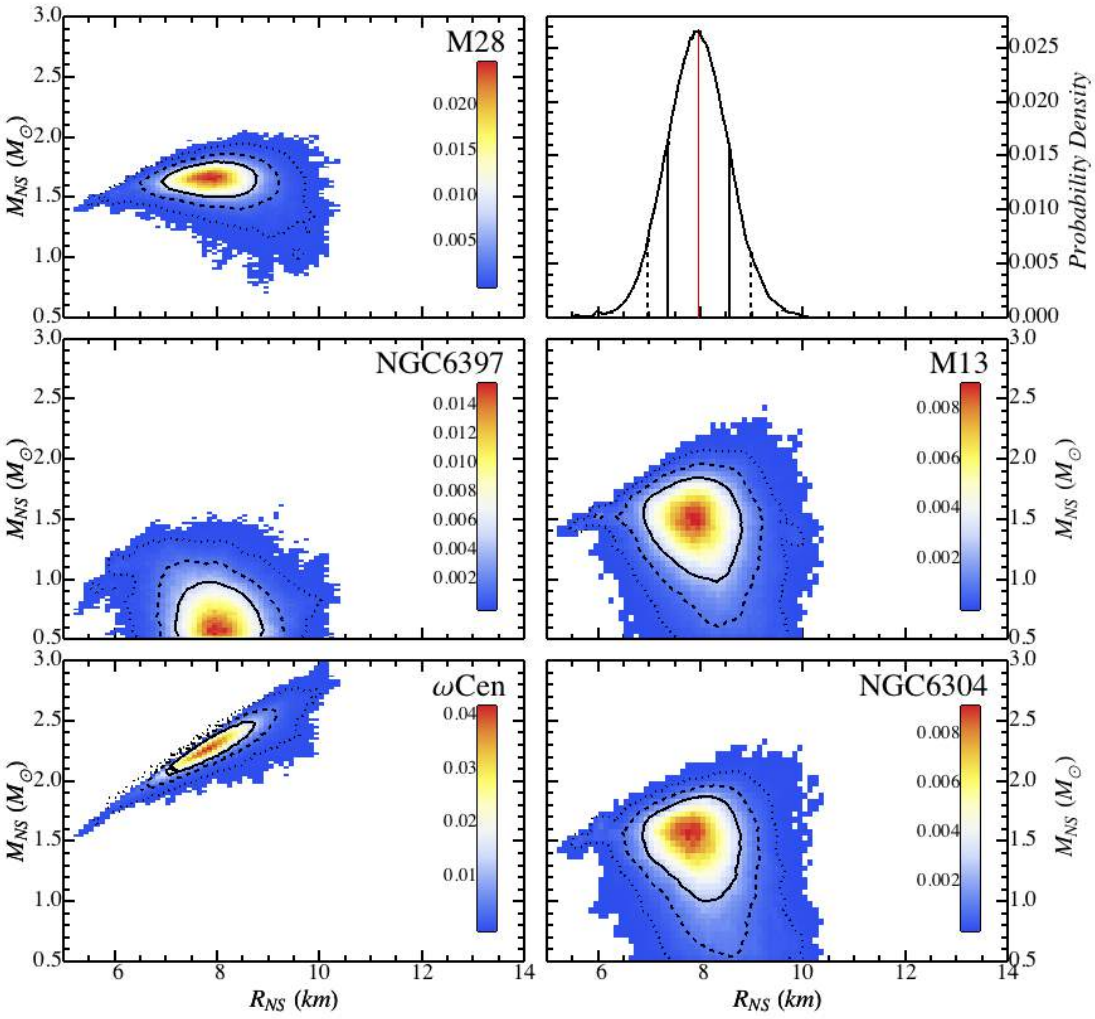

Figure 6.12 – This figure is similar to Figure 6.9, but for Run #4. Here, the Gaussian Bayesian priors on the distances are included, as well as the power-law spectral component, with $N_{\rm H}$ held fixed. The resulting neutron star radius is $R_{\rm NS} = 8.0^{+1.0}_{-1.0}$ km.

assumptions on $d_{\rm GC}$ increases the range of R_∞ values. This effect is mostly noticeable for the two targets observed with the highest S/N, i.e., M28 and NGC 6397. In Run #2, the posterior distribution of $R_{\rm NS}$ corresponds to $R_{\rm NS} = 7.6^{+0.9}_{-0.9}\,{\rm km}$, broader than that of the previous run.

Adding a Power-Law Spectral Component

When adding PL components to account for possible excesses of photons at high energy, one finds NS parameters consistent with those of the previous runs. Most PL normalizations are consistent with zero in Runs #3, #4 and #7. For M28, the PL normalizations in these runs is consistent with zero, within 2.4σ. For NGC 6397 in Runs #3 and #4, the consistency with zero is only marginal, within 2.8σ. Finally, in Run #7, the PL normalization of NGC 6397, ${\rm Norm}_{\rm PL,NGC\ 6397} = 2.7^{+1.3}_{-1.3}\times10^{-7}\,{\rm keV}^{-1}\,{\rm s}^{-1}\,{\rm cm}^{-2}$, is not consistent with zero. This may indicate the possible contribution of a PL component at large energies and it is further discussed in Section 6.4.

Relaxing the $N_{\rm H}$ Assumption

As the constraints on the $N_{\rm H}$ parameters are relaxed, the `nsatmos` best-fit parameters remain consistent with those of the previous runs. The posterior distributions of the five $N_{\rm H}$ parameters are consistent with the X-ray deduced $N_{\rm H}$ values found from the spectral fits of the sources individually, i.e., the values used in Run #1–4.

All Assumptions Relaxed

For this final run (#7), $R_{\rm NS} = 9.1^{+1.3}_{-1.5}\,{\rm km}$ is consistent with the radii obtained in the previous MCMC runs (#1–6). The posterior distributions of $M_{\rm NS}$–$R_{\rm NS}$ are shown in Figure 6.15 and detailed in Table 6.6. Once again, all resulting values are consistent with those of the previous runs. Progressively relaxing assumptions ensures a good understanding of the spectral fit, with no unexpected behaviour.

Table 6.6 – Results from the Simultaneous Spectral Fits, with Free $N_{\rm H}$

Target	$\alpha_{\rm pileup}$	$kT_{\rm eff}$ (eV)	$M_{\rm NS}$ ($M_\odot$)	R_∞ (km)	$N_{H,22}$	PL Norm $\times 10^{-7}$ keV^{-1} s^{-1} cm^{-2}
Run #5: `Free` $N_{\rm H}$, `Fixed` $d_{\rm GC}$, `No PL included`, $R_{\rm NS}=7.5^{+1.1}_{-1.0}$ km χ^2_ν/DOF ($p_{\rm null}$) = 0.98/638 (0.66), 8% accept. rate						
M28	$0.43^{+0.13}_{-0.13}$	165^{+24}_{-22}	$1.60^{+0.21}_{-0.25}$	$12.4^{+1.6}_{-1.5}$	$0.248^{+0.023}_{-0.022}$	–
NGC 6397	–	70^{+8}_{-5}	$0.76^{+0.33}_{-0.22p}$	$9.0^{+1.4}_{-1.1}$	$0.105^{+0.016}_{-0.015}$	–
M13	–	106^{+20}_{-16}	$1.43^{+0.36}_{-0.44p}$	$11.4^{+2.5}_{-1.7}$	$0.010^{+0.024}_{-0.009p}$	–
ω Cen	–	137^{+32}_{-31}	$2.00^{+0.36}_{-0.41}$	$16.7^{+4.7}_{-4.3}$	$0.152^{+0.048}_{-0.049}$	–
NGC 6304	–	120^{+28}_{-14}	$1.13^{+0.59}_{-0.54p}$	$10.1^{+3.2}_{-1.9}$	$0.315^{+0.079}_{-0.060}$	–
Run #6: `Free` $N_{\rm H}$, `Gaussian Bayesian priors for` $d_{\rm GC}$, `No PL included`, $R_{\rm NS}=7.8^{+1.3}_{-1.1}$ km χ^2_ν/DOF ($p_{\rm null}$) = 0.99/633 (0.59), 8% accept. rate						
M28	$0.42^{+0.13}_{-0.13}$	158^{+26}_{-29}	$1.59^{+0.25}_{-0.45p}$	$12.4^{+1.8}_{-1.7}$	$0.248^{+0.023}_{-0.022}$	–
NGC 6397	–	71^{+9}_{-5}	$0.78^{+0.39}_{-0.24p}$	$9.4^{+1.6}_{-1.3}$	$0.104^{+0.016}_{-0.015}$	–
M13	–	100^{+23}_{-18}	$1.38^{+0.42}_{-0.64p}$	$11.3^{+2.6}_{-2.0}$	$0.010^{+0.023}_{-0.009p}$	–
ω Cen	–	133^{+35}_{-30}	$2.07^{+0.41p}_{-0.43}$	$17.1^{+5.2}_{-4.4}$	$0.156^{+0.050}_{-0.048}$	–
NGC 6304	–	116^{+30}_{-14}	$1.09^{+0.68}_{-0.52p}$	$10.3^{+3.4}_{-1.9}$	$0.321^{+0.078}_{-0.061}$	–
Run #7: `Free` $N_{\rm H}$, `Gaussian Bayesian priors for` $d_{\rm GC}$, `PL included`, $R_{\rm NS}=9.1^{+1.3}_{-1.5}$ km χ^2_ν/DOF ($p_{\rm null}$) = 0.98/628 (0.64), 7% accept. rate						
M28	$0.34^{+0.14}_{-0.14}$	137^{+29}_{-22}	$1.50^{+0.37}_{-0.80p}$	$12.6^{+2.0}_{-2.0}$	$0.248^{+0.024}_{-0.023}$	$5.0^{+3.7}_{-3.4p}$
NGC 6397	–	67^{+8}_{-5}	$0.86^{+0.47}_{-0.31p}$	$10.8^{+1.7}_{-1.7}$	$0.116^{+0.017}_{-0.017}$	$2.7^{+1.3}_{-1.3}$
M13	–	92^{+24}_{-15}	$1.47^{+0.62}_{-0.78p}$	$12.6^{+3.7}_{-2.3}$	$0.014^{+0.028}_{-0.012p}$	$2.4^{+4.1}_{-2.1p}$
ω Cen	–	130^{+33}_{-31}	$2.42^{+0.42p}_{-0.54}$	$20.3^{+5.6}_{-5.7}$	$0.172^{+0.047}_{-0.051}$	$2.9^{+3.9}_{-2.6p}$
NGC 6304	–	112^{+31}_{-15}	$1.32^{+0.80}_{-0.71p}$	$12.1^{+4.3}_{-2.5}$	$0.346^{+0.086}_{-0.065}$	$1.8^{+2.6}_{-1.5p}$

Notes: This table is similar to Table 6.5, abbreviations and symbols are the same. The only difference is that the absorption $N_{\rm H}$ remained free for these runs. Quoted uncertainties are 90% confidence as well. "p" indicates that the posterior distribution did not converge to zero probability within the hard limit of the model.

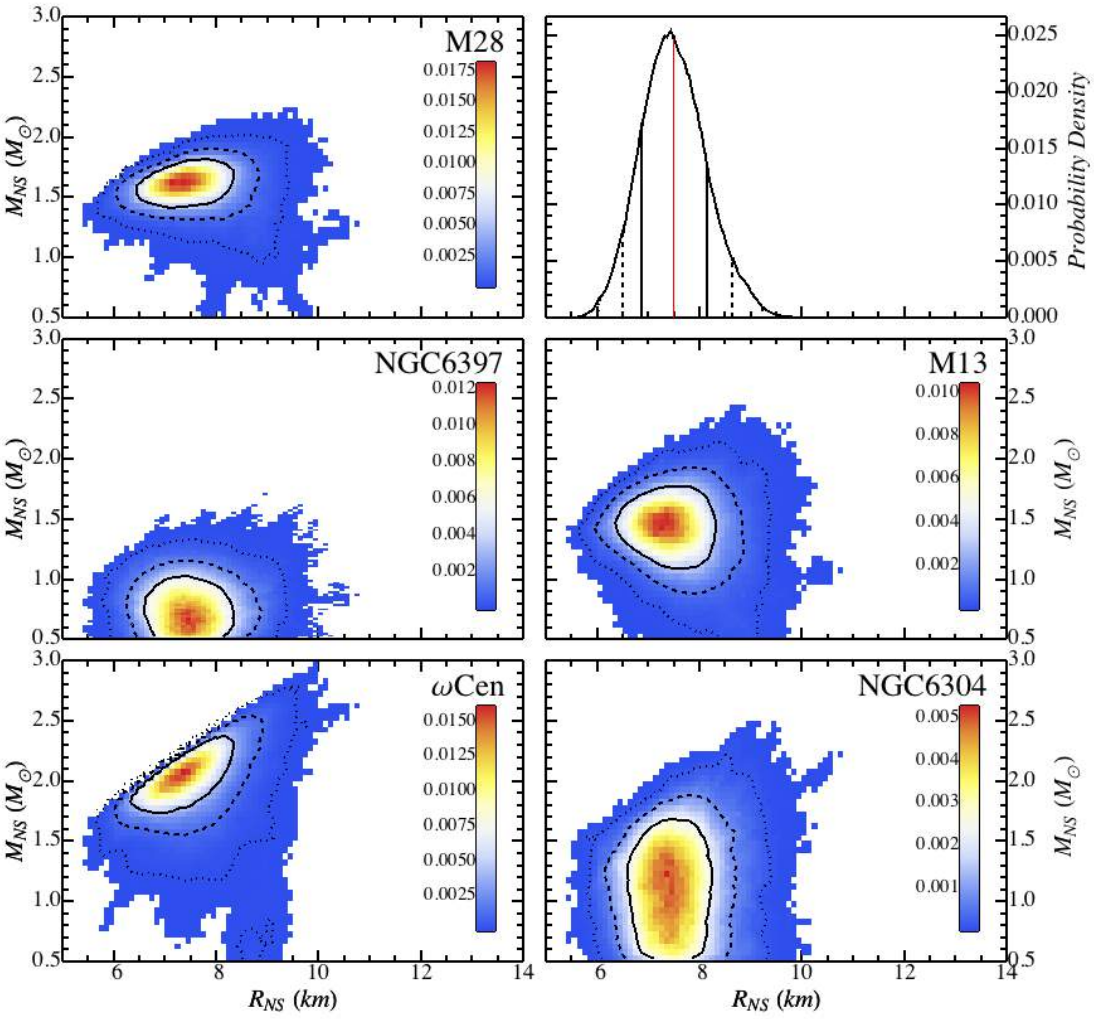

Figure 6.13 – This figure, similar to Figure 6.9, shows the results of Run #5. The hydrogen column density $N_{\rm H}$ is left free in this run, but the distances remained fixed, and no power-law component was added. This run produced $R_{\rm NS} = 7.5^{+1.1}_{-1.0}$ km.

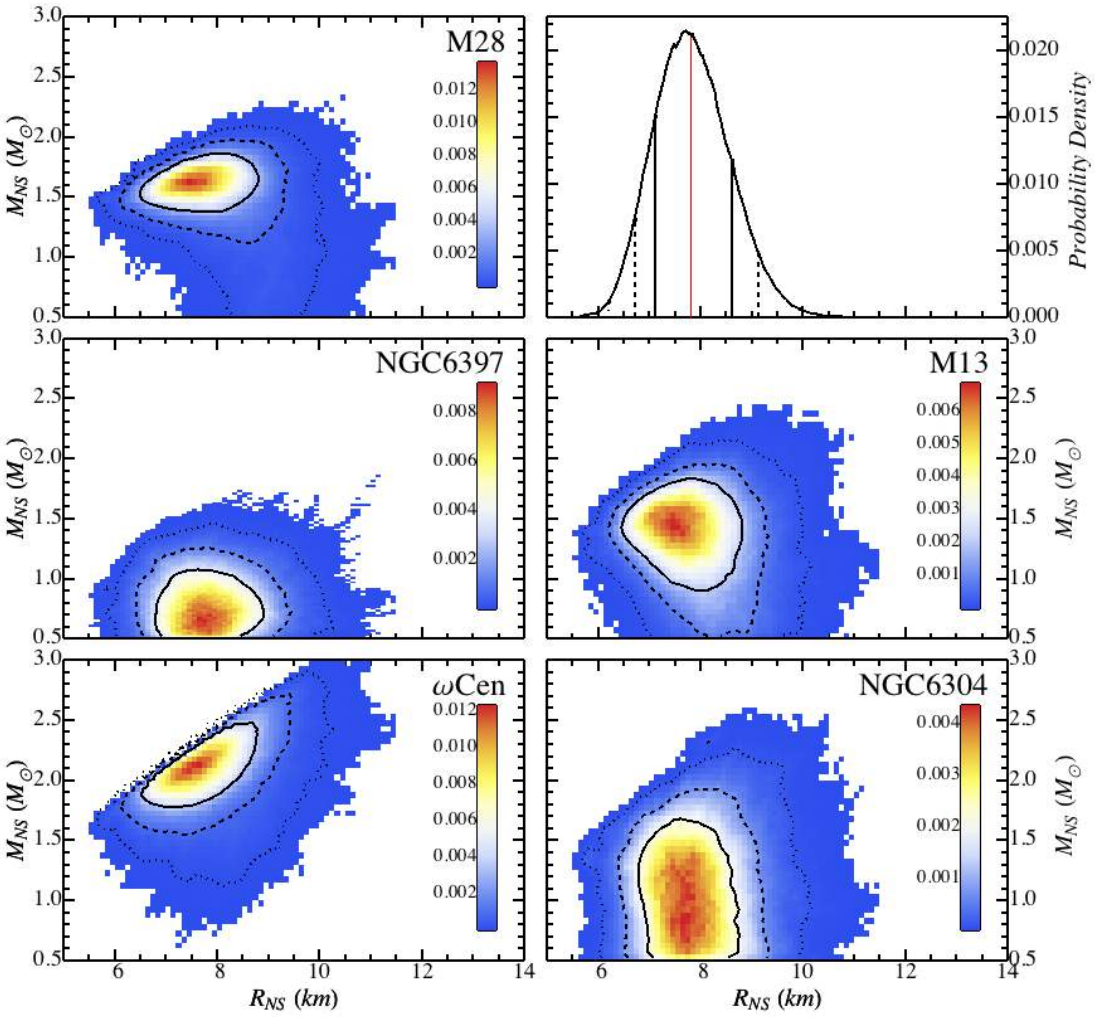

Figure 6.14 – This figure is similar to Figure 6.9, but for the Markov-Chain Monte Carlo Run #6. The characteristics of this run include $N_{\rm H}$ values free to vary in the fit, and the presence of the Gaussian Bayesian priors for the distances. No power-law component was included in run. A value $R_{\rm NS} = 7.8^{+1.3}_{-1.1}$ km was found.

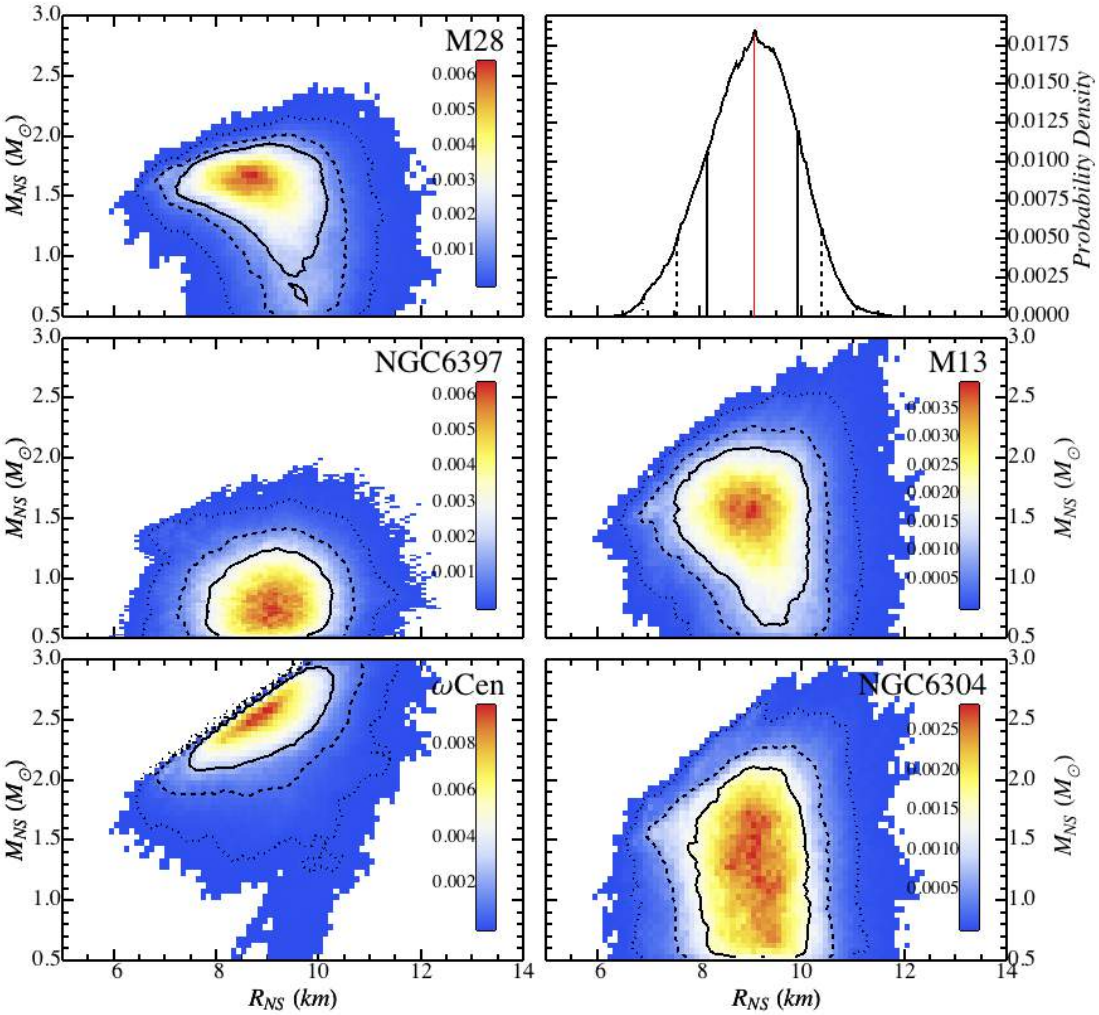

Figure 6.15 – This figure, similar to Figure 6.9, corresponds to Run #7. Here, all the possible assumptions have been relaxed to obtain a $R_{\rm NS}$ measurement the least affected by systematic uncertainties. The $N_{\rm H}$ parameters are left free; and Gaussian Bayesian priors and power-law components are included. This results in an $R_{\rm NS}$ measurement: $R_{\rm NS} = 9.1^{+1.3}_{-1.5}\,{\rm km}$

Table 6.7 – Results from the Simultaneous Spectral Fit with `nsagrav`

Target	$\alpha_{\rm pileup}$	$kT_{\rm eff}$ (eV)	$M_{\rm NS}$ ($M_\odot$)	R_∞ (km)	$N_{H,22}$
Run #8: `Fixed` $N_{\rm H}$, `Fixed` $d_{\rm GC}$, `No PL included`, $R_{\rm NS}$=$7.8^{+0.5}_{-0.3}$ km χ^2_ν/DOF ($p_{\rm null}$) = 1.04/643 (0.25), 10% accept. rate					
M28	$0.46^{+0.11}_{-0.11}$	166^{+4}_{-13}	$2.03^{+0.42p}_{-0.43}$	$16.3^{+12.6}_{-3.9}$	(0.252)
NGC 6397	–	66^{+3}_{-2}	$0.51^{+0.23}_{-0.15p}$	$8.7^{+0.6}_{-0.5}$	(0.096)
M13	–	101^{+12}_{-11}	$1.42^{+0.88p}_{-0.49p}$	$11.5^{+11.2}_{-1.7}$	(0.008)
ω Cen	–	113^{+2}_{-3}	$1.86^{+0.36p}_{-0.15}$	$14.3^{+4.8}_{-1.2}$	(0.182)
NGC 6304	–	126^{+17}_{-19}	$1.41^{+0.97p}_{-0.74p}$	$11.4^{+14.1}_{-2.3}$	(0.346)

Notes: This table is similar to Table 6.5, abbreviations and symbols are the same. But this run was performed with the `nsagrav` model instead of the `nsatmos` model for comparison purposes. The differences between the two models are described in Section 6.3.2, for example, in the high-redshift regime (See Figure 6.16). "p" indicates that the posterior distribution did not converge to zero probability within the hard limit of the model. Quoted uncertainties are 90% confidence.

Comparison with `nsagrav`

A spectral fit using the model `nsagrav` instead of `nsatmos` is also performed for comparison purposes. It has previously been shown that `nsatmos` and `nsagrav` produce similar spectral parameters when fit to experimental data (e.g. Webb and Barret, 2007). In *XSPEC*, for the `nsagrav` model, the $R_{\rm NS}$ range is $[6\,{\rm km}, 20\,{\rm km}]$, and the $M_{\rm NS}$ range is $[0.3\,M_\odot, 2.5\,M_\odot]$ compared to $[5\,{\rm km}, 30\,{\rm km}]$ and $[0.5\,M_\odot, 3.0\,M_\odot]$ with `nsatmos`. This run (#8) was done with the same characteristics as Run #1.

When comparing the posterior distributions of the parameters and $M_{\rm NS}$–$R_{\rm NS}$ contours obtained with `nsagrav` (Figure 6.16 for Run #1 and Table 6.7) to those obtained with `nsatmos` (Figure 6.9 and Table 6.5), some consistencies can be noticed. However, not all distributions are consistent between the two models. Specifically, for M28, M13, and NGC 6304, one can notice that an additional distinct lobe at high $M_{\rm NS}$ appears in the $M_{\rm NS}$–$R_{\rm NS}$ parameter space. This appears to be because the `nsagrav` model as implemented in `XSPEC` gives different values in this parameter space than returned by `nsatmos`; the authors of this model state that this is because the model is inapplicable in this parameter region[13] (Zavlin and Pavlov, priv. comm.).

[13]The $M_{\rm NS}$–$R_{\rm NS}$ space where `nsagrav` is applicable can be seen here `http://heasarc.gsfc.nasa.gov/xanadu/xspec/models/m-r.pdf`

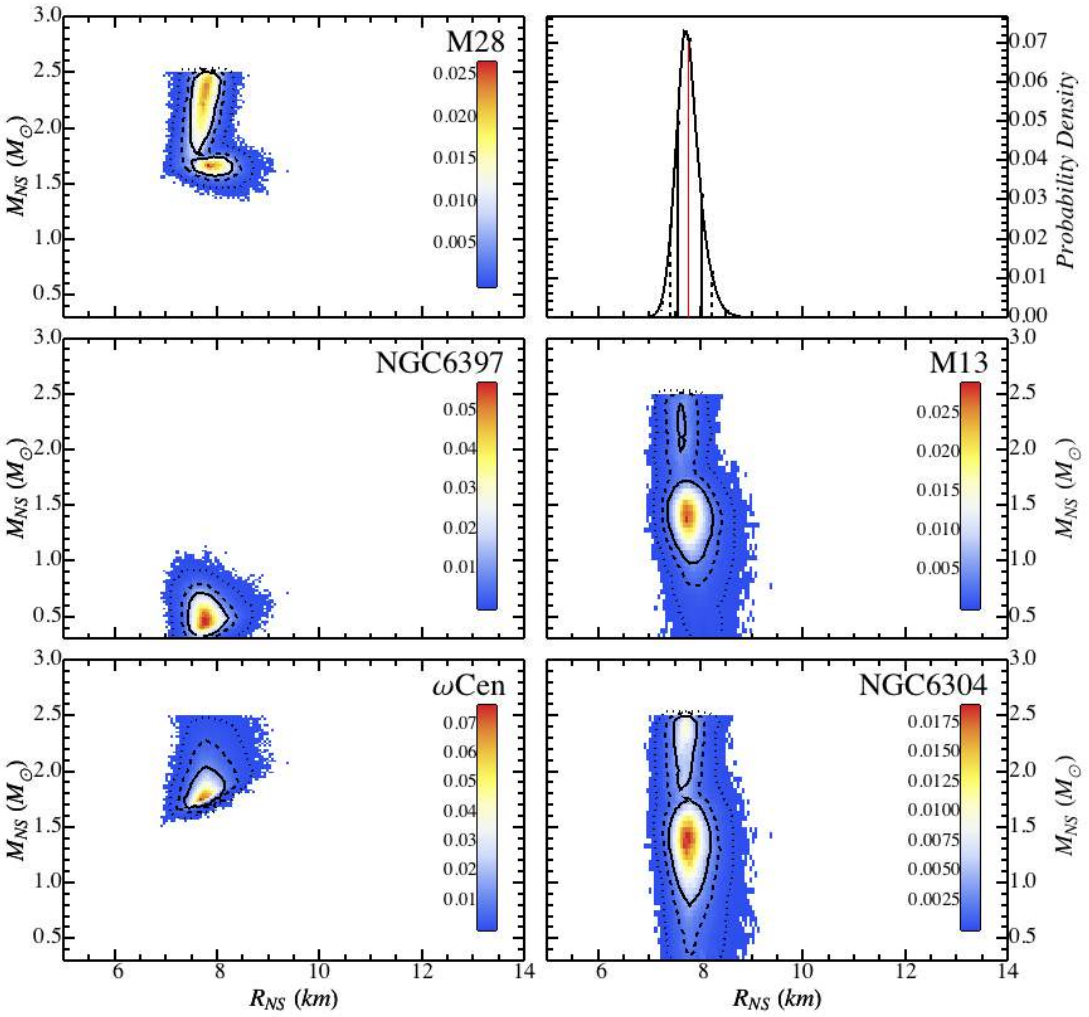

Figure 6.16 – This figure is similar to Figure 6.9, i.e., Run #1 with fixed distances instead of Gaussian Bayesian priors, fixed $N_{\rm H}$ values, and no PL component included. The only difference resides in the H-atmosphere model, where `nsagrav` model was used here instead of `nsatmos`. Note that the parameter limits for `nsagrav` are [6–20] km for $R_{\rm NS}$, and [0.4–2.5] $M_\odot$for $M_{\rm NS}$. The $R_{\rm NS}$ measurement, $R_{\rm NS} = 7.8^{+0.5}_{-0.3}$ km, is consistent with that of Run #1, but the some of the $M_{\rm NS}$–$R_{\rm NS}$ posterior distributions are significantly different from those of Figure 6.9. This is further discussed in Section 6.3.2.

For example, some sets of $M_{\rm NS}$–$R_{\rm NS}$ allowed by `nsagrav` and giving an acceptable χ^2-value lead to imaginary values of R_∞. It is important for an observer to keep this fact in mind, otherwise, results produced by the *XSPEC* implementation of `nsagrav` could be misinterpreted. In light of the pitfall mentioned here, the `nsagrav` model should be used with care.

6.4 Discussion

This chapter presented the simultaneous analysis of the spectra from five qLMXBs in GCs with a common $R_{\rm NS}$ parameter for all targets. The posterior distributions for $R_{\rm NS}$, $M_{\rm NS}$, R_∞, $kT_{\rm eff}$, and $N_{\rm H}$ were obtained from MCMC simulations, which included Gaussian Bayesian priors for the distances to the GCs hosting the targets. In this discussion section, the original work performed here and the data used are summarized. This is followed by a subsection discussing various possible biases resulting from the MCMC analysis. The discussion finishes with the implication that the resulting $R_{\rm NS}$ measurement may have for the determination of the dense matter EoS.

6.4.1 List of New Analysis Methods, Data and Results

The following two paragraphs aim at summarizing the novel approach to the analysis of the NS thermal spectra, and unused data presented in this chapter. The MCMC framework for spectral analysis is a rather recent approach, made convenient by the development of *PyXSPEC*, the Python version of *XSPEC*. The "Stretch-Move" MCMC algorithm used here differs from the usual Metropolis-Hasting (M-H) algorithm of standard MCMC simulations. It has been developed recently and while it presents significant advantages over M-H, it is still scarcely used in astrophysics. This work includes X-ray data not previously presented in the literature, namely the *Chandra* exposure of NGC 6304.

This chapter also contains a more complete presentation of the resulting best-fit NSs physical parameters ($kT_{\rm eff}$, $M_{\rm NS}$, and $R_{\rm NS}$). Specifically, the products of the MCMC simulations in 2-dimensional matrices of posterior distributions (see Fig-

ures 6.3–6.8) are displayed. Such figures better represent the true distributions of the NS physical parameters compared to simple lists of best-fit values with their uncertainties, mostly because the distributions are not necessarily Gaussian (particularly with models like `nsatmos`). Researchers are encouraged to present their results in such a way.

Finally, the approach of this chapter is not dissimilar to the work of Steiner et al. (2010, 2013) in the sense that different targets are combined to produce constraints on the dense matter EoS. However, the present analysis imposes $R_{\rm NS}$ to be quasi-constant for all the targets, as justified by recent observations favouring "normal matter" EoSs. Other differences include two qLMXBs (M28 and NGC 6304) added to the present analysis, and the qLMXB in 47 Tuc not used here because of the uncertainties related to pile-up. Finally, the work of Steiner et al. (2010, 2013) uses type-I X-ray burst sources, which are not considered in the present analysis.

6.4.2 Possible Biases Resulting from the Analysis

Non-Zero Power-Law Contribution for the qLMXB in NGC 6397

The runs that included a PL component (#3, #4, and #7, with photon index $\Gamma = 1$) resulted in PL normalizations consistent with zero for all targets, except for NGC 6397. Specifically, $\mathrm{Norm}_{\mathrm{PL,NGC\ 6397}} = 2.7^{+1.3}_{-1.3}\times10^{-7}\,\mathrm{keV^{-1}\,s^{-1}\,cm^{-2}}$, which is not consistent with zero, at the 3.4σ level, in Run #7. This indicates a possible non-negligible contribution of a PL above $\sim 2\,$keV. Using *XSPEC* (without the MCMC approach), the spectra of NGC 6397 are fitted without the other qLMXBs, and the PL normalization obtained is $\mathrm{Norm_{PL}} = 2.1^{+1.3}_{-1.3}\times10^{-7}\,\mathrm{keV^{-1}\,s^{-1}\,cm^{-2}}$ which corresponds to a contribution of $2.6^{+1.7}_{-1.7}\%$ of the total unabsorbed flux of NGC 6397 in the 0.5–10 keV energy band. Such a contribution is consistent with that measured in the previous results, $\leq 3.3\%$ (Chapter 6), for the same photon index.

Nonetheless, adding a PL contribution for each target does not significantly bias the posterior distribution of $R_{\rm NS}$. Specifically, adding PL components between Runs

#1 and #3 changed the radius measurement from $R_{\rm NS} = 7.1^{+0.5}_{-0.6}$ km (Run #1) to $R_{\rm NS} = 7.3^{+0.5}_{-0.6}$ km (Run #3); between Runs #2 and #4, $R_{\rm NS}$ changed from $R_{\rm NS} = 7.6^{+0.9}_{-0.9}$ km (Run #2) to $R_{\rm NS} = 8.0^{+1.0}_{-1.0}$ km (Run #4). Between runs #6 and #7 (free $N_{\rm H}$), the $R_{\rm NS}$ distributions changed more significantly, but they are nonetheless consistent: $R_{\rm NS} = 7.8^{+1.3}_{-1.1}$ km (Run #6) to $R_{\rm NS} = 9.1^{+1.3}_{-1.5}$ km (Run #7). Therefore, adding PL components does not significantly change the $R_{\rm NS}$ posterior distribution, but nonetheless includes systematic uncertainties related to the possible presence of a PL component into the measured $R_{\rm NS}$. With the limited PL contributions observed ($< 5\%$), the choice of photon index does not affect the `nsatmos` component. This is tested on NGC 6397 alone, the qLMXB with the strongest PL contribution, where the PL photon index is changed from $\Gamma = 1$ to $\Gamma = 2$. Such a change results in consistent PL contributions, but more importantly, it results in a non-significant increase of only $\sim 1\%$ in the value of $R_{\rm NS}$, well within the uncertainties of the measurement. Other parameters such as the mass, temperature and the PL normalization are consistent between the two trials, with $\Gamma = 1$ and with $\Gamma = 2$. Given that NGC 6397 has the strongest PL contribution and that changing the photon index from $\Gamma = 1$ to $\Gamma = 2$ does not modify $R_{\rm NS}$, it is expected to be the same for the simultaneous spectral analysis.

Effects of Individual Targets on the Simultaneous Fit

An additional set of MCMC runs was performed to investigate whether some targets have a dominant biasing effect on the simultaneous spectral fitting presented above. This analysis is performed by excluding each target individually and observing the resulting marginalized posterior distributions of the parameters. Results are listed in Table 6.8. These runs were performed like Run #7, i.e., with the $N_{\rm H}$ value free, with Gaussian Bayesian priors on the distances, and with the additional PL component. The values of $R_{\rm NS}$ obtained when removing each target are all consistent within 2σ of each other, and more importantly, consistent with the $R_{\rm NS}$ distribution obtained when all targets are included (Run #7, in Table 6.6). Similarly, the $kT_{\rm eff}$, $M_{\rm NS}$, R_∞

Table 6.8 – Effect of Individual Targets on the Simultaneous Spectral Fit

Target excluded	$R_{\rm NS}$ (km)	χ^2_ν/DOF ($p_{\rm null}$)	Acceptance rate
NONE (Run #7)	$9.1^{+1.3}_{-1.5}$ km	0.98 / 628 (0.64)	7%
WITHOUT M28	$8.4^{+1.5}_{-1.3}$ km	0.98 / 381 (0.69)	7%
WITHOUT NGC 6397	$10.7^{+1.7}_{-1.4}$ km	0.89 / 428 (0.95)	9%
WITHOUT M13	$8.6^{+1.5}_{-1.3}$ km	0.94 / 588 (0.86)	7%
WITHOUT ω Cen	$8.7^{+1.5}_{-1.4}$ km	0.95 / 601 (0.81)	8%
WITHOUT NGC 6304	$9.0^{+1.5}_{-1.4}$ km	0.93 / 622 (0.88)	8%

NOTES: The spectral fits in this table were performed following Run #7, with free $N_{\rm H}$ values, Gaussian Bayesian priors on the distances and with an additional power-law components in the model. Each target were successively removed to investigate the possible effect of individual sources on the global fit. The $R_{\rm NS}$ values obtained in each of these five tests are consistent with each other, and with that of Run #7. This confirms that none of the five quiescent low-mass X-ray binaries significantly skews the $R_{\rm NS}$ measurement. Quoted uncertainties are 90% confidence, and values in parentheses are held fixed. DOF refers to the number of degrees of freedom.

and the $\alpha_{\rm pileup}$ values of each targets are consistent with each other in all five cases presented in Table 6.8, and also consistent with the values from Run #7. Overall, removal of any individual qLMXB does not change the best-fit radius by more than the 95% confidence region. This ensures that no qLMXB induces a significant bias on $R_{\rm NS}$. This is also compatible with recent results (Steiner et al., 2013), obtained by combining $M_{\rm NS}$–$R_{\rm NS}$ distributions of qLMXBs and type-I X-ray bursts. In that work, it was demonstrated that removing extreme cases (for example the qLMXB X7 in 47Tuc, or the qLMXB in M13) had no or little effect on the resulting empirical EoS.

For completeness, and to confirm this observation, a spectral analysis combining X7 with the other five qLMXBs of this work is performed in *XSPEC* in order to determine $R_{\rm NS}$. Note that the MCMC approach is not used and is not necessary here since this additional analysis is simply a consistency check to determine if outliers can have an impact of the best-fit $R_{\rm NS}$measurement[14]. Furthermore, Gaussian Bayesian priors are not used for this consistency check. The spectral data available for X7 and

[14]As mentioned before, X7 was not used in the main analysis of the present work because of the unquantified systematic errors associated with the correction of the large amount of pile-up affecting the spectra, and its uncertain effect on the final statistical error bars of $R_{\rm NS}$.

used here are described in a previous work (Heinke et al., 2006a). For the distance to the qLMXB, the weighted average of all recent distance estimates listed in another reference (Woodley et al., 2012), i.e., $d_{47\mathrm{Tuc}} = 4.52\,\mathrm{kpc}$, was used. The resulting best-fit NS radius found was $R_{\mathrm{NS}} = 7.0^{+1.0}_{-2.0p}\,\mathrm{km}$ with the acceptable statistics χ^2_ν/DOF $(p_{\mathrm{null}}) = 0.98/1003$ (0.70). This result is consistent with the R_{NS} measurement of Run #1 (performed without adding the spectra of X7) and seem to confirm that outliers, such as the qLMXB X7 in 47Tuc, do not affect the radius measurement, as demonstrated in a previous work (Steiner et al., 2013).

Composition of the Neutron Star Atmosphere

The M_{NS}–R_{NS} measurements of NSs in qLMXBs rely on the atmosphere modeling, which itself relies on a major assumption of this work, namely the composition of the NS atmosphere. It is generally assumed that NS atmosphere are composed exclusively of pure hydrogen (e.g., Rutledge et al., 2002b; Heinke et al., 2006a), since heavier accreted elements will settle through the atmosphere on short time scales (Alcock and Illarionov, 1980; Bildsten et al., 1992). NS He atmospheres could be observed in the case of He accretion from WD donors in ultra-compact X-ray binaries. An He-atmosphere model was used to fit the spectra of M28 and led to a radius 1.5× larger than that obtained with a H-atmosphere, favouring stiff dense matter EoSs (Servillat et al., 2012). Similarly, for the qLMXB in M13, assuming a He composition of the NS atmosphere increases the radius R_{NS} by a factor ~ 1.2 (Catuneanu et al., 2013).

The actual composition of the NS atmosphere can be infered from the identification of the donor companion star, which proves a difficult task in the crowded environment of GCs. Only two GC qLMXBs have identified counterparts, X5 in 47Tuc (Edmonds et al., 2002), and in ω Cen (Haggard et al., 2004), both of which discovered from their strong Hα emission, indicating hydrogen donor stars.

Causality Limit

With the assumptions made and the model chosen in the present work, parts of the $M_{\rm NS}$–$R_{\rm NS}$ contours resulting from the analysis cover a section of the parameter space that goes past the causality limit as set in ealier works (Lattimer et al., 1990; Lattimer and Prakash, 2001). Stricter constraints on the $M_{\rm NS}$–$R_{\rm NS}$ contours could be obtained by imposing that the sets of MCMC accepted points ($R_{\rm NS}$,$M_{\rm NS}$) all obey $R_{\rm NS} \geq 3GM_{\rm NS}/c^2$, i.e., do not cross the causality line. However, no constraint is added; this produces a larger error region than may be necessary (if one were to explicitly adopt causality as an assumption), but the goal of this analysis is to produce the most conservative, assumption-free uncertainty region for $R_{\rm NS}$. Only if much higher S/N data were obtained, and the M-R parameter space required (or strongly preferred) a value in the region excluded by the causality requirement cited above (Lattimer et al., 1990) would it become necessary to revisit this assumption.

Effect of Assumptions

As discussed in this chapter, assumptions can have a strong effect on the interpretation of spectral fits of individual sources and consequently on the simultaneous spectral analysis as well. The selection of the distances to the GCs (fixed or with Gaussian Bayesian priors) can skew the $R_{\rm NS}$ measurement toward smaller or larger values. For instance, in early runs of this analysis, the distance $d_{\rm M28} = 5.1 \pm 0.5\,{\rm kpc}$ (Rees and Cudworth, 1991) was initially used, before it was updated to a more recent value $d_{\rm M28} = 5.5 \pm 0.3\,{\rm kpc}$ (Testa et al., 2001; Servillat et al., 2012). This caused the $R_{\rm NS}$ measurement (of Run #7) to change from $R_{\rm NS} = 8.7^{+1.3}_{-1.1}\,{\rm km}$ to $R_{\rm NS} = 9.1^{+1.3}_{-1.5}\,{\rm km}$ as the distance of M28 was increased. The values are consistent with each other, but this larger $d_{\rm M28}$ shifted the $R_{\rm NS}$ measurement. This is expected since the normalization of a thermal spectrum is $\propto (R_\infty/d)^2$.

Another strongly influential parameter is the Galactic absorption. A change in $N_{\rm H}$ will strongly affect the $M_{\rm NS}$ and $R_{\rm NS}$ best-fit. Specifically, a decrease (increase) in $N_{\rm H}$ results in an decrease (increase) in R_∞, respectively. This was shown for NGC 6397

and ω Cen, in Section 6.3.1. For NGC 6397, the HI-survey $N_{\rm H}$ value ($N_{H,22} = 0.14$) leads to a $R_\infty = 11.8^{+0.8}_{-0.7}$ km, while the X-ray deduced value ($N_{H,22} = 0.096^{+0.017}_{-0.015}$) produces $R_\infty = 8.4^{+1.3}_{-1.1}$ km, a decrease of $\sim 30\%$. For ω Cen, the best-fit R_∞ almost doubles as the constraint on $N_{\rm H}$ is relaxed, causing the value to increase from $N_{H,22} = 0.09$ (HI-survey) to $N_{H,22} = 0.182^{+0.041}_{-0.047}$. Using assumptions for the $N_{\rm H}$ values, like those derived from HI-surveys, can lead to strongly skewed $R_{\rm NS}$ measurements. Consequently, it is preferable to avoid using assumed values, when possible. The $R_{\rm NS}$ measurement from Run #7 is presented as the final result of this work.

6.4.3 The $R_{\rm NS}$ Measurement

The goal of this chapter being to measure $R_{\rm NS}$, the following discussion is focused on the $R_{\rm NS}$ posterior distributions, on the comparison with other $R_{\rm NS}$ measurement, and on the implication that such a radius measurement will have for the determination of the dense matter EoS.

The striking observation one can make pertains to the low range of values of the resulting $R_{\rm NS}$ distributions obtained from the different runs. The $R_{\rm NS}$ distributions remained below $R_{\rm NS} < 10.4$ km (90%-confidence), or $R_{\rm NS} < 11.1$ km (99%-confidence). This resulted from Run #7 (see Figure 6.15), where a particular effort was made to consider all possible sources of systematic uncertainties. The result from Run #7 is the most general $R_{\rm NS}$ distribution, i.e., with the fewest assumptions, that can be produced. Also, the progressive relaxation of the assumptions throughout the analysis demonstrated that no unexpected behaviour was present in the final $M_{\rm NS}$–$R_{\rm NS}$ distributions of Run #7 and that the resulting low-value of $R_{\rm NS}$ was not affected by systematics.

Previous works reported low values of NS radii, but these measurements have high uncertainties due to low S/N, leading to poorly constrained $R_{\rm NS}$ and $M_{\rm NS}$ (e.g., in NGC 2808, Webb and Barret 2007; Servillat et al. 2008). Another qLMXB in NGC 6553 was identified with a small radius, $R_{\rm NS} = 6.3^{+2.3}_{-0.8}$ km (90%-confidence)

for $M_{\rm NS} = 1.4\,M_{\odot}$ (see Chapter 4). However, low-S/N *Chandra* observations demonstrated that the *XMM* spectra of the source was affected by hard X-ray contamination from a marginally resolved nearby source. Higher-S/N observations with *Chandra* are necessary to confirm the qLMXB classification and produce the uncontaminated spectrum necessary for its use in the present analysis.

In addition to qLMXB $R_{\rm NS}$ measurements, low radii were found from the analysis of PRE bursts. A review of the method used to determine $R_{\rm NS}$ from these sources can be found in the literature (Özel, 2006; Suleimanov et al., 2011b). The LMXBs EXO 1745-248, 4U 1608-52, and 4U 1820-30 were found to have respective radii in the 2σ ranges $R_{\rm NS} = [7.5 - 11.0]\,{\rm km}$ (Özel et al., 2009), $R_{\rm NS} = [7.5 - 11.5]\,{\rm km}$ (Güver et al., 2010a) and $R_{\rm NS} = [8.5 - 9.5]\,{\rm km}$ (Güver et al., 2010b), respectively. While such values are on a par with what is found in this chapter, a controversy persists regarding the results (see Section 2.3.2). Therefore, the $M_{\rm NS}$–$R_{\rm NS}$ constraints from type I X-ray bursts should be considered with these results in mind.

More recently, distance independent constraints in $M_{\rm NS}$–$R_{\rm NS}$ space were produced from the analysis of the sub-Eddington X-ray bursts from the type I X-ray burster GS 1826-24 (Zamfir et al., 2012). That analysis, performed for a range of surface gravities ($\log_{10}(g) = 14.0, 14.3, 14.6$) and a range of H/He abundances ($0.01\,{\rm Z}_{\odot}$, $0.1\,{\rm Z}_{\odot}$ and ${\rm Z}_{\odot}$) led to radii $R_{\rm NS} \lesssim 11.5\,{\rm km}$. While distance-independent, the results are highly influenced by the atmosphere composition and metallicity. For pure He composition, the upper limit of $R_{\rm NS}$ becomes $R_{\rm NS} \lesssim 15.5\,{\rm km}$ (Zamfir et al., 2012).

Finally, the multiwavelength spectral energy distribution of the INS RX J185635−3754 was analyzed to produce small values of $R_{\rm NS}$ and $M_{\rm NS}$ with no plausible EoS consistent with these values: $R_{\rm NS} \sim 6\,{\rm km}$ and $M_{\rm NS} \sim 0.9\,M_{\odot}$ for $d = 61\,{\rm pc}$ (Pons et al., 2002). A recent distance estimation to the source $d = 123^{+11}_{-15}\,{\rm pc}$ (Walter et al., 2010) led to revised values: $R_{\rm NS} = 11.5 \pm 1.2\,{\rm km}$ and $M_{\rm NS} = 1.7 \pm 1.3\,M_{\odot}$ (Steiner et al., 2013). While this result is consistent with the $R_{\rm NS}$ measurement obtained in this chapter and with the other works reporting low-$R_{\rm NS}$ values, it has to be taken with

care since the high-magnetic field of the source is not accounted for in the spectral model used by the original analysis.

Recently, it was shown that the dense matter EoS can be empirically determined from $M_{\rm NS}$–$R_{\rm NS}$ measurements of NS, using the thermal spectra of qLMXBs and the PRE of X-ray bursts (Steiner et al., 2010). This method uses MCMC simulation and Bayesian priors to determine the most probable EoS parameters, and equivalently, the corresponding most probable $M_{\rm NS}$–$R_{\rm NS}$ relation for NS. In a recent paper, this method was used with four X-ray bursting sources and four GC qLMXBs. Considering all scenarios, the 2σ lower and upper limits for $R_{\rm NS}$ are 9.17 km and 13.92 km (Steiner et al., 2013). The $R_{\rm NS}$ distribution of the present chapter $R_{\rm NS} = 9.1^{+1.3}_{-1.5}$ km (90%-confidence, from Run #7) is consistent with several of the model variations of Steiner et al. (2013), namely variation C (EoS parameterized with uniform prior in the pressure at four energy density values), variation CII (same as previous, but with low value of the colour correction, $1 < f_C < 1.35$), variation AII/AIII (EoS parameterized as two piecewise continuous power-laws, with $1 < f_C < 1.35$), see Steiner et al. (2013) for details about the variations of the model. Variation E (EoS for quark stars) is incompatible with the original assumption that $R_{\rm NS}$ is quasi-constant for a large range of $M_{\rm NS}$ above $0.5\,M_\odot$.

Theoretical EoSs have been proposed for more than two decades. A non-exhaustive list can be found in the literature (Lattimer and Prakash, 2001, 2007). When comparing the resulting $R_{\rm NS}$ distribution to proposed theoretical "normal matter" EoSs, one can note that most of those are not consistent with the low-$R_{\rm NS}$ result presented in this work. Indeed, most of the EoSs describing "normal matter" correspond to radii larger than 11.5 km (see Figure 6.17). A spread in $R_{\rm NS}$ is observed in these dense matter EoSs at large masses, in the part of the $M_{\rm NS}$–$R_{\rm NS}$ diagram where the compact object approaches collapse. However, this breadth of the $R_{\rm NS}$ variation for a given EoS is well within the uncertainties obtained in this work. Overall, the radius measurement $R_{\rm NS} = 9.1^{+1.3}_{-1.5}$ km constrains the dense matter EoS to those consistent

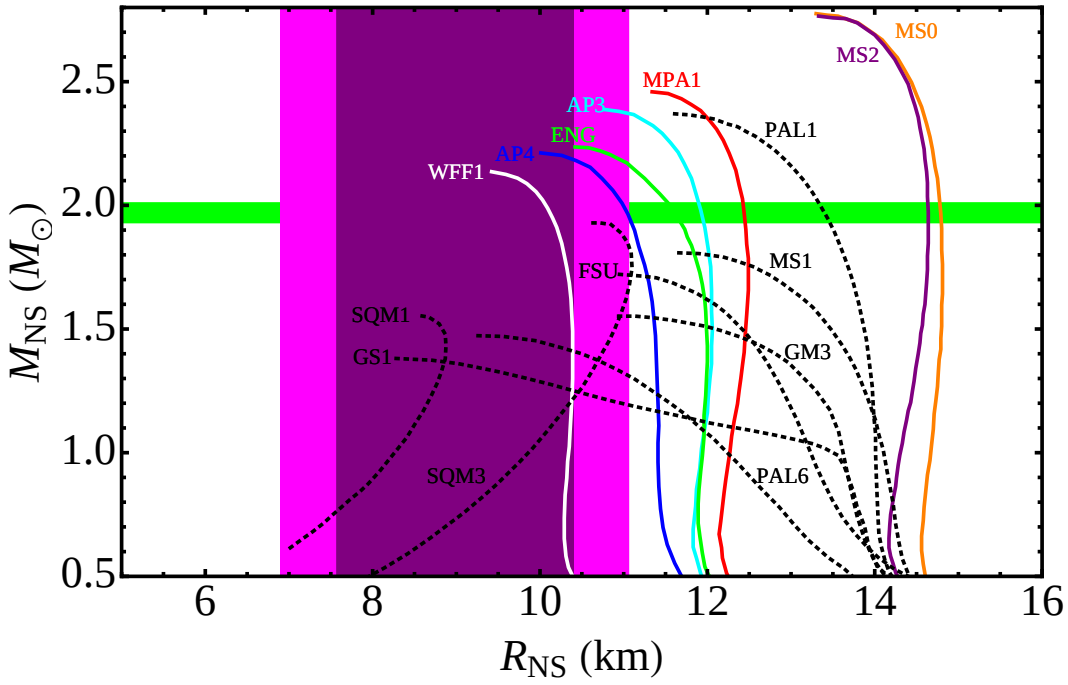

Figure 6.17 – This figure summarizes the results, showing the constraint on the dense matter equation of state imposed by the radius measurement obtained in this work: $R_{\rm NS} = 9.1^{+1.3}_{-1.5}$ km (90%-confidence). The dark and light shaded areas show the 90%-confidence and 99%-confidence constraints of the $R_{\rm NS}$ measurement, respectively. The mass measurement of PSR J1614-2230 is shown as the horizontal band (Demorest et al., 2010). "Normal matter" equations of state are the coloured solid lines. Other types of equations of state, such as the hybrid or quark-matter equations of state are included for comparison, with dashed lines. As mentioned in Section 6.4, the present analysis only places constraints on the "normal matter" equation of state since they are the only family of equation of state included in the constant-$R_{\rm NS}$ assumption. Among them, only the very soft dense matter equation of state (such as WFF1, Wiringa et al. 1988) are consistent with the radius obtained here.

with low-$R_{\rm NS}$, such as WFF1 (Wiringa et al., 1988). Note that this analysis cannot address the veracity of more exotic types of EoSs (hybrid and SQM) or any EoS which does not predict a quasi-constant $R_{\rm NS}$ within the observable mass range.

It is known that $R_{\rm NS}$ is related to fundamental nuclear physics parameters, such as the symmetry energy (Horowitz and Piekarewicz, 2001a,b). The present constraints on $R_{\rm NS}$ can be used to constrain this, and other properties of dense nuclear matter. This is left for future work.

It has been pointed out (Lattimer and Prakash, 2010) that an argument regarding a maximally compact NS (Koranda et al., 1997) results in a relationship between the maximal neutron star radius ($R_{\rm max}$) and the maximal NS mass ($M_{\rm max}$) for a given dense matter EoS:

$$\frac{R_{\rm max}}{M_{\rm max}} = 2.824\frac{G}{c^2} \tag{6.2}$$

where G is Newton's constant and c is the speed of light. Adopting this, the 99% confidence upper limit is $M_{\rm max} < 2.66\,M_{\odot}$, which does not violate any measured NS masses at present.

The small-$R_{\rm NS}$ value found in this work, and other low-$R_{\rm NS}$ results cited above, are consistent with soft EoSs such as WFF1. However, results of $M_{\rm NS}$ and $R_{\rm NS}$ measurements from other sources seem to favour stiffer EoSs. The qLMXB 47Tuc X7 has a reported radius $R_{\rm NS} = 14.5^{+1.6}_{-1.4}\,$km for $M_{\rm NS} = 1.4\,M_{\odot}$ (Heinke et al., 2006a), supporting stiff EoSs, such as MS0/2 (Müller and Serot, 1996). Nonetheless, the range of radii allowed by the published $M_{\rm NS}$–$R_{\rm NS}$ contours for X7 is consistent with the radius measurement presented in the present work. Moreover, the X7 $M_{\rm NS}$–$R_{\rm NS}$ contours are compatible with the EoS WFF1 (Wiringa et al., 1988). Another work used the long PRE X-ray bursts from 4U 1724-307 to conclude that stiff EoSs are describing the dense matter inside NSs (Suleimanov et al., 2011a). Specifically, it was found that $R_{\rm NS} > 13.5\,$km for $M_{\rm NS} < 2.3\,M_{\odot}$, and for a range for NS atmospheric composition. Lower $R_{\rm NS}$ values, in the range 10.5–17 km, are allowed for $M_{\rm NS} > 2.3\,M_{\odot}$, for pure H or solar metallicity composition. This radius measurement is only

marginally consistent with the present work for large masses, $M_{\rm NS} > 2.3\,M_{\odot}$, which implies a dense matter EoS capable of reaching $M_{\rm NS} \sim 2.3\,M_{\odot}$ for $R_{\rm NS} \sim 10-11\,{\rm km}$. Finally, another radius measurement, obtained by modeling the thermal pulses of the millisecond pulsar PSR J0437−4715 (Bogdanov, 2013), leading to values, $R_{\rm NS} > 11\,{\rm km}$ (3σ), is inconsistent with the measurement presented in this work.

6.5 Summary

In this chapter, $R_{\rm NS}$ is measured using the assumption that the radius is quasi-constant for a wide range of $M_{\rm NS}$ larger than $M_{\rm NS} > 0.5\,M_{\odot}$, i.e., constant within the measurement precision. This is justified by recent observations favouring "normal matter" EoSs which are described by this characteristic. For this analysis, the spectra from five GCs qLMXBs observed with the *Chandra X-ray Observatory* and *XMM-Newton* were used in a simultaneous analysis, constraining $R_{\rm NS}$ to be the same for all targets.

For this, an MCMC approach to spectral fitting was used, which offers several advantages over the Levenberg-Marquardt χ^2-minimization technique generally used for spectral fits. For example, the MCMC framework allows imposing Bayesian priors to parameters, namely the distance to the host GCs. By doing do, the distance uncertainties are included into the posterior $R_{\rm NS}$ distribution. In addition, one can marginalize the posterior distributions over any parameters and very easily obtain $M_{\rm NS}$–$R_{\rm NS}$ distributions, while the grid-search method in *XSPEC* can be problematic in the case of spectral fits with many free parameters and complicated χ^2-space. The algorithm chosen in this work is an affine-invariant ensemble sampler, commonly called "Stretch-Move" algorithm, which is particularly appropriate (i.e., converging efficiently) for elongated and curved distributions.

The principal result of the simulations performed in this analysis is that NSs are characterized by small physical radii. Specifically, when the distances and Galactic absorption parameters are fixed, $R_{\rm NS} = 7.1^{+0.5}_{-0.6}\,{\rm km}$ (from Run #1). A more gen-

eral posterior distribution for $R_{\rm NS}$ i.e., less prone to systematic biases, is obtained by applying Gaussian Bayesian priors for the five GC distance, by freeing the $N_{\rm H}$ parameters, and by adding a PL component to the model to account for a possible spectral component at high photon energies. Such a spectral component could be the largest possible source of uncertainty, and could be skewing $R_{\rm NS}$ downward, but it is accounted for in the last and most relaxed MCMC run. In fact, such a spectral component was discovered herein for NGC 6397.

The progressive relaxation of assumptions led us to a good understanding of the spectral fit in Run #7, minimizing systematic uncertainties. Therefore, with the H-atmosphere model `nsatmos`, the measured NS radius is $R_{\rm NS} = 9.1^{+1.3}_{-1.5}\,{\rm km}$ (from Run #7). These results are compatible with other low-$R_{\rm NS}$ measurements from GC qLMXBs or type-I X-ray bursts, but not consistent with some published $R_{\rm NS}$ measurement leading to values $R_{\rm NS} > 11\,{\rm km}$. These $R_{\rm NS}$ constraints, from Run #7, are recommended to be those relied upon for constraints on the EoS and other nuclear physics model parameters, as this run has the fewest associated assumptions behind it.

Among the dense matter EoS listed in previous works (Lattimer and Prakash, 2001, 2007), the $R_{\rm NS}$ measurement presented here is only compatible with "normal matter" EoSs consistent with $R_{\rm NS} \sim 10\,{\rm km}$, e.g. WFF1 (Wiringa et al., 1988). Most dense matter EoSs are compatible with larger radii, at $R_{\rm NS} \gtrsim 12\,{\rm km}$ and above. Given the results presented in this work, the theory of dense nuclear matter may need to be revisited.

The analysis presented in this chapter assumed a simple parametrization for the dense matter EoS, namely, that $R_{\rm NS}$ is constant for any $M_{\rm NS}$. The next chapter proposes to perform the spectral fitting by following alternative parametrizations of the EoS. Specifically, using the $M_{\rm NS}$–$R_{\rm NS}$ relations from theoretical EoSs, one can quantitatively assess whether a particular EoS describes the matter inside NSs, or if the proposed EoS is rejected by the spectral data.

7

Rejecting Proposed Dense Matter Equations of State

The many theoretical approaches aiming at describing matter at nuclear densities lead to a wide variety of dense matter EoSs. NSs are indispensable laboratories to discriminate between the different theories. Using the widely accepted observational scenario of qLMXBs inside the core of GCs, this work presents, for the first time, an analysis combining several qLMXB X-ray spectra to quantifiably confirm or reject a selection of dense matter EoSs, accounting for all quantifiable sources of uncertainties.

The work presented in this chapter will be submitted as a short letter entitled: *Excluding proposed dense-matter equations of state with quiescent low-mass X-ray binaries*. As for the previous chapters, the introduction of the original article to be submitted has been edited to remove redundant information provided in Chapter 2.

7.1 Introduction

Because of their relatively low-S/N, the X-ray spectra of qLMXBs inside GCs are unable to individually place stringent constraints on the dense-matter EoS (see Chapter 5, and Webb and Barret, 2007; Heinke et al., 2006a). However, combining the X-ray spectra of multiple qLMXBs in a simultaneous analysis can prove useful for that purpose. In Chapter 6, the X-ray spectra of five GC qLMXBs were combined to measure the radius of NSs to be $R_{\rm NS} = 9.1^{+2.0}_{-2.2}\,{\rm km}$ (99% confidence), with the assumption that all NSs have the same radius, within measurement uncertainties. This "quasi-constant radius" assumption relied on the observational evidence ($M_{\rm NS}$ measurements of two $\sim 2\,M_\odot$ pulsars, Demorest et al. 2010; Antoniadis et al. 2013) that dense nuclear matter is best described in $M_{\rm NS}$–$R_{\rm NS}$ space by an EoS characterized

with an almost radius-independent relation for a wide range of astronomically-relevant NS masses, i.e., $M_{\rm NS} > 0.5\,M_{\odot}$. As in Chapter 6, this work carefully accounts for and quantifies the dominant sources of uncertainties, and other systematic analysis assumptions are discussed.

Here, the same qLMXBs as in Chapter 6 are used, i.e., the qLMXBs in the GCs M28, NGC 6397, M13, ω Cen, and NGC 6304. These sources were observed with the *Chandra X-ray Observatory* (ACIS-S or ACIS-I detectors) or with the *XMM*-pn camera. To these, a 200 ks archived *Chandra* observation of the qLMXB in the GC ω Cen is added, improving the S/N for this source. The spectrum of the qLMXB in M30 observed with *Chandra*, is also added. Although this qLMXB was not used in Chapter 6, the S/N of its spectrum is comparable to that of other sources considered, and the low column density of Galactic hydrogen in its direction ($N_{H,22} < 0.03$, at 99% c.l.) makes the spectral analysis of the qLMXB in M30 less prone to systematics linked to the absorption of soft X-rays. The added spectral data increase the S/N of the entire data set by 7% compared to the previous analysis of Chapter 6.

The novelty of the present work relies in the parametrization of the $M_{\rm NS}$–$R_{\rm NS}$ relation imposed during the fitting on the qLMXB spectral data sets. Instead of choosing a constant $R_{\rm NS}$ parametrization as was done in Chapter 6, the $M_{\rm NS}$–$R_{\rm NS}$ relations of proposed theoretical dense matter EoSs are used. In other words, the $M_{\rm NS}$ and $R_{\rm NS}$ values resulting from the spectral fits are constrained to be on $M_{\rm NS}$–$R_{\rm NS}$ curve of an EoS. Aside from this analysis difference, data processing and analysis follow the standard procedure, described in more details in Chapter 6.

The structure of the chapter is the following: Section 7.2 presents the measurements of the NS radius under the quasi-constant assumption, with the addition of new data, for comparison with the results of Chapter 6 . Following this, Section 7.3 details the new methods in which the $M_{\rm NS}$–$R_{\rm NS}$ relations of proposed dense matter EoSs are imposed on the spectral data. Finally, Section 7.4 contains a discussion of the results, as well as a list of the analysis assumptions.

Table 7.1 Radius measurements of Neutron Stars

Description of Simulation	$R_{\rm NS}$ (km) 90% c.l.	$R_{\rm NS}$ (km) 99% c.l.	χ^2_ν/DOF ($p_{\rm null}$)	Line style in Figure 7.2
Causality assumption	$9.5^{+1.2}_{-1.2}$	$9.5^{+1.9}_{-1.8}$	1.08 / 476 (0.10)	Solid
No causality assumption	$9.4^{+1.2}_{-1.2}$	$9.4^{+1.9}_{-1.8}$	1.08 / 476 (0.10)	Dashed
Run #7 of Chapter 6	$9.1^{+1.3}_{-1.5}$	$9.1^{+2.0}_{-2.2}$	0.98 / 628 (0.64)	Dotted

NOTES: When adding the quiescent low-mass X-ray binary in M30 and the additional *Chandra* data of ω Cen to the spectra used for the radius measurement presented in Chapter 6, no significant variation of the measured neutron star radius is observed. In addition, considering the assumption of causality does not change the radius by more that 1% (see Figure 7.2). *"c.l"* indicates the confidence level of the measurement. DOF refers to the number of degrees of freedom.

7.2 Measuring $R_{\rm NS}$ with Additional Data

Using the X-ray data from the six qLMXBs in the MCMC framework of Chapter 6, the results from previous analysis are reproduced, fitting the spectra with the `nsatmos` model (Heinke et al., 2006a) modulated by Galactic absorption modeled with `wabs` (Morrison and McCammon, 1983), and assuming that the radius is the same for all six NSs. Other parameters such as the NS temperature and mass are free to vary, and independent for each NS. The distances to each NS is considered using a Gaussian Bayesian prior[1]. Finally, a PL component is also included to model possible flux excesses above 2 keV as observed for some qLMXBs in the field (e.g. Rutledge et al., 2001b). This analysis relies on the least number of assumptions, and produces the most conservative radius measurement. To the analysis presented in Chapter 6, the consideration of the causality limit is added, for comparison purposes. Causality imposes that the speed of sound in the medium should not exceed the speed of light, i.e., $dP/d\rho \leq c^2$. For NSs, this corresponds to $R_{\rm NS} > 3GM_{\rm NS}/c^2$. In the present analysis, this translates into the exclusion of MCMC samples violating this condition.

The radii measured with or without the assumption of causality are consistent with each other and with the previous radius measurement of Chapter 6 (Run #7). In other words, adding the qLMXB in M30 to the sample did not change the measured radius.

[1]The distance used for the GC M30 is $d_{\rm M30} = 9.0 \pm 0.5$ kpc (Carretta et al., 2000), for the other GCs, the same distances as in Chapter 6 are used.

Table 7.2 Testing dense-matter equations of state with quiescent low-mass X-ray binary spectra

Equation of State	Reference	χ^2/DOF [a]	Null Hypothesis Probability $p_{\rm null}$	Acceptance Rate (%)
WFF1	Wiringa et al. (1988)	522.54 / 477	0.073	6.6%
AP4	Akmal and Pandharipande (1997)	531.03 / 477	0.044	7.2%
MPA1	Müther et al. (1987)	536.41 / 477	0.031	7.5%
PAL1	Prakash et al. (1988)	556.99 / 477	0.007	8.5%
MS0	Müller and Serot (1996)	565.04 / 477	0.003	8.2%
CEFT1	Hebeler et al. (2013)	521.73 / 477	0.077	6.5%
CEFT2	Hebeler et al. (2013)	536.15 / 477	0.031	7.3%
CEFT3	Hebeler et al. (2013)	546.94 / 477	0.014	7.8%

Notes: [a] DOF refers to the number of degrees of freedom.

This observation is in agreement with the previous work which demonstrated that the $R_{\rm NS}$ measurement is insensitive to the exclusion of individual NS spectra. These results are shown in Table 7.1. In addition, Figure 7.1 shows the $M_{\rm NS}$–$R_{\rm NS}$ posterior distributions for each targeted (same $R_{\rm NS}$ for all, with causality assumption, first line of Table 7.1), and Figure 7.2 shows the posterior distributions of $R_{\rm NS}$ obtained, comparing it to that from Run #7 of Chapter 6.

7.3 Rejecting Equations of State

In the second part of this work, the degree of certainty to which a selection of popular proposed dense matter EoSs fit the spectra of the six qLMXBs in the sample is evaluated. This spectral analysis is performed by forcing the fitted $M_{\rm NS}$ and $R_{\rm NS}$ parameters to be constrained to the $M_{\rm NS}$–$R_{\rm NS}$ curve[2] of a user-defined EoS. In other words, the simulation are modified such that the MCMC chains are constrained to evolve along the $M_{\rm NS}$–$R_{\rm NS}$ curve of the tested dense matter EoS. This relies on the fact that matter inside all NSs follows the same behaviour and is described by the same EoS. Here, all steps of the MCMC simulations are consistent with causality by assumption, since the dense matter EoSs tested are all consistent with causality.

[2]The $M_{\rm NS}$–$R_{\rm NS}$ curves for the EoSs were kindly provided by J. Lattimer, priv. comm.

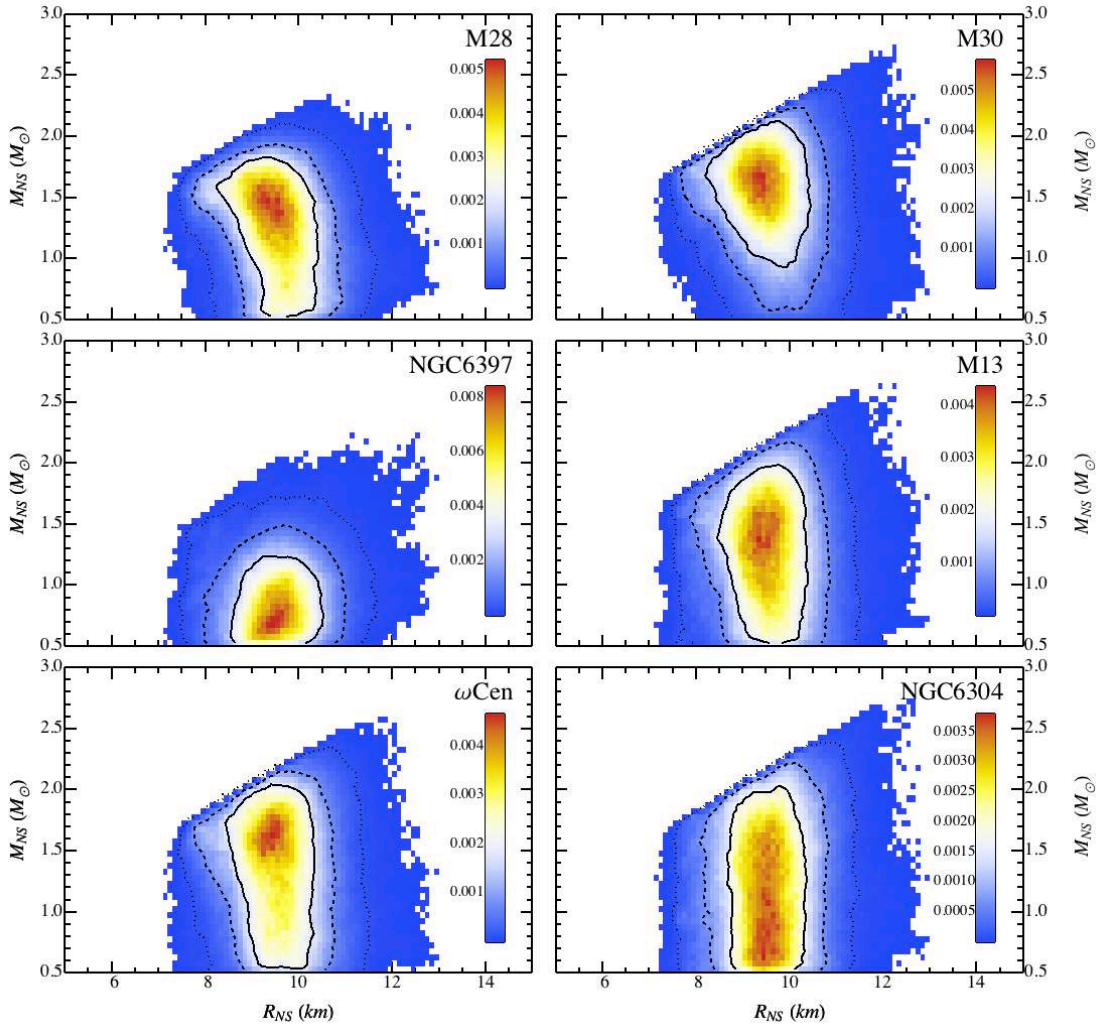

Figure 7.1 – This figure shows the $M_{\rm NS}$–$R_{\rm NS}$ posterior distributions resulting for the Markov-Chain Monte Carlo simulations, when the radius is assumed to be the same for all six neutron stars. This figure is similar to Figure 6.9, and other figures in Chapter 6. Here, the assumption of causality was imposed during the Markov-Chain Monte Carlo runs (see Section 7.2).

Five dense matter EoSs with varied stiffness are tested (see Table 7.2). In addition, the three representative dense matter EoSs obtained from chiral effective field theory (Hebeler et al., 2013, the Soft, Intermediate and Stiff representative EoSs in their Tables 5 and 6, respectively labeled CEFT1, CEFT2, and CEFT3 in this work) are considered. In this analysis, the only variation made to the model consists in the different dense matter EoSs tested. The obtained best-fit statistic for each model tested in each MCMC run provides information of how well the tested EoS describes the matter inside NSs, under the assumptions made in the analysis. The eight MCMC runs testing the eight dense matter EoSs have an acceptance rates in the range $\sim 6-9\%$. For each simulation, the minimum χ^2 and the resulting NHP are obtained. Results are shown in Table 7.2, listed in order of increasing average radius, and presented in Figure 7.2. It is clearly noticeable that the NHP decreases as the stiffness of the EoS increases, i.e., as the average radius of the tested EoS increases.

The NHP indicates the probability of finding by chance a χ^2 as large or larger as the minimum χ^2 found if the model is correct. Assuming that the `nsatmos` model is correct, a resulting NHP smaller than 0.01 (or 1%) excludes the tested dense matter EoS at 99% confidence. Two of the EoSs tested (PAL1 Prakash et al. 1988 and MS0 Müller and Serot 1996) have NHPs lower that 0.01, rejecting these theoretical dense matter EoSs as adequate descriptions of the behaviour of matter in the core of NSs with $> 99\%$ confidence, under the assumptions made in this work.

7.4 Discussion and Conclusion

This is the first time that an analysis quantifiably and conservatively excludes a selection of proposed dense matter EoS from the simultaneous analysis of several NS X-ray spectra. This conservative result is made possible by the inclusion of all quantifiable sources of uncertainties into the NS parameter estimation, and by relying on the fewest assumptions.

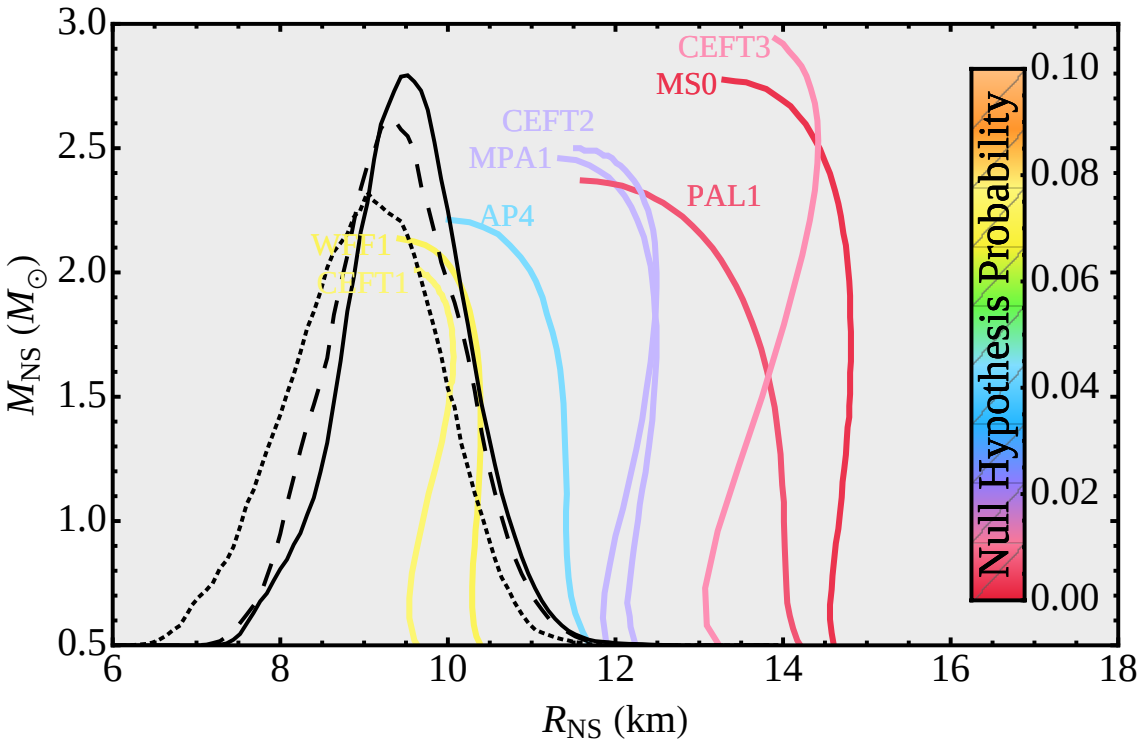

Figure 7.2 – This Figure shows the tested equations of state in $M_{\rm NS}$–$R_{\rm NS}$-space, and colour-coded by null hypothesis probabilities. PAL1 and MS0 are rejected by the analysis at the 99% confidence level since their null hypothesis probabilities are smaller than 0.01. Also shown are the normalized probability density distributions of the radius in the three cases of the constant radius assumption listed in Table 7.1: considering causality (solid black curve), without considering causality (dashed black curve), the radius probability density of the previous work (Chapter 6). Null hypothesis probabilities for each tested equation of state are available in Table 7.2, together with their corresponding references.

To the reader, there may appear to be a discrepancy between the NHP obtained when testing for various dense matter EoSs and the likelihood distributions of the constant radius case (black distributions in Figure 7.2). Specifically, on the one hand, the posterior probability distributions of $R_{\rm NS}$ indicates that $R_{\rm NS} = 14\,{\rm km}$ is $\sim 6\sigma$ away from the median of the distributions. On the other hand, the test for the EoS MSO (which has an average radius of $R_{\rm NS} \sim 14\,{\rm km}$) gives a NHP of $p_{\rm null} = 0.003$. However, what appears to be a mathematical discrepancy is actually a conceptual difference.

The NHP of a best-fit χ^2 value is calculated by integrating the χ^2 distribution with n DOF between the best-fit χ^2 value and ∞. Therefore, the distribution of NHP corresponds to 1 minus the cumulative χ^2 distribution function (CDF) for n DOF. A CDF is not a renormalizable distribution function and differs from a likelihood distribution function. The only information provided by the CDF is the probability of finding –by chance– a χ^2 value as large or larger than the best fit χ^2.

In the constant-radius analysis, the NHP is larger than 1% (Table 7.1), therefore indicating that the model chosen (`nsatmos` with constant $R_{\rm NS}$) adequately describes the data. When testing EoSs, such as MS0 or PAL1, the model fitted to the data is "`nsatmos` with $R_{\rm NS}$ and $M_{\rm NS}$ constrained on the EoSs MS0" (or PAL1). This model (different from "`nsatmos` with constant $R_{\rm NS}$") is rejected on account of the low-NHP of the minimum χ^2 obtained in the MCMC run. Because it is established that the spectral model `nsatmos` appropriately describes the data, as well as the model "`nsatmos` with constant $R_{\rm NS}$", it can be deduced that imposing the EoS models MS0 or PAL1 (e.g., the model "`nsatmos` with $R_{\rm NS}$ and $M_{\rm NS}$ constrained on the EoSs MS0") leads to a poor representation of the data.

Figure 7.3 better illustrates the difference between the radius probability density distribution and the NHPs of the tested dense matter EoSs. It shows the 2-d distribution of the accepted χ^2_ν as a function of radius for each accepted MCMC step, showing the extent of the radius coverage. The plot also shows (in red) the best χ^2_ν

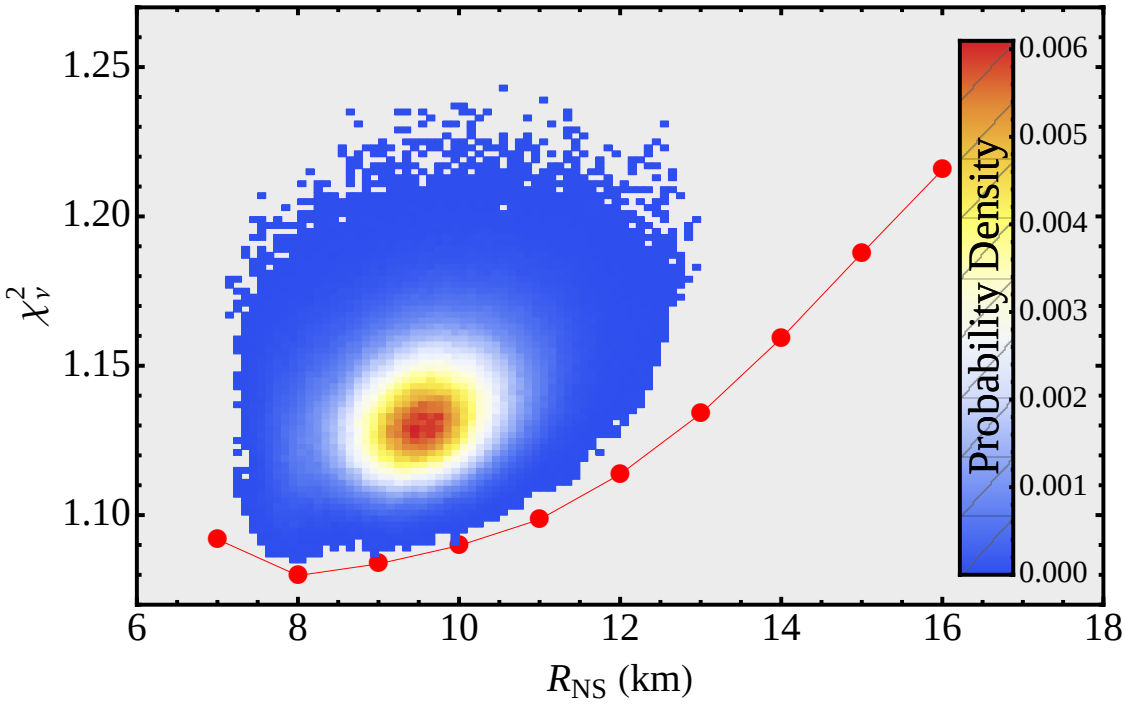

Figure 7.3 – This graph shows the best χ^2_ν obtained when fixing the radius to the values in red (from 7 km to 17 km). Also shown is the 2-dimensions posterior distribution of the χ^2_ν for each accepted radius value resulting from the Markov-Chain Monte Carlo run with the radius imposed to be the same for all neutron stars (without considering causality).

obtained when the radius is fixed to a selection of values (7–16 km). The minimum χ^2_ν of the 2-d distribution follows the best χ^2_ν of the red line in the range 7–12 km. Above that, the minimum χ^2_ν in the 2-d distribution (free radius) is systematically larger than the best χ^2_ν of the fixed radii simulations.

This apparent difference (between the Bayesian-accepted parameter space and the χ^2_ν parameter space) occurs because, during the free radius MCMC simulations, the 32-dimensions χ^2 parameter space above 12 km is "noisy", caused by the many degeneracies between the parameters ($R_{\rm NS}$ and the sources' $M_{\rm NS}$ and distances, see Section 2.2.2). As a consequence of the complicated parameter space above 12 km, the probability of excursion to radii larger than 12 km during the MCMC run is low. Modifying the stretch parameter of the MCMC algorithm (See Section 6.2.6) results in the same posterior distribution of the radius. On the contrary, when the radius is fixed to the values in the range 12–16 km (red line on Figure 7.3), a better χ^2_ν at each radius is found since fixing the radius greatly simplifies the parameter space. Moreover, a separate trial was performed with the Stretch-Move analysis in which the chains all began above 13 km, and, as expected, they "move" into the final parameter space.

Overall, the apparent difference described above emerges from the fact that the Bayesian and χ^2 statistics answer different statistical questions, and rely on different assumptions about the statistical system.

Assumptions in the analysis

While quantifiable sources of uncertainties are carefully included in the present spectral fit, there are analysis assumptions which imply systematic uncertainties, and these assumptions ought to be discussed:

- *Isotropic NS surface emission.* In the DCH theory, the emission comes from the deep crust in thermal equilibrium with the core (Brown et al., 1998). It is therefore safe to assume that the NS surface emits isotropically.

- *Negligible magnetic field NSs.* While it can be observationnally challenging to determine the magnetic field strengh of NS in qLMXBs, there is no evidence of magnetic field with strength $B \gtrsim 10^{9-10}$ Gauss in these systems. This assumption is supported by the measurements of the low-magnetic fields of LMXBs in the field of the Galaxy.

- *Rotation of the NS.* The fast rotation of a NS could alter its shape and make it oblate. A non-spherical NS would have an different surface emisison than in the spherical-assumption. However, the effect of spin on the NS shape is EoS-dependent, and could be, in principle calculated. A perfectly spherical NS is assumed here, a safe assumption for NSs with spin frequency < 300 Hz (See Section 2.2.2, and Bauböck et al. 2013; Psaltis and Ozel 2013).

- *NS with H-atmosphere.* One of the major assumptions of this analysis is the assumed composition of the atmosphere which shapes the emitted thermal spectrum of a NS qLMXB. As mentioned above, a pure hydrogen atmosphere is a reasonable assumption given the short (~ 1 sec) settling time scale of heavier elements (Alcock and Illarionov, 1980; Bildsten et al., 1992), and the composition of the matter accreted from the MS companion star.

Conclusion

In light of the robust assumptions listed above, the spectra of six GC qLMXBs have been used to exclude at the 99% confidence level two proposed EoSs, namely MS0 (Müller and Serot, 1996) and PAL1 (Prakash et al., 1988). Other tested EoSs are not excluded at a confidence level $> 98.5\%$, and no definite conclusions are drawn for those. While deeper X-ray observations would provide increased S/N spectra, the present analysis remains affected by uncertainties (distance to the GCs, and other systematic uncertainties discussed above) which must be better controlled to obtain better constraints on the dense matter EoS.

8

Conclusion

Astrophysical observations of neutron stars remain a major topic of research more than 40 years after their discovery. Numerous efforts seek to shed light on their formation, structure, and emission mechanisms. However, many problems to explain these objects in a coherent manner still persist, and their classification scheme is mostly phenomenological. Nonetheless, neutron stars continue to exist at the forefront of research to probe fundamental physics in regimes otherwise unattainable. The extreme gravitational fields arising in binary systems containing neutron stars, especially double neutron stars systems, provide a unique tool to test general relativity and evaluate alternative theories of gravity. Rotating neutron stars (radio, X-ray, or Gamma-ray pulsars) allow the study of electromagnetic processes in a magnetic field regime many orders of magnitude higher than the largest one ever attained in a laboratory. Finally, probing the interior of neutron stars, using a variety of indirect observational methods, constitute the sole technique to elucidate the mysteries surrounding the behaviour of bulk matter at and above nuclear densities, currently out of reach by experiments in Earth laboratories. In that regard, neutron stars are a unique bridge between astrophysics and nuclear physics.

The work presented in this thesis focused on the observations of a small sub-class of neutron stars: those in the quiescent low-mass X-ray binaries located in globular clusters. These systems, observed with X-ray telescopes, are irreplaceable tools to obtain observational constraints on the dense matter equation of state, which informs on the behaviour of bulk nuclear matter. Quiescent low-mass X-ray binaries in globular

clusters arise from a well understood scenario in which their surface emission is powered by internal heat accumulated during periods of active accretion of matter from the companion onto the neutron star, and in which the contributions of power-law spectral components is $\lesssim 3\%$ of the total flux. Because the neutron star photosphere is exclusively composed of hydrogen (accreted from the companion star in the binary system), it can be precisely modeled with radiative transfer calculations. Applying these models to the X-ray spectra of quiescent low-mass X-ray binaries provides a robust framework to measure the physical properties of neutron stars, namely their masses and radii.

Only a handful of quiescent low-mass X-ray binaries in globular clusters have the potential of producing precise radius measurements, and increasing the sample size of this population remains important to further confirm this observational scenario. To this purpose, surveys of globular clusters with *Chandra* or *XMM* have been performed, leading to the classification of a few more such sources, $\lesssim 1$ per globular cluster surveyed. The discovery method consists of identifying the globular cluster X-ray sources that have spectra consistent with neutron star hydrogen atmosphere models with radii and temperatures in the expected range for these sources at the distance of the host cluster. This thesis reported the discovery with *XMM-Newton* of one such source, in the core of the globular cluster NGC 6553. However, contaminating X-ray sources, unresolved with *XMM*, complicated the spectral identification of the candidate quiescent low-mass X-ray binary, as demonstrated by a short observation with *Chandra*. In the future, higher signal-to-noise ratio spectra with *Chandra* will be necessary to better constrain the radius measurement of this neutron star.

Nonetheless, as demonstrated in this thesis, even precisely-measured R_∞ of neutron stars in quiescent low-mass X-ray binaries have difficulty placing useful constraints on the dense-matter equation of state. This is due to the intrinsically curved shape of R_∞ in $M_{\rm NS}$–$R_{\rm NS}$ space, covering a wide range of proposed dense matter equations of state. This is particularly true when the various sources of systematic

uncertainties (Galactic absorption, distance, ...) are taken into account. Combining the spectra of quiescent low-mass X-ray binaries in a coherent manner emerged as a solution to constrain the dense matter equation of state. By first assuming that all neutron stars have the same radius, based on observational evidence, the work presented here found that the neutron star radius is smaller than initially expected, $R_{\rm NS} < 11.0\,{\rm km}$. This conservative result was obtained with a careful consideration of the various sources of uncertainties involved, and the fewest possible assumptions. Such a neutron star radius measurement implies that the dense matter equation of state must be soft at the "lowest" densities to accommodate small neutron star radii, but then stiffens quickly to accommodate the $2\,M_{\odot}$ mass measurements.

Assuming that all neutron stars have the same radius is equivalent to a simple parameterization of the dense matter equation of state in $M_{\rm NS}$–$R_{\rm NS}$ space. Other parameterizations, justified observationally or theoretically, can be employed. In Chapter 7, the $M_{\rm NS}$–$R_{\rm NS}$ values from the spectral fits of six quiescent low-mass X-ray binaries were constrained to the same equation of state. This opens the possibility to test whether or not a proposed dense matter equation of state describes the matter inside neutron stars, in the observational scenario of these well understood sources. Using this technique, two "stiff" equations of state, MS0 (Müller and Serot, 1996) and PAL1 (Prakash et al., 1988), were firmly rejected, at the 99%-confidence level. No firm results were obtained for the other equations of state tested.

Future Prospects

To improve the radius measurements and the constraints on the dense matter equation of state, the first step consists of obtaining deeper X-ray observations of the current sample of quiescent low-mass X-ray binaries. Increasing the signal-to-noise ratio of the spectra will refine the measurement of R_{∞} for each target, and therefore reduce the uncertainties on $R_{\rm NS}$ (with the constant $R_{\rm NS}$ assumption), or improve the rejection of proposed dense matter equations of state. In a similar manner, adding sources to

the sample used will also prove useful to this goal. In particular, quiescent low-mass X-ray binaries with a low column density of line-of-sight absorbing material could be added to the sample, since such sources would have R_∞ measurements less affected by systematic uncertainties.

In general, it is important to control the various sources of uncertainties to continue refining the understanding of dense nuclear matter. This can be achieved, for example, by obtaining independent measurements of the X-ray absorption, from grating spectrometer observations of other bright sources in a globular cluster. Note that independent measurements of the column density of hydrogen in the line of sight (e.g., via mapping of Galactic neutral hydrogen), is not particularly useful since $N_{\rm H}$ is only used as a proxy for the modeling of X-ray absorption. In addtion, improved distance measurements, free of systematics, will certainly reduce the uncertainties of the measured R_∞ values, and thus permit firmer rejection of proposed equations of state. Precise globular cluster distance measurements are expected to results from the observations of globular cluster member stars with *GAIA*. In the next five years, this *European Space Agency*'s mission will achieve microarcsecond spatial resolution, leading to precise parallax distance measurements for about 10^9 stars in our Galaxy, including the globular cluster system. As a result, the distance to many globular clusters will be known with $\sim 2\%$ uncertainties. With precise distance measurements, the uncertainties related to the amount of Galatic absorption of soft X-rays will dominate in the analyses presented in this thesis. It was noted in Chapter 6 that fixing the distances to the qLMXBs improved the size of the radius error region by $\sim 15\%$.

Observing the optical counterpart to the neutron star in quiescent low-mass X-ray binaries is also an important part of future work. This permits identifying the stellar companion to the neutron star, and therefore to confirm the classification of the system. However, because of the dense stellar environment in the core of globular cluster, even with *Chandra*'s precise (subarcsecond) localization of X-ray sources, firm detections of optical counterparts to quiescent low-mass X-ray binaries are chal-

lenging. The *Hubble Space Telescope* has been used to identify the counterparts to two quiescent low-mass X-ray binaries (one of them used in this thesis), and can be used to search for the optical counterpart to the other neutron stars of the sample presented in this thesis.

In the next 5–10 years, planned and proposed X-ray satellites will focus on large collecting area with high-time resolution (e.g., *NICER*, Gendreau et al. 2012; *LOFT*, Bozzo et al. 2011, 2014), at the expense of the angular resolution. These will be particularly useful for the observations of accreting millisecond pulsars, in the attempt to measure $M_{\rm NS}/R_{\rm NS}$ from the modeling of the observed pulse-profile (see Section 2.3.2). The Japanese mission *ASTRO-H* (Takahashi, 2013) is primarily dedicated to the high spectral resolution of soft and hard X-ray sources. This mission has the potential to measure the gravitational redshift from spectral features. However, the modest expected angular resolutions of these proposed observatories will not be able to resolve individual sources in the core of globular clusters, and will not be readily useful for the work presented here. On a longer time scale, the *European Space Agency*'s plans for a large X-ray telescope mission (launch $\sim$ 2028) will be more suitable for the method of interest in this thesis. While its planned angular resolution ($\sim 3''$) does not match that of *Chandra*, it will still be able to resolve at least some of the quiescent low-mass X-ray binaries used in this work. The $2.5\,{\rm m}^2$ planned effective area will collect large number of X-ray photons resulting in high signal-to-noise ratio spectra for these sources, within moderate exposure times.

Overall, the observational method of neutron stars presented in this thesis represents a small fraction of neutron star research, and an even smaller fraction of astrophysics. The results described in Chapter 6 and 7 made a step toward a global understanding of the behaviour of matter, and the potential for future, more remarkable, results is promising. Nonetheless, the many other observational and theoretical approaches to study neutron stars should still be pursued. The extreme properties of neutron stars and the extreme environments in which they appear offer a unique

window on the Universe, and neutron stars of all classes will certainly continue to have a crucial role for astrophysics and fundamental physics.

A

Un Résumé Détaillé pour les Non-Spécialistes

Cette partie a pour but de décrire mes travaux de thèse pour les lecteurs non-spécialistes en astrophysique. La recherche scientifique, même très spécialisée, se doit d'être rendue accessible à tous, autant que possible. L'astronomie et l'astrophysique ont la chance d'attirer naturellement le public, notamment grâce aux multiples images spectaculaires provenant des nombreux télescopes sur Terre et dans l'espace. Cependant, il n'est pas rare d'entendre des personnes se demander quels sont les impacts et les applications directes des travaux de recherche en astrophysique. Mon but n'est pas vraiment de convaincre le lecteur de l'utilité de ma recherche, mais je suis néanmoins déterminé à rendre ce résumé aussi accessible que possible.

Mes travaux de recherche consistent, en quelques sortes, à faire des autopsies d'étoiles mortes. Je cherche à savoir ce qu'il y a à l'intérieur ; quel type de matière compose leur cœur. Contrairement à un médecin qui peut regarder directement l'intérieur d'un cadavre, il est bien évidemment impossible – pour le moment – d'étudier directement l'intérieur des étoiles ; mortes ou pas ! Si on ajoute à cela le fait qu'elles sont situées à des milliers d'années lumières[1], la tâche est loin d'être triviale. Il existe cependant des méthodes d'observation indirectes pour déduire des informations à propos de l'intérieur des étoiles mortes. Je les décris dans cette section, mais avant cela, il est important de d'expliquer ce qu'est une étoile morte, et de motiver ces autopsies.

[1]Une année-lumière est une unité de distance, qui correspond à la distance parcouru par la lumière en une année, ce qui équivaut à 10 000 milliards de km.

On dit qu'une étoile meurt quand elle épuise le carburant qui nourrit les réactions nucléaires se produisant dans son cœur pendant toute la durée de sa vie. Quand cela arrive, l'équilibre délicat entre la force de gravité (dirigée vers l'intérieur) et la force de pression créée par les réactions nucléaires (dirigée vers l'extérieur) est détruit. Le destin de cette étoile en train de mourir dépend ensuite de sa masse initiale. Une étoile de faible masse, tel notre Soleil, va mourir lentement en grossissant puis en éjectant ses couches extérieures pour former une nébuleuse colorée et en laissant en son centre, un objet appelé naine blanche, un cadavre d'étoile, sans réactions nucléaires et refroidissant lentement. Les naines blanches ont environ la moitié de la masse du Soleil, mais compressée dans une sphère de la taille de la Terre. Cela correspond à environ 1 million de fois la densité de l'eau[2]. Une étoile avec une masse initiale plus large (plus de 8 fois la masse de notre Soleil) va mourir d'une façon très différente, et bien plus spectaculaire, en explosant en supernova. Pendant cette explosion, le cœur de l'étoile mourante est compressé à des densités inimaginables, à cause de la force de gravité. Ce qui reste au centre après l'explosion en supernova dépend à nouveau de la masse initiale. Les étoiles les plus massives laissent ces mystérieux trous noirs dont rien ne s'échappe, pas même la lumière. Par contre, si l'étoile mourante n'est pas assez massive pour créer un trou noir (mais néanmoins au-delà de 8 masses solaires), l'objet central après l'explosion en supernova sera une étoile à neutrons, ces étoiles mortes que j'étudie. Elles sont composées de la matière la plus dense que l'on puisse trouver dans l'Univers. En compressant une étoile à neutrons un peu plus, la matière s'effondrerait sur elle-même pour former un trou noir, duquel on ne pourrait obtenir aucune information puisque la lumière ne s'en échapperait pas.

En ce sens, les étoiles à neutrons sont plus intéressantes que les trous noirs puisqu'elles possèdent une surface observable qui permet aux astrophysiciens d'étudier leurs propriétés. Ce sont néanmoins des objets très mystérieux. J'ai mentionné leur densité extrême : Essayez d'imaginer, si cela est possible, de compacter la masse du Soleil[3]

[2]Une cuillère de naine blanche aurait une masse de 5000 kg

[3]Soit 2×10^{30} kg, c'est-à-dire, 2 000 000 000 000 000 000 000 000 000 000 kg, ou deux milliards de mil-

dans une sphère de la taille d'une grande ville (Figure 1.1). Pour reprendre l'analogie utilisée ci-dessus, une cuillère d'étoile à neutrons aurait une masse de 3 milliards de tonnes, 600 millions de fois plus que la cuillère de naine blanche. Cette densité indescriptible est due au fait que les atomes ont été tellement compressés que tout le vide à l'intérieur des atomes (et il y a plus de 99.99% de vide dans les atomes à des densités normales) a été remplacé par le noyau d'autres atomes. Une analogie astronomique pour visualiser ce concept serait de complètement remplir l'espace interplanétaire de notre système Solaire par des planètes. Aucun laboratoire sur Terre n'est capable de reproduire le genre de densité rencontrée à l'intérieur des étoiles à neutrons. Par conséquent, l'observation de ces objets est l'unique moyen de comprendre comment ce type de matière peut exister. C'est l'une des pièces cruciales pour compléter le grand puzzle de la physique de la matière.

En l'absence de données expérimentales, les physiciens nucléaires proposent une pléthore de modèles théoriques pour tenter d'expliquer le comportement de la matière ultra-dense, c'est-à-dire, l'évolution de la pression de la matière quand la densité augmente. Sans aucun moyen expérimental de tester ces modèles, les étoiles à neutrons deviennent les laboratoires tant nécessaires. Il y a différentes manières de sonder l'intérieur des étoiles à neutrons et ainsi de déterminer le bon modèle théorique parmi ceux proposés. La méthode la plus commune est de mesurer le rayon et/ou la masse des étoiles à neutrons. En effet, chacun de ces modèles de physique nucléaire correspond à une relation masse-rayon très spécifique pour les étoiles à neutrons. Par conséquent, avec la mesure précise de la masse et du rayon d'étoiles à neutrons, on peut déterminer si un modèle proposé décrit de manière approprié la matière ultra-dense qui existe à l'intérieur des étoiles à neutrons.

La méthode utilisée dans cette thèse consiste à mesurer le rayon d'une sélection d'étoiles à neutrons. En quelques mots, cela se fait en observant leur surface très chaude (de l'ordre du million de degrés) et en mesurant leur température et leur

liards de milliards de tonnes.

flux lumineux, c'est-à-dire, leur brillance apparente. Un modèle d'émission lumineuse d'étoile à neutrons nous permet ensuite de convertir la brillance apparente en rayon réel de l'étoile à neutrons. Cependant, et c'est très important, cette méthode nécessite de connaître la distance de l'objet observé. C'est un problème très fréquent en astronomie. Sans connaître leur distance, il est très difficile de mesurer la plupart des propriétés des objets dans l'Univers. Par exemple, cela revient à regarder une source lumineuse (sans aucun autre point de référence), par exemple une ampoule, et d'essayer d'en estimer sa luminosité. Est-ce une ampoule peu brillante mais relativement proche, ou bien une ampoule très brillante mais à une distance plus grande ? Notre cerveau interprète l'environnement et nos connaissances des ampoules afin de déduire la distance ou la brillance. De manière similaire, les astronomes obtiennent des mesures indépendantes de distance, ce qui n'est pas toujours facile, afin d'obtenir les informations voulues à propos de la brillance et des propriétés de l'objet observé.

De retour à nos mesures de rayons d'étoiles à neutrons: nous avons choisi d'observer des étoiles à neutrons situées à l'intérieur d'amas d'étoiles (non-mortes). Les astronomes ont développé des méthodes indépendantes pour mesurer la distance de ces amas d'étoiles. Par conséquent, les étoiles à neutrons à l'intérieur des amas ont des brillances intrinsèques mesurables relativement précisément, comparées à celles des étoiles à neutrons dont on ne connait pas la distance, par exemple, celles en errance dans notre Galaxie,

Pour que cette méthode de mesure de rayon fonctionne correctement, il faut observer les étoiles à neutrons qui sont inactives. La plupart des étoiles à neutrons qui pourraient être utilisés pour des mesures de rayons sont dans des systèmes binaires très actifs, avec des explosions spectaculaires à leur surface, ce qui rend la mesure de leur rayon très difficile. De plus, les étoiles à neutrons dans les systèmes binaires ont souvent un disque de matière qui les entoure et qui domine la brillance, et par conséquent qui complique l'observation. Pour éviter ce genre de problèmes, nous observons des étoiles à neutrons inactives dont l'émission de lumière est calme et

provient exclusivement de la surface de l'étoile à neutrons. Il n'y a cependant qu'une poignée connue de ces objets dans tous les amas d'étoiles de notre Galaxie.

Avec ces quelques rares objets, j'ai mesuré leur rayon entre 7 km et 11 km (effectivement la taille d'une ville). C'est cependant plus petit que la taille prédite par la plupart des modèles de physique nucléaire. L'incertitude de notre mesure est assez grande, et il y a encore beaucoup de travail afin d'obtenir des mesures plus précises. Mais si le rayon des étoiles à neutrons est confirmé en dessous de 10 km, il faudra revoir en grande partie les modèles théoriques de la matière ultra-dense. Il y a plusieurs moyens de réduire l'incertitude de notre mesure. Par exemple, les distances des amas d'étoiles qui hébergent nos étoiles à neutrons ne sont pas parfaitement connues, et ce manque de précision affecte notre mesure du rayon des étoiles à neutrons.

Il y a donc encore beaucoup de travail à effectuer dans la quête pour comprendre la matière ultra-dense et finir le grand puzzle de la physique de la matière. Cependant, les travaux de recherches présentés dans cette thèse ont permis de faire un grand pas dans ce sens.

Bibliography

A. Akmal and V. R. Pandharipande. Spin-isospin structure and pion condensation in nucleon matter. *Phys. Rev. C*, 56:2261–2279, October 1997.

C. Alcock and A. Illarionov. The surface chemistry of stars. I - Diffusion of heavy ions in white dwarf envelopes. II - Fractionated accretion of interstellar matter. *ApJ*, 235:534–553, January 1980.

V. A. Ambartsumyan and G. S. Saakyan. The Degenerate Superdense Gas of Elementary Particles. *Soviet Ast.*, 4:187, October 1960.

J. Antoniadis, P. C. C. Freire, N. Wex, T. M. Tauris, R. S. Lynch, M. H. van Kerkwijk, M. Kramer, C. Bassa, V. S. Dhillon, T. Driebe, et al. A Massive Pulsar in a Compact Relativistic Binary. *Science*, 340:448, April 2013.

A. M. Archibald, I. H. Stairs, S. M. Ransom, V. M. Kaspi, V. I. Kondratiev, D. R. Lorimer, M. A. McLaughlin, J. Boyles, J. W. T. Hessels, R. Lynch, et al. A Radio Pulsar/X-ray Binary Link. *Science*, 324:1411–, June 2009.

K. A. Arnaud. XSPEC: The First Ten Years. In G. H. Jacoby and J. Barnes, editors, *Astronomical Data Analysis Software and Systems V*, volume 101 of *Astronomical Society of the Pacific Conference Series*, pages 17–+, 1996.

H. C. Arp, W. A. Baum, and A. R. Sandage. The HR diagrams for the globular clusters M 92 and M 3. *AJ*, 57:4–5, April 1952.

H. C. Arp, W. A. Baum, and A. R. Sandage. The color-magnitude diagram of the globular cluster M 92. *AJ*, 58:4, February 1953.

K. Asai, T. Dotani, K. Mitsuda, R. Hoshi, B. Vaughan, Y. Tanaka, and H. Inoue. ASCA Observations of Soft X-Ray Transients in Quiescence : X1608-52 and CEN X-4. *PASJ*, 48:257–263, April 1996.

K. Asai, T. Dotani, R. Hoshi, Y. Tanaka, C. R. Robinson, and K. Terada. ASCA Observations of Transient X-Ray Sources in Quiescence. *PASJ*, 50:611–619, December 1998.

W. Baade. The Resolution of Messier 32, NGC 205, and the Central Region of the Andromeda Nebula. *ApJ*, 100:137, September 1944.

W. Baade and F. Zwicky. Cosmic Rays from Super-novae. *Proceedings of the National Academy of Science*, 20:259–263, May 1934.

A. Bahramian, C. O. Heinke, G. R. Sivakoff, D. Altamirano, R. Wijnands, J. Homan, M. Linares, D. Pooley, N. Degenaar, and J. C. Gladstone. Discovery of the Third Transient X-Ray Binary in the Galactic Globular Cluster Terzan 5. *ApJ*, 780:127, January 2014.

M. Bauböck, E. Berti, D. Psaltis, and F. Özel. Relations between Neutron-star Parameters in the Hartle-Thorne Approximation. *ApJ*, 777:68, November 2013.

H. Baumgardt. Star cluster kinematics in the GAIA era. *Astronomische Nachrichten*, 329:881, December 2008.

H. Baumgardt and P. Kroupa. Globular Cluster Kinematics with Gaia. In C. Turon, K. S. O'Flaherty, and M. A. C. Perryman, editors, *The Three-Dimensional Universe with Gaia*, volume 576 of *ESA Special Publication*, page 681, January 2005.

W. Becker, D. A. Swartz, G. G. Pavlov, R. F. Elsner, J. Grindlay, R. Mignani, A. F. Tennant, D. Backer, L. Pulone, V. Testa, et al. Chandra X-Ray Observatory Observations of the Globular Cluster M28 and Its Millisecond Pulsar PSR B1821-24. *ApJ*, 594:798–811, September 2003.

L. R. Bedin, G. Piotto, J. Anderson, S. Cassisi, I. R. King, Y. Momany, and G. Carraro. ω Centauri: The Population Puzzle Goes Deeper. *ApJ*, 605:L125–L128, April 2004.

I. Bednarek, P. Haensel, J. L. Zdunik, M. Bejger, and R. Mańka. Hyperons in neutron-star cores and a 2 M pulsar. *A&A*, 543:A157, July 2012.

D. Bhattacharya and E. P. J. van den Heuvel. Formation and evolution of binary and millisecond radio pulsars. *Phys. Rep.*, 203:1–124, 1991.

E. Bica, C. Bonatto, B. Barbuy, and S. Ortolani. Globular cluster system and Milky Way properties revisited. *A&A*, 450:105–115, April 2006.

L. Bildsten, E. E. Salpeter, and I. Wasserman. The fate of accreted CNO elements in neutron star atmospheres - X-ray bursts and gamma-ray lines. *ApJ*, 384:143–176, January 1992.

E. D. Bloom, D. H. Coward, H. Destaebler, J. Drees, G. Miller, L. W. Mo, R. E. Taylor, M. Breidenbach, J. I. Friedman, G. C. Hartmann, et al. High-Energy Inelastic e-p Scattering at 6° and 10°. *Physical Review Letters*, 23:930–934, October 1969.

G. R. Blumenthal and W. H. Tucker. Compact X-ray sources. *ARA&A*, 12:23–46, 1974.

S. Bogdanov. The Nearest Millisecond Pulsar Revisited with XMM-Newton: Improved Mass-radius Constraints for PSR J0437-4715. *ApJ*, 762:96, January 2013.

G. Bono, F. Caputo, and M. Di Criscienzo. RR Lyrae stars in Galactic globular clusters. VI. The period-amplitude relation. *A&A*, 476:779–790, December 2007.

G. Bono, P. B. Stetson, N. Sanna, A. Piersimoni, L. M. Freyhammer, Y. Bouzid, R. Buonanno, A. Calamida, F. Caputo, C. E. Corsi, et al. On the Relative Distances of ω Centauri and 47 Tucanae. *ApJ*, 686:L87–L90, October 2008.

J. Bovy, H.-W. Rix, C. Liu, D. W. Hogg, T. C. Beers, and Y. S. Lee. The Spatial Structure of Mono-abundance Sub-populations of the Milky Way Disk. *ApJ*, 753: 148, July 2012.

E. Bozzo, J. W. den Herder, M. Feroci, and L. Stella. LOFT - Large area Observatory For X-ray Timing. In *Extreme and Variable High Energy Sky (Extremesky 2011)*, 2011.

E. Bozzo, L. Stella, M. van der Klis, A. Watts, D. Barret, J. Wilms, P. Uttley, J. W. den Herder, and M. Feroci. The LOFT mission: new perspectives in the research field of (accreting) compact objects. In *European Physical Journal Web of Conferences*, volume 64 of *European Physical Journal Web of Conferences*, page 9002, January 2014.

H. V. D. Bradt, T. Ohashi, and K. A. Pounds. X-ray astronomy missions. *ARA&A*, 30:391–427, 1992.

A. C. Brinkman, J. Heise, and C. de Jager. Observation of cosmic X-ray sources with the Netherlands astronomical satellite (ANS). *Philips Technical Review*, 34:43–59, 1974.

E. F. Brown. Nuclear Heating and Melted Layers in the Inner Crust of an Accreting Neutron Star. *ApJ*, 531:988–1002, March 2000.

E. F. Brown and A. Cumming. Mapping Crustal Heating with the Cooling Light Curves of Quasi-Persistent Transients. *ApJ*, 698:1020–1032, June 2009.

E. F. Brown, L. Bildsten, and R. E. Rutledge. Crustal Heating and Quiescent Emission from Transiently Accreting Neutron Stars. *ApJ*, 504:L95+, September 1998.

E. F. Brown, L. Bildsten, and P. Chang. Variability in the Thermal Emission from Accreting Neutron Star Transients. *ApJ*, 574:920–929, August 2002.

M. Burgay, N. D'Amico, A. Possenti, R. N. Manchester, A. G. Lyne, B. C. Joshi, M. A. McLaughlin, M. Kramer, J. M. Sarkissian, F. Camilo, et al. An increased estimate of the merger rate of double neutron stars from observations of a highly relativistic system. *Nature*, 426:531–533, December 2003.

A. Burrows. Supernova explosions in the Universe. *Nature*, 403:727–733, February 2000.

A. Burrows. Colloquium: Perspectives on core-collapse supernova theory. *Reviews of Modern Physics*, 85:245–261, January 2013.

E. M. Cackett, R. Wijnands, C. O. Heinke, P. D. Edmonds, W. H. G. Lewin, D. Pooley, J. E. Grindlay, P. G. Jonker, and J. M. Miller. X-Ray Variability during the Quiescent State of the Neutron Star X-Ray Transient in the Globular Cluster NGC 6440. *ApJ*, 620:922–928, February 2005.

E. M. Cackett, R. Wijnands, M. Linares, J. M. Miller, J. Homan, and W. H. G. Lewin. Cooling of the quasi-persistent neutron star X-ray transients KS 1731-260 and MXB 1659-29. *MNRAS*, 372:479–488, October 2006.

E. M. Cackett, E. F. Brown, J. M. Miller, and R. Wijnands. Quiescent X-ray Emission From Cen X-4: A Variable Thermal Component. *ApJ*, 720:1325–1332, September 2010.

C. Cadeau, S. M. Morsink, D. Leahy, and S. S. Campbell. Light Curves for Rapidly Rotating Neutron Stars. *ApJ*, 654:458–469, January 2007.

A. G. W. Cameron. Pycnonuclear reactions and nova explosions. *AJ*, 64:325, October 1959.

S. Campana and L. Stella. On the Bolometric Quiescent Luminosity and Luminosity Swing of Black Hole Candidate and Neutron Star Low-Mass X-Ray Transients. *ApJ*, 541:849–859, October 2000.

S. Campana, L. Stella, S. Mereghetti, M. Colpi, M. Tavani, D. Ricci, D. D. Fiume, and T. Belloni. Aquila X-1 from Outburst to Quiescence: The Onset of the Propeller Effect and Signs of a Turned-on Rotation-powered Pulsar. *ApJ*, 499:L65+, May 1998.

S. Campana, L. Stella, S. Mereghetti, and D. Cremonesi. BeppoSAX observation of Cen X-4 in quiescence. *A&A*, 358:583–586, June 2000.

S. Campana, P. D'Avanzo, J. Casares, S. Covino, G. Israel, G. Marconi, R. Hynes, P. Charles, and L. Stella. Indirect Evidence of an Active Radio Pulsar in the Quiescent State of the Transient Millisecond Pulsar SAX J1808.4-3658. *ApJ*, 614: L49–L52, October 2004.

M. A. Caprio. LevelScheme: A level scheme drawing and scientific figure preparation system for Mathematica. *Computer Physics Communications*, 171:107–118, September 2005.

F. Caputo. Globular clusters. *Reports on Progress in Physics*, 48:1235–1282, September 1985.

E. Carretta, R. G. Gratton, G. Clementini, and F. Fusi Pecci. Distances, Ages, and Epoch of Formation of Globular Clusters. *ApJ*, 533:215–235, April 2000.

B. W. Carroll and D. A. Ostlie. *An Introduction to Modern Astrophysics*. 1996.

W. Cash. Parameter estimation in astronomy through application of the likelihood ratio. *ApJ*, 228:939–947, March 1979.

A. Catuneanu, C. O. Heinke, G. R. Sivakoff, W. C. G. Ho, and M. Servillat. Mass/radius Constraints on the Quiescent Neutron Star in M13 Using Hydrogen and Helium Atmospheres. *ApJ*, 764:145, February 2013.

J. Chadwick. Possible Existence of a Neutron. *Nature*, 129:312–+, February 1932.

N. Chamel and P. Haensel. Physics of Neutron Star Crusts. *Living Reviews in Relativity*, 11:10, December 2008.

S. Chandrasekhar. The Maximum Mass of Ideal White Dwarfs. *ApJ*, 74:81, July 1931.

S. Chaty. Nature, Formation, and Evolution of High Mass X-Ray Binaries. In L. Schmidtobreick, M. R. Schreiber, and C. Tappert, editors, *Evolution of Compact Binaries*, volume 447 of *Astronomical Society of the Pacific Conference Series*, page 29, September 2011.

G. W. Clark. Balloon Observation of the X-Ray Spectrum of the Crab Nebula Above 15 keV. *Physical Review Letters*, 14:91–94, January 1965.

G. W. Clark. X-ray binaries in globular clusters. *ApJ*, 199:L143–L145, August 1975.

G. W. Clark, J. W. Woo, F. Nagase, K. Makishima, and T. Sakao. Discovery of a cyclotron absorption line in the spectrum of the binary X-ray pulsar 4U 1538 - 52 observed by GINGA. *ApJ*, 353:274–280, April 1990.

R. Cornelisse, R. Wijnands, and J. Homan. An XMM-Newton observation of the neutron star X-ray transient 2S 1803-245 in quiescence. *MNRAS*, 380:1637–1641, October 2007.

J. Cottam, F. Paerels, and M. Mendez. Gravitationally redshifted absorption lines in the X-ray burst spectra of a neutron star. *Nature*, 420:51–54, November 2002.

J. Cottam, F. Paerels, M. Méndez, L. Boirin, W. H. G. Lewin, E. Kuulkers, and J. M. Miller. The Burst Spectra of EXO 0748-676 during a Long 2003 XMM-Newton Observation. *ApJ*, 672:504–509, January 2008.

T. J. Davidge, P. Cote, and W. E. Harris. Deep Infrared Array Photometry of Globular Clusters. V. M28 (NGC 6626). *ApJ*, 468:641, September 1996.

J. E. Davis. Event Pileup in Charge-coupled Devices. *ApJ*, 562:575–582, November 2001.

P. A. J. de Korte, J. A. M. Bleeker, S. P. McKechnie, A. J. F. den Boggende, A. C. Brinkman, E. H. B. M. Gronenschild, G. Branduardi-Raymont, J. L. Culhane, and I. Mason. The X-ray imaging telescopes on EXOSAT. *Space Sci. Rev.*, 30:495–511, March 1981.

P. B. Demorest, T. Pennucci, S. M. Ransom, M. S. E. Roberts, and J. W. T. Hessels. A two-solar-mass neutron star measured using Shapiro delay. *Nature*, 467:1081–1083, October 2010.

R. C. Dempsey, J. L. Linsky, J. H. M. M. Schmitt, and T. A. Fleming. The ROSAT All-Sky Survey of active binary coronae. II - Coronal temperatures of the RS Canum Venaticorum systems. *ApJ*, 413:333–338, August 1993.

J. W. den Herder, A. C. Brinkman, S. M. Kahn, G. Branduardi-Raymont, K. Thomsen, H. Aarts, M. Audard, J. V. Bixler, A. J. den Boggende, J. Cottam, et al. The Reflection Grating Spectrometer on board XMM-Newton. *A&A*, 365:L7–L17, January 2001.

J. S. Deneva, P. C. C. Freire, J. M. Cordes, A. G. Lyne, S. M. Ransom, I. Cognard, F. Camilo, D. J. Nice, I. H. Stairs, B. Allen, et al. Two Millisecond Pulsars Discovered by the PALFA Survey and a Shapiro Delay Measurement. *ApJ*, 757:89, September 2012.

R. Di Stefano and S. Rappaport. Predictions of a population of cataclysmic variables in globular clusters. *ApJ*, 423:274–293, March 1994.

J. M. Dickey and F. J. Lockman. H I in the Galaxy. *ARA&A*, 28:215–261, 1990.

R. C. Duncan and C. Thompson. Formation of very strongly magnetized neutron stars - Implications for gamma-ray bursts. *ApJ*, 392:L9–L13, June 1992.

R. J. Edgar and A. A. Vikhlinin. Absolute QE of ACIS S1, S2 and S3 from XRCF data at selected energies. *Chandra X-ray Center Calibration Memo, available at* `http://cxc.harvard.edu/cal/Acis/Cal_prods/qe/qe_memo.ps`, August 2004.

P. D. Edmonds, C. O. Heinke, J. E. Grindlay, and R. L. Gilliland. Hubble Space Telescope Detection of a Quiescent Low-Mass X-Ray Binary Companion in 47 Tucanae. *ApJ*, 564:L17–L20, January 2002.

G. Endrodi. QCD phase diagram: overview of recent lattice results. *ArXiv e-prints*, November 2013.

L. Engvik, E. Osnes, M. Hjorth-Jensen, G. Bao, and E. Ostgaard. Asymmetric Nuclear Matter and Neutron Star Properties. *ApJ*, 469:794, October 1996.

G. Fabbiano. Observations of supernova remnants with the Einstein Observatory. In R. Giacconi and G. Setti, editors, *NATO ASIC Proc. 60: X-Ray Astronomy*, pages 15–34, 1980.

G. Fabbiano, R. E. Griffiths, R. E. Doxsey, and M. D. Johnston. Study of the structure of the TYCHO SNR with the HEAO 1 scanning modulation collimator experiment. *ApJ*, 235:L163–L166, February 1980.

F. R. Ferraro, P. Montegriffo, L. Origlia, and F. Fusi Pecci. A New Infrared Array Photometric Survey of Galactic Globular Clusters: A Detailed Study of the Red Giant Branch Sequence as a Step toward the Global Testing of Stellar Models. *AJ*, 119:1282–1295, March 2000.

D. Foreman-Mackey, D. W. Hogg, D. Lang, and J. Goodman. emcee: The MCMC Hammer. *PASP*, 125:306–312, March 2013.

F. Foucart, L. Buchman, M. D. Duez, M. Grudich, L. E. Kidder, I. MacDonald, A. Mroue, H. P. Pfeiffer, M. A. Scheel, and B. Szilagyi. First direct comparison of nondisrupting neutron star-black hole and binary black hole merger simulations. *Phys. Rev. D*, 88(6):064017, September 2013.

P. C. C. Freire, C. G. Bassa, N. Wex, I. H. Stairs, D. J. Champion, S. M. Ransom, P. Lazarus, V. M. Kaspi, J. W. T. Hessels, M. Kramer, et al. On the nature and evolution of the unique binary pulsar J1903+0327. *MNRAS*, 412:2763–2780, April 2011.

J. K. Fridriksson, J. Homan, R. Wijnands, M. Méndez, D. Altamirano, E. M. Cackett, E. F. Brown, T. M. Belloni, N. Degenaar, and W. H. G. Lewin. Rapid Cooling of the Neutron Star in the Quiescent Super-Eddington Transient XTE J1701-462. *ApJ*, 714:270–286, May 2010.

M. Frigo and S. G. Johnson. "fftw: An adaptive software architecture for the fft". In The Institute of Electrical and New Jersey Electronical Engineers, editors, *Acoustics, Speech and Signal Processing, 1998. Proceedings of the 1998 IEEE International Conference, in Seattle, WA, USA*, pages 1381–1384, 1998.

H. Fritzsch. *Quarks: the stuff of matter*. 1983.

A. Fruscione, J. C. McDowell, G. E. Allen, N. S. Brickhouse, D. J. Burke, J. E. Davis, N. Durham, M. Elvis, E. C. Galle, D. E. Harris, et al. CIAO: Chandra's data analysis system. In *Society of Photo-Optical Instrumentation Engineers (SPIE) Conference Series*, volume 6270 of *Society of Photo-Optical Instrumentation Engineers (SPIE) Conference Series*, page 62701V, July 2006.

M. R. Garcia. X-ray emission from 4U 2129+47 (= V1727 Cygni) in quiescence. *ApJ*, 435:407–410, November 1994.

G. Garmire. X-Ray Astronomy. *New York Academy Sciences Annals*, 140:172–174, December 1966.

G. P. Garmire, M. W. Bautz, P. G. Ford, J. A. Nousek, and G. R. Ricker, Jr. Advanced CCD imaging spectrometer (ACIS) instrument on the Chandra X-ray Observatory. In J. E. Truemper & H. D. Tananbaum, editor, *Society of Photo-Optical Instrumentation Engineers (SPIE) Conference Series*, volume 4851 of *Society of Photo-Optical Instrumentation Engineers (SPIE) Conference Series*, pages 28–44, March 2003.

N. Gehrels, G. Chincarini, P. Giommi, K. O. Mason, J. A. Nousek, A. A. Wells, N. E. White, S. D. Barthelmy, D. N. Burrows, L. R. Cominsky, et al. The Swift Gamma-Ray Burst Mission. *ApJ*, 611:1005–1020, August 2004.

M. Gellmann. A schematic model of baryons and mesons. *Physics Letters*, 8:214–215, February 1964.

B. Gendre, D. Barret, and N. A. Webb. An XMM-Newton observation of the globular cluster Omega Centauri. *A&A*, 400:521–531, March 2003a.

B. Gendre, D. Barret, and N. A Webb. Discovery of a quiescent neutron star binary in the globular cluster M 13. *A&A*, 403:L11–L14, May 2003b.

K. C. Gendreau, Z. Arzoumanian, and T. Okajima. The Neutron star Interior Composition ExploreR (NICER): an Explorer mission of opportunity for soft x-ray timing spectroscopy. In *Society of Photo-Optical Instrumentation Engineers (SPIE) Conference Series*, volume 8443 of *Society of Photo-Optical Instrumentation Engineers (SPIE) Conference Series*, September 2012.

R. Giacconi, H. Gursky, F. R. Paolini, and B. B. Rossi. Evidence for x Rays From Sources Outside the Solar System. *Physical Review Letters*, 9:439–443, December 1962.

R. Giacconi, E. Kellogg, P. Gorenstein, H. Gursky, and H. Tananbaum. An X-Ray Scan of the Galactic Plane from UHURU. *ApJ*, 165:L27+, April 1971.

R. Giacconi, G. Branduardi, U. Briel, A. Epstein, D. Fabricant, E. Feigelson, W. Forman, P. Gorenstein, J. Grindlay, H. Gursky, et al. The Einstein /HEAO 2/ X-ray Observatory. *ApJ*, 230:540–550, June 1979.

N. K. Glendenning and S. A. Moszkowski. Reconciliation of neutron-star masses and binding of the Lambda in hypernuclei. *Physical Review Letters*, 67:2414–1417, October 1991.

N. K. Glendenning and J. Schaffner-Bielich. First order kaon condensate. *Phys. Rev. C*, 60(2):025803, August 1999.

J. Goodman and J. Weare. Ensemble samplers with affine invariance. *CAMCoS*, 5: 65–80, January 2010.

N. M. Gosnell, D. Pooley, A. M. Geller, J. Kalirai, R. D. Mathieu, P. Frinchaboy, and E. Ramirez-Ruiz. An Unexpected Discovery in the Rich Open Cluster NGC 6819 Using XMM-Newton. *ApJ*, 745:57, January 2012.

D. E. Graessle, I. N. Evans, K. Glotfelty, X. H. He, J. D. Evans, A. H. Rots, G. Fabbiano, and R. J. Brissenden. The Chandra X-ray Observatory Calibration Database (CALDB): Building, Planning, and Improving. *Chandra News*, 14:33–+, March 2007.

C. E. Grant. *Charge-coupled devices*, pages 39–58. Cambridge University Press, September 2011.

R. G. Gratton, A. Bragaglia, E. Carretta, G. Clementini, S. Desidera, F. Grundahl, and S. Lucatello. Distances and ages of NGC 6397, NGC 6752 and 47 Tuc. *A&A*, 408:529–543, September 2003.

R. G. Gratton, E. Carretta, A. Bragaglia, S. Lucatello, and V. D'Orazi. The second and third parameters of the horizontal branch in globular clusters. *A&A*, 517:A81, July 2010.

R. G. Gratton, E. Carretta, and A. Bragaglia. Multiple populations in globular clusters. Lessons learned from the Milky Way globular clusters. *A&A Rev.*, 20:50, February 2012.

E. K. Grebel and W. J. Roberts. Heterochromatic extinction. I. Dependence of interstellar extinction on stellar temperature, surface gravity, and metallicity. *A&AS*, 109:293–312, February 1995.

Phil Gregory. *Bayesian Logical Data Analysis for the Physical Sciences*. Cambridge University Press, New York, NY, USA, 2005. ISBN 052184150X.

J. Grindlay, H. Gursky, H. Schnopper, D. R. Parsignault, J. Heise, A. C. Brinkman, and J. Schrijver. Discovery of intense X-ray bursts from the globular cluster NGC 6624. *ApJ*, 205:L127–L130, May 1976.

J. E. Grindlay, C. Heinke, P. D. Edmonds, and S. S. Murray. High-Resolution X-ray Imaging of a Globular Cluster Core: Compact Binaries in 47Tuc. *Science*, 292: 2290–2295, June 2001a.

J. E. Grindlay, C. O. Heinke, P. D. Edmonds, S. S. Murray, and A. M. Cool. Chandra Exposes the Core-collapsed Globular Cluster NGC 6397. *ApJ*, 563:L53–L56, December 2001b.

M. Guainizzi. EPIC status of calibration and data analysis. *XMM-Newton Calibration Technical Note, available at* `http://xmm2.esac.esa.int/docs/documents/CAL-TN-0018.pdf`, July 2012.

S. Guillot, R. E. Rutledge, L. Bildsten, E. F. Brown, G. G. Pavlov, and V. E. Zavlin. X-ray spectral identification of three candidate quiescent low-mass X-ray binaries in the globular cluster NGC 6304. *MNRAS*, 392:665–681, January 2009a.

S. Guillot, R. E. Rutledge, E. F. Brown, G. G. Pavlov, and V. E. Zavlin. Chandra Observation of Quiescent Low-Mass X-Ray Binaries in the Globular Cluster NGC 6304. *ApJ*, 699:1418–1422, July 2009b.

Sebastien Guillot. An XMM Search for Quiescent Low-Mass X-Ray Binaries in Globular Clusters using Spectral Identification. Master's thesis, McGill University, 2009.

S. Gupta, E. F. Brown, H. Schatz, P. Möller, and K.-L. Kratz. Heating in the Accreted Neutron Star Ocean: Implications for Superburst Ignition. *ApJ*, 662: 1188–1197, June 2007.

M. E. Gusakov, A. I. Chugunov, and E. M. Kantor. Instability windows and evolution of rapidly rotating neutron stars. *ArXiv e-prints*, October 2013.

T. Güver and F. Özel. The Mass and the Radius of the Neutron Star in the Transient Low-mass X-Ray Binary SAX J1748.9–2021. *ApJ*, 765:L1, March 2013.

T. Güver, F. Özel, A. Cabrera-Lavers, and P. Wroblewski. The Distance, Mass, and Radius of the Neutron Star in 4U 1608–52. *ApJ*, 712:964–973, April 2010a.

T. Güver, P. Wroblewski, L. Camarota, and F. Özel. The Mass and Radius of the Neutron Star in 4U 1820–30. *ApJ*, 719:1807–1812, August 2010b.

C. B. Haakonsen, M. L. Turner, N. A. Tacik, and R. E. Rutledge. The McGill Planar Hydrogen Atmosphere Code (McPHAC). *ApJ*, 749:52, April 2012.

F. Haberl. The magnificent seven: magnetic fields and surface temperature distributions. *Ap&SS*, 308:181–190, April 2007.

P. Haensel and J. L. Zdunik. Nuclear composition and heating in accreting neutron-star crusts. *A&A*, 404:L33–L36, June 2003.

P. Haensel and J. L. Zdunik. Models of crustal heating in accreting neutron stars. *A&A*, 480:459–464, March 2008.

P. Haensel and J. L. Zdunik. Non-equilibrium processes in the crust of an accreting neutron star. *A&A*, 227:431–436, January 1990.

P. Haensel, A. Y. Potekhin, and D. G. Yakovlev. *Neutron Stars 1: Equation of State and Structure*. 2007.

D. Haggard, A. M. Cool, J. Anderson, P. D. Edmonds, P. J. Callanan, C. O. Heinke, J. E. Grindlay, and C. D. Bailyn. Hubble Space Telescope Advanced Camera for Surveys Imaging of ω Centauri: Optical Counterpart for the Quiescent Low-Mass X-Ray Binary. *ApJ*, 613:512–516, September 2004.

J. P. Halpern and S. S. Holt. Discovery of soft X-ray pulsations from the gamma-ray source Geminga. *Nature*, 357:222–224, May 1992.

T. H. Hankins, J. M. Rankin, and J. A. Eilek. What is the Physics of Pulsar Radio Emission? In *astro2010: The Astronomy and Astrophysics Decadal Survey*, volume 2010 of *Astronomy*, page 112, 2009.

B. M. S. Hansen, J. Anderson, J. Brewer, A. Dotter, G. G. Fahlman, J. Hurley, J. Kalirai, I. King, D. Reitzel, H. B. Richer, et al. The White Dwarf Cooling Sequence of NGC 6397. *ApJ*, 671:380–401, December 2007.

W. E. Harris. Globular clusters: The view from HST. In M. Livio, K. Noll, and M. Stiavelli, editors, *A Decade of Hubble Space Telescope Science*, pages 78–100, 2003.

W. E. Harris. A New Catalog of Globular Clusters in the Milky Way. *ArXiv e-prints*, December 2010.

W. E. Harris. A Catalog of Parameters for Globular Clusters in the Milky Way. *AJ*, 112:1487–+, October 1996.

E. R. Harrison. Thermonuclear and pycnonuclear reactions. *Proceedings of the Physical Society*, 84:213–229, August 1964.

F. A. Harrison, W. W. Craig, F. E. Christensen, C. J. Hailey, W. W. Zhang, S. E. Boggs, D. Stern, W. R. Cook, K. Forster, P. Giommi, et al. The Nuclear Spectroscopic Telescope Array (NuSTAR) High-energy X-Ray Mission. *ApJ*, 770:103, June 2013.

K. Hebeler, J. M. Lattimer, C. J. Pethick, and A. Schwenk. Equation of State and Neutron Star Properties Constrained by Nuclear Physics and Observation. *ApJ*, 773:11, August 2013.

A. Heger, C. L. Fryer, S. E. Woosley, N. Langer, and D. H. Hartmann. How Massive Single Stars End Their Life. *ApJ*, 591:288–300, July 2003.

C. O. Heinke and W. C. G. Ho. Direct Observation of the Cooling of the Cassiopeia A Neutron Star. *ApJ*, 719:L167–L171, August 2010.

C. O. Heinke, P. D. Edmonds, J. E. Grindlay, D. A. Lloyd, H. N. Cohn, and P. M. Lugger. A Chandra X-Ray Study of the Dense Globular Cluster Terzan 5. *ApJ*, 590:809–821, June 2003a.

C. O. Heinke, J. E. Grindlay, P. D. Edmonds, D. A. Lloyd, S. S. Murray, H. N. Cohn, and P. M. Lugger. A Chandra X-Ray Study of the Globular Cluster M80. *ApJ*, 598:516–526, November 2003b.

C. O. Heinke, J. E. Grindlay, D. A. Lloyd, and P. D. Edmonds. X-Ray Studies of Two Neutron Stars in 47 Tucanae: Toward Constraints on the Equation of State. *ApJ*, 588:452–463, May 2003c.

C. O. Heinke, J. E. Grindlay, P. M. Lugger, H. N. Cohn, P. D. Edmonds, D. A. Lloyd, and A. M. Cool. Analysis of the Quiescent Low-Mass X-Ray Binary Population in Galactic Globular Clusters. *ApJ*, 598:501–515, November 2003d.

C. O. Heinke, J. E. Grindlay, and P. D. Edmonds. Three Additional Quiescent Low-Mass X-Ray Binary Candidates in 47 Tucanae. *ApJ*, 622:556–564, March 2005.

C. O. Heinke, G. B. Rybicki, R. Narayan, and J. E. Grindlay. A Hydrogen Atmosphere Spectral Model Applied to the Neutron Star X7 in the Globular Cluster 47 Tucanae. *ApJ*, 644:1090–1103, June 2006a.

C. O. Heinke, R. Wijnands, H. N. Cohn, P. M. Lugger, J. E. Grindlay, D. Pooley, and W. H. G. Lewin. Faint X-Ray Sources in the Globular Cluster Terzan 5. *ApJ*, 651:1098–1111, November 2006b.

M. Hénon. Sur l'évolution dynamique des amas globulaires. II. Amas isolés. *Annales d'Astrophysique*, 28:62, February 1965.

P. Hertz and J. E. Grindlay. An X-ray survey of globular clusters and their X-ray luminosity function. *ApJ*, 275:105–119, December 1983.

J. W. T. Hessels, S. M. Ransom, I. H. Stairs, P. C. C. Freire, V. M. Kaspi, and F. Camilo. A Radio Pulsar Spinning at 716 Hz. *Science*, 311:1901–1904, March 2006.

A. Hewish, S. J. Bell, J. D. H. Pilkington, P. F. Scott, and R. A. Collins. Observation of a Rapidly Pulsating Radio Source. *Nature*, 217:709–713, February 1968.

J. S. Heyl, H. Richer, J. Anderson, G. Fahlman, A. Dotter, J. Hurley, J. Kalirai, R. M. Rich, M. Shara, P. Stetson, et al. Deep Hubble Space Telescope Imaging in NGC 6397: Stellar Dynamics. *ApJ*, 761:51, December 2012.

E. Høg, A. Kuzmin, U. Bastian, C. Fabricius, K. Kuimov, L. Lindegren, V. V. Makarov, and S. Roeser. The TYCHO Reference Catalogue. *A&A*, 335:L65–L68, July 1998.

E. Høg, C. Fabricius, V. V. Makarov, S. Urban, T. Corbin, G. Wycoff, U. Bastian, P. Schwekendiek, and A. Wicenec. The Tycho-2 catalogue of the 2.5 million brightest stars. *A&A*, 355:L27–L30, March 2000.

C. J. Horowitz and J. Piekarewicz. Neutron Star Structure and the Neutron Radius of ^{208}Pb. *Physical Review Letters*, 86:5647–5650, June 2001a.

C. J. Horowitz and J. Piekarewicz. Neutron radii of ^{208}Pb and neutron stars. *Phys. Rev. C*, 64(6):062802, December 2001b.

C. J. Horowitz, M. A. Pérez-García, D. K. Berry, and J. Piekarewicz. Dynamical response of the nuclear "pasta" in neutron star crusts. *Phys. Rev. C*, 72(3):035801, September 2005.

C. J. Horowitz, Z. Ahmed, C.-M. Jen, A. Rakhman, P. A. Souder, M. M. Dalton, N. Liyanage, K. D. Paschke, K. Saenboonruang, R. Silwal, et al. Weak charge form factor and radius of ^{208}Pb through parity violation in electron scattering. *Phys. Rev. C*, 85(3):032501, March 2012.

N. Houk and M. Smith-Moore. *Michigan Catalogue of Two-dimensional Spectral Types for the HD Stars. Volume 4, Declinations -26°.0 to -12°.0.* 1988.

F. Hund. Materie unter sehr hohen Drucken und Temperaturen. *Ergebnisse der exakten Naturwissenschaften*, 15:189, 1936.

P. Hut, S. McMillan, J. Goodman, M. Mateo, E. S. Phinney, C. Pryor, H. B. Richer, F. Verbunt, and M. Weinberg. Binaries in globular clusters. *PASP*, 104:981–1034, November 1992.

J. J. M. in't Zand, M. H. van Kerkwijk, D. Pooley, F. Verbunt, R. Wijnands, and W. H. G. Lewin. Identification of the Optical and Quiescent Counterparts to the Bright X-Ray Transient in NGC 6440. *ApJ*, 563:L41–L44, December 2001.

D. Ivanenko and D. F. Kurdgelaidze. Remarks on quark stars. *Indian Journal of Pure and Applied Physics*, 7:585–586, 1969.

D. D. Ivanenko and D. F. Kurdgelaidze. Hypothesis concerning quark stars. *Astrophysics*, 1:251–252, October 1965.

N. Ivanova. Low-Mass X-Ray Binaries and Metallicity Dependence: Story of Failures. *ApJ*, 636:979–984, January 2006.

F. Jansen, D. Lumb, B. Altieri, J. Clavel, M. Ehle, C. Erd, C. Gabriel, M. Guainazzi, P. Gondoin, R. Much, et al. XMM-Newton observatory. I. The spacecraft and operations. *A&A*, 365:L1–L6, January 2001.

J. G. Jernigan, H. V. Bradt, R. E. Doxsey, J. E. McClintock, and K. M. V. Apparao. Positions of three X-ray burst sources. *Nature*, 270:321–323, November 1977.

P. G. Jonker, C. G. Bassa, and S. Wachter. The quasi-persistent neutron star soft X-ray transient 1M 1716-315 in quiescence. *MNRAS*, 377:1295–1300, May 2007a.

P. G. Jonker, D. Steeghs, D. Chakrabarty, and A. M. Juett. The Cold Neutron Star in the Soft X-Ray Transient 1H 1905+000. *ApJ*, 665:L147–L150, August 2007b.

K. J. Joshi, F. A. Rasio, and S. Portegies Zwart. Monte Carlo Simulations of Globular Cluster Evolution. I. Method and Test Calculations. *ApJ*, 540:969–982, September 2000.

P. M. W. Kalberla, W. B. Burton, D. Hartmann, E. M. Arnal, E. Bajaja, R. Morras, and W. G. L. Pöppel. The Leiden/Argentine/Bonn (LAB) Survey of Galactic HI. Final data release of the combined LDS and IAR surveys with improved stray-radiation corrections. *A&A*, 440:775–782, September 2005.

A. D. Kaminker, G. G. Pavlov, and I. A. Shibanov. Spectra of radiation from a strongly magnetized plasma. *Ap&SS*, 91:167–214, March 1983.

V. M. Kaspi. Grand unification of neutron stars. *Proceedings of the National Academy of Science*, 107:7147–7152, April 2010.

V. M. Kaspi, F. P. Gavriil, D. Chakrabarty, J. R. Lackey, and M. P. Muno. Long-Term Rossi X-Ray Timing Explorer Monitoring of the Anomalous X-Ray Pulsar 1E 1048.1-5937. *ApJ*, 558:253–262, September 2001.

J. I. Katz. Two kinds of stellar collapse. *Nature*, 253:698, February 1975.

I. King. The structure of star clusters. I. an empirical density law. *AJ*, 67:471, October 1962.

S. Koranda, N. Stergioulas, and J. L. Friedman. Upper Limits Set by Causality on the Rotation and Mass of Uniformly Rotating Relativistic Stars. *ApJ*, 488:799, October 1997.

K. Koyama, H. Inoue, K. Makishima, M. Matsuoka, T. Murakami, M. Oda, Y. Osgawara, T. Ohashi, N. Shibazaki, Y. Tanaka, et al. Discovery of X-ray bursts from Aquila X-1. *ApJ*, 247:L27–L29, July 1981.

M. Kramer. Pulsar Timing - From Astrophysics to Fundamental Physics (With 10 Figures). In S. Röser, editor, *Reviews in Modern Astronomy*, volume 20 of *Reviews in Modern Astronomy*, page 255, October 2008.

E. Kuulkers, P. R. den Hartog, J. J. M. in't Zand, F. W. M. Verbunt, W. E. Harris, and M. Cocchi. Photospheric radius expansion X-ray bursts as standard candles. *A&A*, 399:663–680, February 2003.

B. D. Lackey, K. Kyutoku, M. Shibata, P. R. Brady, and J. L. Friedman. Extracting equation of state parameters from black hole-neutron star mergers: Nonspinning black holes. *Phys. Rev. D*, 85(4):044061, February 2012.

X.-Y. Lai and R.-X. Xu. A note on the discovery of a $2M_{odot}$ pulsar. *Research in Astronomy and Astrophysics*, 11:687–691, June 2011.

J.-P. Lasota. The disc instability model of dwarf novae and low-mass X-ray binary transients. *New Astronomy Reviews*, 45:449–508, June 2001.

J.-P. Lasota. ADAFs, accretion discs and outbursts in compact binaries. *New Astronomy Reviews*, 51:752–758, May 2008.

J. M. Lattimer. The Nuclear Equation of State and Neutron Star Masses. *Annual Review of Nuclear and Particle Science*, 62:485–515, November 2012.

J. M. Lattimer and M. Prakash. Neutron Star Structure and the Equation of State. *ApJ*, 550:426–442, March 2001.

J. M. Lattimer and M. Prakash. The Physics of Neutron Stars. *Science*, 304:536–542, April 2004.

J. M. Lattimer and M. Prakash. Neutron star observations: Prognosis for equation of state constraints. *Phys. Rep.*, 442:109–165, April 2007.

J. M. Lattimer and M. Prakash. What a Two Solar Mass Neutron Star Really Means. *ArXiv e-prints*, December 2010.

J. M. Lattimer and B. F. Schutz. Constraining the Equation of State with Moment of Inertia Measurements. *ApJ*, 629:979–984, August 2005.

J. M. Lattimer and D. Swesty. A generalized equation of state for hot, dense matter. *Nuclear Physics A*, 535:331–376, December 1991.

J. M. Lattimer, M. Prakash, D. Masak, and A. Yahil. Rapidly rotating pulsars and the equation of state. *ApJ*, 355:241–254, May 1990.

L. Laudau. On the theory of stars. *Phys. Z. Sowjetunion*, 1:285–288, 1932.

D. R. Law, S. R. Majewski, M. F. Skrutskie, J. M. Carpenter, and H. F. Ayub. 2MASS Studies of Differential Reddening across Three Massive Globular Clusters. *AJ*, 126:1871–1887, October 2003.

D. A. Leahy, W. Darbro, R. F. Elsner, M. C. Weisskopf, S. Kahn, P. G. Sutherland, and J. E. Grindlay. On searches for pulsed emission with application to four globular cluster x-ray sources - ngc 1851, 6441, 6624, and 6712. *ApJ*, 266:160, March 1983.

D. A. Leahy, S. M. Morsink, and C. Cadeau. Limits on Mass and Radius for the Millisecond-Period X-Ray Pulsar SAX J1808.4-3658. *ApJ*, 672:1119–1126, January 2008.

D. A. Leahy, S. M. Morsink, Y.-Y. Chung, and Y. Chou. Constraints on the Properties of the Neutron Star XTE J1814-338 from Pulse-Shape Models. *ApJ*, 691:1235–1242, February 2009.

H. S. Leavitt and E. C. Pickering. Periods of 25 Variable Stars in the Small Magellanic Cloud. *Harvard College Observatory Circular*, 173:1–3, March 1912.

A. M. Levine, F. L. Lang, W. H. G. Lewin, F. A. Primini, C. A. Dobson, J. P. Doty, J. A. Hoffman, S. K. Howe, A. Scheepmaker, W. A. Wheaton, et al. The HEAO 1 A-4 catalog of high-energy X-ray sources. *ApJS*, 54:581–617, April 1984.

W. H. G. Lewin, J. Doty, G. W. Clark, S. A. Rappaport, H. V. D. Bradt, R. Doxsey, D. R. Hearn, J. A. Hoffman, J. G. Jernigan, F. K. Li, et al. The discovery of rapidly repetitive X-ray bursts from a new source in Scorpius. *ApJ*, 207:L95–L99, July 1976a.

W. H. G. Lewin, J. A. Hoffman, J. Doty, D. R. Hearn, G. W. Clark, J. G. Jernigan, F. K. Li, J. E. McClintock, and J. Richardson. Discovery of X-ray bursts from several sources near the galactic centre. *MNRAS*, 177:83P–92P, December 1976b.

W. H. G. Lewin, F. K. Li, J. A. Hoffman, J. Doty, J. Buff, G. W. Clark, and S. Rappaport. Discovery of X-ray bursts from two sources in Aquila. *MNRAS*, 177: 93P–100P, December 1976c.

W. H. G. Lewin, W. D. Vacca, and E. M. Basinska. Precursors to X-ray bursts - The result of expansion and subsequent contraction of the neutron star's photosphere. *ApJ*, 277:L57–L60, February 1984.

D. R. Lorimer. The Galactic Pulsar Population. *Highlights of Astronomy*, 15:807–807, November 2010.

P. M. Lugger, H. N. Cohn, C. O. Heinke, J. E. Grindlay, and P. D. Edmonds. Chandra X-Ray Sources in the Collapsed-Core Globular Cluster M30 (NGC 7099). *ApJ*, 657: 286–301, March 2007.

D. H. Lumb, G. D. Berthiaume, D. N. Burrows, G. P. Garmire, and J. A. Nousek. Charge coupled devices (CCDs) in X-ray astronomy. *Experimental Astronomy*, 2: 179–201, May 1991.

A. G. Lyne, M. Burgay, M. Kramer, A. Possenti, R. N. Manchester, F. Camilo, M. A. McLaughlin, D. R. Lorimer, N. D'Amico, B. C. Joshi, et al. A Double-Pulsar System: A Rare Laboratory for Relativistic Gravity and Plasma Physics. *Science*, 303:1153–1157, February 2004.

S. N. MacEachern and L. M. Berliner. Subsampling the Gibbs sampler. *The American Statistician*, 48(3):188–190, 1994.

K. Makishima, K. Mitsuda, H. Inoue, K. Koyama, M. Matsuoka, T. Murakami, M. Oda, Y. Ogawara, T. Ohashi, N. Shibazaki, et al. Discovery of X-ray bursts from GX 3+1 /4U 1744-26/. *ApJ*, 267:310–314, April 1983.

R. N. Manchester, G. B. Hobbs, A. Teoh, and M. Hobbs. The Australia Telescope National Facility Pulsar Catalogue. *AJ*, 129:1993–2006, April 2005.

M. Marconi, F. Caputo, M. Di Criscienzo, and M. Castellani. RR Lyrae Stars in Galactic Globular Clusters. II. A Theoretical Approach to Variables in M3. *ApJ*, 596:299–313, October 2003.

B. Margon, B. Beck-Winchatz, L. Homer, D. Pooley, C. G. Bassa, S. F. Anderson, W. H. G. Lewin, F. Verbunt, A. K. H. Kong, and R. M. Plotkin. Cataclysmic Variables and Other Compact Binaries in the Globular Cluster NGC 362: Candidates from Chandra and HST. In V. Kalogera and M. van der Sluys, editors, *American Institute of Physics Conference Series*, volume 1314 of *American Institute of Physics Conference Series*, pages 163–168, December 2010.

M. Matsuoka, H. Inoue, K. Koyama, K. Makishima, T. Murakami, M. Oda, Y. Ogawara, T. Ohashi, N. Shibazaki, Y. Tanaka, et al. Discovery of a large X-ray burst from an X-ray nova, Centaurus X-4. *ApJ*, 240:L137–L141, September 1980.

M. Matsuoka, K. Kawasaki, S. Ueno, H. Tomida, M. Kohama, M. Ishikawa, H. Katayama, M. Suzuki, T. Miyakawa, T. Mihara, et al. An overview of MAXI onboard JEM-EF of the International Space Station. In *Society of Photo-Optical Instrumentation Engineers (SPIE) Conference Series*, volume 6686 of *Society of Photo-Optical Instrumentation Engineers (SPIE) Conference Series*, September 2007.

M. Matsuoka, K. Kawasaki, S. Ueno, H. Tomida, M. Kohama, M. Suzuki, Y. Adachi, M. Ishikawa, T. Mihara, M. Sugizaki, et al. The MAXI Mission on the ISS: Science and Instruments for Monitoring All-Sky X-Ray Images. *PASJ*, 61:999–, October 2009.

J. E. McClintock, R. Narayan, and G. B. Rybicki. On the Lack of Thermal Emission from the Quiescent Black Hole XTE J1118+480: Evidence for the Event Horizon. *ApJ*, 615:402–415, November 2004.

I. McDonald, J. T. van Loon, L. Decin, M. L. Boyer, A. K. Dupree, A. Evans, R. D. Gehrz, and C. E. Woodward. Giants in the globular cluster ω Centauri: dust production, mass-loss and distance. *MNRAS*, 394:831–856, April 2009.

D. E. McLaughlin, J. Anderson, G. Meylan, K. Gebhardt, C. Pryor, D. Minniti, and S. Phinney. Hubble Space Telescope Proper Motions and Stellar Dynamics in the Core of the Globular Cluster 47 Tucanae. *ApJS*, 166:249–297, September 2006a.

M. A. McLaughlin, A. G. Lyne, D. R. Lorimer, M. Kramer, A. J. Faulkner, R. N. Manchester, J. M. Cordes, F. Camilo, A. Possenti, I. H. Stairs, et al. Transient radio bursts from rotating neutron stars. *Nature*, 439:817–820, February 2006b.

D. B. Melrose. The Models for Radio Emission from Pulsars - the Outstanding Issues. *Journal of Astrophysics and Astronomy*, 16:137, June 1995.

S. Mereghetti. The strongest cosmic magnets: soft gamma-ray repeaters and anomalous X-ray pulsars. *A&A Rev.*, 15:225–287, July 2008.

A. Merloni, P. Predehl, W. Becker, H. Böhringer, T. Boller, H. Brunner, M. Brusa, K. Dennerl, M. Freyberg, P. Friedrich, et al. eROSITA Science Book: Mapping the Structure of the Energetic Universe. *ArXiv e-prints*, September 2012.

A. B. Migdal. Superfluidity and the moments of inertia of nuclei. *Nucl. Phys. A*, 13: 655–674, November 1959.

D. Mihalas. *Stellar atmospheres /2nd edition/*. 1978.

M. C. Miller. Astrophysical Constraints on Dense Matter in Neutron Stars. *ArXiv e-prints*, November 2013.

M. C. Miller, F. K. Lamb, and D. Psaltis. Constraints on the Equation of State of Neutron Star Matter from Observations of Kilohertz QPOs. In L. Scarsi, H. Bradt, P. Giommi, and F. Fiore, editors, *The Active X-ray Sky: Results from BeppoSAX and RXTE*, pages 123–+, 1998.

S. Miyamoto. Japanese satellite programs in X-ray astronomy. *Advances in Space Research*, 2:285–291, 1982.

R. Morrison and D. McCammon. Interstellar photoelectric absorption cross sections, 0.03-10 keV. *ApJ*, 270:119–122, July 1983.

S. M. Morsink and D. A. Leahy. Multi-epoch Analysis of Pulse Shapes from the Neutron Star SAX J1808.4-3658. *ApJ*, 726:56, January 2011.

H. Müller and B. D. Serot. Relativistic mean-field theory and the high-density nuclear equation of state. *Nuclear Physics A*, 606:508–537, February 1996.

H. Müther, M. Prakash, and T. L. Ainsworth. The nuclear symmetry energy in relativistic Brueckner-Hartree-Fock calculations. *Physics Letters B*, 199:469–474, December 1987.

G. Nelemans and P. G. Jonker. Ultra-compact (X-ray) binaries. *New Astronomy Reviews*, 54:87–92, March 2010.

W. G. Newton, M. Gearheart, J. Hooker, and B.-A. Li. The nuclear symmetry energy, the inner crust, and global neutron star modeling. *ArXiv e-prints*, December 2011.

W. G. Newton, K. Murphy, J. Hooker, and B.-A. Li. The Cooling of the Cassiopeia A Neutron Star as a Probe of the Nuclear Symmetry Energy and Nuclear Pasta. *ApJ*, 779:L4, December 2013.

S. A. Olausen and V. M. Kaspi. The McGill Magnetar Catalog. *ApJS*, 212:6, May 2014.

S. A. Olausen, W. W. Zhu, J. K. Vogel, V. M. Kaspi, A. G. Lyne, C. M. Espinoza, B. W. Stappers, R. N. Manchester, and M. A. McLaughlin. X-Ray Observations of High-B Radio Pulsars. *ApJ*, 764:1, February 2013.

J. Olofsson, A. Juhász, T. Henning, H. Mutschke, A. Tamanai, A. Moór, and P. Ábrahám. Transient dust in warm debris disks. Detection of Fe-rich olivine grains. *A&A*, 542:A90, June 2012.

J. R. Oppenheimer and G. M. Volkoff. On Massive Neutron Cores. *Physical Review*, 55:374–381, February 1939.

S. Ortolani, A. Renzini, R. Gilmozzi, G. Marconi, B. Barbuy, E. Bica, and R. M. Rich. Near-coeval formation of the Galactic bulge and halo inferred from globular cluster ages. *Nature*, 377:701–704, October 1995.

C. D. Ott, E. Abdikamalov, P. Mösta, R. Haas, S. Drasco, E. P. O'Connor, C. Reisswig, C. A. Meakin, and E. Schnetter. General-relativistic Simulations of Three-dimensional Core-collapse Supernovae. *ApJ*, 768:115, May 2013.

F. Özel. Soft equations of state for neutron-star matter ruled out by EXO 0748 - 676. *Nature*, 441:1115–1117, June 2006.

F. Özel, T. Güver, and D. Psaltis. The Mass and Radius of the Neutron Star in EXO 1745–248. *ApJ*, 693:1775–1779, March 2009.

F. Özel, A. Gould, and T. Güver. The Mass and Radius of the Neutron Star in the Bulge Low-mass X-Ray Binary KS 1731-260. *ApJ*, 748:5, March 2012a.

F. Özel, D. Psaltis, R. Narayan, and A. Santos Villarreal. On the Mass Distribution and Birth Masses of Neutron Stars. *ApJ*, 757:55, September 2012b.

F. Pacini. Gravitational collapse and scalar interaction in superdense matter. *Annales d'Astrophysique*, 29:193, February 1966.

D. Page and S. Reddy. Thermal and transport properties of the neutron star inner crust. *ArXiv e-prints*, January 2012.

D. M. Palmer, S. Barthelmy, N. Gehrels, R. M. Kippen, T. Cayton, C. Kouveliotou, D. Eichler, R. A. M. J. Wijers, P. M. Woods, J. Granot, et al. A giant γ-ray flare from the magnetar SGR 1806 - 20. *Nature*, 434:1107–1109, April 2005.

V. R. Pandharipande and R. A. Smith. A model neutron solid with π^0 condensate. *Nuclear Physics A*, 237:507–532, January 1975.

A. Papitto, C. Ferrigno, E. Bozzo, N. Rea, L. Pavan, L. Burderi, M. Burgay, S. Campana, T. di Salvo, M. Falanga, et al. Swings between rotation and accretion power in a binary millisecond pulsar. *Nature*, 501:517–520, September 2013.

G. G. Pavlov, V. E. Zavlin, B. Aschenbach, J. Trümper, and D. Sanwal. The Compact Central Object in Cassiopeia A: A Neutron Star with Hot Polar Caps or a Black Hole? *ApJ*, 531:L53–L56, March 2000.

M. E. Peskin and D. V. Schroeder. *An Introduction to Quantum Field Theory*. Westview Press, 1995.

G. Piccinotti, R. F. Mushotzky, E. A. Boldt, S. S. Holt, F. E. Marshall, P. J. Serlemitsos, and R. A. Shafer. A complete X-ray sample of the high-latitude /absolute value of B greater than 20 deg/ sky from HEAO 1 A-2 - Log N-log S and luminosity functions. *ApJ*, 253:485–503, February 1982.

G. Piotto, I. R. King, S. G. Djorgovski, C. Sosin, M. Zoccali, I. Saviane, F. De Angeli, M. Riello, A. Recio-Blanco, R. M. Rich, et al. HST color-magnitude diagrams of 74 galactic globular clusters in the HST F439W and F555W bands. *A&A*, 391: 945–965, September 2002.

G. Piotto, L. R. Bedin, J. Anderson, I. R. King, S. Cassisi, A. P. Milone, S. Villanova, A. Pietrinferni, and A. Renzini. A Triple Main Sequence in the Globular Cluster NGC 2808. *ApJ*, 661:L53–L56, May 2007.

J. A. Pons, F. M. Walter, J. M. Lattimer, M. Prakash, R. Neuhäuser, and P. An. Toward a Mass and Radius Determination of the Nearby Isolated Neutron Star RX J185635-3754. *ApJ*, 564:981–1006, January 2002.

J. A. Pons, D. Viganò, and N. Rea. A highly resistive layer within the crust of X-ray pulsars limits their spin periods. *Nature Physics*, 9:431–434, July 2013.

D. Pooley, W. H. G. Lewin, S. F. Anderson, H. Baumgardt, A. V. Filippenko, B. M. Gaensler, L. Homer, P. Hut, V. M. Kaspi, J. Makino, et al. Dynamical Formation of Close Binary Systems in Globular Clusters. *ApJ*, 591:L131–L134, July 2003.

D. Pooley, J. Homan, C. Heinke, M. Linares, D. Altamirano, and W. Lewin. Chandra Identification of the Transient in Terzan 5: Not the 2000 Transient. *The Astronomer's Telegram*, 2974:1–+, October 2010.

P. Popowski and A. Gould. The RR Lyrae Distance Scale. *Post-Hipparcos Cosmic Candles*, 237:53, 1999.

M. Prakash, J. M. Lattimer, and T. L. Ainsworth. Equation of state and the maximum mass of neutron stars. *Physical Review Letters*, 61:2518–2521, November 1988.

M. Prakash, J. R. Cooke, and J. M. Lattimer. Quark-hadron phase transition in protoneutron stars. *Phys. Rev. D*, 52:661–665, July 1995.

P. Predehl and J. H. M. M. Schmitt. X-raying the interstellar medium: ROSAT observations of dust scattering halos. *A&A*, 293:889–905, January 1995.

W. Press, B. Flannery, S. Teukolsky, and W. Vetterling. *Numerical Recipies in C. The art of scientific computing*. Cambridge University Press, Cambridge, UK, 1995.

D. Psaltis and F. Ozel. Pulse Profiles from Spinning Neutron Stars in the Hartle-Thorne Approximation. *ArXiv e-prints*, May 2013.

M. Rajagopal and R. W. Romani. Model Atmospheres for Low-Field Neutron Stars. *ApJ*, 461:327–+, April 1996.

S. M. Ransom, I. H. Stairs, A. M. Archibald, J. W. T. Hessels, D. L. Kaplan, M. H. van Kerkwijk, J. Boyles, A. T. Deller, S. Chatterjee, A. Schechtman-Rook, et al. A millisecond pulsar in a stellar triple system. *Nature*, 505:520–524, January 2014.

D. G. Ravenhall, C. J. Pethick, and J. R. Wilson. Structure of Matter below Nuclear Saturation Density. *Physical Review Letters*, 50:2066–2069, June 1983.

N. Rea, P. Esposito, R. Turolla, G. L. Israel, S. Zane, L. Stella, S. Mereghetti, A. Tiengo, D. Götz, E. Göğüş, et al. A Low-Magnetic-Field Soft Gamma Repeater. *Science*, 330:944–, November 2010.

N. Rea, G. L. Israel, P. Esposito, J. A. Pons, A. Camero-Arranz, R. P. Mignani, R. Turolla, S. Zane, M. Burgay, A. Possenti, et al. A New Low Magnetic Field Magnetar: The 2011 Outburst of Swift J1822.3-1606. *ApJ*, 754:27, July 2012.

A. Recio-Blanco, G. Piotto, F. de Angeli, S. Cassisi, M. Riello, M. Salaris, A. Pietrinferni, M. Zoccali, and A. Aparicio. A homogeneous set of globular cluster relative distances and reddenings. *A&A*, 432:851–859, March 2005.

R. F. Rees and K. M. Cudworth. A new look at the globular cluster M28. *AJ*, 102: 152–158, July 1991.

R. F. Rees, Jr. Astrometric Distances to Globular Clusters: New Results. In H. L. Morrison & A. Sarajedini, editor, *Formation of the Galactic Halo...Inside and Out*, volume 92 of *Astronomical Society of the Pacific Conference Series*, page 289, April 1996.

B. Riaz, J. E. Gizis, and J. Harvin. Identification of New M Dwarfs in the Solar Neighborhood. *AJ*, 132:866–872, August 2006.

R. T. Ritchings. Pulsar single pulse intensity measurements and pulse nulling. *MNRAS*, 176:249–263, August 1976.

L. F. Roberts, G. Shen, V. Cirigliano, J. A. Pons, S. Reddy, and S. E. Woosley. Protoneutron Star Cooling with Convection: The Effect of the Symmetry Energy. *Physical Review Letters*, 108(6):061103, February 2012.

R. W. Romani. Model atmospheres for cooling neutron stars. *ApJ*, 313:718–726, February 1987.

R. W. Romani. A unified model of neutron-star magnetic fields. *Nature*, 347:741–743, October 1990.

A. Rosenberg, G. Piotto, I. Saviane, and A. Aparicio. Photometric catalog of nearby globular clusters. I. A large homogeneous (V,I) color-magnitude diagram data-base. *A&AS*, 144:5–38, May 2000.

E. Rutherford. The scattering of alpha and beta particles by matter and the structure of the atom. *Philosophical Magazine*, 21:669–688, 1911.

E. Rutherford. Collision of Alpha Particles with Light Atoms. *Philosophical Magazine*, 37:537–587, 1919.

E. Rutherford. Bakerian Lecture. Nuclear Constitution of Atoms. *Royal Society of London Proceedings Series A*, 97:374–400, July 1920.

E. Rutherford. The Disintegration of Elements by Alpha Particles. */nat*, 107:41+, 1921.

R. E. Rutledge and M. Sako. Statistical re-examination of reported emission lines in the X-ray afterglow of GRB 011211. *MNRAS*, 339:600–606, March 2003.

R. E. Rutledge, L. Bildsten, E. F. Brown, G. G. Pavlov, and V. E. Zavlin. The Thermal X-Ray Spectra of Centaurus X-4, Aquila X-1 , and 4U 1608-522 in Quiescence. *ApJ*, 514:945–951, April 1999.

R. E. Rutledge, L. Bildsten, E. F. Brown, G. G. Pavlov, and V. E. Zavlin. A Method for Distinguishing between Transiently Accreting Neutron Stars and Black Holes, in Quiescence. *ApJ*, 529:985–996, February 2000.

R. E. Rutledge, L. Bildsten, E. F. Brown, G. G. Pavlov, and V. E. Zavlin. The Quiescent X-Ray Spectrum of the Neutron Star in Centaurus X-4 Observed with Chandra/ACIS-S. *ApJ*, 551:921–928, April 2001a.

R. E. Rutledge, L. Bildsten, E. F. Brown, G. G. Pavlov, and V. E. Zavlin. Quiescent Thermal Emission from the Neutron Star in Aquila X-1. *ApJ*, 559:1054–1059, October 2001b.

R. E. Rutledge, L. Bildsten, E. F. Brown, G. G. Pavlov, and V. E. Zavlin. Variable Thermal Emission from Aquila X-1 in Quiescence. *ApJ*, 577:346–358, September 2002a.

R. E. Rutledge, L. Bildsten, E. F. Brown, G. G. Pavlov, and V. E. Zavlin. A Possible Transient Neutron Star in Quiescence in the Globular Cluster NGC 5139. *ApJ*, 578:405–412, October 2002b.

R. E. Rutledge, L. Bildsten, E. F. Brown, G. G. Pavlov, V. E. Zavlin, and G. Ushomirsky. Crustal Emission and the Quiescent Spectrum of the Neutron Star in KS 1731-260. *ApJ*, 580:413–422, November 2002c.

G. Sala, F. Haberl, J. José, A. Parikh, R. Longland, L. C. Pardo, and M. Andersen. Constraints on the Mass and Radius of the Accreting Neutron Star in the Rapid Burster. *ApJ*, 752:158, June 2012.

M. Salaris, E. V. Held, S. Ortolani, M. Gullieuszik, and Y. Momany. Deep near-infrared photometry of the globular cluster 47 Tucanae. Reconciling theory and observations. *A&A*, 476:243–253, December 2007.

E. E. Salpeter. Matter at high densities. *Annals of Physics*, 11:393–413, December 1960.

E. L. Sandquist, M. Gordon, D. Levine, and M. Bolte. A Re-evaluation of the Evolved Stars in the Globular Cluster M13. *AJ*, 139:2374–2409, June 2010.

A. S. Schneider, C. J. Horowitz, J. Hughto, and D. K. Berry. Nuclear "pasta" formation. *Phys. Rev. C*, 88(6):065807, December 2013.

M. Servillat, N. A. Webb, and D. Barret. XMM-Newton observations of the Galactic globular clusters NGC 2808 and NGC 4372. *A&A*, 480:397–407, March 2008.

M. Servillat, C. O. Heinke, W. C. G. Ho, J. E. Grindlay, J. Hong, M. van den Berg, and S. Bogdanov. Neutron star atmosphere composition: the quiescent, low-mass X-ray binary in the globular cluster M28. *MNRAS*, 423:1556–1561, June 2012.

H. Shapley. Globular Clusters and the Structure of the Galactic System. *PASP*, 30: 42, February 1918.

G. Shen, C. J. Horowitz, and S. Teige. Equation of state of dense matter from a density dependent relativistic mean field model. *Phys. Rev. C*, 82(1):015806, July 2010a.

G. Shen, C. J. Horowitz, and S. Teige. Equation of state of nuclear matter in a virial expansion of nucleons and nuclei. *Phys. Rev. C*, 82(4):045802, October 2010b.

I. S. Shklovsky. On the Nature of the Source of X-Ray Emission of SCO XR-1. *ApJ*, 148:L1+, April 1967.

L. Sidoli, A. N. Parmar, and T. Oosterbroek. The broad-band X-ray spectrum of the dipping low mass X-ray binary EXO 0748-676. *A&A*, 429:291–296, January 2005.

T. Skyrme. The effective nuclear potential. *Nucl. Phys. A*, 9:615–634, 1959.

S. J. Smartt, J. R. Maund, M. A. Hendry, C. A. Tout, G. F. Gilmore, S. Mattila, and C. R. Benn. Detection of a Red Supergiant Progenitor Star of a Type II-Plateau Supernova. *Science*, 303:499–503, January 2004.

H. A. Smith. RR Lyrae stars. *Cambridge Astrophysics Series*, 27, 1995.

S. L. Snowden and J. H. M. M. Schmitt. The ROSAT diffuse X-ray background survey. *Ap&SS*, 171:207–212, September 1990.

A. W. Steiner, J. M. Lattimer, and E. F. Brown. The Equation of State from Observed Masses and Radii of Neutron Stars. *ApJ*, 722:33–54, October 2010.

A. W. Steiner, J. M. Lattimer, and E. F. Brown. The Neutron Star Mass-Radius Relation and the Equation of State of Dense Matter. *ApJ*, 765:L5, March 2013.

T. E. Sterne. The equilibrium theory of the abundance of the elements: a statistical investigation of assemblies in equilibrium in which transmutations occur. *MNRAS*, 93:736, June 1933.

R. R. Strickler, A. M. Cool, J. Anderson, H. N. Cohn, P. M. Lugger, and A. M. Serenelli. Helium-core White Dwarfs in the Globular Cluster NGC 6397. *ApJ*, 699: 40–55, July 2009.

L. Strüder, U. Briel, K. Dennerl, R. Hartmann, E. Kendziorra, N. Meidinger, E. Pfeffermann, C. Reppin, B. Aschenbach, W. Bornemann, et al. The European Photon Imaging Camera on XMM-Newton: The pn-CCD camera. *A&A*, 365:L18–L26, January 2001.

V. Suleimanov, J. Poutanen, M. Revnivtsev, and K. Werner. A Neutron Star Stiff Equation of State Derived from Cooling Phases of the X-Ray Burster 4U 1724-307. *ApJ*, 742:122, December 2011a.

V. Suleimanov, J. Poutanen, and K. Werner. X-ray bursting neutron star atmosphere models: spectra and color corrections. *A&A*, 527:A139, March 2011b.

J. H. Swank. The Rossi X-Ray Timing Explorer. *Nuclear Physics B Proceedings Supplements*, 69:12–19, January 1999.

J. H. Swank, R. H. Becker, E. A. Boldt, S. S. Holt, S. H. Pravdo, and P. J. Serlemitsos. Spectral evolution of a long X-ray burst. *ApJ*, 212:L73–L76, March 1977.

F. D. Swesty, J. M. Lattimer, and E. S. Myra. The role of the equation of state in the 'prompt' phase of type II supernovae. *ApJ*, 425:195–204, April 1994.

T. Takahashi. The ASTRO-H mission . *Mem. Soc. Astron. Italiana*, 84:776, 2013.

Y. Tanaka, M. Fujii, H. Inoue, N. Kawai, K. Koyama, Y. Maejima, F. Makino, K. Makishima, M. Matsuoka, and K. Mitsuda. X-ray astronomy satellite Tenma. *PASJ*, 36:641–658, 1984.

Y. Tanaka, H. Inoue, and S. S. Holt. The X-ray astronomy satellite ASCA. *PASJ*, 46:L37–L41, June 1994.

T. M. Tauris and E. P. J. van den Heuvel. *Formation and evolution of compact stellar X-ray sources*, pages 623–665. April 2006.

J. H. Taylor and J. M. Weisberg. A new test of general relativity - Gravitational radiation and the binary pulsar PSR 1913+16. *ApJ*, 253:908–920, February 1982.

J. H. Taylor and J. M. Weisberg. Further experimental tests of relativistic gravity using the binary pulsar PSR 1913 + 16. *ApJ*, 345:434–450, October 1989.

V. Testa, C. E. Corsi, G. Andreuzzi, G. Iannicola, G. Marconi, A. M. Piersimoni, and R. Buonanno. Horizontal-Branch Morphology and Dense Environments: Hubble Space Telescope Observations of Globular Clusters NGC 2298, 5897, 6535, and 6626. *AJ*, 121:916–934, February 2001.

C. Thompson and R. C. Duncan. Neutron star dynamos and the origins of pulsar magnetism. *ApJ*, 408:194–217, May 1993.

C. Thompson, M. Lyutikov, and S. R. Kulkarni. Electrodynamics of Magnetars: Implications for the Persistent X-Ray Emission and Spin-down of the Soft Gamma Repeaters and Anomalous X-Ray Pulsars. *ApJ*, 574:332–355, July 2002.

I. B. Thompson, J. Kaluzny, S. M. Rucinski, W. Krzeminski, W. Pych, A. Dotter, and G. S. Burley. The Cluster AgeS Experiment (CASE). IV. Analysis of the Eclipsing Binary V69 in the Globular Cluster 47 Tuc. *AJ*, 139:329–341, February 2010.

R. C. Tolman. Static Solutions of Einstein's Field Equations for Spheres of Fluid. *Physical Review*, 55:364–373, February 1939.

J. A. Tomsick, D. M. Gelino, J. P. Halpern, and P. Kaaret. The Low Quiescent X-Ray Luminosity of the Neutron Star Transient XTE J2123-058. *ApJ*, 610:933–940, August 2004.

J. A. Tomsick, D. M. Gelino, and P. Kaaret. The Low Quiescent X-Ray Luminosity of the Transient X-Ray Burster EXO 1747-214. *ApJ*, 635:1233–1238, December 2005.

J. A. Tomsick, D. M. Gelino, and P. Kaaret. Uncovering the Nature of the X-Ray Transient 4U 1730-22: Discovery of X-Ray Emission from a Neutron Star in Quiescence with Chandra. *ApJ*, 663:461–467, July 2007.

A. Treves, S. B. Popov, M. Colpi, M. E. Prokhorov, and R. Turolla. The Magnificient Seven: Close-by Cooling Neutron Stars? In R. Giacconi, S. Serio, and L. Stella, editors, *X-ray Astronomy 2000*, volume 234 of *Astronomical Society of the Pacific Conference Series*, page 225, 2001.

A. Turlione, D. N. Aguilera, and J. A. Pons. Quiescent thermal emission from neutron stars in LMXBs. *ArXiv e-prints*, September 2013.

M. J. L. Turner, H. D. Thomas, B. E. Patchett, D. H. Reading, K. Makishima, T. Ohashi, T. Dotani, K. Hayashida, H. Inoue, H. Kondo, et al. The large area counter on GINGA. *PASJ*, 41:345–372, 1989.

G. Ushomirsky and R. E. Rutledge. Time-variable emission from transiently accreting neutron stars in quiescence due to deep crustal heating. *MNRAS*, 325:1157–1166, August 2001.

E. Valenti, F. R. Ferraro, and L. Origlia. Near-Infrared Properties of 24 Globular Clusters in the Galactic Bulge. *AJ*, 133:1287–1301, April 2007.

G. van de Ven, R. C. E. van den Bosch, E. K. Verolme, and P. T. de Zeeuw. The dynamical distance and intrinsic structure of the globular cluster ω Centauri. *A&A*, 445:513–543, January 2006.

M. van den Berg, G. Tagliaferri, T. Belloni, and F. Verbunt. A Chandra observation of the old open cluster M 67. *A&A*, 418:509–523, May 2004.

S. van den Bergh. Globular clusters and dwarf spheroidal galaxies. *MNRAS*, 385: L20–L22, March 2008.

M. van der Sluys. *Formation and evolution of compact binaries*. PhD thesis, Utrecht University, 2006.

M. H. van Kerkwijk and D. L. Kaplan. Timing the Nearby Isolated Neutron Star RX J1856.5-3754. *ApJ*, 673:L163–L166, February 2008.

M. H. van Kerkwijk, R. P. Breton, and S. R. Kulkarni. Evidence for a Massive Neutron Star from a Radial-velocity Study of the Companion to the Black-widow Pulsar PSR B1957+20. *ApJ*, 728:95, February 2011.

J. van Paradijs, F. Verbunt, R. A. Shafer, and K. A. Arnaud. Soft X-ray transients in quiescence - Observations of AQL X-1 and CEN X-4. *A&A*, 182:47–50, August 1987.

F. Verbunt. Binary Evolution and Neutron Stars in Globular Clusters. In G. Piotto, G. Meylan, S. G. Djorgovski, and M. Riello, editors, *New Horizons in Globular Cluster Astronomy*, volume 296 of *Astronomical Society of the Pacific Conference Series*, pages 245–+, 2003.

F. Verbunt and C. Bassa. X-ray sources in globular clusters. *Chinese Journal of Astronomy and Astrophysics Supplement*, 3:225–234, December 2003.

F. Verbunt, T. Belloni, H. M. Johnston, M. van der Klis, and W. H. G. Lewin. ROSAT observations of soft X-ray transients in quiescence. *A&A*, 285:903–911, May 1994.

D. Viganò, N. Rea, J. A. Pons, R. Perna, D. N. Aguilera, and J. A. Miralles. Unifying the observational diversity of isolated neutron stars via magneto-thermal evolution models. *MNRAS*, 434:123–141, September 2013.

A. R. Villarreal and T. E. Strohmayer. Discovery of the Neutron Star Spin Frequency in EXO 0748-676. *ApJ*, 614:L121–L124, October 2004.

W. Voges, B. Aschenbach, T. Boller, H. Bräuninger, U. Briel, W. Burkert, K. Dennerl, J. Englhauser, R. Gruber, F. Haberl, et al. The ROSAT all-sky survey bright source catalogue. *A&A*, 349:389–405, September 1999.

W. Voges, B. Aschenbach, T. Boller, H. Brauninger, U. Briel, W. Burkert, K. Dennerl, J. Englhauser, R. Gruber, F. Haberl, et al. Rosat All-Sky Survey Faint Source Catalogue. *IAU Circ.*, 7432:3–+, May 2000.

J. H. Waite, Jr., G. R. Gladstone, K. Franke, W. S. Lewis, A. C. Fabian, W. N. Brandt, C. Na, F. Haberl, J. T. Clarke, K. C. Hurley, et al. ROSAT Observations of X-Ray Emissions from Jupiter During the Impact of Comet Shoemaker-Levy 9. *Science*, 268:1598–1601, June 1995.

F. M. Walter, T. Eisenbeiß, J. M. Lattimer, B. Kim, V. Hambaryan, and R. Neuhäuser. Revisiting the Parallax of the Isolated Neutron Star RX J185635-3754 Using HST/ACS Imaging. *ApJ*, 724:669–677, November 2010.

Z. Wang, R. P. Breton, C. O. Heinke, C. J. Deloye, and J. Zhong. Multiband Studies of the Optical Periodic Modulation in the X-Ray Binary SAX J1808.4-3658 during Its Quiescence and 2008 Outburst. *ApJ*, 765:151, March 2013.

L. L. Watkins, G. van de Ven, M. den Brok, and R. C. E. van den Bosch. Discrete dynamical models of ω Centauri. *MNRAS*, 436:2598–2615, December 2013.

M. G. Watson, A. C. Schröder, D. Fyfe, C. G. Page, G. Lamer, S. Mateos, J. Pye, M. Sakano, S. Rosen, J. Ballet, et al. The XMM-Newton serendipitous survey. V. The Second XMM-Newton serendipitous source catalogue. *A&A*, 493:339–373, January 2009.

N. A. Webb and D. Barret. Constraining the Equation of State of Supranuclear Dense Matter from XMM-Newton Observations of Neutron Stars in Globular Clusters. *ApJ*, 671:727–733, December 2007.

N. A. Webb, P. J. Wheatley, and D. Barret. XMM-Newton X-ray and optical observations of the globular clusters M 55 and NGC 3201. *A&A*, 445:155–165, January 2006.

F. Weber. Strangeness in Compact Stars. In *29th Johns Hopkins Workshop on Current Problems in Particle Theory: Strong Matter in the Heavens*, September 2006.

F. Weber, R. Negreiros, and P. Rosenfield. Neutron Star Interiors and the Equation of State of Superdense Matter. *ArXiv e-prints*, May 2007.

J. M. Weisberg and J. H. Taylor. The Relativistic Binary Pulsar B1913+16: Thirty Years of Observations and Analysis. In F. A. Rasio and I. H. Stairs, editors, *Binary Radio Pulsars*, volume 328 of *Astronomical Society of the Pacific Conference Series*, pages 25–+, July 2005.

S. Weissenborn, D. Chatterjee, and J. Schaffner-Bielich. Hyperons and massive neutron stars: The role of hyperon potentials. *Nuclear Physics A*, 881:62–77, May 2012.

M. C. Weisskopf, H. D. Tananbaum, L. P. Van Speybroeck, and S. L. O'Dell. Chandra X-ray Observatory (CXO): overview. In J. E. Truemper and B. Aschenbach, editors, *X-Ray Optics, Instruments, and Missions III*, volume 4012 of *Society of Photo-Optical Instrumentation Engineers (SPIE) Conference Series*, pages 2–16, July 2000.

R. M. West, A. Lauberts, H.-E. Schuster, and H. E. Jorgensen. Astrometry of SN 1987A and Sanduleak-69 202. *A&A*, 177:L1–L3, May 1987.

N. E. White and A. Peacock. The EXOSAT observatory. *Mem. Soc. Astron. Italiana*, 59:7–31, 1988.

R. Wijnands and M. van der Klis. A millisecond pulsar in an X-ray binary system. *Nature*, 394:344–346, July 1998.

R. Wijnands, C. O. Heinke, and J. E. Grindlay. A Chandra Observation of the Globular Cluster Terzan 1: The Neutron Star X-Ray Transient X1732-304 in Quiescence. *ApJ*, 572:1002–1005, June 2002.

R. Wijnands, C. O. Heinke, D. Pooley, P. D. Edmonds, W. H. G. Lewin, J. E. Grindlay, P. G. Jonker, and J. M. Miller. The Hard Quiescent Spectrum of the Neutron Star X-Ray Transient EXO 1745-248 in the Globular Cluster Terzan 5. *ApJ*, 618:883–890, January 2005.

R. Wijnands, N. Degenaar, and D. Page. Testing the deep-crustal heating model using quiescent neutron-star very-faint X-ray transients and the possibility of partially accreted crusts in accreting neutron stars. *MNRAS*, 432:2366–2377, July 2013.

R. B. Wiringa, V. Fiks, and A. Fabrocini. Equation of state for dense nucleon matter. *Phys. Rev. C*, 38:1010–1037, August 1988.

R. A. Wolf. Some Effects of the Strong Interactions on the Properties of Neutron-Star Matter. *ApJ*, 145:834, September 1966.

H. Wolter. Spiegelsysteme streifenden Einfalls als abbildende Optiken für Röntgenstrahlen. *Annalen der Physik*, 445:94–114, 1952.

K. S. Wood, J. F. Meekins, D. J. Yentis, H. W. Smathers, D. P. McNutt, R. D. Bleach, H. Friedman, E. T. Byram, T. A. Chubb, and M. Meidav. The HEAO A-1 X-ray source catalog. *ApJS*, 56:507–649, December 1984.

K. A. Woodley, R. Goldsbury, J. S. Kalirai, H. B. Richer, P.-E. Tremblay, J. Anderson, P. Bergeron, A. Dotter, L. Esteves, G. G. Fahlman, et al. The Spectral Energy Distributions of White Dwarfs in 47 Tucanae: The Distance to the Cluster. *AJ*, 143:50, February 2012.

P. M. Woods and C. Thompson. *Soft gamma repeaters and anomalous X-ray pulsars: magnetar candidates*, pages 547–586. April 2006.

S. E. Woosley and T. A. Weaver. The physics of supernova explosions. *ARA&A*, 24: 205–253, 1986.

H. Yukawa. On the interaction of elementary particles. i. *Progress of Theoretical Physics Supplement*, 1:1–10, 1935. URL `http://ptps.oxfordjournals.org/content/1/1.1.short`.

N. Zacharias, D. G. Monet, S. E. Levine, S. E. Urban, R. Gaume, and G. L. Wycoff. NOMAD Catalog (Zacharias+ 2005). *VizieR Online Data Catalog*, 1297:0–+, November 2005.

M. Zamfir, A. Cumming, and D. K. Galloway. Constraints on Neutron Star Mass and Radius in GS 1826-24 from Sub-Eddington X-Ray Bursts. *ApJ*, 749:69, April 2012.

V. E. Zavlin and G. G. Pavlov. Modeling Neutron Star Atmospheres. In W. Becker, H. Lesch, and J. Trümper, editors, *Neutron Stars, Pulsars, and Supernova Remnants*, page 263, 2002.

V. E. Zavlin, G. G. Pavlov, and Y. A. Shibanov. Model neutron star atmospheres with low magnetic fields. I. Atmospheres in radiative equilibrium. *A&A*, 315:141–152, November 1996.

G. Zweig. An SU(3) Model for Strong Interaction Symmetry and its Breaking. *CERN Report*, 8182:TH.401, January 1964.